Mesenchymal Stromal Cells to Treat Lung and Brain Injury in Neonatal Models of Chronic Lung Disease

By: Marissa Athena Lithopoulos

Thesis submitted to the University of Ottawa in partial fulfillment of the requirements for the PhD degree in Cellular and Molecular Medicine.

Department of Cellular and Molecular Medicine
Faculty of Medicine
University of Ottawa

Dedication

This dissertation is affectionately dedicated to my brother, Eric.

You lost the fight as you struggled to breathe

You received your wings far too soon

Although you were born silent, your short life spoke volumes

For it was you, little one, who inspired me to pursue neonatal research

My fervent hope is that the work presented in this dissertation will one day help other preterm babies to thrive and flourish.

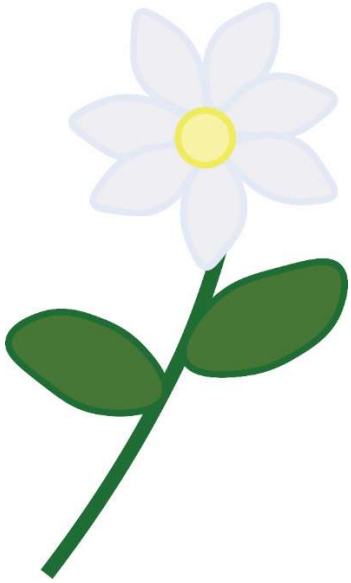

Table of Contents

List of Figures

List of Appendix Figures

List of Appendix Tables

List of Abbreviations

α-MEM	Minimum essential medium–α modification
APC	Allophycocyanin
Arg-1	Arginase-1
AT1	Alveolar type 1
AT2	Alveolar type 2
BLBP	Brain lipid binding protein
BM	Bone marrow
BPD	Bronchopulmonary dysplasia
BSA	Bovine serum albumin
BV421	Brilliant violet 421
CA	Cornu ammonis
CBF	Cerebral blood flow
CD	Cluster of differentiation
CDM	Conditioned media
cDNA	Complementary deoxyribonucleic acid
ChIP-seq	Chromatin immunoprecipitation sequencing
CNS	Central nervous system
CXCL-1	C-X-C motif ligand-1
CXCR4	C-X-C chemokine receptor type 4
DAB	3,3′-Diaminobenzidine
DAPI	4',6-Diamidino-2-phenylindole
DCX	Doublecortin

DG	Dentate gyrus
DiR	1,1'-Dioctadecyl-3,3,3',3'-tetramethylindotricarbocyanine iodide
DLS	Dynamic light scattering
Dlx2	Distal-less homeobox 2
DMEM/F-12	Dulbecco's modified eagle medium/nutrient mixture media/F-12
EC	Endothelial cell
EDTA	Ethylenediaminetetraacetic acid solution
EGF	Epidermal growth factor
ERG	Electroretinography
EV	Extracellular vesicle
FACS	Fluorescence-activated cell sorting
FBS	Fetal bovine serum
FEV_1	Forced expiratory volume in 1 second
FITC	Fluorescein isothiocyanate
FSC	Forward scatter
GAD65	Glutamic acid decarboxylase 65
GCL	Granule cell layer
GCSF	Granulocyte colony stimulating factor
GFAP	Glial fibrillary acidic protein
GMCSF	Granulocyte-macrophage colony-stimulating factor
HBSS	Hank’s balanced salt solution
HIF-1α	Hypoxia-inducible factor 1-α
HLA-DR	Human leukocyte antigen-DR isotype

HPF	High-power field
HRP	Horseradish peroxide
IFN-γ	Interferon-γ
IL	Interleukin
ISCT	International Society for Cellular Therapy
IVH	Intraventricular hemorrhage
KC	Keratinocyte chemoattractant
LIF	Leukemia inhibitory factor
LIX	C-X-C motif ligand-5
LPS	Lipopolysaccharide
LV	Lateral ventricle
MA	Mantle
Mash1	Mammalian achaete-scute homolog 1
MCM2	Minichromosome maintenance complex component 2
MCP-1	Monocyte chemoattractant protein-1
MCSF	Macrophage colony-stimulating factor
MIG	Monocyte induced by gamma interferon
MIP	Macrophage inflammatory protein
miRNA	Micro ribonucleic acid
ML	Molecular layer
MLI	Mean linear intercept
MRI	Magnetic resonance imaging
mRNA	Messenger ribonucleic acid

MSC	Mesenchymal stromal cell
MZ	Marginal zone
NE	Neuroepithelium
NeuN	Neuronal nuclei
nIPC	Neurogenic progenitor cell
NPC	Neural progenitor cell
NSC	Neural stem cell
NTA	Nanoparticle tracking analysis
NVC	Neurovascular coupling
NVU	Neurovascular unit
OB	Olfactory bulb
OCT	Optimal cutting temperature compound
oIPC	Oligodendrocyte progenitor cell
O_2	Oxygen
O4	Oligodendrocyte marker O4
PBS	Phosphate buffered saline
PE	Phycoerythrin
PFA	Paraformaldehyde
PLO	Poly-L-ornithine
PNVP	Perineural vascular plexus
Prox1	Prospero-related homeobox 1
PVL	Periventricular leukomalacia
PVP	Periventricular vascular plexus

RANTES	Regulated on activation, normal T cell expressed and secreted
RGC	Radial glial cell
RIPA	Radioimmunoprecipitation assay buffer
RMS	Rostral migratory stream
RNA	Ribonucleic acid
ROP	Retinopathy of prematurity
ROS	Reactive oxygen species
RT-qPCR	Reverse transcription-quantitative polymerase chain reaction
SDF1	Stromal cell-derived factor 1
SEM	Standard error of the mean
SGZ	Subgranular zone
siRNA	Small interfering ribonucleic acid
SVZ	Subventricular zone
Tbr2	T-box brain protein-2
TBS-T	Tris buffered saline with tween 20
TGF-β	Transforming growth factor-β
TNF-α	Tumour necrosis factor-α
Tuj1	Neuron-specific β3 tubulin
UC	Umbilical cord
UC-MSC	Umbilical cord-mesenchymal stromal cell
VEGF	Vascular endothelial growth factor
VILI	Ventilation-induced lung injury
vWF	von Willebrand factor

VZ	Ventricular zone
YFP	Yellow fluorescence protein

Acknowledgements

"If I have seen further it is by standing on the shoulders of giants." – *Sir Isaac Newton*

This dissertation would not have materialized without the tireless contributions of many wonderful people who helped me on this journey. *I want to take a moment to thank them.*

I am immensely grateful to my supervisor, Dr. Bernard Thébaud, who works tirelessly to advance neonatal lung care. Thank you for your guidance and wisdom, and for believing in my potential. You are an incredible mentor. You taught me important lessons for success, both in science and in life. You taught me to believe in myself and my intuition. You showed me how to focus my energy and enthusiasm to make a real difference in the world. These pivotal lessons will remain with me wherever I go. You and the Xplore Lab will always be close to my heart.

Next, I would like to thank the exceptional examiners for their helpful feedback and guidance. I also wish to express my sincere gratitude to the stellar members of my dissertation committee, Dr. Ruth Slack, Dr. Jing Wang, and Dr. Bill Stanford, for their guidance, helpful career advice, and feedback. You are all exceptional role models and mentors. I am especially grateful to Dr. Slack and Dr. Wang for the training in neuroscience techniques received in your labs. And to Dr. Stanford, your thought-provoking questions and critiques always elevated the project.

My deepest gratitude to our incredible collaborators. To Dr. Diane Lagace, thank you for your assistance in deciphering behavior experiments and for being readily available to offer guidance. To Dr. Baptiste Lacoste and Dr. Xavier Toussay, I am immensely grateful for your guidance, training, and invaluable feedback. Special thanks also to Julie Ouellette, Dr. Dylan Burger, Dr. Catherine Tsilfidis, Hayam Bassam, Adam Baker, Dr. Cesar Comin, Dr. Megan O'Reilly, Dr. Marius Möbius, Farah Eaton, Dr. Moses Fung, Dr. Maria Hurskainen, Dr. Chanèle Cyr-Depauw, Dr. Colin Suen, and Dr. Duncan Stewart, for your skillful contributions to the

project. To the entire team in Texas, thank you for your expertise and dedication to the work and for welcoming me so warmly. To Dr. Steven Seidner, thank you for providing me with an incredible training opportunity. To Dr. Shamimunisa Mustafa, my excellent supervisor and friend, it was a wonderful opportunity to learn from you. You went above and beyond to help me reach my goal, and I will never forget how generous you were with your time. My heartfelt thanks also to Dr. Cynthia Blanco for your assistance and support. To Dr. Alvaro Moreira, I am especially grateful for your kindness and for being readily available to provide intellectual guidance and advice. And special thanks to the lovely Cristalina Trevino for making me feel so welcome and for giving the workplace a little extra sparkle.

I wish to also express my sincere gratitude to my affiliated institutions, the Ottawa Hospital Research Institute and the University of Ottawa, as well as the University of Texas Health Science Center at San Antonio, for providing top tier environments to allow for cutting-edge research and also for being like a second home to me at some point during this incredible journey.

Thank you to the University of Ottawa and the Ontario Government for their financial support through an Ontario Graduate Scholarship, Admission and Excellence Scholarships, and philosophy teaching assistantships. I am grateful to the Canadian Institutes of Health Research for the Frederick Banting and Charles Best Doctoral Scholarship, and the Michael Smith Foreign Study Supplement. Also, thank you to the Stem Cell Network for generous funding support.

To Dr. Nigel DeSouza, my philosophy professor, teaching assistant supervisor, and friend, I profoundly appreciate your ongoing support. Thank you for preparing numerous letters of support towards my grant applications—I very much appreciate the time, effort, and our success rate! I am also grateful for your words of wisdom, your kindness, and your enthusiasm for learning.

To Xplore lab members and alumni, thank you so much for your support. I am particularly grateful for the assistance given by Dr. Arul Vadivel, Shumei Zhong, and Liqun Xu towards the success of our projects and for your friendship. To Dr. Jennifer Collins, thanks for being an excellent mentor in my early years in the lab! To Dr. Lannae Strueby, thank you for your hard work and dedication to the project (many early mornings!). I also wish to thank Dr. Lars Mense for his friendship, enthusiastic support, and for being a fantastic tour guide in Germany. Thank you also to Adrienne Szalamin, who has always been there to offer help and guidance. You are all wonderful colleagues!

To my friends, I thank you for your love and support through the good and the challenging times. I am grateful to have every one of you in my life. To my gymnastics coach Dasa, I will be forever grateful for your wisdom, encouragement, and support. Thank you for offering me my first job as a coach.

To my family, Mom and Dad, I love you and I am proud to call you my parents. You are strong, inspiring, and kind. Thank you for encouraging me to pursue my dreams. To my brother, Alex, who thinks he is funnier than he really is, you are an amazing big brother and role model! Thank you for the laughs, guidance, and support and for acknowledging that you have an incredible sister! To Andrew, thank you for your support and love and for all the wonderful things that you continue to do for me. I am excited to start this next chapter with you by my side. And lastly, to my fur babies, Finn, Faye, Dimos, and Kristal, you are the best stress relievers I know. My beloved Kristal—I miss you and I am grateful for your friendship of 17 years! And to Finn—thank you for curling up beside me late into the night, month after month as I worked, always keeping an eye on me—the truth is Finn, although I rescued you from a shelter, in the end, it was you who rescued me.

Abstract

Preterm birth (<37 weeks) is the world's principal cause of death of children <5 years of age. Bronchopulmonary dysplasia (BPD) is the most common complication of preterm birth. BPD is characterized by an arrest in alveolar and vascular development within the lung. It is a multifactorial disease, caused by a combination of supplemental oxygen, mechanical ventilation, and inflammation. BPD is also an independent risk factor for abnormal neurodevelopment. The link between BPD and abnormal neurodevelopment is poorly understood and there are currently no effective cures for these complications. We hypothesized that a crucial cell population for brain development, i.e., the neural progenitor cell (NPC) is functionally impaired in BPD and that this impairment is associated with abnormal neurodevelopment. Based on our previous findings, we also predicted that human umbilical cord-mesenchymal stromal cell (UC-MSC) extracellular vesicles (EVs), could mitigate both the lung and brain injuries in experimental BPD. We utilized several animal models of BPD, across multiple species, to determine the effects of hyperoxia, mechanical ventilation, and inflammation on the developing lungs and brain. We also utilized UC-MSC therapy to mitigate these injuries. We discovered that hyperoxia exposure damages the developing lungs as well as the brain, leading to cerebrovascular and NPC impairments, as well as reduced neurogenesis. These impairments were associated with neurobehavioural deficits in adulthood. Furthermore, we found that inflammation in combination with mechanical ventilation and hyperoxia also impairs NPC function. Importantly, we demonstrated that UC-MSC EVs can reduce inflammation, improve vascular growth, restore lung growth, and mitigate impairments in NPC self-renewal. This work highlights novel mechanisms of BPD-associated abnormal neurodevelopment and offers potential regenerative medicine therapies to alleviate these outcomes for this vulnerable population.

Authorizations

Animal Care

All procedures involving mice were approved by the University of Ottawa Animal Care Committee or the University of Alberta Institutional Animal Care and Use Committee. All procedures involving baboons were approved by the University of Texas Health Science Center at San Antonio Institutional Animal Care and Use Committee.

Copyright

Figure 2: Reprinted with permission from Springer Nature: Springer Nature, Nature Reviews Primer, Bronchopulmonary dysplasia, Thébaud B. et al., Copyright © 2020. The material was originally adapted from Whitsett, J. A., Wert, S. E. & Trapnell, B. C. Genetic disorders influencing lung formation and function at birth. *Hum. Mol. Genet.* **13 Spec No 2**, R207-215 (2004) and reprinted with permission from Oxford University Press.

Figure 3: Reprinted with permission of the American Thoracic Society.

Copyright © 2020 American Thoracic Society. All rights reserved.

Bernard Thébaud, Steven H Abman/ 2007/ Where Have All the Vessels Gone? Roles of Angiogenic Growth Factors in Chronic Lung Disease/ American Journal of Respiratory Critical Care Medicine/ Vol 175/ Pages 978-985.

The American Journal of Respiratory and Critical Care Medicine is an official journal of the American Thoracic Society.

Figure 4: Reprinted with permission from Pediatrics, Vol. 141, Copyright © 2020 by the AAP.

Figure 6: Republished with permission from Annual Reviews, Inc., from The Adaptive Brain: Aging and Neurocognitive Scaffolding, Park DC, Reuter-Lorenz P, Vol 60, Copyright © 2020; permission conveyed through Copyright Clearance Center, Inc. The material was originally

adapted from Park, D. C. *et al.* Models of visuospatial and verbal memory across the adult life span. *Psychol Aging* **17**, 299–320 (2002) with permission from the American Psychological Association.

Figure 7: Reprinted with permission from Springer Nature: Springer Nature, Nature Reviews Cancer, Vescovi AL, Galli R, Reynolds BA, Copyright © 2020. The material was originally adapted and reproduced with permission from Sanai, N., Alvarez-Buylla, A. & Berger, M. S. Neural stem cells and the origin of gliomas. N Engl J Med 353, 811–822 (2005), Copyright Massachusetts Medical Society.

Figure 8: Republished with permission from Annual Reviews, Inc., from The Glial Nature of Embryonic and Adult Neural Stem Cells, Kriegstein A, Alvarez-Buylla A, Vol 32, Copyright © 2020; permission conveyed through Copyright Clearance Center, Inc.

Figures 9 & 10: Reprinted with permission from Elsevier, Guo-li Ming, Hongjun Song, 2011, Neuron, Vol. 70, Pages 687-702, Copyright © 2020.

Figure 11: Adapted with permission from Springer Nature: Springer Nature, Nature Reviews Neuroscience, New neurons and new memories: how does adult hippocampal neurogenesis affect learning and memory?, Wei Deng et al., Copyright © 2020.

Figure 33: Reprinted with permission from CMAJ (Copyright © 2020): Luu TM, Katz SL, Leeson P, Thébaud B, and Nuyt A, Preterm birth: risk factor for early-onset chronic diseases, CMAJ July 12, 2016; 188 (10) 736-746, www.cmaj.ca, © 2016 Joule Inc. or its licensors.

Figure 35: Reprinted and modified in accordance with the Creative Commons Attribution License (CC BY). Copyright © 2019 Karakatsani, Shah and Ruiz de Almodovar. Figure 1A from Karakatsani A, Shah B, and Ruiz de Almodovar C, Blood Vessels as Regulators of Neural Stem Cell Properties, Front Mol Neurosci. 2019; 12: 85.

https://creativecommons.org/licenses/by/4.0/legalcode

Figure 36: Reproduced with permission from (Baraldi, E. & Filippone, M. Chronic lung disease after premature birth. *N. Engl. J. Med.* **357**, 1946–1955 (2007)), Copyright Massachusetts Medical Society. The material was originally adapted from Fletcher, C. & Peto, R. The natural history of chronic airflow obstruction. Br Med J 1, 1645–1648 (1977) with permission from BMJ Publishing Group Ltd.

Introduction

Preterm Birth—A Global Healthcare Concern

Preterm birth is a global healthcare concern, remaining the worldwide principal cause of death of children under five-years-old[1]. Preterm birth is defined as any birth occurring before 37 weeks of gestation[1]. There are several risk factors for premature delivery. These include low socioeconomic status[2], smoking[3,4], substance abuse[5–8], inflammation/infections such as chorioamnionitis[9], and multiple pregnancy (twins or triplets)[10,11]. Annually, preterm birth accounts for approximately 8% of births across Canada[12].

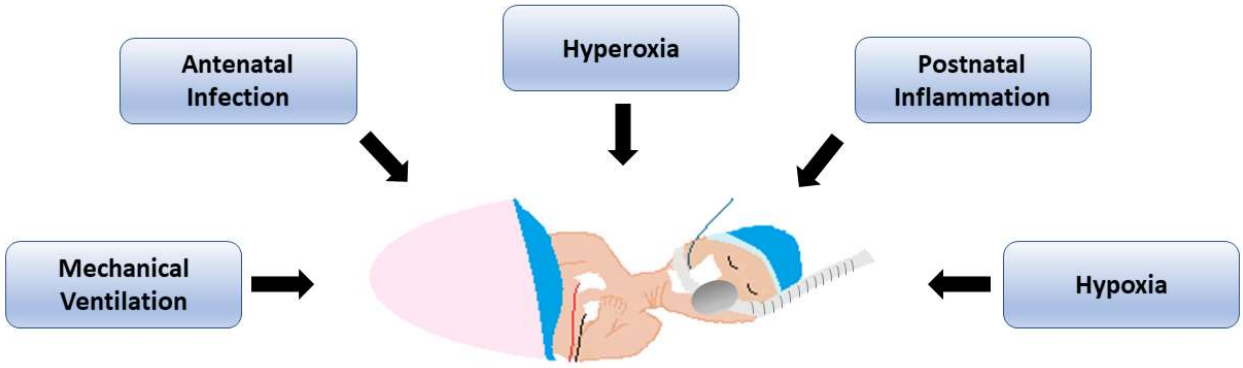

Figure 1. Multiple factors leading to preterm birth complications.

The most vulnerable preterm patients are infants born extremely premature (<28 weeks of gestation)[13]. An extremely premature infant has a wide range of challenges to overcome in order to survive (Figure 1). Intrauterine inflammation, or chorioamnionitis, resulting from an antenatal infection, is present in approximately 25-40% of preterm births[14–16]. Preterm infants are also at a high risk of postnatal inflammation, such as sepsis[13]. Moreover, extremely preterm infants often experience acute respiratory distress and periods of hypoxia due to their underdeveloped lungs[17].

Extremely preterm infants are born during the late canalicular or early saccular stage of lung development[18], whereas term infants are born during the final stage of lung development, i.e., the alveolar stage[19] (Figure 2). The canalicular stage is defined by the maturation of the distal airways, which form the bronchioles and alveolar ducts[20]. The completion of the canalicular stage is marked by thinning of the air-blood barrier to facilitate gas exchange[21]. The saccular stage follows, which is characterized by the differentiation of alveolar type 1 (AT1) and type 2 (AT2) cells[22]. AT1 cells play an important role in the gas exchange between air spaces and capillaries[23]. AT2 cells secrete surfactant, a crucial compound which reduces the surface tension of alveoli, in order to maintain alveolar structure[24,25]. The pulmonary vascular system develops in parallel with the respiratory architecture. In fact, studies show that the respiratory and vascular structures within the developing lung provide a mutually beneficial role for proper branching[26,27]. Extreme prematurity disrupts these critical processes[28].

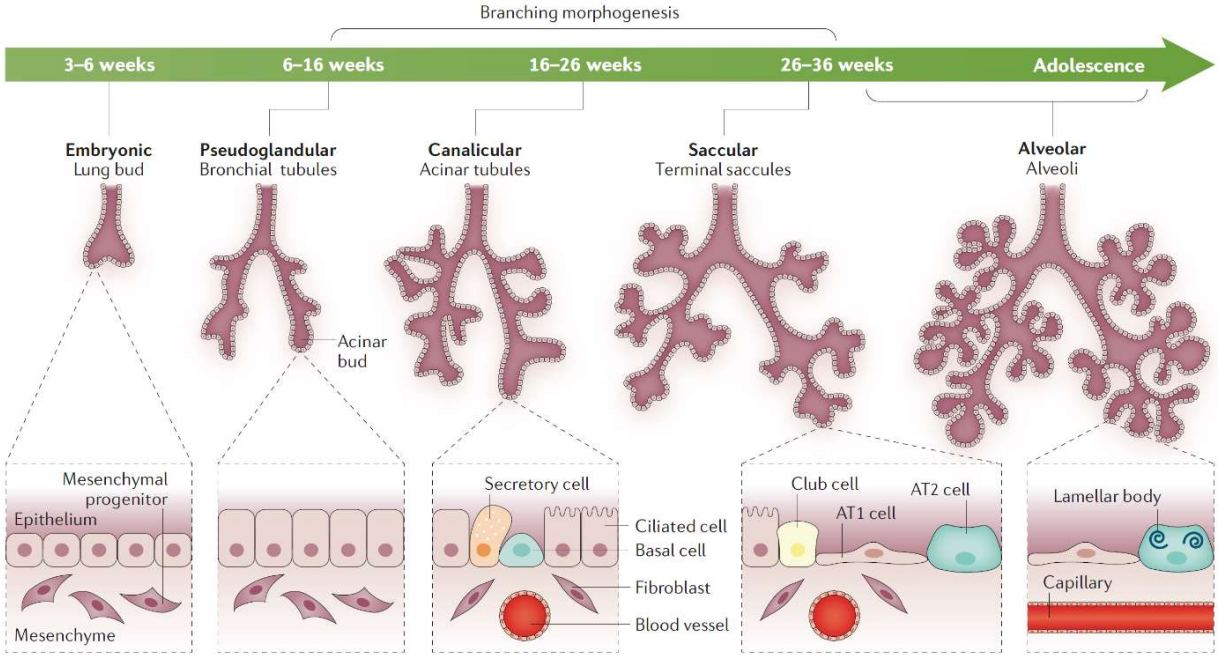

Figure 2. The stages of lung development. AT1 cell, alveolar type 1; AT2 cell, alveolar type 2 cell. Adopted from Thébaud et al.[22], with permission (*see* authorizations).

To overcome respiratory distress due to lung immaturity, extremely preterm infants receive mechanical ventilation and supplemental oxygen to survive. Mechanical ventilation delivers oxygen to the developing lung by means of positive pressure. Under normal physiological conditions, the human lung supports breathing via negative pressure; therefore, oxygen delivered by positive pressure can lead to an overdistension of the tissue, damaging the lung[29]. Furthermore, depending on the severity of the respiratory distress experienced by the preterm infant, supplemental oxygen can be administered at varying concentrations, ranging from 21% - 100% O_2[30]. Extremely preterm infants are selectively vulnerable to oxygen for 3 main reasons. First, *in utero*, the fetus develops within a hypoxic environment until birth[31]. Second, preterm infants have immature vascular autoregulation systems[32–35]. Third, a preterm infant's antioxidant defenses are not fully developed[31]. Hence, a preterm infant will be exposed to hyperoxic conditions at birth and will be poorly equipped to respond to this physiological challenge.

Bronchopulmonary Dysplasia—The Most Common Complication of Extreme Prematurity

The multiple factors of inflammation, hypoxia, mechanical ventilation, and hyperoxia contribute to the most prevalent complication of extreme prematurity, bronchopulmonary dysplasia (BPD)[36], a chronic lung disease (Figure 3).

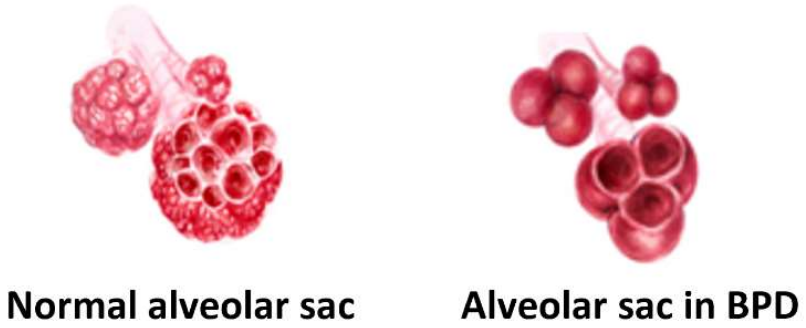

Figure 3. Bronchopulmonary dysplasia (BPD) is characterized by abnormal lung growth. Modified from Thébaud et al.[37], with permission (*see* authorizations).

BPD was first characterized in 1967 by Northway et al.[38], where inflammation, perimucosal fibrosis, and peribronchial smooth muscle hypertrophy were the main reported pathologies of the disease. More than half a century later, this is now referred to as the "old BPD". Improvements in neonatal care, such as milder ventilation practices, surfactant therapy, and prenatal steroid administration have: i) greatly reduced the chance of BPD in infants born >30 weeks of gestation and ii) increased survival of extremely premature infants, which also increased their risk of developing the disease[36]. This shift in age of patients developing BPD led to a distinct change in disease pathology[36]. The "new BPD", first described in 1998 by Hussain et al.[39], differs from the "old BPD" in two fundamental ways. First, there is significantly less fibrosis. Second, there is an arrest in lung growth. This includes an interruption in alveolar and vascular development[22,40]. Specifically, there is abnormal alveolar growth, leading to larger and fewer alveoli, which greatly decreases the surface area available for gas exchange to occur[40]. Moreover, the secretion of angiogenic growth factors, such as vascular endothelial growth factor (VEGF), from respiratory epithelial cells is reduced and there is a reduction and irregular distribution of the microvasculature[41–43]. The current clinical definition of BPD is the requirement for oxygen supplementation at 36 weeks postmenstrual age for infants born earlier than 32 weeks of gestation[36]. Approximately 40% of extremely preterm infants will be diagnosed with BPD[13].

BPD—An Independent Risk Factor for Abnormal Neurodevelopment

BPD has been identified as an independent risk factor for abnormal neurodevelopment[44]. The term "abnormal neurodevelopment" is defined as moderate to severe cerebral palsy, hearing loss, bilateral blindness, and cognitive impairments, i.e., scoring <70 on the Psychomotor Developmental Index and the Bayley Mental Development Index[44]. Motor impairments of children born extremely premature, covered under the cerebral palsy diagnosis, occur in approximately 7-

20% of the patient population[45–50]. These include gait phenotypes such as slow movements, tip-toeing, and taking fewer steps during walking[51,52]. Hearing and vision loss occur in an estimated 2-3% or 0.7-9% of extremely preterm infants, respectively. These descriptions include conductive and sensorineural hearing loss, as well as a range of visual impairments, from poor visual acuity to complete blindness[53]. Lastly, cognitive and intelligence impairments are observed in 25-50% of extremely preterm infants. These include deficits in reasoning, listening comprehension, working memory, learning, executive functions, and verbal and performance IQ[54–56] (Figure 4).

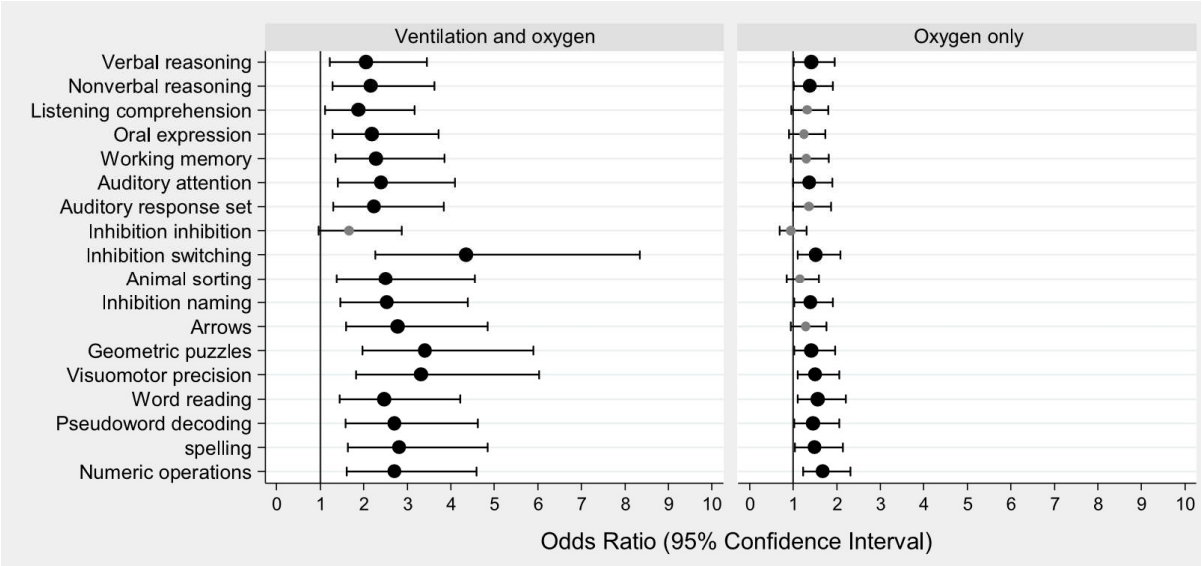

Figure 4. Extremely preterm infants are at a high risk of abnormal neurodevelopment. Adopted from Sriram et al.[56], with permission (*see* authorizations).

Critically, preterm patients who develop BPD show significantly greater neurodevelopmental impairments compared to their non-BPD peers, as measured by multiple factors including cognition, intelligence, and motor function[57,58]. Compared to non-BPD preterm patients, patients diagnosed with BPD are at a 10-fold higher risk of executive function deficits[57], poorer academic results in reading and mathematics[58], lower IQ scores[59], and ranking lower on cognitive and motor function assessments[56,60]. This suggests that preterm-born patients with BPD display a more severe brain injury compared to preterm-born patients who do not develop the lung disease.

Long-Term Effects of BPD-Associated Injuries

Although BPD is characterized as a neonatal injury, its effects are chronic, continuing into adulthood. Childhood assessments of patients diagnosed with BPD during infancy report worse lung function outcomes compared to their age-matched peers, including lower forced expiratory volume and forced mid-expiratory flow[61]. Approximately 30% of BPD patients will report asthma symptoms during follow-up at 11 years of age[62]. These poor lung function outcomes continue into adolescence and adulthood[63–66]. As adults, BPD subjects have a two-fold greater risk of reporting wheezing and a two to three-fold greater risk of requiring asthma medication compared to non-BPD preterm birth survivors and term control peers[67]. Moreover, adult BPD patients challenged with exercise on a bicycle demonstrate limited exercise capacity, with a significant increase in heart rate during exercise[68] and a significantly greater limitation of exercise-induced expiratory flow[69] compared to non-BPD preterm born patients and term control patients. Furthermore, the neurodevelopmental impairments described above, including motor, cognitive, and sensory deficits, continue into adulthood[70–72].

Clinical follow-up of preterm-born patients is limited to early adulthood (<30 years of age). Surprisingly, the effects of extreme prematurity, or more specifically, BPD-associated injuries during the aging process are poorly understood (Figure 5).

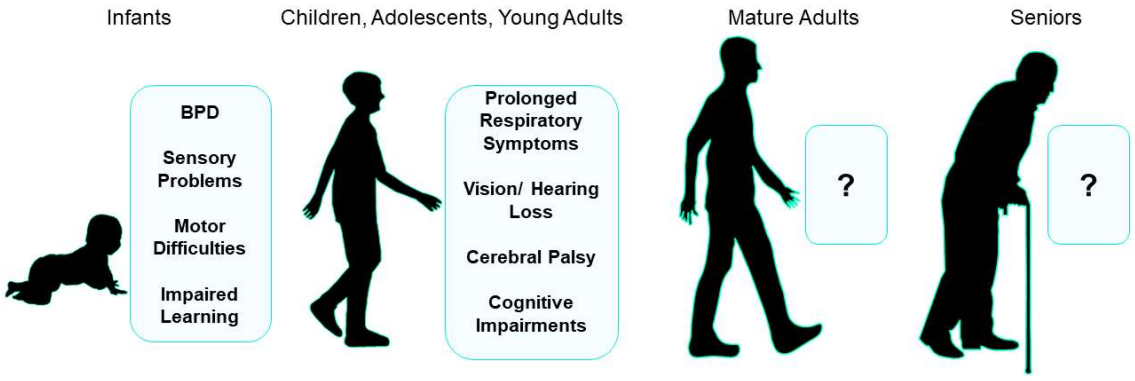

Figure 5: The lifelong effects of BPD-associated injury remain poorly understood.

Linsell et al.[73] reported that they observed no significant cognitive recovery or deterioration from the neonatal period to 19 years of age in a cohort of over 300 patients born prior to 26 weeks of gestation. Since neuroimaging studies reveal that brain maturation continues into the 20s[74,75], the current longitudinal studies of preterm born patients assessed a relatively young adult brain. There is considerable evidence that during the normal aging process cognitive abilities change (Figure 6). A slow deterioration in conceptual reasoning, memory, and speed of cognitive and motor activities occurs with aging[76]. Whether or not these changes become more pronounced in extremely preterm born patients is unknown. Hence, there is a critical need to further explore BPD-associated outcomes throughout the lifespan.

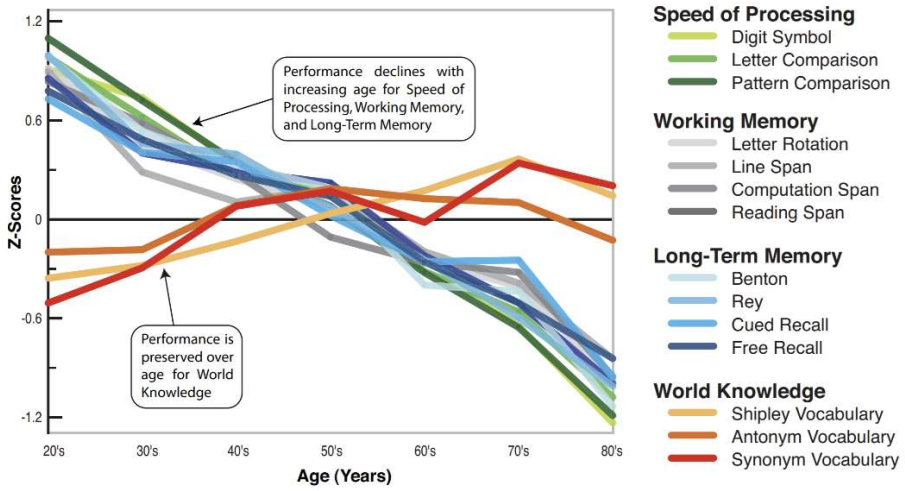

Figure 6. Deterioration of cognitive abilities with age. Adopted from Park et al.[77], with permission (*see* authorizations).

Neural Progenitor Cells—Critical for Brain Development—Remain Unexplored in BPD

The relationship between BPD and its associated abnormal neurodevelopment is not well understood. It is unclear whether the lung injury directly affects brain development or if both injuries occur in parallel. The neonatal field has identified and described two main brain injuries observed in premature infants in the clinic—intraventricular hemorrhage and encephalopathy of prematurity. These are described as bleeding within the lateral ventricles and periventricular

leukomalacia (white matter injury), respectively[78–80]. However, these pathologies are not always detected in preterm infants who later show cognitive impairments[81]. This therefore suggests that other brain injuries are contributing to the abnormal neurodevelopmental outcomes of preterm infants. Neural progenitor cells (NPCs) constitute a brain cell population that is crucial for brain development and cognition throughout the lifespan[82–85]. NPC is a broad identifier for both neural stem cells (NSCs) and their progenitors[83,86]. NPCs have not been investigated in BPD and thus, it remains unknown whether their function is impaired in preterm infants with BPD, contributing to abnormal neurodevelopment. NPCs reside postnatally in the subventricular zone (SVZ) and subgranular zone of the dentate gyrus (DG) of the hippocampus (Figure 7)[87].

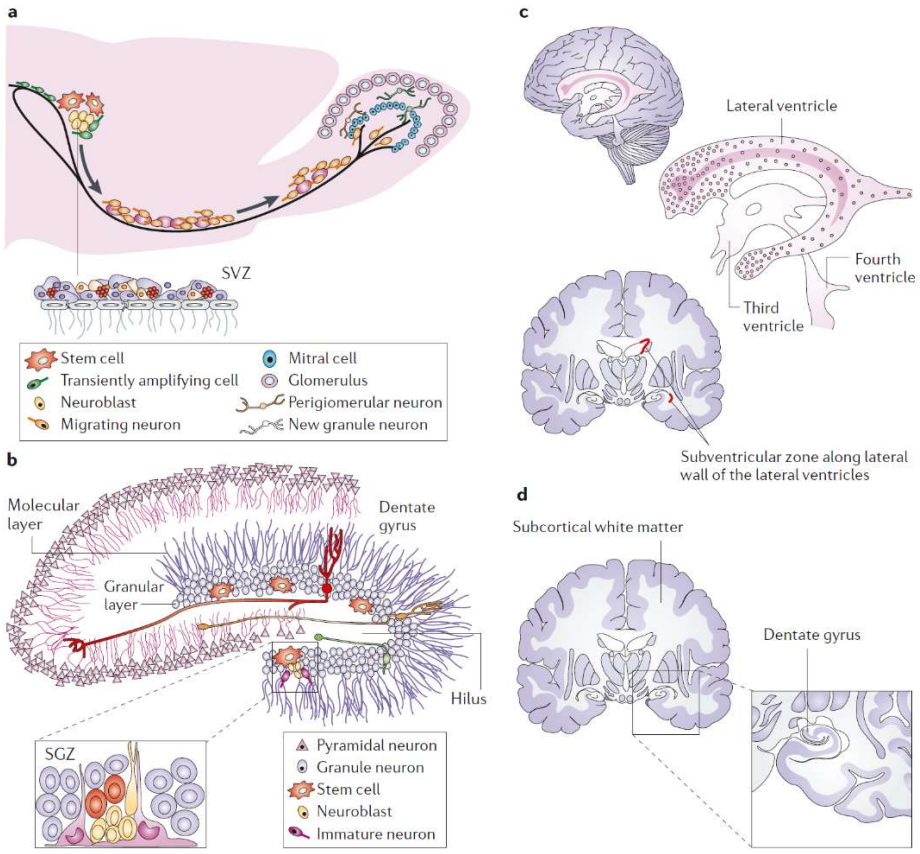

Figure 7. Postnatal neural progenitor cell (NPC) niche regions. a, NPCs residing in the subventricular zone differentiate into neuroblasts and immature neurons which migrate along the rostral migratory stream to the olfactory bulb. **b**, NPCs also reside within the subgranular zone of the dentate gyrus, **c**, **d**, The anatomical location of the subventricular zone and dentate gyrus within the human brain. SVZ, subventricular zone; SGZ subgranular zone. Adopted from Vescovi et al.[87], with permission (*see* authorizations).

Primary NPCs (NSCs)[83] have two main functions. First, the cell is required to maintain its ability to self-renew. Hence, primary NPCs can maintain their population throughout adult life[88]. Second, the cell must be capable of differentiating into the three main lineages of the brain, i.e., astrocytes, neurons, and oligodendrocytes[89] (Figure 8). Thus, life-long NPC differentiation plays an important role in critical brain development and functions, such as neurogenesis, i.e., the formation of newborn neurons[90].

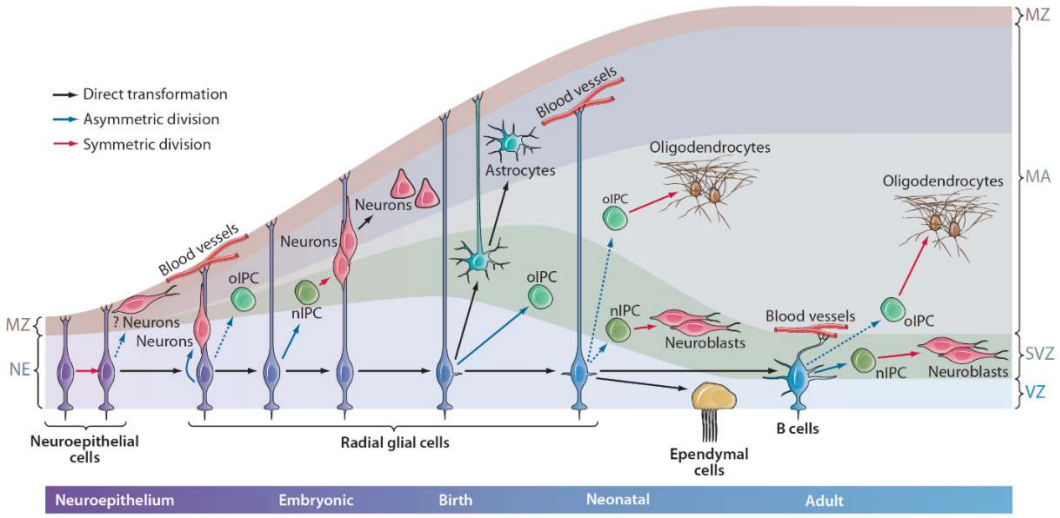

Figure 8. Primary NPCs contribute to brain development by self-renewing and differentiating into the main brain lineages. Early NSCs (neuroepithelial cells) divide symmetrically to self-renew and divide asymmetrically to generate early neurons. As development progresses, neuroepithelial cells elongate and become radial glial cells (embryonic/ neonatal NSCs). Radial glial cells can divide asymmetrically to directly form new neurons and astrocytes, or to indirectly form these cells through intermediate progenitors. Radial glial cells also form oligodendrocytes by means of intermediate progenitor cells. As the brain continues to develop and thicken, radial glial cells form ependymal cells which line the ventricles or transform to B cells (mature NSCs) which will continue to populate the brain with newborn cells during adulthood. MZ, marginal zone; NE, neuroepithelium; oIPC, oligodendrocyte progenitor cell; nIPC, neurogenic progenitor cell; MA, mantle; SVZ, subventricular zone; VZ, ventricular zone. Adopted from Kriegstein et al.[83], with permission (*see* authorizations).

Postnatal Neurogenesis is Crucial for Olfaction, Learning, and Memory Formation

Postnatal neurogenesis originating from the SVZ is critical for olfaction[91]. NPCs residing in the SVZ contribute to postnatal neurogenesis by differentiating along the neuronal lineage and migrating as part of the rostral migratory stream (RMS) to the olfactory bulb[92]. The NSC,

otherwise termed as a radial glia-like cell, differentiates into its progenitor, the transient amplifying cell, which in turn produces an immature neuronal cell type called a neuroblast[90]. Neuroblasts and their more specified immature neurons migrate along the RMS until they reach the olfactory bulb, at which point, immature neurons will leave the RMS and migrate in a radial fashion to become more specified interneurons of the olfactory bulb[93,94] (Figure 9).

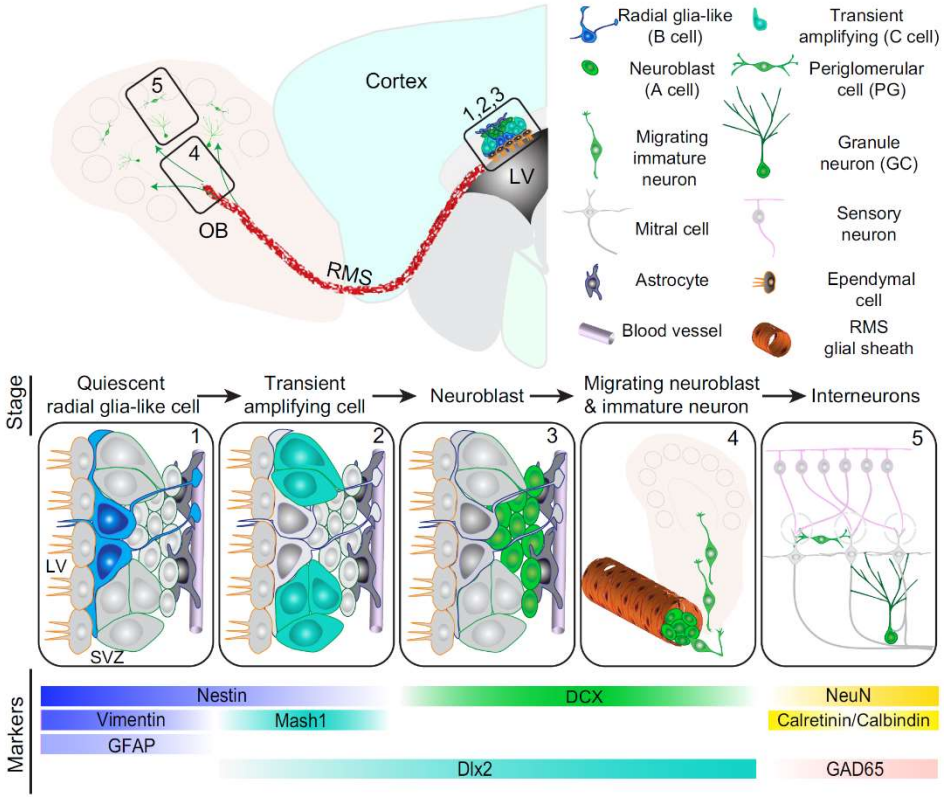

Figure 9. Postnatal neurogenesis originating from the subventricular zone (SVZ). Illustration depicting neuronal differentiation in 5 stages of development, from quiescent radial glia-like cell (stem cell) to mature interneuron. Neuroblasts migrate from the SVZ along the rostral migratory stream (RMS) to the olfactory bulb (OB). LV, lateral ventricle; GFAP, glial fibrillary acidic protein; Mash1, mammalian achaete-scute homolog 1; Dlx2, distal-less homeobox 2; DCX, doublecortin; NeuN, neuronal nuclei; GAD65, glutamic acid decarboxylase 65. Adopted from Ming et al. [90], with permission (*see* authorizations).

Within the DG, NSCs, or radial glial-like cells, produce non-radial precursors. Both cell types can generate intermediate progenitor cells. Intermediate progenitor cells differentiate into neuroblasts, which then migrate from the subgranular zone, to the granule cell layer, where they differentiate into granule cells[90]. These newborn neurons will extend their dendrites into the molecular layer

and their axons into the hilus near the cornu ammonis 3 (CA3) region in the hippocampus[95]. Here, the neurons can integrate with the existing neuronal network, including local interneurons of the hilus and CA3 pyramidal cells[96,97] (Figure 10).

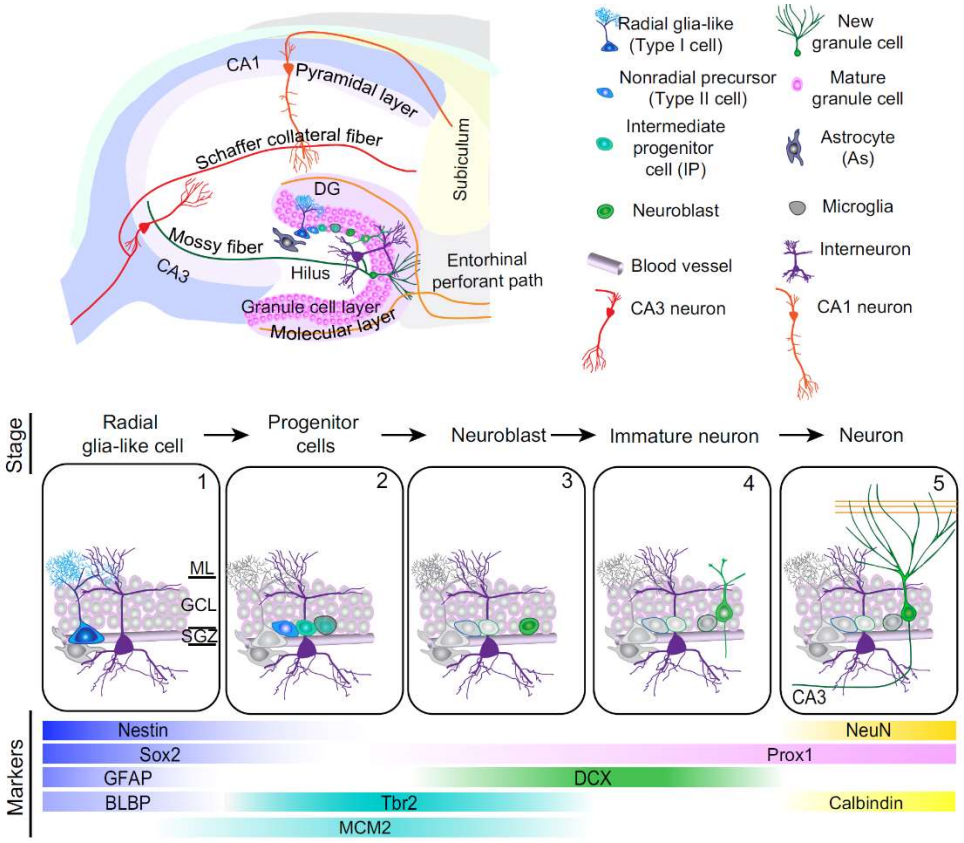

Figure 10. Postnatal neurogenesis within the dentate gyrus (DG). Illustration depicting neuronal differentiation in 5 stages of development, from radial glia-like cell (stem cell) to mature neuron. CA3, Cornu Ammonis 3; ML, molecular layer; GCL, granule cell layer; SGZ, subgranular zone; GFAP, glial fibrillary acidic protein; BLBP, brain lipid binding protein; Tbr2, T-box brain protein-2; MCM2, minichromosome maintenance complex component 2; DCX, doublecortin; NeuN, neuronal nuclei; Prox1, prospero-related homeobox 1. Adopted from Ming et al. [90], with permission (*see* authorizations).

Postnatal neurogenesis within the DG contributes to learning and memory[98]. However, there are some discrepancies in the field as to the specific memory functions of newborn neurons within the DG[98]. These conflicting findings may be due to differences in species, strain, timing, injury model, and assessment task. Moreover, some studies may test hippocampal functions, rather than DG-specific functions[98]. Though further work in the area is required, there is strong evidence

supporting the conclusion that neurogenesis within the DG is crucial for spatial learning[99], flexibility in learning approaches[100], and contextual fear conditioning[101].

Without the ability to produce new neurons, the DG must rely on the mature granule cell population to store new memories and retrieve old memories. This is restrictive and may lead to interference between nearby memory networks (Figure 11a). Neurogenesis allows for separateness between neuronal networks, i.e., new information can be encoded in the newborn neurons, without disrupting older memories (Figure 11b)[98].

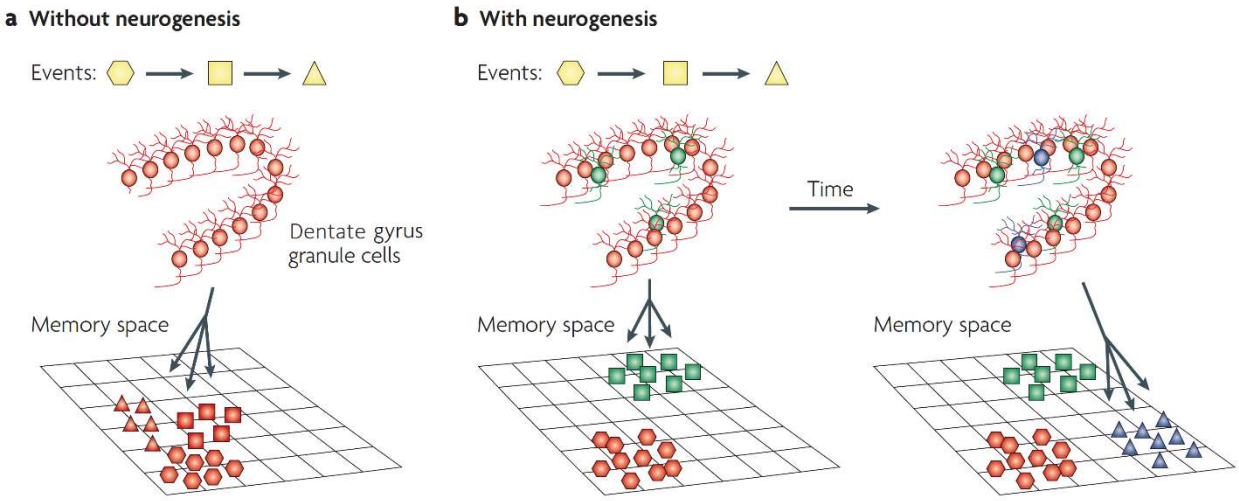

Figure 11. Neurogenesis in the dentate gyrus plays a crucial role in learning and memory. a, A proposed mechanism by which memories form in the dentate gyrus (DG) without neurogenesis. The memories are formed and stored in close proximity to one another. **b**, A proposed mechanism by which memories are produced and stored when the DG has the capacity to form new neurons. There is ultimately more space available and less overlap between neuronal networks when neurogenesis is possible. Adapted from Deng et al. [98], with permission (*see* authorizations).

The Perivascular Niche for Neurogenesis

Stem and progenitor cells can have high metabolic requirements and thus, these cells are often found adjacent to blood vessels to maximize their supply of nutrients[102]. Both the SVZ and the SGZ contain a dense network of blood vessels with less curvature compared to non-neurogenic brain regions[103–106]. Palmer et al.[107] were the first to describe the perivascular niche for neurogenesis, showing physical connections between vascular endothelial cells (ECs) and

newborn neurons within the DG. The niche is comprised of many cell types—NPCs, neurons, ECs, astrocytes, and pericytes—all interacting and influencing the function of one another[108]. Physical interactions[103,109], as well as secreted factors[110–114] between ECs and NPCs provide important cues for proper NPC function. More recently, cell-cell interactions, where specialized endfeet of NPCs make physical contact to ECs, have been shown to maintain the NPC population by promoting quiescence. In order for NPCs to adhere to ECs, NPC endfeet express the α6β1 integrin receptor which allows binding via the laminin ligand on ECs[103]. To maintain NPC quiescence, EC ligands, EphrinB2 and Jagged1, bind to Eph and Notch receptors on NPCs, respectively[109].

The perivascular niche for neurogenesis is not well understood within the context of BPD. Licht et al.[115] demonstrated that preterm infants are selectively vulnerable to neurovascular impairments due to their developmentally immature blood vessels. Further, they showed that the periventricular vessels within the germinal matrix, i.e., the perivascular niche for neurogenesis, are the last of the brain's blood vessels to mature. This may indicate a uniquely vulnerable brain region to neonatal noxious stimuli. Further work in this area is required to gain a better understanding of the effects of extreme prematurity on NPCs and their perivascular niche.

Modelling BPD and Associated Brain Injury using Animal Subjects

There are many variations of animal models used to mimic BPD phenotypes. Although mouse models cannot fully recapitulate the disease, they offer many similarities. In terms of timing and development, a neonatal mouse is at a similar biological stage as an extremely preterm human infant. At postnatal day (P)0, mouse lungs are in the saccular stage of development[116] and their brains are in the early period of gliogenesis[117]. The most well-established BPD model is one that exposes mice to high concentrations of oxygen (hyperoxia) for an extended period. This model was first used by Bonikos et al.[118,119] in the 1970s, where mice were exposed to 100% O_2 from 7

days to 6 weeks, creating an "old BPD" phenotype. To better mimic the "new BPD", investigators adjusted O_2 exposure time from prolonged periods (28 days)[120] to shorter periods (usually 4-14 days)[121,122]. Overall, this model mimics BPD and its associated complications, i.e., larger and fewer alveoli[123], reduced microvasculature[124], inflammation[125], and white matter brain injury[126]. The main caveat of this model is that it does not incorporate all the pathophysiological mechanisms that contribute to BPD. However, if the main goal is to investigate the effects of hyperoxia on development, then its reproducibility[127] makes it an ideal model. Another less commonly used model, because of its complexity, is a ventilation-induced lung injury (VILI) model which mimics the mechanical stress injury induced by ventilation of preterm lungs. The first mouse VILI model was created in 2007, by Bland et al.[128], in which 2-6-day-old mice were exposed to ventilation for 8 or 24 hours at 21% or 40% O_2. Investigators found an "evolving" BPD phenotype, i.e., underdeveloped alveoli with no inflammation. An advantage of this model over the hyperoxia model is that it is more clinically relevant, as it combines two BPD-associated factors, i.e., hyperoxia and mechanical ventilation. However, a limitation is that in mice it is mainly used as an acute model, as the mice are usually not resuscitated following ventilation exposure. Additionally, systemic inflammation can be incorporated into hyperoxia[129] and mechanical ventilation[130] models to better mimic the clinical conditions of preterm birth. Lipopolysaccharide (LPS) is the primary endotoxin used to investigate the effects of inflammation on the developing lung as it mimics inflammatory-induced outcomes of preterm birth, such as recruitment of pro-inflammatory immune cells to the lung and reduced lung growth[131].

A more clinically relevant animal model which closely mimics human preterm birth conditions is the neonatal baboon model (*Papio* species). This model was established at The University of Texas Health Science Center at San Antonio and the Texas Biomedical Research

Institute[132,133]. A term birth for this species occurs at 185 days of gestation[132]. To induce the "new" BPD phenotype, i.e., restricted lung growth, investigators expose 125-day-old baboons to positive pressure ventilation and supplemental oxygen for 14 days[134]. At 125 days, baboons are in the canalicular stage of lung development[132], correlating with ~26 weeks of gestation in humans. In terms of baboon brain development, at 125 days, the 6 neocortical layers are formed, the primary gyri and sulci folds are present, and gliogenesis has begun with the diencephalon and internal capsule[135]. In humans, this mirrors 26-28 weeks gestational age[136–138]. A preterm neonatal baboon exposed to supplemental oxygen and ventilation, develops a similar phenotype of brain injury as human preterm infants, i.e., IVH and PVL[139]. One caveat of studying both the lungs and the brain in the baboon model is that in late gestation, the brain develops faster than the lung, as it undergoes a rapid growth period from gestational day 140-160. At term, the baboon brain has a more advanced myelination pattern than the human brain[135]. However, this model provides an important advantage over murine models of BPD, as baboons are biologically and genetically very similar to humans[140]. Furthermore, no one has previously assessed the NPC population in preterm and term neonatal baboons. Therefore, a critical gap exists in our knowledge of NPCs in this important non-human primate model.

Umbilical Cord-Mesenchymal Stromal Cells and their Extracellular Vesicles Prevent and Repair Lung Injury in a BPD Model

Presently, there is no treatment that can effectively prevent lung injury or the abnormal neurodevelopmental outcomes of prematurity. However, mesenchymal stromal cells (MSCs), which are non-hematopoietic, multipotent cells, show promise for therapeutic applications in preclinical models[125,141,142]. There are two potential mechanisms by which MSCs exert their therapeutic benefit. The first mechanism is via a paracrine effect, i.e., they release bioactive

molecules, accounting for their anti-inflammatory[143], -oxidant[144], -apoptotic[145], as well as pro-angiogenic[145] effects. MSCs also produce neurotrophic factors[146]. The second mechanism, thought to apply more broadly to cell therapy, is that transplantation of exogenous cells stimulates an innate immune response, creating a more favourable environment for tissue regeneration[147]. The International Society for Cellular Therapy define the minimal criteria for MSCs as: i) *in vitro* plastic adherence; ii) cell marker presence ($CD105^+$, $CD73^+$, $CD90^+$) and absence ($CD45^-$, $CD34^-$, $CD14^-$ or $CD11b^-$, $CD79\alpha^-$ or $CD19^-$ and HLA-DR surface molecule$^-$); and iii) *in vitro* differentiation into adipocytes, chondrocytes, and osteocytes[148]. It is important to note that this definition is broad and thus, the term "MSC" encompasses a wide variety of cells for which there is mounting evidence to create smaller sub-classes describing tissue-specific mesoderm-derived progenitor cells[149]. Moreover, despite the therapeutic benefit of MSC treatment exhibited in preclinical models, this benefit has not yet been demonstrated in clinical trials[150]. Therefore, when investigating the therapeutic potential of cells termed "MSCs", it is crucial that researchers conduct rigorous science and report all findings to improve the likelihood of successful clinical translation.

We have previously shown that intratracheal administration of umbilical cord-mesenchymal stromal cells (UC-MSCs), prevents and rescues lung structural abnormalities and functional deficits in a rodent model of BPD[142,151]. Our lab also conducted a systematic review and meta-analysis of the literature, to further assess the effectiveness of MSCs in improving lung injury in hyperoxia rodent models of BPD[152]. We found strong confirmation that MSC administration significantly mitigates the arrest in lung growth, pulmonary hypertension, lung inflammation, restricted blood vessel formation, and apoptosis associated with BPD models.

A recent development within the field is that the paracrine benefits of MSCs come from their secretion of extracellular vesicles (EVs)[153]. EVs are a heterogeneous population of vesicles

with a phospholipid bilayer that are secreted from cells into the extracellular space[154]. Their size ranges from ~40-1,000 nm[155]. They provide a mechanism for cells to deliver potential therapeutic factors, molecules, and organelles, such as protein, mRNA, miRNA, and mitochondria[154,155]. Several groups have demonstrated the efficacy of MSC-derived EVs to attenuate lung injury[156–158], including in a BPD-specific model[159]. A major therapeutic benefit of MSC-derived EVs in lung injury is their ability to modulate inflammation by supressing pro-inflammatory cytokines and shifting the polarization of lung macrophages from a pro-inflammatory M1 state to an anti-inflammatory M2 state[159]. Moreover, Alvarez-Erviti et al.[160] demonstrated that EVs administered via a tail-vein injection in mice can deliver siRNA to multiple regions within the brain. Furthermore, Kaminski et al.[161], showed that MSC-derived EVs administered intraperitoneally significantly reduced inflammation within the brain in a neonatal hypoxic-ischemic rodent model. The inflammatory modulation was associated with increased neuronal proliferation and oligodendrocyte maturation. Further work is required to elucidate the exact mechanisms of action; however, the potential therapeutic effects of MSC-derived EVs in BPD and brain injury models is promising.

Rationale and Hypothesis

BPD, a neonatal chronic lung disease, is a risk factor for abnormal neurodevelopment. It is unknown whether NPCs are perturbed in BPD, and whether this NPC impairment is associated with abnormal neurodevelopmental outcomes. Furthermore, there is no effective treatment for BPD and its associated brain injuries. Our previous work, as well as the work of other investigators, demonstrate the therapeutic effectiveness of UC-MSCs and MSC-derived EVs to mitigate lung injury in BPD models. Further studies also demonstrate the ability of MSC-derived EVs to cross the blood-brain barrier and exert therapeutic effects in brain injury. Thus, we hypothesize that: i) NPC function is impaired in experimental models of BPD and that this is associated with abnormal neurodevelopment and ii) UC-MSC therapy ameliorates lung injury and NPC functional impairments. The main objectives of Manuscript 1 were to determine: i) whether a hyperoxia-induced BPD model impaired NPCs, their progeny, and the perivascular niche for neurogenesis, and ii) whether this impairment correlates with neurobehavioural deficits. This was accomplished by assessing murine and baboon NPC function, cerebrovascular structure and function, as well as motor and cognitive abilities throughout the lifespan in experimental BPD models. The main objective of Manuscript 2 was to describe the novel protocol used to isolate neonatal baboon-derived NPCs. This was accomplished by providing a detailed description of the isolation and culture process. The main objectives of Manuscript 3 were to determine whether hyperoxia, mechanical ventilation, and inflammation created a clinically relevant BPD murine model; to determine whether NPCs were functionally impaired in this multifactorial BPD model; and to assess whether UC-MSC-derived EVs delivered intratracheally could mitigate the lung and brain injury in this model. This was accomplished by a histopathological assessment of the lung injury, NPC neurosphere and differentiation assays, and inflammatory cytokine measurements.

Preface to Manuscripts

The manuscripts presented in this dissertation were designed, produced, and written during my graduate studies in the Department of Cellular and Molecular Medicine at the University of Ottawa. The organization of the dissertation is in accordance with the University of Ottawa guidelines as follows. The manuscripts and their associated figures, figure legends, and references follow the formatting of their respective journals and can be found within each dissertation chapter. The references for the introduction and discussion portions of the dissertation can be found towards the end of the dissertation. Supplemental information can be found in the Appendix.

Manuscript 1 is under revision at The Journal of Clinical Investigation and is subject to change.

Manuscript 2 will be submitted to Nature Protocols (following the publication of Manuscript 1) and is subject to change.

Manuscript 3 is under revision at the American Journal of Respiratory and Critical Care Medicine and is subject to change.

Manuscripts

Manuscript 1: Neonatal hyperoxia in mice impairs cerebrovascular function, neurogenesis, and behavior into adulthood

Authors: Marissa A. Lithopoulos[1,2], Xavier Toussay[2,3,4], Shumei Zhong[1], Liqun Xu[1], Shamimunisa B. Mustafa[5], Cesar H. Comin[6], Hayam A. Bassam[3,7], Adam N. Baker[3], Alvaro Moreira[5], Cynthia L. Blanco[5], Arul Vadivel[1], Catherine Tsilfidis[2,3], Steven Seidner[5], Ruth Slack[2,4], Diane Lagace[2,3,4], Jing Wang[1,2,4], Baptiste Lacoste[2,3,4], Bernard Thébaud[1,2,8]

Affiliations:

1 Regenerative Medicine Program, Ottawa Hospital Research Institute, Ottawa, ON, K1H 8L6, Canada
2 Department of Cellular and Molecular Medicine, Faculty of Medicine, University of Ottawa, Ottawa, ON, K1H 8M5, Canada
3 Neuroscience Program, Ottawa Hospital Research Institute, Ottawa, ON, K1H 8L6, Canada
4 University of Ottawa Brain and Mind Research Institute, Ottawa, ON, K1H 8M5, Canada
5 University of Texas Health Sciences Center at San Antonio, San Antonio, Texas, 78229, USA
6 Department of Computer Science, Federal University of São Carlos, SC, 13565-905, Brazil
7 Department of Biochemistry, Microbiology, and Immunology, Faculty of Medicine, University of Ottawa, Ottawa, ON, K1H 8M5, Canada
8 Children's Hospital of Eastern Ontario Research Institute, Ottawa, ON, K1H 8L1, Canada

Graphical Abstract

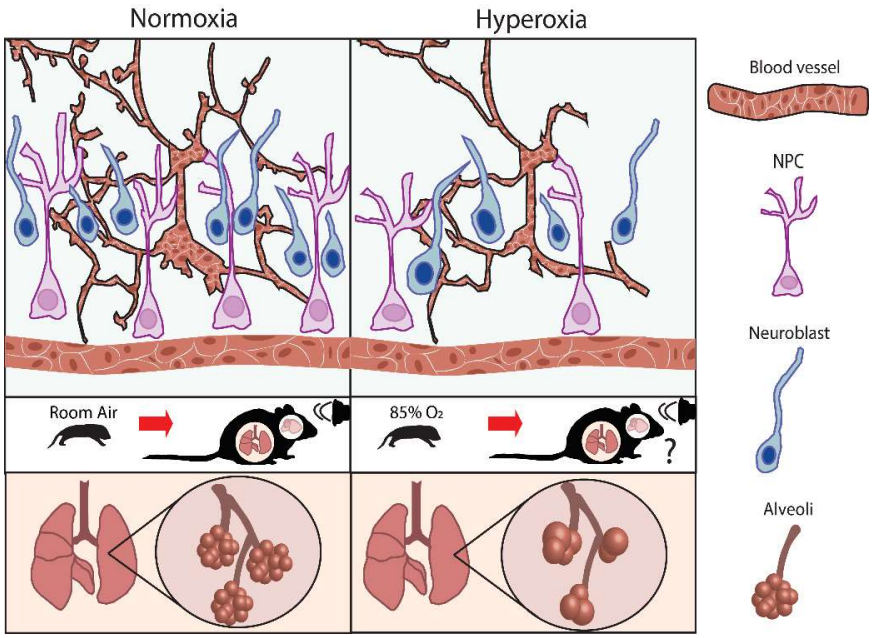

Connection to Hypothesis: This manuscript confirms that NPC function is impaired in experimental models of BPD and that this impairment is associated with abnormal neurodevelopment.

Current Manuscript Status: Under revision at the Journal of Clinical Investigation.

Author Contributions: I designed the experiments, established the BPD murine model, processed the brain tissue, acquired the images (lung, brain, *in vitro* NPCs), conducted the image quantification/analysis, conducted the systolic blood pressure experiment, and performed the neurosphere assays (murine and baboon). I assisted with the CBF and O_2 concentration measurements and conducted the analyses of these experiments. I assisted with the analyses of the behavior tests, vision function tests, and metabolic treadmill assessment. I interpreted the data of all experiments and wrote/ edited the manuscript. The University of Ottawa Histology Core Facility processed the lung sections. X.T. conducted the CBF and O_2 concentration measurements. S.Z. and L.X. assisted with processing the lung tissue and the murine neurosphere assays. S.M. assisted with the baboon neurosphere assay. C.C. analyzed the vasculature in the cerebral cortex. The University of Ottawa Preclinical Imaging Core Facility conducted the MRI. The University of Ottawa Behavior and Physiology Core Facility conducted the behavioral experiments and analysis. H.B. and A.B. conducted the ERG experiments. A.M. provided intellectual guidance and experimental material. C.L.B. assisted with the collection of baboon tissue. A.V. helped with the set-up of the hyperoxia chambers. S.S. provided intellectual guidance and assisted with the baboon tissue isolation procedure. R.S., D.L., J.W., and B.L provided experimental material and methods. B.T. financed and supervised the study. S.M., A.V., S.S., R.S., D.L., J.W., B.L., and B.T. provided guidance/ edited the manuscript.

Abstract

Preterm birth is the leading cause of death in children under 5 years of age. Premature infants who receive life-saving oxygen therapy often develop bronchopulmonary dysplasia (BPD), a chronic lung disease. Infants with BPD are at a high risk of poor neurodevelopment, including motor and cognitive difficulties. Neural progenitor cells (NPCs) are crucial for proper brain development. It is unclear whether NPCs play a role in BPD-associated poor neurodevelopmental outcomes. Here, we show that early exposure to hyperoxia in experimental BPD in mice leads to life-long impairments in cerebrovascular structure and function, as well as impairments in NPC self-renewal and neurogenesis. A neurosphere assay with non-human primate preterm baboon NPCs confirms this impairment in NPC function. These impairments are associated with motor and cognitive decline in aging hyperoxia-exposed mice, reminiscent of deficits observed in patients with BPD. Our findings establish a link between BPD and poor neurodevelopmental outcomes and identify novel cellular players of neonatal brain injury that persist throughout adulthood, that may be targeted to aid this vulnerable patient population.

Key words: Behavior, neurodevelopment, neuronal stem cells

Introduction

Preterm birth (<37 weeks) is the leading cause of death in children under the age of five (1). A chronic lung disease known as bronchopulmonary dysplasia (BPD) represents the most common complication of extreme prematurity (<28 weeks) (1) and affects ~40% of patients (2-5). BPD is characterized by an arrest in lung development that occurs in extremely premature newborns exposed to supplemental oxygen and ventilatory support. In addition to lifelong pulmonary sequalae, BPD is an independent risk factor for abnormal neurodevelopment (6). Even in the absence of the primary reported neonatal brain injuries—intraventricular hemorrhage (IVH) and periventricular leukomalacia (PVL) (7-9)—preterm infants remain at a high risk of life-long cognitive impairment (10, 11). Specifically, 25-50% of extremely preterm infants develop deficits in working memory, learning, and executive function, as well as verbal and performance IQ (12-15). Furthermore, children born premature are at higher risk for cerebral palsy (16) and autism (17). Notably, preterm infants diagnosed with BPD perform significantly poorer on all neurodevelopmental measures including cognition, intelligence, and motor functions, compared to non-BPD preterm born patients (18-21).

Supplemental oxygen administered for respiratory distress is life-saving, but is also one of the main contributors of neonatal morbidity (22, 23), and thus may play an important role in BPD-associated abnormal neurodevelopment. Preterm infants are particularly vulnerable to oxygen toxicity for three main reasons. First, the fetus' environment is hypoxic relative to room air (24); therefore, administering oxygen adds to the oxidative stress at birth. Second, preterm infants have not developed the ability to autoregulate their vascular responses to oxygen fluctuations (25-28). Finally, preterm infants have immature antioxidant defenses (24), allowing for high amounts of oxygen and subsequent reactive oxygen species (ROS) to reach the developing brain (10).

Neural progenitor cells (NPCs) are crucial for neurodevelopment and cognitive function throughout our lifespan (29-31). Whether NPCs are functionally impaired in preterm infants with BPD remains unexplored. Postnatally, NPCs reside in niches of neurogenesis, i.e., the subventricular zone (SVZ) of the lateral ventricle and the subgranular zone (SGZ) in the dentate gyrus (DG) of the hippocampus (32-37). NPCs are particularly vulnerable to oxidative stress (38-41). Furthermore, NPC fate relies heavily on the surrounding cerebrovasculature (42). The effects of hypoxia on disrupting brain development in cases of apnea (43), hypoxia-ischemic injury (44), IVH (45), and PVL (46) are well established. However, little is known regarding the effects of hyperoxia on: (i) the developing brain vasculature, (ii) NPC function, and (iii) cognitive performance.

Here, we designed a hyperoxia-induced preclinical model of BPD during early postnatal development and investigated the lifelong implication on the brain vasculature, NPCs, and behavior. We found that experimental postnatal hyperoxia induced a BPD-like lung disease as well as cerebrovascular deficits. This early perivascular perturbation correlated with NPC functional impairments and ultimately permanent cognitive deficits. These findings establish a link between BPD and abnormal neurodevelopment and identify the vascular niche of neurogenesis and NPCs as important targets for future investigations.

Results

Hyperoxia-exposed mice maintain arterial oxygen levels in experimental BPD. To mimic BPD, we exposed C57BL/6 Wild-Type (WT) mice to 85% O_2 from postnatal day (P)0 to P14 (Figure 12A). At P0, mice are in the saccular stage of lung development and the beginning stages of gliogenesis within the brain, recapitulating extremely preterm human lung (47) and brain development (48). Age-matched control mice were housed in room air. We observed that hyperoxia exposure from P0-P14 significantly decreased the survival rate of P14 pups by 13% (Figure 12B). The survival rate from P14 to 12 months of age did not differ significantly (Figure 12C). Therefore, 14 days of neonatal hyperoxia exposure does not affect survival in adulthood.

No difference in the arterial blood oxygen saturation was detected at P14 (Figure 12D), yet hyperoxia-exposed mice showed alveolar rarefication characteristic of BPD (Figure 12E). This was reminiscent of a chronic lung injury, with no signs of recovery as adults (Figure 12F), consistent with recent observations of humans born preterm (49, 50). Next, we tested whether hyperoxia-exposed mice maintained their arterial oxygen levels within a normal physiological range when physically challenged by exercise. Hyperoxia-exposed mice showed impairments on the treadmill compared to normoxia-exposed mice (e.g., running for shorter durations and at a lower maximum speed; Figure 1, G and H). These changes in performance occurred in the absence of differences in arterial oxygen saturation between groups (Supplemental Figure 1A and Figure 12I). Metabolic analysis as measured by the comprehensive lab monitoring system (CLAMS) (e.g., oxygen consumption, carbon dioxide production) revealed no differences (Supplemental Figure 1B); however, hyperoxia-exposed mice displayed a significantly increased heart rate and a trend of an increased respiratory rate following exercise (Figure 12I).

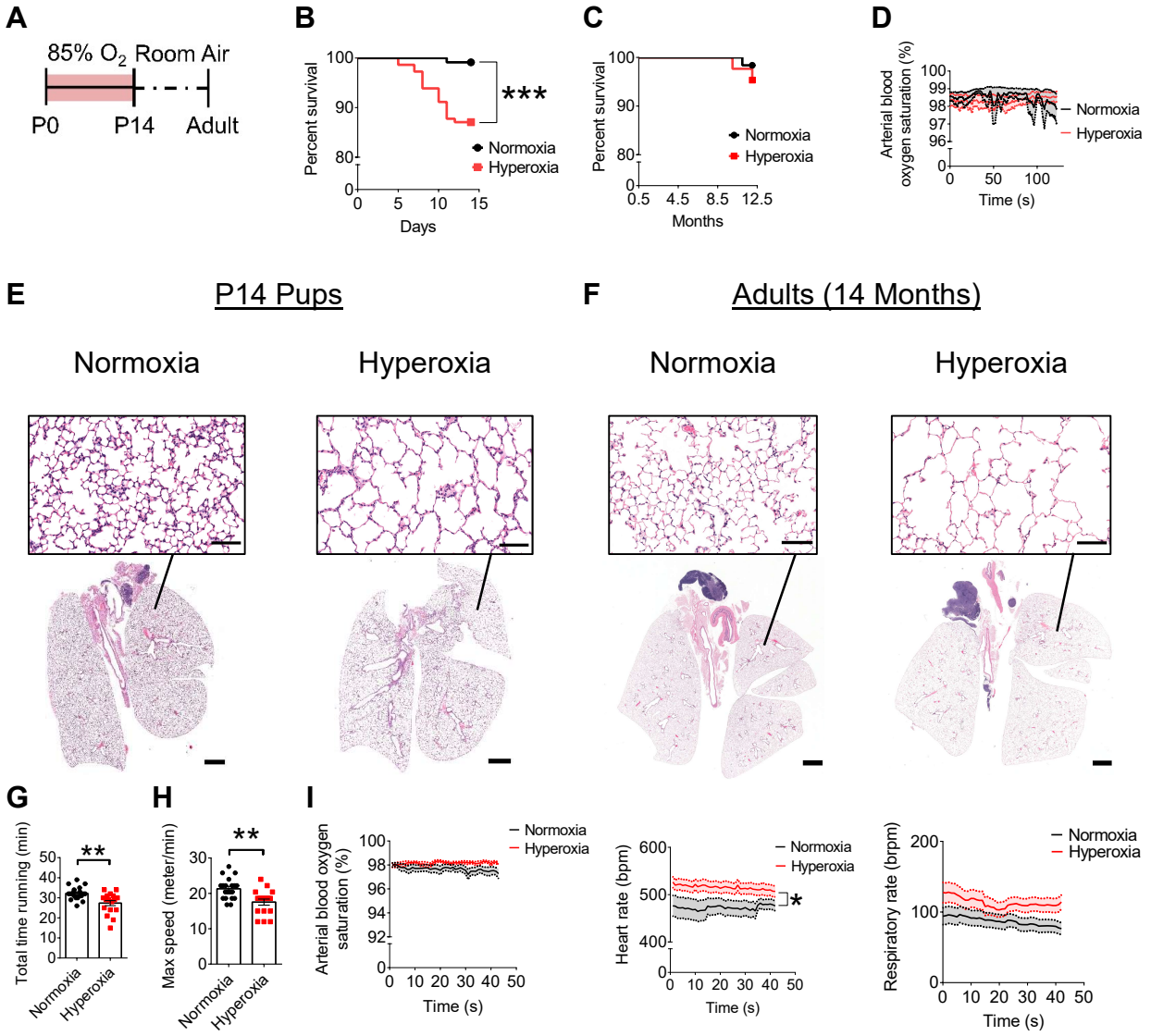

Figure 12. Early developmental hyperoxia exposure induces a lung injury phenotype reminiscent of BPD yet does not lead to arterial hypoxia. (**A**) Representation of the experimental design. Wild-type, C57 BL/6 mice were exposed to 85% O_2 from P0-P14. (**B**) Percent survival of mice after 14 days of room air exposure (normoxia) or 85% O_2 exposure (hyperoxia) (normoxia, n=115; hyperoxia, n=147; ***$P < 0.001$; log-rank test). (**C**) Percent survival of mice 12 months after exposure to neonatal normoxia or hyperoxia (normoxia, n=62; hyperoxia, n=43; log-rank test). (**D**) Blood oxygen saturation measurements of the femoral artery at rest at P14 (normoxia, n=16; hyperoxia, n=13; two-way ANOVA with Sidak post hoc test for group comparisons). (**E**) Representative images of hematoxylin and eosin (H&E) -stained lung sections of normoxia (left) and hyperoxia (right) mice at P14. (**F**) Representative H&E-stained lung sections of mice 14 months after exposure to neonatal normoxia or hyperoxia. (**G**) Total duration spent on the metabolic treadmill (normoxia, n=20, hyperoxia, n=17; **$P < 0.01$; unpaired Student's t test). (**H**) The maximum speed reached on the metabolic treadmill (normoxia, n=20, hyperoxia, n=17; **$P < 0.01$; unpaired Student's t test). (**I**) Three outcome measures were assessed for 12-14-month-old mice following exercise. From left to right: blood oxygen saturation of the femoral artery; heart rate (beats per minute, bpm); and respiratory rate (breaths per minute, brpm) (normoxia, n=20; hyperoxia, n=17; *$P < 0.05$; two-way ANOVA with Sidak post hoc test for group comparisons). Scale bar for full lung sections, 1,000 µm. Scale bar for high magnification field of view, 100 µm. Data are expressed as mean (solid line) ± SEM (shaded area around line).

Early postnatal hyperoxia exposure delays brain growth. The brains of hyperoxia-exposed mice appeared significantly smaller at P14 and 12 months of age (Supplemental Figure 2A). This result was not associated with differences in total body weight for P14 or adult mice (Supplemental Figure 2A). Hyperoxia-exposed pups had a reduced brain weight even when normalized to body weight (Supplemental Figure 2A). Magnetic resonance imaging (MRI) (Supplemental Figure 2B) in adulthood further confirmed the reduction in total brain size in hyperoxia-exposed mice (Supplemental Figure 2, B and C), with an absence of any significant differences in ventricular size (Supplemental Figure 2D). The reduction in total brain size was associated with a significant reduction in hippocampal volume in the hyperoxia-exposed mice (Supplemental Figure 2E). Overall, these results indicate that neonatal hyperoxia exposure leads to a reduction in brain growth during early development that is sustained into adulthood.

Early postnatal hyperoxia exposure impairs cerebrovascular function. Increases in neural activity are coupled with increases in cerebral blood flow (CBF) through neurovascular coupling (NVC), a critical process for the blood supply to adapt to the metabolic needs of the surrounding tissue (51-53). The anatomical structure underlying this process, the neurovascular unit (NVU) (51, 54), matures postnatally (52). Here, we tested whether early postnatal hyperoxia impacts NVC maturation using minimally invasive laser Doppler flowmetry to measure CBF over the primary somatosensory cortex (Figure 13A) (55, 56).

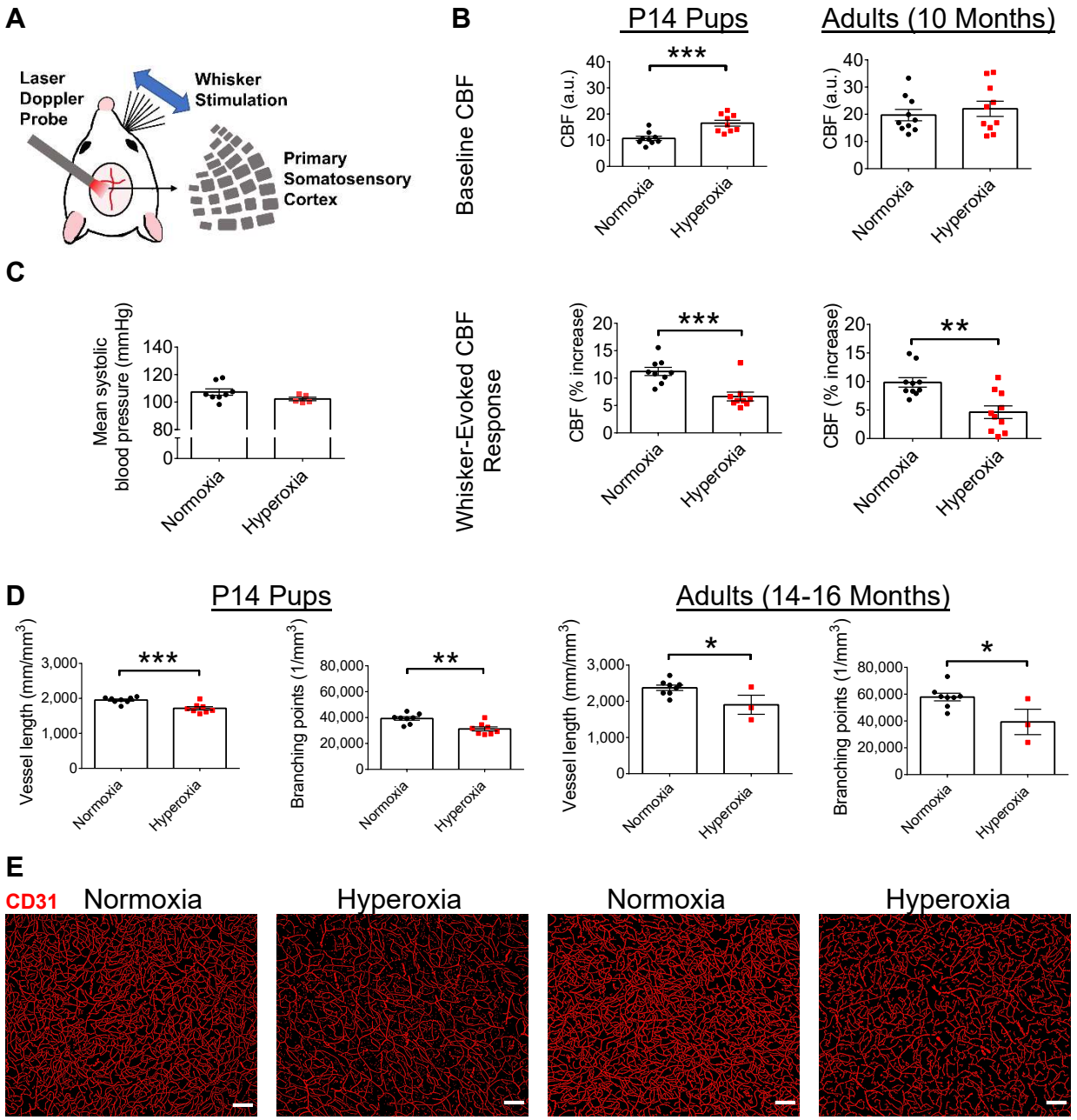

Figure 13. Early developmental hyperoxia exposure leads to neurovascular uncoupling and vascular remodelling. (**A**) Methods used to measure CBF in P14 and 10-month-old mice. (**B**) Baseline CBF (arbitrary units, a.u.) and percent change in CBF after whisker stimulation (P14 mice, normoxia, n= 9, hyperoxia, n=9; 10-month-old mice, normoxia, n= 10, hyperoxia, n=10; $^{**}P < 0.01$, $^{***}P < 0.001$, $^{****}P < 0.0001$; unpaired Student's t test). (**C**) Mean systolic blood pressure of 10-month-old mice (normoxia, n= 8, hyperoxia, n=5; unpaired Student's t test). (**D**) Average vessel length and number of branching points from cortical layers II/III, IV, and V for P14 and 14-16-month-old mice (P14 mice, normoxia, n=8, hyperoxia, n=8; 14-16-month-old mice , normoxia, n=8, hyperoxia, n=3; $^{*}P < 0.05$, $^{**}P < 0.01$, $^{***}P < 0.001$; unpaired Student's t test). (**E**) Representative images of cortical layers in P14 and adult mice. Scale bar, 100 µm. Data are expressed as mean ± SEM.

At P14, hyperoxia-exposed mice had a higher relative baseline CBF compared to control animals (Figure 13B). There was no baseline difference for adult mice (Figure 13B). To assess NVC, we measured CBF responses to whisker stimulation over the contralateral somatosensory cortex (57). Remarkably, hyperoxia-exposed mice displayed lower evoked CBF responses compared to control mice (Figure 13B). Thus, early hyperoxia resulted in abnormal CBF regulation. However, hyperoxia-exposed adults maintained a similar systolic blood pressure as control animals when measured using tail-cuffs (Figure 13C), suggesting that the observed CBF impairments do not result from peripheral dysregulation.

Cerebrovascular alterations in hyperoxia-exposed mice. Under normal atmospheric conditions (21% O_2 at 1 atmosphere), 98% of oxygen is delivered to tissues through binding to hemoglobin in the blood, while 2% is dissolved in the plasma (58). Once the hemoglobin in the blood becomes fully saturated with oxygen, the blood has reached its oxygen carrying capacity; however, during hyperoxia exposure, the oxygen tension gradient between blood and tissue can significantly increase, leading to tissue hyperoxygenation (59). Considering our observation that early postnatal hyperoxia exposure led to long-term CBF alterations, we tested whether the brain parenchyma displayed oxygen concentration changes. We used an intracerebral oxygen microsensor to measure the oxygen concentration in the primary somatosensory cortex and neurogenic regions *in vivo* in anesthetized mice. At P14, no difference was found between normoxia- and hyperoxia-exposed mice; however, the brain regions of hyperoxia-exposed mice showed a trend of becoming progressively hyperoxic as the mice aged (Supplemental Figure 3A-C).

We next asked whether the relatively hyperoxic microenvironment was associated with vascular structural changes within the brain during this critical period of development. To test this,

we used an approach combining immunofluorescent staining of endothelial networks and automatic computational analysis of 3D images/ reconstructions for unbiased quantification of cerebrovascular density and branching in the cortex. We identified vascular remodelling in the cortex of hyperoxia-exposed mice. Neonatal hyperoxia exposure led to reduced vessel length and branch point number early in life and continuing into adulthood (Figure 13, D and E; Supplemental Figure 4). Thus, hyperoxia exposure during early postnatal development in mice leads to long-term vascular structural impairments in the cerebral cortex.

Hyperoxia-induced NPC depletion is associated with vascular remodelling and impaired neurogenesis. To determine the effect of early life hyperoxia on NPCs, we quantified NPCs ($Sox2^+$, $nestin^+$ cells) in the neurogenic niche regions, the subventricular zone (SVZ) and dentate gyrus (DG) (Figure 14A) of P14 and 12-month-old mice. Animals exposed to hyperoxia showed significantly fewer NPCs in the SVZ and DG compared to control mice at P14 and 12 months (Figure 14B-E). At P14, hyperoxia-exposed mice have an average of ~15% fewer NPCs in the SVZ and DG than control mice. At 12 months, hyperoxia-exposed mice have an average of 33% fewer NPCs located within the SVZ and 47% fewer NPCs located within the DG compared to normoxia-exposed mice. Therefore, neonatal hyperoxia exposure leads to a significant, long-term NPC population decline.

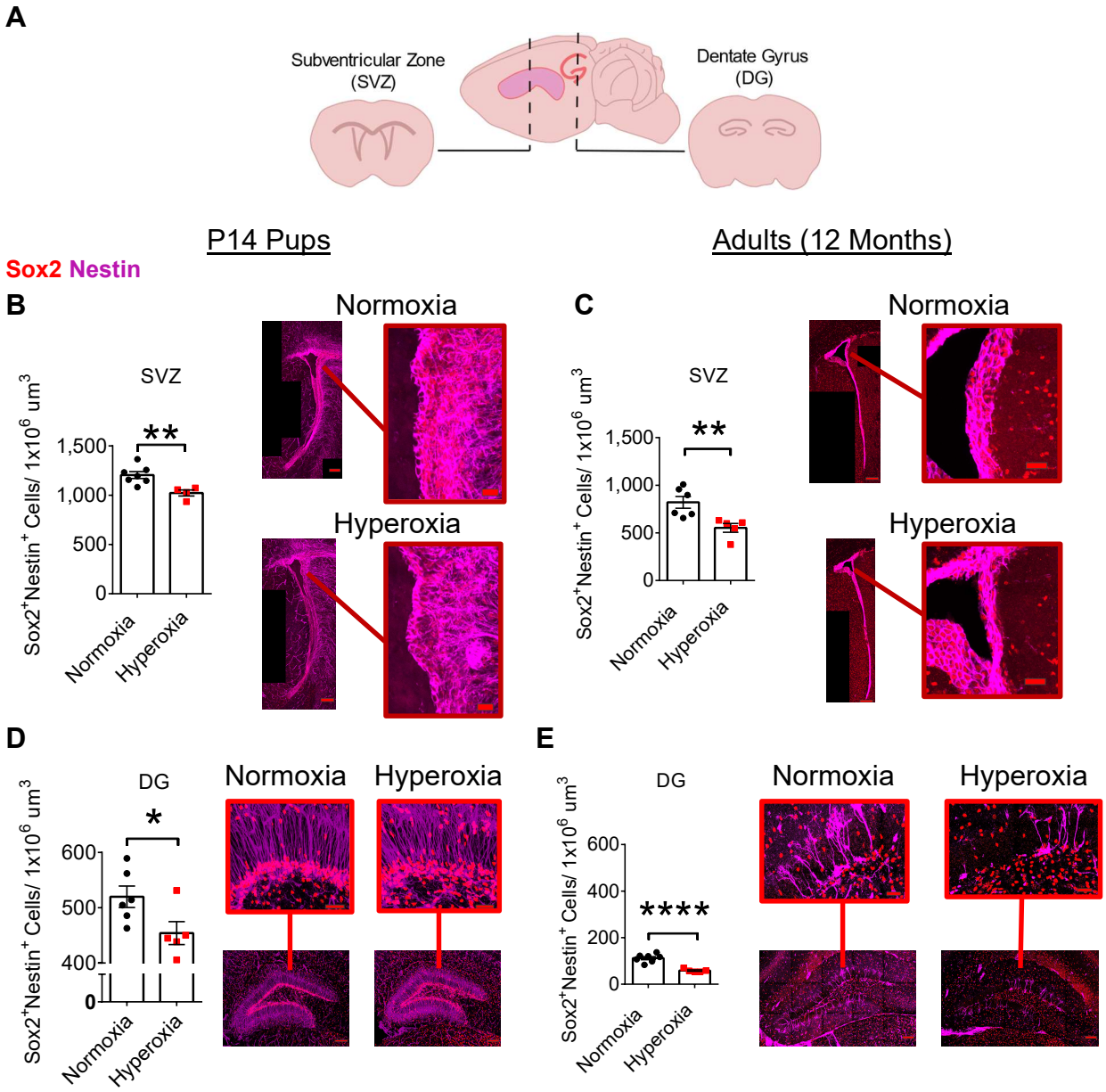

Figure 14. Early developmental hyperoxia exposure leads to long-term NPC depletion. (**A**) Schematic of the NPC niche regions, the subventricular zone (SVZ) and dentate gyrus (DG). (**B** and **C**) Quantification (left) and representative images (right) of NPCs ($Sox2^+$, $nestin^+$) in the SVZ of P14 mice (B, normoxia, n=7, hyperoxia, n=4; unpaired Student's t test) and 12-month-old mice (C, normoxia, n=6, hyperoxia, n=5; unpaired Student's t test), $^{**}P < 0.01$; scale bar, whole ventricle, 150 µm; magnified image, 20 µm for P14 and 30 µm for 12-month-old mice. (**D** and **E**) Quantification (left) and representative images (right) of NPCs ($Sox2^+$, $nestin^+$) in the DG of P14 mice (D, normoxia, n=6, hyperoxia, n=5; $^{*}P < 0.05$; unpaired Student's t test) and 12-month-old mice (E, normoxia, n=7, hyperoxia, n=5; $^{****}P < 0.0001$; unpaired Student's t test). Scale bar, whole DG, 100 µm; magnified image, 30 µm. Data are expressed as mean ± SEM.

We next assessed the vasculature within the DG. The physical and molecular cross-talk between vascular endothelial cells (ECs) and NPCs within neurogenic niches guides NPC maturation and function (42). To examine this relationship in the context of hyperoxia, we investigated the anchorage of NPC processes (nestin$^+$) onto ECs (CD31$^+$). On average, P14 hyperoxia-exposed mice had 27% fewer anchorage points compared to control mice (Figure 15A). This dramatic phenotype became more pronounced with age, as 12-month-old hyperoxia-exposed mice showed an average of 48% fewer anchorage points compared to normoxia, control mice (Figure 15B). Thus, after neonatal hyperoxia exposure, NPCs lack the essential scaffold provided by the vascular niche necessary to maintain the postnatal NPC population.

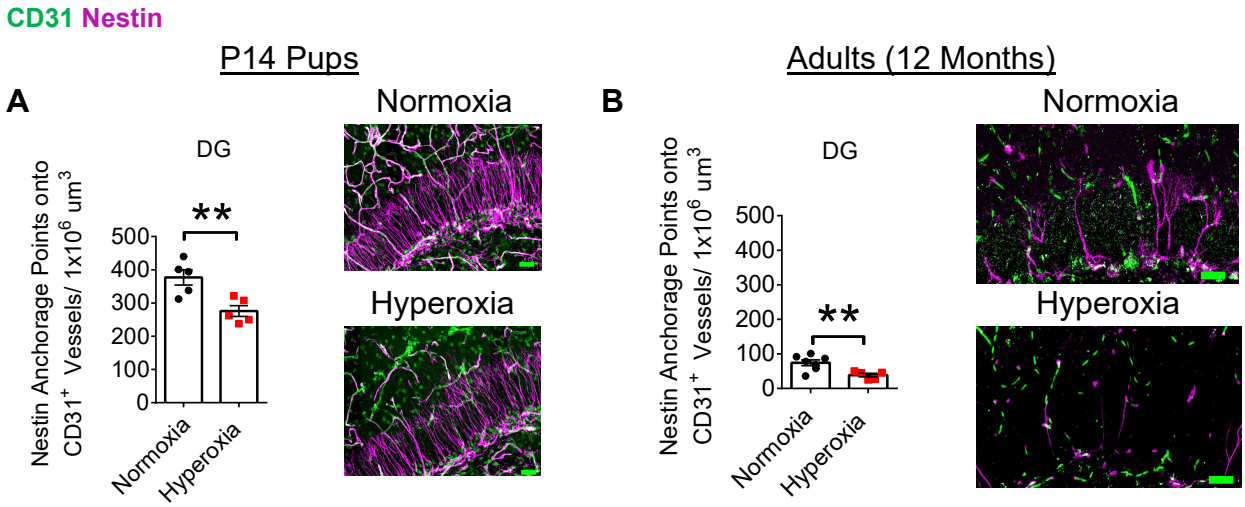

Figure 15. Long-term reduction in NPC anchorage to CD31$^+$ vessels in the DG of hyperoxia-exposed mice. (**A** and **B**) Quantification (left) and representative images (right) of the anchorage points of NPC processes (nestin$^+$) connecting to vascular endothelial cells (CD31$^+$) in the DG of P14 mice (A, normoxia, n=5; hyperoxia, n=5; unpaired Student's t test) and 12-month-old mice (B, normoxia, n=7; hyperoxia, n=5; unpaired Student's t test), $^{**}P < 0.01$; scale bar, whole DG 30 µm. Data are expressed as mean ± SEM.

To examine whether an impairment in intrinsic NPC self-renewal capabilities may be contributing to the reduced NPC population in hyperoxia-exposed mice, we isolated NPCs from the SVZ of P14 and 14-month-old mice and conducted neurosphere assays. Hyperoxia exposure led to fewer neurospheres at P14 (Figure 16, A and B) and remarkably, also at 14 months (Figure 16, C and D). There was no difference between groups in terms of neurosphere size (Figure 16, E

and F; Supplemental Figure 5A-H). This indicates that it is not the proliferation within a neurosphere that is affected after *in vivo* hyperoxia exposure, but rather, it is the ability of NPCs to form new neurospheres, i.e., self-renewal, that is impaired.

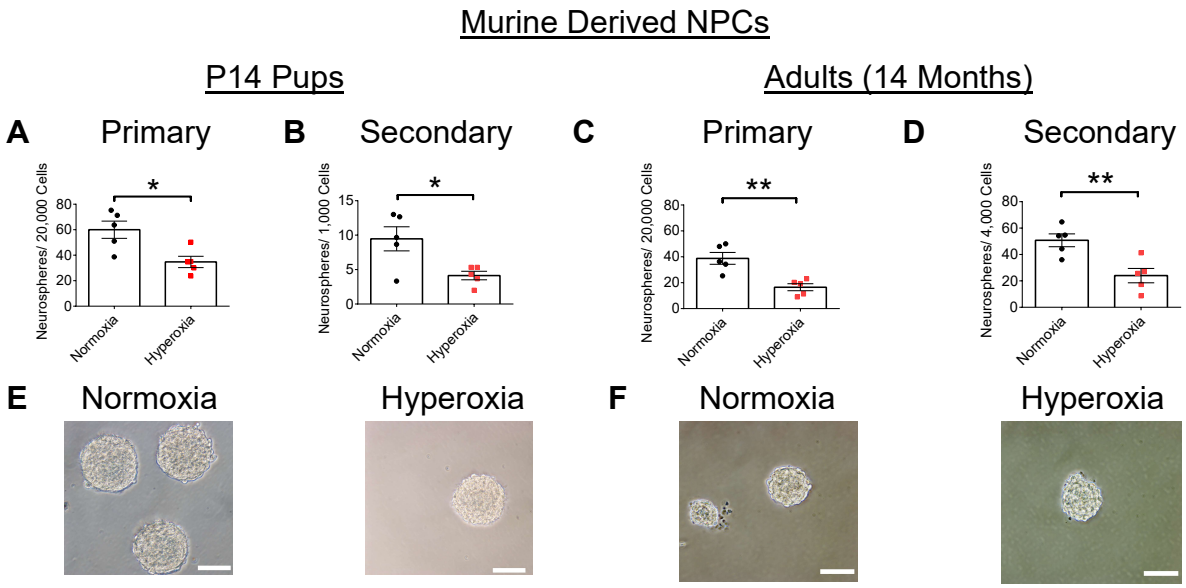

Figure 16. Hyperoxia-induced NPC depletion is associated with reduced NPC self-renewal. (**A-D**) Quantification of neurospheres formed by NPCs from the SVZ of P14 (left) and 14-month-old (right) mice (normoxia, n=5; hyperoxia, n=5; **P* < 0.05, ***P* < 0.01; unpaired Student's t test). (**E** and **F**) Representative images of neurospheres formed by NPCs from P14 (E) and 14-month-old (F) mice. Scale bar, 100 µm. Data are expressed as mean ± SEM.

To confirm our findings, we conducted similar studies with non-human primates (baboons). This model more closely mimics the preterm human condition, as baboons share many biological and genetic characteristics with humans (60). To this end, we isolated NPCs from the SVZ and DG of extremely preterm and term neonatal baboons, an animal model which has previously been shown to recapitulate human preterm birth complications (61-63). NPCs isolated from preterm neonatal baboons and exposed to 60% O_2 *in vitro* for 48 hours formed fewer neurospheres (Figure 17A) and formed smaller neurospheres (Figure 17B) compared to NPCs from control (term) baboons, although these effects appeared transient. The baboon cells showed greater variability between samples compared to murine cells, likely due to the greater genetic variability in the baboon population. It is also clear that a combination of hyperoxia and vascular

deficits *in vivo* contributes to a more robust impaired NPC phenotype than hyperoxia alone *in vitro*. Overall, these findings demonstrate that hyperoxia exposure in early developmental life in two independent preclinical models leads to deficits in the NPC population.

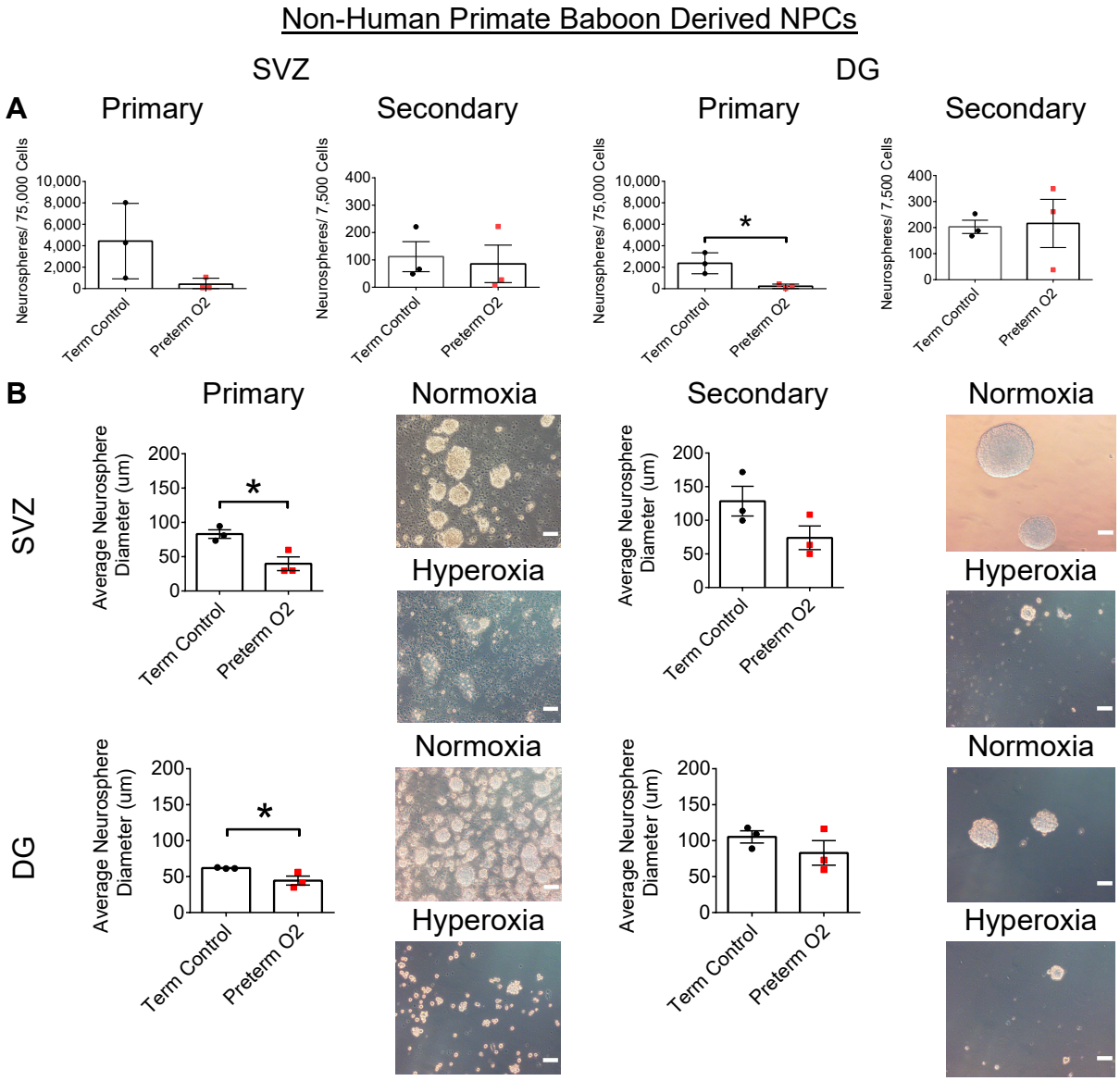

Figure 17. Hyperoxia-exposed preterm baboon derived NPCs form fewer and smaller neurospheres compared to term control NPCs. (**A**) Quantification of primary and secondary neurospheres formed by NPCs from the SVZ (left) and DG (right) of neonatal baboons (term control, n=3; preterm O_2, n=3; **P* < 0.05; unpaired Student's t test). (**B**) Quantification and representative images of the average primary (left) and secondary (right) neurosphere diameter formed by NPCs from the SVZ (top) and DG (bottom) of neonatal baboons (term control, n=3; preterm O_2, n=3; **P* < 0.05; unpaired Student's t test). Scale bar, 100 µm. Data are expressed as mean ± SEM.

We hypothesized that the decline in the NPC population would result in an overall reduction in the generation of adult-born neurons. The NPCs of the SVZ differentiate to immature neurons (neuroblasts) which migrate along the rostral migratory stream to produce neurons in the olfactory bulb (64). NPCs of the DG differentiate into neuroblasts and form new granule neurons within the DG (36). We identified newborn neurons with doublecortin (DCX). At P14, we found that hyperoxia-exposed mice had reduced DCX^+ cells in the SVZ and significantly reduced DCX^+ cells in the DG (Figure 18, A and B). Of note, investigation in 12-month-old mice demonstrated that hyperoxia-exposed animals have significantly impaired neurogenesis in adulthood in both regions (Figure 18, C and D). Therefore, these data demonstrate reduced neurogenesis in NPC niches from hyperoxia-exposed mice. This is in alignment with the reduced hippocampal volume measured via MRI (Supplemental Figure 2E) and thus, limited neurogenesis after early life hyperoxia exposure may contribute to a smaller hippocampal structure.

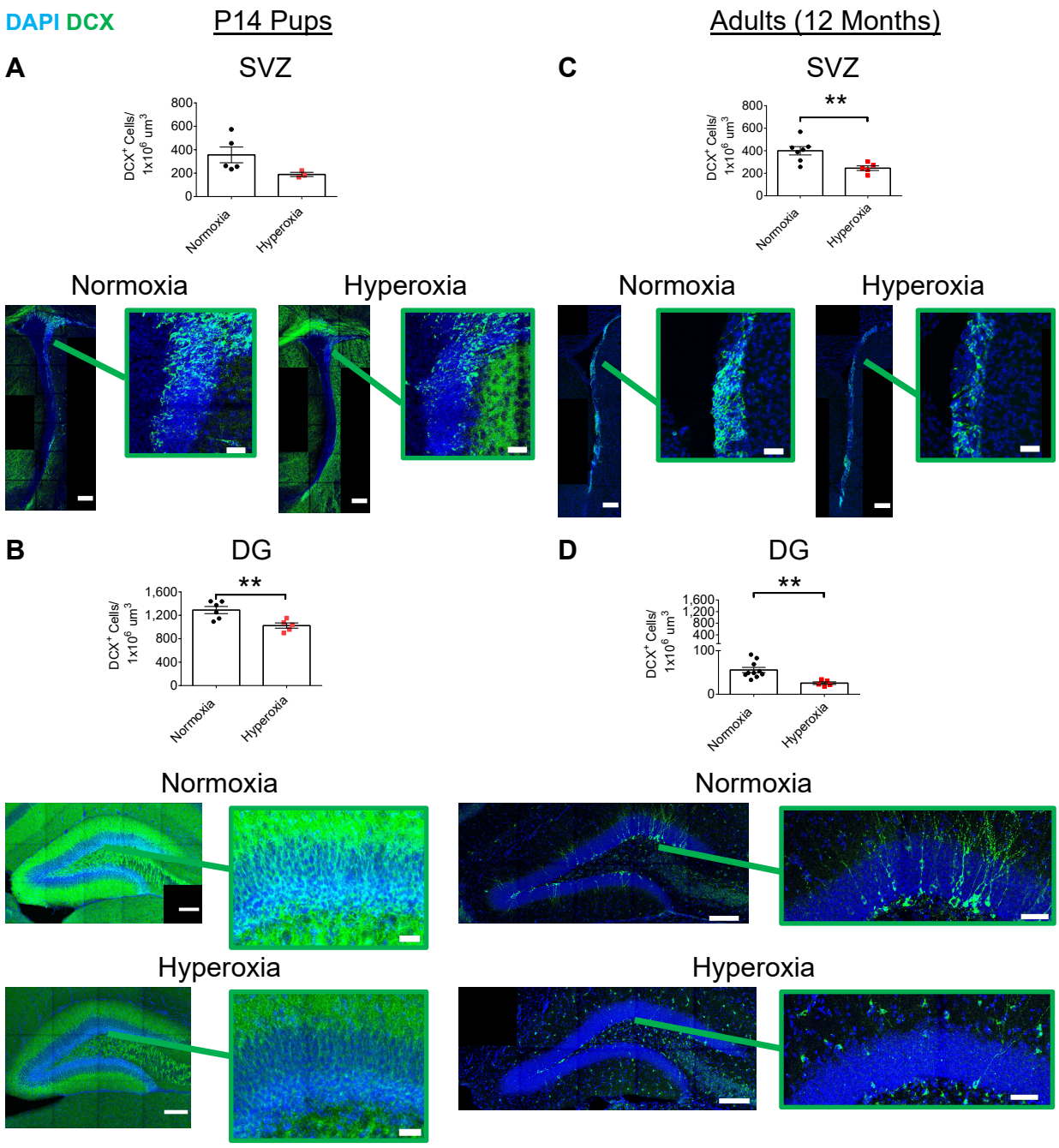

Figure 18. Early developmental hyperoxia exposure leads to reduced neurogenesis which persists into adulthood. (**A**) Quantification (top) and representative images (bottom) of newborn neurons (DCX^+) in the SVZ of P14 mice (normoxia, n=5; hyperoxia, n=3; Student's t test). Scale bar, whole ventricle, 150 µm; magnified image, 30 µm. (**B**) Quantification (top) and representative images (bottom) of newborn neurons (DCX^+) in the DG of P14 mice (normoxia, n=6; hyperoxia, n=5; $^{**}P < 0.01$; unpaired Student's t test). Scale bar, whole DG, 150 µm; magnified image, 30 µm. (**C**) Quantification (top) and representative images (bottom) of newborn neurons (DCX^+) in the SVZ of 12-month-old mice (normoxia, n=7; hyperoxia, n=5; $^{**}P < 0.01$; unpaired Student's t test). Scale bar, whole ventricle, 150 µm; magnified image, 30 µm. (**D**) Quantification (top) and representative images (bottom) of newborn neurons (DCX^+) in the DG of 12-month-old mice (normoxia, n=10; hyperoxia, n=5; $^{**}P < 0.01$; unpaired Student's t test). Scale bar, whole DG, 150 µm; magnified image, 50 µm. Data are expressed as mean ± SEM.

Hyperoxia exposure during early postnatal development leads to long-term locomotor and cognitive deficits. While abnormal neurodevelopmental outcomes of preterm birth have been well studied in childhood and early adulthood (65-67), long-term follow-up to middle age has rarely been investigated. Here, we aimed to test whether neurodevelopmental outcomes commonly reported in this BPD patient population occur in our BPD mouse model and if these outcomes change with aging. We used multiple well-described behavioral tests (68) to assess motor and cognitive abilities at 7 and 12 months of age. When we assessed motor learning and coordination on the rotarod test, there was no difference between the groups at 7 months (Figure 19A). In contrast, 12-month-old normoxia mice were able to stay on the rod significantly longer than hyperoxia-exposed mice (Figure 19B). Given that the 12-month-old mice had profound deficits on the rotarod, we conducted a detailed analysis of motor skills by recording mouse gait when walking on an inclined treadmill. At 7 months, no difference was found between the groups (Figure 19C-E). At 12 months of age, the hyperoxia-exposed mice placed a smaller area of their paws on the treadmill, took fewer steps, and walked more slowly compared to control mice on the treadmill (Figure 19F-H). These are common observations in human preterm infants that later develop motor impairments (69, 70). Provided the changes in gait, we wondered if these motor deficits would alter home cage activity when placed into a novel cage. At 7 months, mice from both groups had a similar amount of activity within the cage (Supplemental Figure 6A); however, there was a trend that 12-month-old hyperoxia-exposed mice had less activity (Supplemental Figure 6B). Overall, on three different tasks the motor phenotypes did not appear until 12 months, which is suggestive of a faster decline in motor abilities with aging in mice exposed to hyperoxia during the neonatal period.

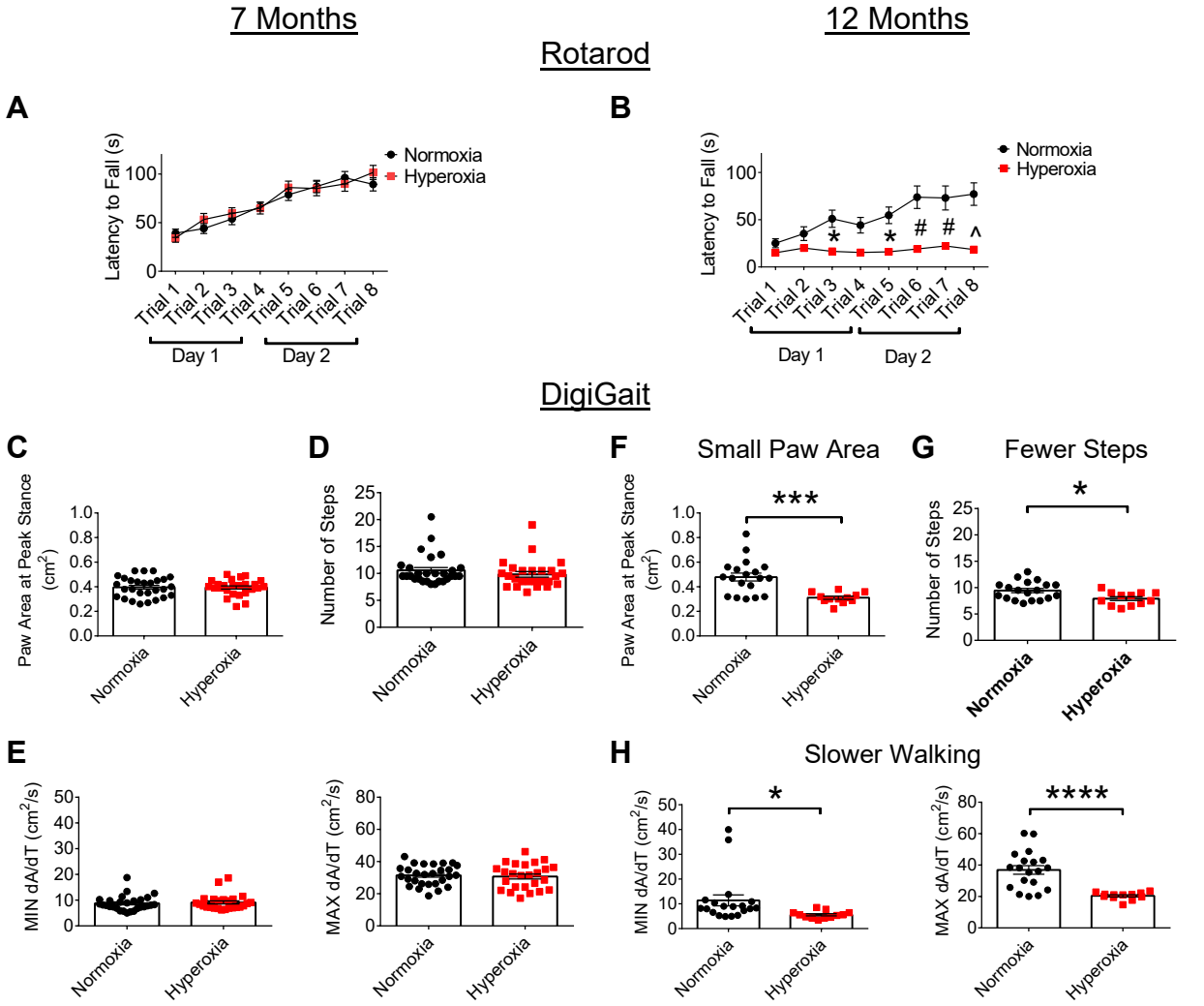

Figure 19. Motor decline with age as a result of developmental hyperoxia exposure. (**A** and **B**) Latency to fall (s) on the rotarod test for 7-month-old mice (A, normoxia, n=28; hyperoxia, n=25) and 12-month-old mice (B, normoxia, n=19; hyperoxia, n=12). *P < 0.05, #p<0.001; ^p<0.0001. Two-way ANOVA with Sidak post hoc test for group comparisons. (**C**-**E**) Quantification of DigiGait™ outcomes for 7-month-old mice (normoxia, n=28, hyperoxia, n=25; unpaired Student's t test), including paw area (cm^2) at peak stance (C), number of steps on the treadmill (D), and maximal rate of change in paw area during the propulsion phase (MIN dA/dT) and braking phase (MAX dA/dT) of walking (E). (**F**-**H**) Quantification of DigiGait™ outcome measures for 12-month-old mice (normoxia, n=19, hyperoxia, n=12; *P < 0.05; ***P < 0.001; ****P < 0.0001; unpaired Student's t test). Data are expressed as mean ± SEM.

In adulthood, the formation of new neurons within the DG can promote learning and memory (36, 71). This led us to reason that the impaired NPC function following early life hyperoxia may be associated with deficits in learning and memory in mice (72). To test this, we conducted behavioral tests known to assess these specific cognitive abilities including spatial

learning and memory using the Morris Water Maze (MWM) task and associative learning using the fear conditioning test (68). Hyperoxia-exposed mice were completely unable to learn the MWM (Supplemental Figure 7A-D). The distinction between groups was so striking that it was suggested that the mice may have visual deficits. Therefore, we conducted electroretinography to assess retinal function. The retinal cells of hyperoxia-exposed mice showed no excitation to light, indicating blindness. Normoxia-exposed animals displayed normal retinal function (Supplemental Figure 8, A and B). Although blindness is a confounding factor on the MWM test, we were able to further investigate learning and memory using the fear conditioning tests. The fear conditioning tests train mice to associate a cue (context or tone) with a shock. If the mice learn to make this association, they will freeze when exposed to the cue (68). During fear conditioning training, there were no significant differences between groups in baseline freezing prior to pairing the shock with the cue and context. In the context test, during the first and last 3 minutes of exposure to the context, the 7-month-old hyperoxia-exposed mice froze less frequently compared to the control mice (Figure 20A), suggesting deficits in hippocampal dependent associative learning. In the 12-month-old animals, there was a reduction in freezing in the last 3 minutes, but not the first 3 minutes of exposure to context (Figure 20B). This could be due to relatively lower levels of freezing in the older mice. On the cue test, which is more dependent on the hippocampus and amygdala, the hyperoxia compared to normoxia mice at both ages had a significant decline in cue recall (Figure 20, C and D). Thus overall, the fear conditioning test showed that hyperoxia-exposed mice have learning and memory deficits that occur at both 7 months and 12 months of age, which correlates with the hyperoxia-associated reduced hippocampal size, impairments in NPC self-renewal and neurogenesis, and neurovascular deficits. Given that supplemental oxygen is a

treatment routinely used for respiratory distress of extremely preterm infants, these findings have major implications on the long-term safety of oxygen administration for neonates.

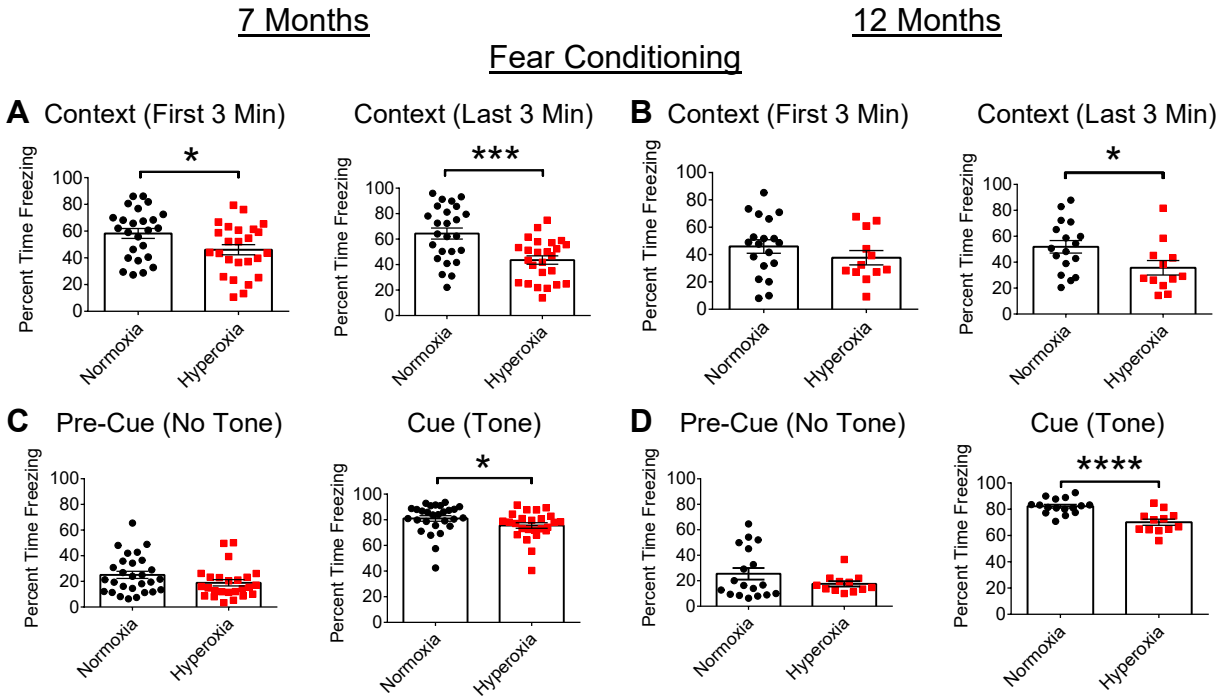

Figure 20. Long-term cognitive deficits following developmental hyperoxia exposure. (**A** and **B**) Quantification of the context fear conditioning task for 7-month-old mice (A, normoxia/hyperoxia, n=25) and 12-month-old mice (B, context first 3 min, normoxia, n=19; hyperoxia, n=12; context last 3 min, normoxia, n=17; hyperoxia, n=12). (**C** and **D**) Quantification of the auditory tone fear conditioning task of 7-month-old mice (C, normoxia, n=28, hyperoxia, n=25) and 12-month-old mice (D, pre-cue (no tone), normoxia, n=19; hyperoxia, n=12; cue (tone), normoxia, n=17; hyperoxia, n=12). *$P < 0.05$, ***$P < 0.001$; ****$P < 0.0001$; unpaired Student's t test. Data are expressed as mean ± SEM.

Discussion

Our study reveals that early life hyperoxia exposure leads to long-term impairments in cerebrovascular function, neurogenesis, and cognitive deficits. This study also provides insight into an underlying mechanism contributing to BPD-associated neurodevelopmental deficits.

We found that hyperoxia exposure during early development increased baseline CBF and led to neurovascular uncoupling, as well as to higher oxygen concentrations in the brain. Under these conditions, we showed dramatic vascular remodelling in the cerebral cortex and DG. We demonstrated that NPC depletion was associated with impaired NPC self-renewal using murine and baboon cells. Finally, we found that the NPC functional impairments correlated with motor and cognitive deficits during adulthood. These results strongly support the argument that NPCs and their vascular niche play a crucial role for appropriate brain development, and that when impaired with hyperoxia, this leads to abnormal brain development and behavioral deficits.

The hyperoxia model mimicking preterm birth-associated brain injury has widespread clinical implications. For example, one hypothesis linking BPD to abnormal neurodevelopment is that the lung injury causes global hypoxia, and subsequent brain damage. However, we provide strong evidence that hyperoxia-exposed mice, even following exercise, maintained their arterial oxygen saturation levels within a normal physiological range. This is critical as it indicates that in experimental BPD the lungs and the brain are directly affected by hyperoxia. Therefore, our data supports the notion that therapies directly targeted to NPCs and the developing brain vasculature are of immense clinical value. A limitation of our study is that it does not incorporate all preterm birth-associated noxious stimuli, such as ante- and postnatal inflammation, sedation, and steroids (3-5, 73). However, this can also be considered a strength of the model's focus on supplemental

oxygen, providing a detailed examination of the effects of hyperoxia on lung and brain development, without these confounding factors.

A major question that arises from our model is: how can an excess of oxygen reach and damage the brain? There are several possible contributors. First, one of the most striking results from our study is that early developmental hyperoxia impairs neurovascular function and this injury continues into adulthood. The hyperoxia-induced increased baseline CBF fits well with human data, showing that preterm infants cannot autoregulate their vasculature in response to oxygen treatment (74). Second, in hyperoxia, an increased oxygen tension gradient between the blood and tissue can lead to tissue hyperoxygenation (59). Together, these potential contributors can lead to hyperoxic brain tissue, which coincides with our finding that brain regions of hyperoxia-exposed mice were becoming progressively hyperoxic. A probable source of this progressive hyperoxia is the neurovascular uncoupling observed during development and into adulthood. Due to the sustained impairment in NVC, an improper amount of oxygen may be delivered to the brain throughout life.

One likely cause of the neurovascular uncoupling is oxygen-induced damage to the vascular structure within the brain, since the integrity of cerebrovascular networks is crucial for proper autoregulation (75). In fact, delayed vascular growth in mouse models of neurodevelopmental disorders, such as autism spectrum disorder, has been previously associated with neurovascular uncoupling in adult mice (56). We found delayed vascular growth in the cerebral cortex and DG. This is a novel observation in experimental BPD and was further supported by damage to another organ of the central nervous system: the retina. Retinopathy of prematurity (ROP) is a hyperoxia-induced disease, leading to vascular remodelling within the eyes. The pathology occurs in two phases: first, an impairment in vessel formation; second, an

overgrowth of the vasculature (76, 77). Notably, our data demonstrates both retinal phenotypes. The first phase is caused by a deficit in vascular autoregulation, leading to an excess of oxygen reaching the retina and a downregulation of hypoxia-inducible factor 1-α (HIF-1α) (78). Suppression of HIF-1α, leads to reduced expression of vascular endothelial growth factor (VEGF), a crucial factor required for the development of vessels (79-81). Furthermore, oxygen itself is damaging when administered at high levels, as incomplete reduction of oxygen leads to the production of ROS (82). An increase of ROS within ECs leads to EC dysfunction, apoptosis, and reduced vessel growth (78). This mechanism fits well with our data, although, we do not observe the second phase of neovascularization within the brain. This is likely because in the retina, the reduced vessel growth leads to a hypoxic microenvironment, causing dysregulated vessel growth, whereas in the brain, although there is reduced vasculature, the microenvironment shows a trend of becoming hyperoxic.

We also demonstrate that early life hyperoxia leads to NPC functional impairments. We show that hyperoxia alone can directly impair NPC function. Another critical environmental factor that influences NPCs is the surrounding vasculature (83-89). We demonstrate that the reduced vessel formation decreased the amount of anchorage points for NPCs. These anchorage points are crucial for maintaining this NPC population (90, 91). Both factors, (i.e., hyperoxia and vascular impairments), act as an initial insult to NPCs. Impaired NPC self-renewal is associated with a long-term deficiency in neurogenesis, as well as learning and memory deficits in adult mice. While the precise causal relationship remains unclear, this is similar to the cognitive impairments associated with preterm birth in humans (65-67).

It is important to note that the initial hyperoxic injury occurred during a critical period of brain development and led to long-term abnormal neurodevelopmental outcomes. Moreover, we

report that with age, there is a decline in NPC anchorage points onto blood vessels, the NPC population, newborn neurons, motor learning, and motor coordination abilities. Thus, our data demonstrates that early life insults on the brain vasculature and neurogenic regions lead to a deterioration in brain structures and function that continues into adulthood. This suggests the importance of an early intervention therapy to mitigate developmental impairments that may have life-long consequences.

Together, these results highlight a novel mechanism that contributes to preterm birth-associated brain injury. They also demonstrate the need for judicious oxygen administration in the clinic and provide insight into potential therapeutic targets to mitigate the complications faced by this vulnerable neonatal patient population.

Methods

Animal model of hyperoxia-induced lung injury. Pregnant C57 BL/6 mice were shipped from Charles River Laboratories to the University of Ottawa at E13-16. The pregnant mice were singly housed. The mice were maintained in standard conditions (free access to food and water, 22°C). Mice were housed in a normal 12-hour light/ dark cycle (7AM-7PM), except for the metabolic treadmill test and the behavioral experiments (for which the cycle was reversed for a minimum of 2 weeks prior to the experiments and for the duration of the experiments). Once the pups were born, the mice were exposed to normoxia (21% O_2, room air control group) or hyperoxia (85% O_2, BPD group) using the OxyCycler A84X0V (Biospherix) in Plexiglass chambers (Biospherix) (92) from P0 to P14. Dams were switched every 24-48 hours between normoxic and hyperoxic conditions to ensure that the pups received adequate nutrition. Both sexes were assessed in this study. At weaning, mice of the same sex were housed in 2-4/ cage, unless separated due to fighting. Survival was recorded from P0-P14 or from P14 to 12 months of age. Body and brain weight were recorded for a subset of P14 and 12-14-month-old mice (Supplemental Figure 2A).

Arterial blood oxygen saturation measurements. The oxygen saturation measurements were conducted at P14 and at 12-14-months of age. Adult mice had undergone behavioral testing (see behavioral methods) at 7 months of age. Both age groups were tested at rest; however, adult mice were also assessed immediately following treadmill exercise (see treadmill methods). Methods were modified from Spitalieri et al. (93). Mice were anesthetized with isoflurane and the Mouse Ox Plus® oximeter sensor (Starr Life Sciences Corp.) was placed over the shaved, right thigh of each mouse to detect blood oxygen saturation of the femoral artery. Arterial blood oxygen saturation, heart rate (beats per minute), and respiratory rate (breaths per minute) were recorded for a minimum of 25 seconds using the Mouse Ox Plus® basic software.

Lung histopathology & image acquisition. Lung tissue was collected at P14 and 14 months of age. Adult mice had undergone behavioral testing (see behavioral methods) at 12 months of age. Lungs were processed using methods from Vadivel et al. (94). Lungs were intratracheally inflation fixed with 10% buffered formalin, under 20 cm H_2O pressure, for 5 minutes. Lungs were immersion fixed in 10% buffered formalin for 48 hours at room temperature and immersed in 70% ethanol for 24 hours at room temperature. Lungs were then paraffin-embedded, cut into 4 µm sections, and stained with hematoxylin and eosin at the University of Ottawa Histology Core Facility. To visualize lung structure, images (x20 magnification) were acquired on an Aperio CS2 slide scanner (Leica) using the Aperio eSlide Manager (Leica).

Metabolic treadmill test. Adult mice at 12-14 months of age (as described in arterial blood oxygen saturation methods) were tested during the dark cycle and habituated to the dark testing room (red light) for 30 minutes before the treadmill procedure. Each mouse was individually placed into the 1012M-1 Modular Enclosed Metabolic Treadmill for Mice (Columbus Instruments), as adapted by Marcaletti et al. (95). The treadmill speed increased as follows: 0 cm/s for 5 minutes, 8cm/s for 5 min, 15cm/s for 5 min, 20 cm/s for 5 min, 25 cm/s for 5 min, then increased by 3 cm/s every 2 minutes. Mice remained on the treadmill until exhaustion, as determined by the mouse remaining on the shock bar (~0.5mA) for 10 seconds, the mouse being unable to run, or if the respiratory exchange ratio becomes greater than or equal to 1 or dramatically increases within 4-6 minutes and then reaches a plateau. Oxygen consumption and carbon dioxide release were measured every 30 seconds using the Oxymax®/ comprehensive lab animal monitoring system (CLAMS) and software (Columbus Instruments).

MRI. All MRI images were acquired by the University of Ottawa Preclinical Imaging Core Facility. Mice were 14 months of age at time of testing and had previously been assessed for

behavior at 12 months of age (see behavior methods). MRI was conducted using a 7 Tesla General Electric/Agilent MR901 machine. Coronal, 2D fast spin echo T_2-weighted brain images were acquired (TE = 25 ms, TR = 6000 ms, ETL = 8, bandwidth = 15.6 KHz, FOV = 2.5 cm, slice thickness = 0.5 mm, matrix = 265 x 256, scan time = 7 min). The size of the whole brain, lateral ventricles, and hippocampal regions were measured using Fiji (96). The total area of anatomically comparable sections was measured using the polygon tool and was multiplied by the thickness of each MRI slice.

Laser doppler flowmetry and analysis. CBF was measured using laser doppler flowmetry as described previously (55). The same cohorts of animals were tested at P14 and 10 months of age. Briefly, once the animal was mounted in the stereotactic equipment and the skull was exposed, the flowmeter (BLF22, single-channel tissue perfusion monitor, Transonic Systems Inc.) was placed above the left somatosensory cortex. Baseline CBF measurements were recorded. To assess neurovascular coupling, whiskers on the right side of the animal were stimulated for 20 second intervals a minimum of 3 times. An average of three stimuli was used for the baseline and whisker stimulated CBF values for each animal.

Systolic blood pressure. Mice at 10 months of age were housed in the testing room for a minimum of 1 week prior to training. These mice were previously tested for arterial blood oxygen saturation (see methods above) at P14. To reduce stress, mice were tested by the same handler, at the same time each day. Mice were placed on a BP-2000 Series II Blood Pressure Analysis System™ (Visitech Systems, Inc.), in individual compartments. Tails were confined in the tail-cuff holders (97). Systolic blood pressure was measured 5 times, to ensure consistency, followed by 10 trials which were recorded. Training occurred over 5 consecutive days. After a 2-day interval, systolic blood pressure was measured on the acclimatized mice over 5 consecutive days, following the

same procedure as during the training sessions. Only consistent measurements of at least 8 of the 10 trials, per day, were used in the analysis. The average systolic blood pressure of approximately 50 trials per mouse was calculated.

Oxygen microsensor measurements and analysis. Mice at P14 and 10 months of age were anesthetised and mounted according to methods previously described in the laser doppler flowmetry section. These were the same cohorts of adult mice assessed for CBF and allowed a minimum recovery of one week before proceeding to oxygen measurements. The oxygen microsensor (OX-10, Unisense A/S) is 2 μm in diameter at the tip, which allowed for a direct, minimally invasive measurement of the oxygen concentration of the brain tissue (98) in the somatosensory cortex, SVZ, and hippocampal regions. Only animals with consistent oxygen concentrations over a period of 2 minutes were used in the analysis.

Cerebral vasculature processing and imaging. At P14 and 14-16 months of age, brain tissue was collected from normoxia and hyperoxia-exposed mice. Adult mice had undergone behavioral testing (see behavior methods) at 12 months of age. Brains were cut sagitally in half, immersion fixed in 4% paraformaldehyde for 24 hours at 4°C, and embedded in agarose gel. Using a vibratome, brains were sagitally cut into 120 μm sections, as previously described (99). Sections were then processed, incubated with an antibody against CD31 (1:200; BD Pharmingen, 553370), and mounted onto slides, as previously described (56). Three-dimensional 50 μm z-stack images were acquired (x10 magnification) on a Zeiss Axio Imager M2 microscope with an ApoTome.2 system of three fields of view for each of the represented cortical layers (II/III, IV, & V). The average values of the 3 layers (Supplemental Figure 4) were calculated and displayed. Representative images were 3D modelled using the surfaces module of Imaris 9.3 (Bitplane Inc.) (99, 100).

Cerebrovascular image analysis. All image analysis was conducted while blinded to the experimental groups. Computational analysis using Python 2.7 was adapted from protocols previously described (101). Briefly, the following modules were used: Numpy, Scipy, Matplotlib, Opencv2, Igraph and Scikit-Image. These allowed for immunofluorescent images to be segmented, skeletonized, and quantified for vessel length and branching points.

Code availability. The final version of custom scripts for blood vessel quantification, written in Python, will be made available at publication.

NPC niche region processing, imaging, and quantification. Brain tissue was collected from mice at P14 and 12 months of age. Adult mice had previously been assessed for CBF and oxygen microsensor measurements (see methods above) at 10 months of age. Brains were cut sagitally in half and the side that was not assessed during the CBF and oxygen measurements was immersion fixed overnight at 4°C in 4% paraformaldehyde. Brains were embedded in agarose and cut coronally into 60 μm thick, serial free-floating sections, as modified by previously described methods (101). Sections were incubated for 2 hours in blocking solution (1X phosphate buffered saline (PBS), 10% donkey serum, 0.5% Triton X-100, 0.5% fish gelatin). To visualize NPCs and the surrounding vasculature, starting from the 1st serial section, every 4th section throughout the SVZ and DG was incubated in PBT solution (1X PBS with 0.5% Triton X-100) with antibodies against nestin (1:500; R&D Systems, AF2736), Sox2 (1:500; Abcam, ab97959), and CD31 (1:200) overnight at room temperature with gentle shaking. The following day, sections were washed 4 times (5 minutes each) with PBT solution. This was followed by an incubation with secondary antibodies (All Invitrogen; 1:300, donkey α-rat AlexaFluor® 488, A-21208; 1:1000, donkey α-rabbit AlexaFluor® 555, A-32794; 1:1000, donkey α-goat AlexaFluor® 647, A-32849), as well as immunostained with DAPI (Invitrogen, D1306), for 3 hours at room temperature with gentle

shaking. To visualize newborn neurons, starting from the second serial section, every 4th section throughout the SVZ, and DG was processed and incubated as described above, with antibodies against DCX (1:500; Santa Cruz, SC-8066; secondary antibody, 1:1000; Invitrogen, donkey α-goat AlexaFluor® 647, A-32849), as well as immunostained with DAPI. Sections were washed twice with PBT solution, followed by two washes in phosphate buffer solution to remove the salt and triton. Sections were then mounted onto slides using Fluoromount-G (Fisher Scientific, 5025973). Three-dimensional 20 μm z-stack images were acquired (x20 magnification) on a Zeiss LSM800 Axio Observer Z1 confocal microscope using ZEN 2.6 (blue edition). All image analysis was conducted while blinded to the experimental groups. 3D modelling of z-stack images was conducted using the surfaces module of Imaris 9.3 to measure the volume of i) the SVZ and ii) the SGZ (for NPC quantification) or DG (for newborn neuron quantification) of sections. For P14 mice, a total sum of 2 sections per region, per animal was used in the analysis. For 12-month-old mice, a total sum of 3 sections per region, per animal was used in the analysis. For NPC quantification, computational analysis of the SGZ was conducted with Imaris 9.3 (Bitplane Inc.) using the spots module to quantify NPCs (Sox2$^+$, nestin$^+$) and confirmed with manual inspection. For the SVZ, images were manually quantified using the cell counter module of Fiji. The contact points of CD31$^+$ ECs with nestin processes of NPCs in the DG was quantified manually using the cell counter module of Fiji. Newborn neurons (DCX$^+$) were manually quantified in the SVZ and DG using the cell counter module of Fiji. A maximum intensity Z-projection is displayed for all NPC niche images.

Neurosphere assays with murine-derived NPCs. NPCs from mice at P14 and 14 months of age were isolated and cultured using adapted methods from Fujitani et al. (102). Adult mice had previously been assessed for behavior at 12 months of age (see behavior methods). Briefly, the

subependyma of the lateral ventricles was removed, digested with papain (Worthington, PAPL LS003118), and mechanically dissociated. Cells were filtered through a 40 μm mesh (Corning, 352340) and plated for a primary neurosphere assay at a cell density of 10 cells/μL in Dulbecco's Modified Eagle Medium/Nutrient Mixture F-12 (DMEM/F-12) media (Thermo Fisher Scientific, 11330057) containing 20 ng/mL fibroblast growth factor-2 (FGF) (Sigma, F0291), 20 ng/mL epidermal growth factor (EGF) (Sigma, E1257), 2 μg/mL heparin (Sigma, H3149), 2% B-27 (Life Technologies, 10889-038), and 1% antibiotic-antimycotic (Thermo Fisher Scientific, 15240-062). Primary neurospheres were counted and imaged 7-8 days after plating. Neurospheres were then dissociated with TrypLE™ Express Enzyme (Thermo Fisher Scientific, 12605-028), washed in DMEM/F-12, and plated in media (described above) at a density of 2 cells/μL. Secondary neurospheres were counted and imaged 7-8 days after plating. Images were acquired (x20 magnification) on a Nikon Eclipse TE2000-E microscope using NIS-Elements AR 3.0 (Nikon).

Baboon NPC isolation and neurosphere assays. We enrolled 6 neonatal baboons (male and female) in our study, housed at the Texas Biomedical Research Institute, San Antonio, Texas, USA. Three baboons were term animals, delivered vaginally. NPCs were isolated from these animals at gestational days 185, 190 and 194. Three baboons were preterm, delivered via C-section. NPCs were isolated from these animals at gestational days 141, 127, and 125. Brain tissue was collected and stored in artificial cerebral spinal fluid on ice. The subependyma of the lateral ventricles and the DG of the hippocampus were dissected, digested with papain, and mechanically dissociated. Cells were filtered through a 40 μm mesh before being plated at a density of 37,500 cells/mL in DMEM/F-12 media containing 20 ng/mL FGF (Sigma, F0291), 20 ng/mL EGF (Sigma, E9644), 8 μg/mL heparin, 2% B-27, 1% N-2 (Thermo Fisher Scientific, 17502048), and 1% antibiotic-antimycotic. Cells isolated from preterm baboons were cultured overnight and then

exposed to 60% O_2 for 48 hours. Cells were then transferred to 21% O_2. Control term baboon cells remained in 21% O_2 for the duration of the experiment. Primary neurospheres were counted and imaged once the majority of neurospheres cultured at 21% O_2 (controls) reached a minimum diameter of 50 μm. Neurospheres were dissociated with TrypLE™ Express Enzyme, washed in DMEM/F-12, and plated in media described above at a density of 3,750 cells/mL. Secondary neurospheres were counted and imaged once the majority of neurospheres cultured at 21% O_2 (controls) reached a minimum diameter of approximately 50 μm. Images of neurospheres were acquired (x10 magnification) using ToupView 3.7 (ToupTek) on an Olympus IX 50 inverted system microscope.

Behavioral experiments. The behavioral experiments were conducted at the University of Ottawa Behavior and Physiology Core Facility as per previously established protocols (68). Adult mice at 7 months and 12 months of age were handled for 2 days before the experiments commenced and the person conducting the testing was blinded to the treatment groups. All testing was conducted during the dark cycle and in red light, with the mice being habituated to the red-light testing room for ~30-60 minutes prior to testing, unless otherwise indicated.

Rotarod. Mice had four trials (10-minute inter-trial interval (ITI)) over a period of 2 consecutive days on an accelerating rotarod (IITC Life Science Inc.). For each trial, the rod was set to accelerate from 4 to 45 rpm in 300 seconds, followed by 300 seconds at 45 rpm.

DigiGait™. Mouse gait was recorded for a minimum of 3 seconds on the transparent DigiGait™ treadmill (Mouse Specifics, Inc.) that was set to a speed of 18 cm/sec, and an incline of 8 degrees. Videos were blindly analyzed using DigiGait™ Analysis software (Mouse Specifics, Inc.).

Home cage locomotor activity. Mice were placed individually into clean housing cages which were then placed for 4 hours into the Home Cage Locomotor Activity Infrared Beam Break frames that were paired with the Fusion software (Omnitech Electronics, Inc.).

Morris water maze. Each mouse was habituated to the testing room in 140 lux light for 30 minutes. A single black X (2.8 cm thick, 15cm long x 13.5cm wide) was placed on the back wall of the room as a cue. Each mouse was placed in a circular pool, measuring 132 cm in diameter, filled with water colored white with tempera paint maintained at 23°C. The pool contained a hidden platform (10 cm in diameter) in one of its 4 quadrants. Each mouse was trained to find the platform for four trials each day (ITI of 30 minutes) for nine days total. During each trial, the mouse had 1 minute to find the platform. On the 10^{th} day, the platform was removed, and the mouse was given one minute to search for the platform. Each trial was tracked and analyzed using Ethovision software (Noldus). If the mouse did not find the platform within 1 minute, the program automatically stopped.

Fear conditioning. Mice were not habituated to the testing room prior to the experiment and the experiment was performed using the PhenoTyper® boxes (Noldus) with grid shock floors (Med Associates). The overhead room lights were on and no lights were projected by the boxes. On the training day, mice were placed into the box. The mice remained in the box for 2 minutes, after which a 30 second 80 dB tone played, followed by a 2 second 0.45mA foot shock. This tone-shock pairing was repeated three times with a 1-minute interval. The final tone-shock pair was followed by a 30-second interval, for a total testing time of 6 minutes. The mice were then returned to their home cages. On day 2, to assess contextual memory, mice were placed in the same box for 6 minutes with no tone or shock. On day 3, to assess cued memory, mice were placed in a different Phenotyper® box from the one used for training and the contextual memory test. This box was

altered through the addition of a plastic floor, triangular plastic walls, and a vanilla scent. The room was lit with red light and the boxes were lit with both white and yellow light simultaneously. The mice were in the modified box for six minutes with the 80 dB tone playing during the last three minutes, in the absence of any shock. All trials were recorded and freezing behavior was scored using Ethovision software (Noldus). Mice that froze less than 10 seconds were not included in the analysis.

Electroretinography (ERG). Retinal function was assessed at 6, 9, and 15-17 months of age. Animals at 9 months of age had previously been tested for arterial blood oxygen saturation at P14 and animals at 15-17 months of age had previously been tested for behavior at 7 months of age (see methods above). Mice were weighed and habituated to the dark testing room overnight prior to the ERG. ERGs were conducted on a CELERIS system (Diagnosys LLC) with Espion software (Diagnosys LLC) using modified methods from Wassmer et al. (103). Animals were anesthetized with an intraperitoneal injection of ketamine hydrochloride (50 mg kg^{-1}; Narketan®) and medetomidine hydrochloride (1 mg kg^{-1}; Cepetor®). Anesthesia was maintained throughout the test and the medetomidine was reversed after 1 hour using atipamezole hydrochloride (1 mg kg^{-1}; Antisedan®). Eyes were dilated for 10 minutes prior to ERG testing with one drop each of 1% tropicamide (Mydriacyl, Alcon) and 2.5% phenylephrine hydrochloride (Mydfrin, Alcon). A topical anesthetic (0.5% proparacaine hydrochloride; Alcain, Alcon) was applied to each eye. 1 mL of saline was administered subcutaneously, prior to testing. Ag/AgCl contact stimulators were placed on both corneas in combination with Optixcare Veterinary Eye Lube (Aventix) to ensure stimulator contact and corneal hydration. A gold loop reference electrode was placed on the tongue, a needle electrode was placed sub-dermally in the head, and a grounding needle electrode was placed subcutaneously in the tail. Retinal function was assessed with the following

3 protocols. The simultaneous ERG and visually evoked potentials (VEP) protocol stimulates the retina with a blue and green coloured flash at an intensity of 0.05 candela seconds (cd.s)/m^2 and a frequency of 1 Hz. The c-wave protocol stimulates the retina with a white-6500K flash at an intensity of 150 cd.s/m^2 and a frequency of 1 Hz. The photopic negative response (PhNR) protocol stimulates the retina with a white-6500K flash at an intensity of 20 cd.s/m^2 and a frequency of 2 Hz.

Fundus photography. Mice were anesthetized, dilated, and maintained as described in the ERG protocol above. Fundus imaging was acquired using Streampix 3 (Norpix) on a Micron III microscope (Phoenix Technology Group) to inspect retinal morphology.

Statistics. Statistical analyses were conducted using GraphPad Prism 6.0 software. All values were expressed as mean ± standard error of the mean. An unpaired, two-tailed Student's t test was used to compare two groups. A one-way ANOVA with post hoc Tukey test or a two-way ANOVA with post hoc Sidak test were used to compare multiple groups. A $P < 0.05$ was considered statistically significant. Statistical details of all experiments can be found in the figure legends.

Study approval. All mouse procedures were approved by the University of Ottawa Animal Care Committee. All nonhuman primate baboon procedures were approved by the University of Texas Health Science Center at San Antonio Institutional Animal Care and Use Committee.

Author Contributions

M.A.L. designed experiments, established the animal model, assisted with and analyzed the oxygen saturation, CBF, and oxygen concentration experiments, conducted blood pressure measurements, acquired and analyzed lung and brain images, performed neurosphere assays, and assisted with the analysis of the metabolic treadmill, behavioral, and visual experiments, interpreted data, and wrote the manuscript. X.T. performed the CBF and oxygen concentration experiments. S.Z. and L.X. assisted with lung processing and mouse neurosphere assays. S.B.M. contributed intellectual guidance and assisted with baboon neurosphere assays. C.H.C. conducted the vascular quantification of the cortical brain regions. H.A.B. and A.N.B. conducted and analyzed the vision function tests. A.M. contributed material and intellectual guidance. C.L.B. assisted with the collection of baboon tissue and contributed intellectual guidance. A.V. contributed intellectual guidance and assisted with establishing the animal model. C.T. supervised the vision function tests. S.S. contributed intellectual guidance and assisted with the collection of baboon tissue. R.S., D.L., J.W., and B.L., contributed intellectual guidance, provided training and material, and edited the manuscript. B.T. supervised the study, contributed intellectual guidance, provided financial support, and edited the manuscript.

Acknowledgements

The authors thank the University of Ottawa Behavior and Physiology, Histology, Preclinical Imaging, and Cell Biology and Image Acquisition core facilities for their equipment and services. The authors also thank the University of Texas Health Science Center at San Antonio and the Texas Biomedical Research Institute for their collaboration with the baboon study. M.A.L. was supported by a Canadian Institutes of Health Research (CIHR) Frederick Banting and Charles Best Doctoral Award and a CIHR Canada Graduate Scholarship Michael Smith Foreign Study Supplement. B.T. is supported by CIHR, The Stem Cell Network, the Ontario Institute of Regenerative Medicine, and the Children's Hospital of Eastern Ontario Foundation.

References

1. Lawn JE, Kinney M. Preterm birth: now the leading cause of child death worldwide. *Sci Transl Med.* 2014;6(263):263ed21.
2. Stoll BJ, et al. Trends in Care Practices, Morbidity, and Mortality of Extremely Preterm Neonates, 1993-2012. *JAMA.* 2015;314(10):1039-1051.
3. Jobe AH, Bancalari E. Bronchopulmonary dysplasia. *Am J Respir Crit Care Med.* 2001;163(7):1723-1729.
4. Jobe AH. The new bronchopulmonary dysplasia. *Curr Opin Pediatr.* 2011;23(2):167-172.
5. Thébaud B, et al. Bronchopulmonary dysplasia. *Nat Rev Dis Primers.* 2019;5(1):78.
6. Vohr BR, et al. Neurodevelopmental outcomes of extremely low birth weight infants <32 weeks' gestation between 1993 and 1998. *Pediatrics.* 2005;116(3):635-643.
7. Brouwer A, et al. Neurodevelopmental outcome of preterm infants with severe intraventricular hemorrhage and therapy for post-hemorrhagic ventricular dilatation. *J Pediatr.* 2008;152(5):648-654.
8. Cheong JLY, et al. Abnormal white matter signal on MR imaging is related to abnormal tissue microstructure. *AJNR Am J Neuroradiol.* 2009;30(3):623-628.
9. Volpe JJ. The encephalopathy of prematurity--brain injury and impaired brain development inextricably intertwined. *Semin Pediatr Neurol.* 2009;16(4):167-178.
10. Reich B, et al. Hyperoxia and the Immature Brain. *Dev Neurosci.* 2016;38(5):311-330.
11. Blencowe H, et al. Preterm birth-associated neurodevelopmental impairment estimates at regional and global levels for 2010. *Pediatr Res.* 2013;74 Suppl 1:17-34.
12. Breeman LD, et al. Preterm Cognitive Function Into Adulthood. *Pediatrics.* 2015;136(3):415-423.

13. Volpe JJ. Brain injury in premature infants: a complex amalgam of destructive and developmental disturbances. *Lancet Neurol.* 2009;8(1):110-124.

14. Omizzolo C, et al. Neonatal brain abnormalities and memory and learning outcomes at 7 years in children born very preterm. *Memory.* 2014;22(6):605-615.

15. Sriram S, et al. Cognitive Development and Quality of Life Associated With BPD in 10-Year-Olds Born Preterm. *Pediatrics.* 2018;141(6).

16. Wood NS, et al. Neurologic and developmental disability after extremely preterm birth. EPICure Study Group. *N Engl J Med.* 2000;343(6):378-384.

17. Johnson S, Marlow N. Preterm birth and childhood psychiatric disorders. *Pediatr Res.* 2011;69(5 Pt 2):11R-8R.

18. Gough A, et al. Executive functioning deficits in young adult survivors of bronchopulmonary dysplasia. *Disabil Rehabil.* 2015;37(21):1940-1945.

19. Short EJ, et al. Cognitive and academic consequences of bronchopulmonary dysplasia and very low birth weight: 8-year-old outcomes. *Pediatrics.* 2003;112(5):e359.

20. Robertson CM, et al. Eight-year school performance, neurodevelopmental, and growth outcome of neonates with bronchopulmonary dysplasia: a comparative study. *Pediatrics.* 1992;89(3):365-372.

21. Singer L, et al. A longitudinal study of developmental outcome of infants with bronchopulmonary dysplasia and very low birth weight. *Pediatrics.* 1997;100(6):987-993.

22. Jobe AH, Kallapur SG. Long term consequences of oxygen therapy in the neonatal period. *Semin Fetal Neonatal Med.* 2010;15(4):230-235.

23. Perrone S, et al. Oxygen Use in Neonatal Care: A Two-edged Sword. *Front Pediatr.* 2016;4:143.

24. Gitto E, et al. Oxidative stress in resuscitation and in ventilation of newborns. *Eur Respir J.* 2009;34(6):1461-1469.

25. Milligan DW. Failure of autoregulation and intraventricular haemorrhage in preterm infants. *Lancet.* 1980;1(8174):896-898.

26. Pryds O, et al. Heterogeneity of cerebral vasoreactivity in preterm infants supported by mechanical ventilation. *J Pediatr.* 1989;115(4):638-645.

27. Perlman JM, et al. Reduction in intraventricular hemorrhage by elimination of fluctuating cerebral blood-flow velocity in preterm infants with respiratory distress syndrome. *N Engl J Med.* 1985;312(21):1353-1357.

28. Hoffman SB, et al. Cerebral autoregulation in premature infants during the first 96 hours of life and relationship to adverse outcomes. *Arch Dis Child Fetal Neonatal Ed.* 2019;104(5):F473-F479.

29. Ming G, Song H. Adult neurogenesis in the mammalian central nervous system. *Annu Rev Neurosci.* 2005;28:223-250.

30. Kriegstein A, Alvarez-Buylla A. The glial nature of embryonic and adult neural stem cells. *Annu Rev Neurosci.* 2009;32:149-184.

31. Moreno-Jiménez EP, et al. Adult hippocampal neurogenesis is abundant in neurologically healthy subjects and drops sharply in patients with Alzheimer's disease. *Nat Med.* 2019;25(4):554-560.

32. Reynolds BA, Weiss S. Generation of neurons and astrocytes from isolated cells of the adult mammalian central nervous system. *Science.* 1992;255(5052):1707-1710.

33. Richards LJ, et al. De novo generation of neuronal cells from the adult mouse brain. *Proc Natl Acad Sci USA.* 1992;89(18):8591-8595.

34. Gage FH, et al. Survival and differentiation of adult neuronal progenitor cells transplanted to the adult brain. *Proc Natl Acad Sci USA.* 1995;92(25):11879-11883.

35. Morrison SJ, et al. Regulatory mechanisms in stem cell biology. *Cell.* 1997;88(3):287-298.

36. Ming G-L, Song H. Adult neurogenesis in the mammalian brain: significant answers and significant questions. *Neuron.* 2011;70(4):687-702.

37. Emsley JG, et al. Adult neurogenesis and repair of the adult CNS with neural progenitors, precursors, and stem cells. *Prog Neurobiol.* 2005;75(5):321-341.

38. Panchision DM. The role of oxygen in regulating neural stem cells in development and disease. *J Cell Physiol.* 2009;220(3):562-568.

39. Prozorovski T, et al. Redox-regulated fate of neural stem progenitor cells. *Biochim Biophys Acta.* 2015;1850(8):1543-1554.

40. Khacho M, et al. Mitochondrial Dynamics Impacts Stem Cell Identity and Fate Decisions by Regulating a Nuclear Transcriptional Program. *Cell Stem Cell.* 2016;19(2):232-247.

41. Khacho M, Slack RS. Mitochondrial and Reactive Oxygen Species Signaling Coordinate Stem Cell Fate Decisions and Life Long Maintenance. *Antioxid Redox Signal.* 2018; 28(11):1090-1101.

42. Goldman SA, Chen Z. Perivascular instruction of cell genesis and fate in the adult brain. *Nat Neurosci.* 2011;14(11):1382-1389.

43. Martin RJ, Wilson CG. Apnea of prematurity. *Compr Physiol.* 2012;2(4):2923-2931.

44. Hartman RE, et al. A Biomarker for Predicting Responsiveness to Stem Cell Therapy Based on Mechanism-of-Action: Evidence from Cerebral Injury. *Cell Rep.* 2020;31(6):107622.

45. Ballabh P. Intraventricular hemorrhage in premature infants: mechanism of disease. *Pediatr Res.* 2010;67(1):1-8.

46. Khwaja O, Volpe JJ. Pathogenesis of cerebral white matter injury of prematurity. *Arch Dis Child Fetal Neonatal Ed.* 2008;93(2):F153-161.

47. Berger J, Bhandari V. Animal models of bronchopulmonary dysplasia. The term mouse models. *Am J Physiol Lung Cell Mol Physiol.* 2014;307(12):L936-947.

48. Semple BD, et al. Brain development in rodents and humans: Identifying benchmarks of maturation and vulnerability to injury across species. *Prog Neurobiol.* 2013;106-107:1-16.

49. Wong PM, et al. Emphysema in young adult survivors of moderate-to-severe bronchopulmonary dysplasia. *Eur Respir J.* 2008;32(2):321-328.

50. Goss KN, et al. Early Pulmonary Vascular Disease in Young Adults Born Preterm. *Am J Respir Crit Care Med.* 2018;198(12):1549-1558.

51. Zlokovic BV. Neurodegeneration and the neurovascular unit. *Nat Med.* 2010;16(12):1370-1371.

52. Lacoste B, Gu C. Control of cerebrovascular patterning by neural activity during postnatal development. *Mech Dev.* 2015;138 Pt 1:43-49.

53. Andreone BJ, et al. Neuronal and vascular interactions. *Annu Rev Neurosci.* 2015;38:25-46.

54. Attwell D, et al. Glial and neuronal control of brain blood flow. *Nature.* 2010;468(7321):232-243.

55. Toussay X, et al. Laser Doppler Flowmetry to Study the Regulation of Cerebral Blood Flow by G Protein-Coupled Receptors in Rodents. *Methods Mol Biol.* 2019;1947:377-387.

56. Ouellette J, et al. Vascular contributions to 16p11.2 deletion autism syndrome modeled in mice. *Nat Neurosci.* 2020;23(9):1090-1101.

57. Lecrux C, et al. Pyramidal neurons are "neurogenic hubs" in the neurovascular coupling response to whisker stimulation. *J Neurosci.* 2011;31(27):9836-9847.

58. Widmaier EP, et al. Vander AJ. *Vander's Human Physiology: The Mechanisms of Body Function.* 12th ed. McGraw-Hill; 2011.

59. Bitterman H. Bench-to-bedside review: oxygen as a drug. *Crit Care.* 2009;13(1):205.

60. Cox LA, et al. Baboons as a model to study genetics and epigenetics of human disease. *ILAR J*. 2013;54(2):106-121.

61. Seidner SR, et al. Abnormal surfactant metabolism and function in preterm ventilated baboons. *Am J Respir Crit Care Med.* 1998;158(6):1982-1989.

62. Yoder BA, Coalson JJ. Animal models of bronchopulmonary dysplasia. The preterm baboon models. *Am J Physiol Lung Cell Mol Physiol.* 2014;307(12):L970-977.

63. Verney C, et al. Neuronal damage in the preterm baboon: impact of the mode of ventilatory support. *J Neuropathol Exp Neurol.* 2010;69(5):473-482.

64. Lledo P-M, et al. Adult neurogenesis and functional plasticity in neuronal circuits. *Nat Rev Neurosci.* 2006;7(3):179-193

65. Allotey J, et al. Cognitive, motor, behavioural and academic performances of children born preterm: a meta-analysis and systematic review involving 64 061 children. *BJOG.* 2018;125(1):16-25.

66. Linsell L, et al. Cognitive trajectories from infancy to early adulthood following birth before 26 weeks of gestation: a prospective, population-based cohort study. *Arch Dis Child.* 2018;103(4):363-370.

67. Marlow N. Neurocognitive outcome after very preterm birth. *Arch Dis Child Fetal Neonatal Ed.* 2004;89(3):F224-228.

68. Crawley J. *What's Wrong with My Mouse?: Behavioral Phenotyping of Transgenic and Knockout Mice.* 2nd ed. Wiley-Liss; 2007.

69. Hagmann-von Arx P, et al. Gait in Very Preterm School-Aged Children in Dual-Task Paradigms. *PLoS ONE.* 2015;10(12):e0144363.

70. Church C, et al. Longitudinal change in foot posture in children with cerebral palsy. *J Child Orthop.* 2017;11(3):229-236.

71. Deng W, et al. New neurons and new memories: how does adult hippocampal neurogenesis affect learning and memory? *Nat Rev Neurosci.* 2010;11(5):339-350.

72. Garthe A, et al. Adult-generated hippocampal neurons allow the flexible use of spatially precise learning strategies. *PLoS ONE.* 2009;4(5):e5464.

73. Stolp HB, et al. Interneuron Development Is Disrupted in Preterm Brains With Diffuse White Matter Injury: Observations in Mouse and Human. *Front Physiol.* 2019;10:955.

74. Wong FY, et al. Impaired autoregulation in preterm infants identified by using spatially resolved spectroscopy. *Pediatrics.* 2008;121(3):e604-611.

75. Chow BW, et al. Caveolae in CNS arterioles mediate neurovascular coupling. *Nature.* 2020;579(7797):106-110.

76. Chen J, Smith LEH. Retinopathy of prematurity. *Angiogenesis.* 2007;10(2):133-140.

77. International Committee for the Classification of Retinopathy of Prematurity. The International Classification of Retinopathy of Prematurity revisited. *Arch Ophthalmol.* 2005;123(7):991-999.

78. Sapieha P, et al. Retinopathy of prematurity: understanding ischemic retinal vasculopathies at an extreme of life. *J Clin Invest.* 2010;120(9):3022-3032.

79. Liu Y, et al. Hypoxia regulates vascular endothelial growth factor gene expression in endothelial cells. Identification of a 5' enhancer. *Circ Res.* 1995;77(3):638-643.

80. Pierce EA, et al. Regulation of vascular endothelial growth factor by oxygen in a model of retinopathy of prematurity. *Arch Ophthalmol.* 1996;114(10):1219-1228.

81. Alon T, et al. Vascular endothelial growth factor acts as a survival factor for newly formed retinal vessels and has implications for retinopathy of prematurity. *Nat Med.* 1995;1(10):1024-1028.

82. Turrens JF. Mitochondrial formation of reactive oxygen species. *J Physiol (Lond).* 2003;552(Pt 2):335-344.

83. Palmer TD, et al. Vascular niche for adult hippocampal neurogenesis. *J Comp Neurol.* 2000;425(4):479-494.

84. Shen Q, et al. Endothelial cells stimulate self-renewal and expand neurogenesis of neural stem cells. *Science.* 2004;304(5675):1338-1340.

85. Tavazoie M, et al. A specialized vascular niche for adult neural stem cells. *Cell Stem Cell.* 2008;3(3):279-288.

86. Mirzadeh Z, et al. Neural stem cells confer unique pinwheel architecture to the ventricular surface in neurogenic regions of the adult brain. *Cell Stem Cell.* 2008;3(3):265-278.

87. Culver JC, et al. A specialized microvascular domain in the mouse neural stem cell niche. *PLoS ONE.* 2013;8(1):e53546.

88. Fuentealba LC, et al. Adult neural stem cells bridge their niche. *Cell Stem Cell.* 2012;10(6):698-708.

89. Sun GJ, et al. Tangential migration of neuronal precursors of glutamatergic neurons in the adult mammalian brain. *Proc Natl Acad Sci USA.* 2015;112(30):9484-9489.

90. Shen Q, et al. Adult SVZ stem cells lie in a vascular niche: a quantitative analysis of niche cell-cell interactions. *Cell Stem Cell.* 2008;3(3):289-300.

91. Ottone C, et al. Direct cell-cell contact with the vascular niche maintains quiescent neural stem cells. *Nat Cell Biol.* 2014;16(11):1045-1056.

92. Alphonse RS, et al. Existence, functional impairment, and lung repair potential of endothelial colony-forming cells in oxygen-induced arrested alveolar growth. *Circulation.* 2014;129(21):2144-2157.

93. Spitalieri P, et al. Rescue of murine silica-induced lung injury and fibrosis by human embryonic stem cells. *Eur Respir J.* 2012;39(2):446-457.

94. Vadivel A, van Haaften T, Alphonse RS, Rey-Parra G-J, Ionescu L, Haromy A, Eaton F, Michelakis E, Thébaud B. Critical role of the axonal guidance cue EphrinB2 in lung growth, angiogenesis, and repair. *Am J Respir Crit Care Med* 2012;185(5):564–74.

95. Marcaletti S, et al. Exercise Performance Tests in Mice. *Curr Protoc Mouse Biol.* 2011;1(1):141-154.

96. Schindelin J, et al. Fiji: an open-source platform for biological-image analysis. *Nat Methods.* 2012;9(7):676-682.

97. Zhao X, et al. Vatner SF. Arterial Pressure Monitoring in Mice. *Curr Protoc Mouse Biol.* 2011;1:105-122.

98. Pospelov AS, et al. Endogenous brain-sparing responses in brain pH and PO2 in a rodent model of birth asphyxia. *Acta Physiol (Oxf).* 2020;229(3):e13467.

99. Tang C, et al. Neural Stem Cells Behave as a Functional Niche for the Maturation of Newborn Neurons through the Secretion of PTN. *Neuron.* 2019;101(1):32-44.e6.

100. Yousef H, et al. Aged blood impairs hippocampal neural precursor activity and activates microglia via brain endothelial cell VCAM1. *Nat Med.* 2019;25(6):988-1000.

101. Lacoste B, et al. Sensory-related neural activity regulates the structure of vascular networks in the cerebral cortex. *Neuron.* 2014;83(5):1117-1130.

102. Fujitani M, et al. TAp73 acts via the bHLH Hey2 to promote long-term maintenance of neural precursors. *Curr Biol.* 2010;20(22):2058-2065.

103. Wassmer S, et al. Chitosan microparticles for delivery of proteins to the retina. *Acta Biomater.* 2013;9(8):7855-7864.

Manuscript 2: Isolation of neural progenitor cells from neonatal baboons: implications for neurodevelopmental disorders

Authors: Marissa A. Lithopoulos[1, 2], Shamimunisa B. Mustafa[3], Cynthia L. Blanco[3], Alvaro Moreira[3], Steven Seidner[3], Bernard Thébaud[1,2,4]

Affiliations:

[1] Regenerative Medicine Program, Ottawa Hospital Research Institute, Ottawa, ON, Canada
[2] Department of Cellular and Molecular Medicine, University of Ottawa, Ottawa, ON, Canada
[3]University of Texas Health Science Center at San Antonio, San Antonio, Texas, USA
[4]Children's Hospital of Eastern Ontario Research Institute, Ottawa, ON, Canada

Connection to Hypothesis: This manuscript is the first methods protocol that describes the isolation and culture of NPCs derived from neonatal baboons. This critically important preclinical animal model was used to demonstrate hyperoxia-induced NPC functional impairments in Manuscript 1. This manuscript is a more detailed description of the cell isolation and culture protocol used in Manuscript 1.

Current Manuscript Status: To be submitted to Nature Protocols (following the publication of Manuscript 1).

Author Contributions: I designed the experiments and developed the baboon NPC isolation protocol. I isolated the NPCs and cultured them for serial neurosphere assays. I acquired images of the neurospheres. I interpreted the data, wrote, and edited the manuscript. S.M. aided with the culture of NPCs. C.L.B. assisted with the collection of baboon tissue. A.M. provided material and intellectual guidance. S.S. aided with isolating baboon derived tissue. B.T. supervised and financed the experiment. S.M., S.S., B.T. provided guidance and edited the manuscript.

Abstract

Neurodevelopmental disorders affect approximately one in six children in industrialized countries, such as the United States. The origin of many of these disorders can be traced to the neonatal period, with symptoms continuing throughout the lifetime of the patient. There are currently no effective cures, in part, due to the lack of clinically pertinent models during neonatal development. Here, we describe the isolation of neural progenitor cells (NPCs) from preterm and term neonatal baboons. The subventricular zone and the dentate gyrus of the hippocampus are dissected and enzymatically digested. NPCs are seeded using a limiting dilution in neural growth conditions. Cells demonstrate the defining ability of primary NPCs to self-renew via the neurosphere assay. This can be completed within 3-4 weeks. The isolation and culture of neonatal baboon-derived NPCs will aid in the discovery of therapies for neurodevelopmental disorders.

Key words: Neural progenitor cell, neurodevelopmental disorder, preterm, neonatal, baboon

Introduction

Neurodevelopmental disorders are a global healthcare concern, affecting approximately one in six children in industrialized countries, such as the United States[1]. The term, neurodevelopmental disorder, covers a wide range of conditions in which brain injury during development leads to deficits in motor, cognitive, communicative, and behavioural abilities[2]. Many of these conditions originate during the neonatal period as a result of complications due to preterm birth[3-7] and continue into adulthood[8]. Preterm birth is defined as any birth before 37 weeks of gestation[9]. Currently there are no effective treatments targeting neurodevelopmental disorders associated with preterm birth. This is partly due to the fact that brain development during the late gestational period is poorly understood in humans, as there is a lack of clinically pertinent animal models, as well as limited access and ethical concerns related to age-matched human fetal tissue.

Neural progenitor cells (NPCs) play a key role in brain development of the fetus and infant[10,11]. Primary NPCs (neural stem cells)[11] are characterized by their ability to self-renew and differentiate into the three main lineages of the brain, i.e., astrocytes, neurons, and oligodendrocytes. Postnatally, these cells reside in the subventricular zone (SVZ) and the dentate gyrus (DG) of the hippocampus[12]. Postnatal mammalian NPCs were first identified in adult mice by Reynolds and Weiss[13]. NPCs were isolated and plated as free-floating cells in media containing epidermal growth factor (EGF), and formed colonies, or neurospheres. Reynolds and Weiss demonstrated, using serial neurosphere assays, that NPCs can self-renew. Furthermore, they showed that NPCs can be multipotent by plating the cells as a monolayer in culture dishes and stimulating their differentiation into neuronal and glial lineages. NPCs are an excellent tool to study brain development during injury and repair under controlled conditions.

Development of the protocol

There has been extensive work describing the isolation and culture of mouse NPCs[14-16]. While these models have greatly aided our understanding of NPC contribution to brain development[12,17,18], the rodent-derived NPC population cannot fully replicate the complexity of human NPC function[19,20]. Moreover, isolating NPCs from preterm human fetal tissue at time of autopsy is ethically controversial. Additionally, human induced pluripotent derived-NPCs provide unique technical and biological limitations to replicate functional NPCs at the appropriate gestational age.

Since the contribution of non-human primate models has immensely advanced our understanding of the human brain[21], we aimed to use a non-human primate model of premature birth which closely mimics the human condition, providing a similar NPC population, at an age-matched stage of brain development. The University of Texas Health Science Center at San Antonio, with services from the Texas Biomedical Research Institute, established the neonatal baboon model of preterm birth, which recapitulates developmental stages of human neonates and the clinical conditions of preterm birth[22-24]. Working with these institutions, we developed the proper techniques necessary to isolate the baboon-derived neonatal brain tissue. Our laboratory previously established the isolation and culture of NPCs derived from neonatal baboons (M.A.L. et al., unpublished data) and is the first and only team to conduct these experiments. For tissue storage, we utilized the artificial cerebral spinal fluid protocol outlined by Ostrem et al.[25], originally intended for human fetal tissue. To determine the correct anatomical location of the SVZ and the DG of the hippocampus, we studied the work of several groups which visualized the NPC niche regions in adult baboon brain tissue[26-28]. The NPC isolation and culture protocol was adapted from previous techniques used to isolate NPCs from murine[14,29] and human fetal tissue[25,30-36].

These previous techniques have key overlapping steps and reagents. Papain is a common enzyme used to digest brain tissue. The base medium used to culture NPCs is usually a variety of Dulbecco's Modified Eagle Medium/Nutrient Mixture media (DMEM)/F-12. Crucial growth factors for NPC maintenance include epidermal growth factor (EGF) and fibroblast growth factor-2 (FGF). Furthermore, NPCs differentiate in the presence of serum, therefore; common serum substitutes for NPCs include B-27 and N-2 supplements. In our previous work (M.A.L. et al., unpublished data), the effect of hyperoxia on NPC function was assessed and therefore, when possible, we used reagents in the absence of antioxidants.

In this article, we provide a detailed stepwise process for the isolation and culture of baboon-derived NPCs, with an additional troubleshooting guide (Table 1), to assist with common obstacles that may arise when replicating the procedure. This protocol focuses on the ability of primary NPCs to self-renew via serial neurosphere assays.

Applications of the method

We isolated NPCs from preterm and term neonatal baboons (M.A.L. et al., unpublished data). The isolation and culture procedure can assess functional ability of the cells, i.e., self-renewal. The baboon model can be used to induce *in vivo* preterm birth complications or more widespread neurodevelopmental disorders, from which NPCs can be isolated and their specific contribution to abnormal neurodevelopmental outcomes can be studied. Additionally, *in vitro* manipulations (e.g., exposing NPCs to high oxygen or to an inflammatory stimulus) can mimic the adverse conditions preterm newborns experience in the intensive care unit. Moreover, this protocol could be expanded upon to use the isolated baboon-derived NPCs to form brain organoids, which would offer a complex *in vitro* environment to study brain development[37,38]. Therefore, this technique can be used to develop reductionist, clinically relevant models, to study NPC function at a unique

gestational timepoint of primate brain development, which will accelerate the advancement of therapies for neurodevelopmental disorders. Studying these novel cells can provide unparalleled mechanistic insight to processes central to normal human brain development.

Comparison with other methods

This is the first neonatal baboon-derived NPC isolation and culture reported in the literature. NPCs have previously been isolated from the SVZ of adult baboons[27,39], however their application in a rapidly developing brain is limited. In previous studies, the isolated brain tissue was digested using Accutase, for 10 minutes. An enzymatic digestion that works on adult tissue (which is much firmer) may not be optimal for the delicate nature of neonatal tissue. Additionally, the cells were used for a chromatin immunoprecipitation sequencing (ChIP-Seq) or flow cytometry experiments, rather than an *in vitro* culture assay as our protocol. Furthermore, our protocol fully explains the isolation and culture of NPCs from both the SVZ and the DG of neonatal baboons in sufficient detail to repeat the procedure.

Experimental design

This protocol describes the isolation and culture of primary NPCs derived from premature and term delivered neonatal baboons. A summary of the methods explained in this protocol is provided in Figure 21. Briefly, the brain tissue is collected and immediately stored in artificial cerebrospinal fluid on ice until the dissection procedure. NPCs reside postnatally in two main brain regions i.e., the SVZ and DG[12].

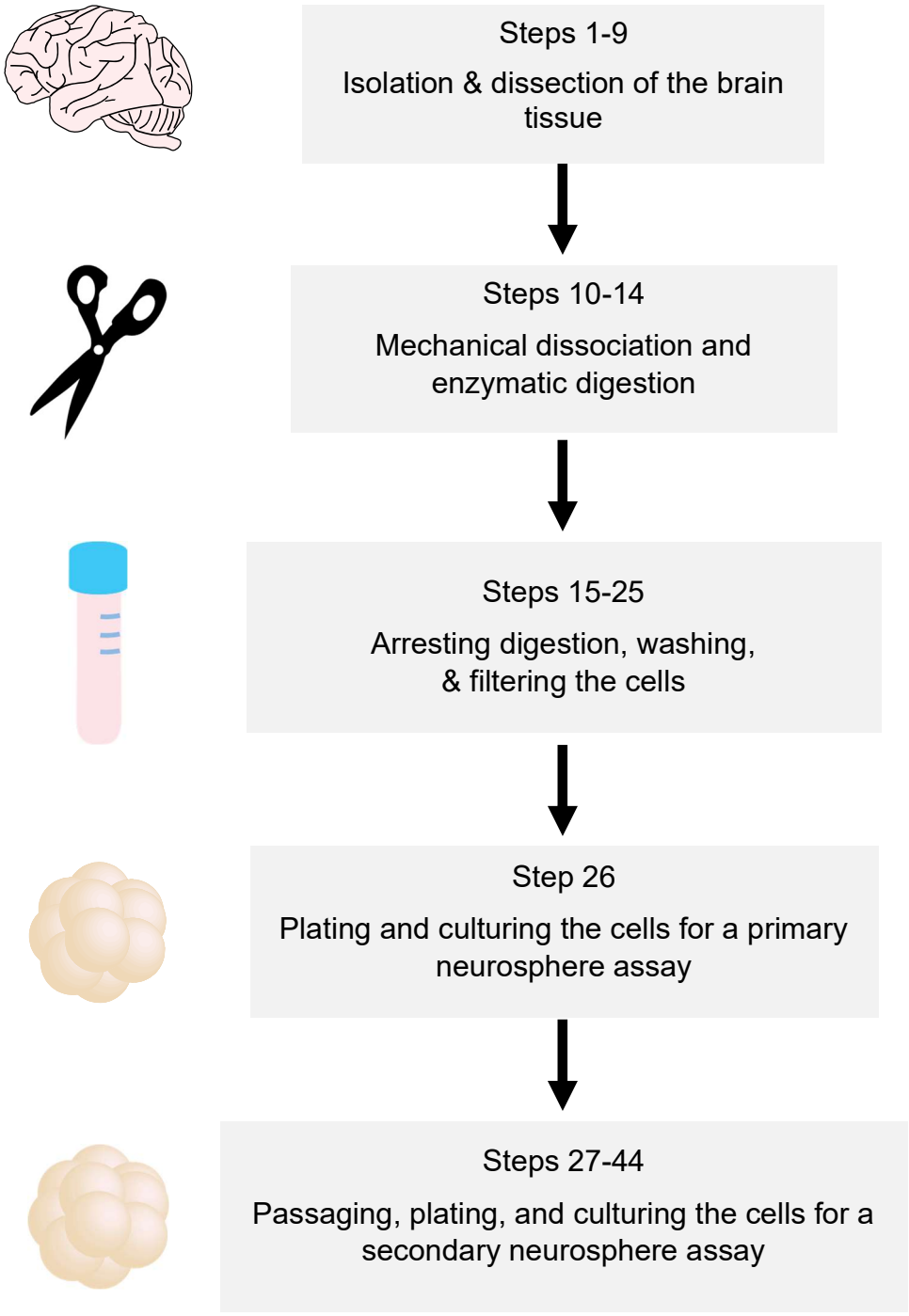

Figure 21. Flow diagram of the steps required to isolate and culture neonatal baboon-derived NPCs.

These brain regions are isolated from the collected brain tissue (Figure 22), mechanically dissociated, and enzymatically digested with papain. The enzyme is then inhibited with serum. This is followed by 2 washes in DMEM/F-12 and filtration through a 40 μm cell strainer. The cells are then plated at a limited dilution of 37,500 cells/mL in ultra-low attachment 6 well plates in stem cell media (Figure 23). The cells are cultured at 37°C, under standard atmospheric conditions (21% O_2, 5% CO_2, 74% N_2). It is important to minimize the agitation of the plates to ensure proper neurosphere formation. Solely the primary NPCs will form free-floating primary neurospheres, which are capable of forming secondary neurospheres (Figure 24). For the secondary neurosphere assay, the cells are plated at a more stringent limiting dilution of 3,700 cells/mL. Neurospheres will take several days to form and are usually ready to passage once the majority are >50 μm in diameter. The neurosphere assays demonstrate the self-renewal potential of primary NPCs[14].

Expertise needed to implement the protocol

Nonhuman primate expertise is required to house and care for the animals. The University of Texas Health Science Center at San Antonio and the Texas Biomedical Research Institute have extensive expertise housing and humanely caring for baboons[22,23].

Limitations

The main limitations of this protocol come from a cost perspective. First, there is the ethical cost of working with nonhuman primates. While this may be considered less controversial than procuring and experimenting on human fetal tissue, it is important to acknowledge that nonhuman primates are organisms with special animal care considerations[40,41]. Second, there is the financial cost of conducting such experiments. The cost of the animals, their housing, and their care is expensive due to their more complex needs. Both points considered, it is therefore crucial that the experiments utilizing this protocol have a strong rationale for being conducted. To effectively

manage these challenges, researchers should consider sharing tissue, resources, and expertise to conduct these experiments with optimal efficiency and minimal waste[42,43]. A further limitation regarding the NPC isolation is that during the first passage, there will be cell debris and aggregates, reducing the visibility of neurospheres. Each passage will purify the culture conditions; however, it is important that the NPCs are continually monitored for proper functioning.

Materials

Reagents

- Pentobarbital
- Milli-Q® water
- 70% ethanol (vol/vol with Milli-Q® water)
- NaCl (MilliporeSigma, S9888-25G)
- KCl (MilliporeSigma, P3911-25G)
- $MgCl_2$ (MilliporeSigma, M8266-100G)
- $CaCl_2$ (MilliporeSigma, C1016-100G)
- NaH_2PO_4 (MilliporeSigma, S8282-500G)
- NaH_2CO_3 (MilliporeSigma, S6297-250G)
- d-(+)-glucose (MilliporeSigma, G8270-100G)
- Hank's Balanced Salt Solution (HBSS) (Thermo Fisher Scientific, 14025092)
- Antibiotic-antimycotic (Thermo Fisher Scientific, 15240-062)
- Papain (Worthington, PAPL LS003118)
- DMEM/ F-12 (Thermo Fisher Scientific, 11330057)

- 0.5 M Ethylenediaminetetraacetic acid solution (EDTA) (MilliporeSigma,03690)
- FBS (MilliporeSigma, F1051)
- B-27 (Life Technologies, 10889-038)
- N-2 (Thermo Fisher Scientific, 17502048)
- Heparin (MilliporeSigma, H3149)
- FGF (MilliporeSigma, F0291)
- EGF (MilliporeSigma, E1257)
- Trypan Blue Stain (Thermo Fisher Scientific, 1843573)
- TrypLE™ Express Enzyme (Thermo Fisher Scientific, 12605028)
- 10X phosphate buffered saline (PBS) (Bio-Rad Laboratories, 161-0780)

Equipment

- Surgical scissors and forceps
- Large shears
- Scalpel or hand-held circular saw
- Laminar flow hood
- Sterile filter units, 0.2 μm membrane (Thermo Fisher Scientific, 09-741-03)
- 150 mm dish (Sigma, CLS430597)
- Disposable scalpel blades (VWR, 21909-644)
- Dissection forceps (Fine Science Tools, 11252-21)
- 2 mL microcentrifuge tubes (VWR, 89511-264)
- 50 mL Falcon tubes (Thermo Fisher Scientific, 14-959-49A)
- 15 mL Falcon tubes (Thermo Fisher Scientific, 14-959-70C)
- 100 mm dish (Thermo Fisher Scientific, 08-772E)

- 37°C water bath
- Centrifuge
- 37°C cell culture incubator
- P1000 pipette
- 40 µm cell strainer (Corning, 352340)
- P20 pipette
- 50 mL Falcon Tube Top Filtration System (MilliporeSigma, SE1M179M6)
- Ultra-low attachment 6 well plates (VWR, 29443-030)
- 10 mL stripettes
- Inverted microscope

Reagent Setup

Artificial Cerebrospinal Fluid

MilliQ water with 125 mM NaCl, 2.5 mM KCl, 1 mM $MgCl_2$, 2 mM $CaCl_2$, 1.25 mM NaH_2PO_4, 25 mM NaH_2CO_3, and 25 mM d-(+)-glucose. Sterilize by filtering through a 0.2 µm membrane sterile filter unit. Store at 4°C for up to 2 months.

CRITICAL: Prepare the following reagents under sterile conditions in a laminar flow hood.

Antibiotic-antimycotic

Thaw the antibiotic-antimycotic in a 37°C water bath. Aliquot in 15 mL Falcon tubes and store at -20°C.

1X HBSS

1X HBSS with 1% antibiotic-antimycotic (vol/vol). Store at 4°C for 36 months from date of manufacture.

Papain Solution

Add 375 µL of DMEM/ F-12 to a 25 mg papain bottle to activate at least 1 unit per mg of protein. Pipette up and down well. Store in 25 µL aliquots at 4°C for up to 12 months.

Digestion Media

DMEM/ F-12 with 2.4 µL of 0.5 M EDTA and 20 µL of the papain solution, to make a final volume of 1 mL. Prepare the digestion media fresh on the day of isolation, a minimum of 5 minutes before tissue digestion.

FBS

Thaw in a 37°C water bath. Aliquot in 15 mL Falcon tubes and store at -20°C.

10% FBS Solution

DMEM/ F-12 with 10% FBS (vol/vol). Prepare fresh on the day of isolation.

B-27

Thaw overnight at 4°C. Make 1 mL aliquots and store at -20°C for up to 12 months.

CRITICAL: Do not thaw at room temperature or in a hot water bath.

N-2

Thaw in a 37°C water bath until a thin layer of ice remains. Make 0.5 mL aliquots and store at -20°C.

Heparin

For every 10 mg of heparin required, resuspend in 1 mL of DMEM/F-12. Filter the solution through a 0.22 µm membrane using the 50 mL Falcon Tube Top Filtration System. Make 15 µL aliquots and store at 4°C for up to 2 years.

FGF

Resuspend 25 µg of FGF in 1 mL of DMEM/F-12. Make 45 µL aliquots and store at -20°C or -80°C for up to 6 months.

EGF

Resuspend 100 µg of EGF in 1 mL of DMEM/F-12. Make 15 µL aliquots and store at -20°C or -80°C.

CAUTION: Prolonged storage is not recommended by the manufacturer.

Stem Cell Medium

DMEM/F-12 with 2% B-27 (vol/vol), 1% N-2 (vol/vol), 1% antibiotic-antimycotic (vol/vol), 8 µg/mL heparin, 0.02 µg/mL FGF, and 0.02 µg/mL EGF.

CRITICAL: Prepare the stem cell medium fresh on the day of isolation. Thaw all growth factors at room temperature. Thaw antibiotic-antimycotic in a 37°C water bath. Store at 4°C. Incubate the media in a 37°C water bath for a minimum of 20 minutes before plating cells.

Procedure

Tissue Isolation -Timing: ~2 hours

1) Preterm animals (~125-140 days of gestation) are delivered via C-section and term animals (~185 days of gestation) are delivered vaginally.

CAUTION: For baboon handling methods, follow an approved procedure from your institution's animal care and use committee. All procedures described herein were approved by the University of Texas Health Science Center at San Antonio Institutional Animal Care and Use Committee.

2) Euthanize the neonatal baboon. We euthanize via pentobarbital (10 mg/kg) using a peripherally inserted central catheter in the lower leg (inferior vena cava or femoral vein).

3) Using surgical scissors and forceps, remove the salivary glands and neck tissues. Cut the vertebrae of the neck below the proximal cervical spinal cord using large shears.

4) Open the skull via a longitudinal incision along the sagittal suture. For preterm animals, use a scalpel blade. For term animals, use a hand-held circular saw.

CAUTION: Take necessary safety measures when working with sharp tools.

5) Transfer the brain to the artificial cerebral spinal fluid on ice.

CRITICAL STEP: Isolate the brain as quickly as possible. The brain can be stored in artificial cerebrospinal fluid on ice for up to 2 hours. Beyond this critical window, cell viability will greatly decrease.

Dissection, Digestion, and Purification -Timing: ~3 hours

CRITICAL STEP: Work under sterile conditions (under a laminar flow hood) for the remainder of the procedure. Use ≥70% (vol/vol) ethanol to sterilize all items entering the hood.

6) Pour the 1X HBSS into a 150 mm dish.

7) Transfer the brain tissue from the artificial cerebrospinal fluid to the dish (Figure 22a).

CRITICAL STEP: Avoid transferring excess blood to the dish.

8) Use the dissection forceps to stabilize the brain tissue. Make thin coronal incisions, approximately 1-2 cm in thickness, with the scalpel blade to visualize the SVZ and DG (Figure 22b). The SVZ is located directly adjacent to the lateral ventricles. The DG is located within the hippocampus in the temporal lobe. Dissect both regions with the dissection forceps and store in microcentrifuge tubes filled with artificial cerebrospinal fluid on ice until the dissection is complete.

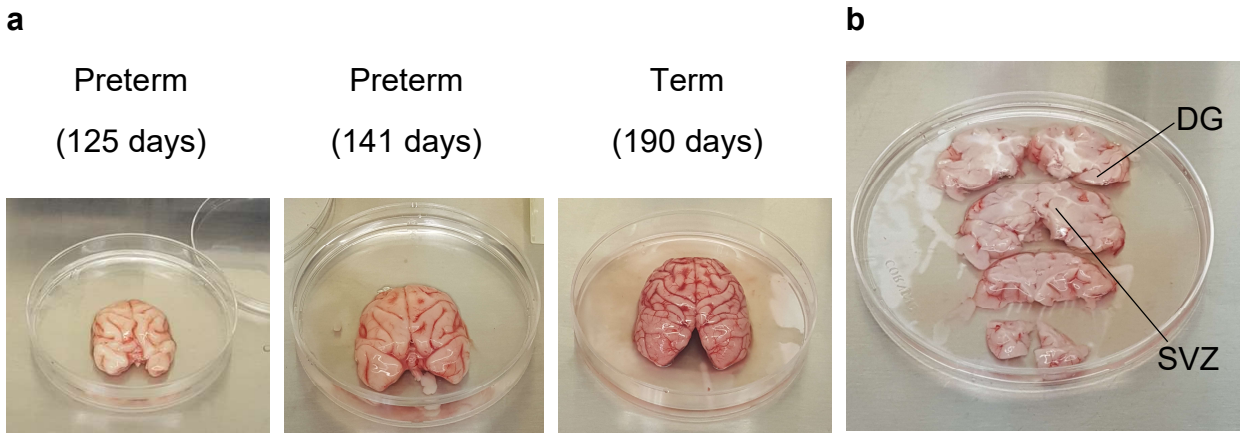

Figure 22. Dissection of the subventricular zone (SVZ) and dentate gyrus (DG) region of the hippocampus. (**a**) Representative images of preterm and term baboon brains (from left to right, 125, 141, and 190 days from the beginning of gestation). (**b**) Coronal sections of the brain tissue provide a visualization of the SVZ and the DG. The brain tissue is shown in a 150 mm dish.

CRITICAL STEP: The tissue should be submerged in the artificial cerebrospinal fluid once inside the microcentrifuge tube. If any tissue is exposed, transfer the excess tissue to another tube.

10) Prepare the digestion media in 50 mL Falcon tubes. For each 1 mL tube of dissected tissue, prepare 1 mL of digestion media.

CRITICAL STEP: Prepare the digestion media fresh, a minimum of 5 minutes before use.

11) Pour the contents of the dissected tissue onto a 100 mm dish. Aspirate the artificial cerebral spinal fluid from the dish.

CRITICAL STEP: Be careful not to aspirate any brain tissue.

12) Use a scalpel blade to chop the tissue into fine pieces (approximately 5 minutes). Add the digestion media to the dish and use a P1000 pipette to transfer the digestion media and brain tissue back to the 50 mL Falcon tube.

CRITICAL STEP: The contents of 3 microcentrifuge tubes can be combined to a single 50 mL Falcon tube. If you have collected more tissue, we recommend splitting the sample over multiple Falcon tubes.

13) Pipette up and down approximately 40 times with a P1000 pipette to break up the tissue.

14) Incubate the sample for 30 minutes in a 37°C water bath with gentle agitation.

CRITICAL STEP: Do not extend the incubation period, as excess exposure to papain will reduce the viability of the cells.

15) Prepare the 10% FBS solution and incubate in the 37°C water bath.

CRITICAL STEP: You will require 30 mL of the 10% FBS solution for every 3 mL of digestion medium in order to neutralize the papain.

16) Following the 30-minute incubation, pipette up and down 40 times with a P1000 pipette.

17) Add 30 mL of 10% FBS solution to the digestion media and pipette up and down 10 times to mix the solution.

CRITICAL STEP: Do not let the cells remain in the 10% FBS solution for longer than necessary, as FBS induces differentiation of NPCs.

18) Centrifuge the sample for 10 minutes at 750 *g* at 22°C.

CRITICAL STEP: If the supernatant remains very cloudy, centrifuge for another 10-minute period.

19) To wash the cells, aspirate the supernatant and resuspend the pellet in 10 mL of DMEM/ F-12. Pipette up and down 40 times with a P1000 pipette. Add 30 mL of DMEM/ F-12 to the tube.

20) Centrifuge the sample for 10 minutes at 750 *g* at 22°C.

21) Repeat steps 19 and 20 once more.

22) Aspirate the supernatant and resuspend the pellet in 40 mL of DMEM/ F-12. Filter the sample through a 40 μm cell strainer.

23) Mix the cell suspension well with a P1000 pipette. Using a P20 pipette, add 15 μL of the cell suspension to a 1.5 mL microcentrifuge tube. Add 15 μL of Trypan Blue Stain to the microcentrifuge tube and mix well. Count the cells with an automatic cell counter.

CRITICAL STEP: The cells will sink to the bottom of the tube. Ensure that the cell suspension is mixed well before removing the 15 µL sample and before counting the cells.

TROUBLESHOOTING

24) Centrifuge the sample for 10 minutes at 750 *g* at 22°C.

25) Aspirate the supernatant and resuspend the pellet in 10 mL of stem cell media.

Primary Neurosphere Assay – Timing: ~8-14 days

26) Plate the primary cells at a density of 37,500 cells/mL in ultra-low attachment 6 well plates. Incubate at 37°C (21% O_2, 5% CO_2, 74% N_2) for 8-14 days. Approximately 8-14 days will allow for the formation of primary neurospheres (Figure 24a,b). The majority of neurospheres should be larger than 50 µm in diameter before passaging the cells. After 7 days in culture, a minimum of 300 µL of fresh stem cell media should be added to the plates.

CRITICAL STEP: During the first passage, cell debris will form aggregates, resembling neurospheres. Aggregates can be distinguished from neurospheres, as they do not have the same spherical morphology or mass as neurospheres (aggregates move more in the media when the plate is agitated)[14] (Figure 23). Moreover, it is important to manipulate the plates as little as possible during the culture period, as excessive movement will interfere with neurosphere formation. Monitor the physical appearance of the neurospheres when adding the culture media. If the spheres are >200 µm in diameter and appear to have a dark circle in the middle, consider passaging the cells to minimize hypoxic conditions at the center of the neurospheres.

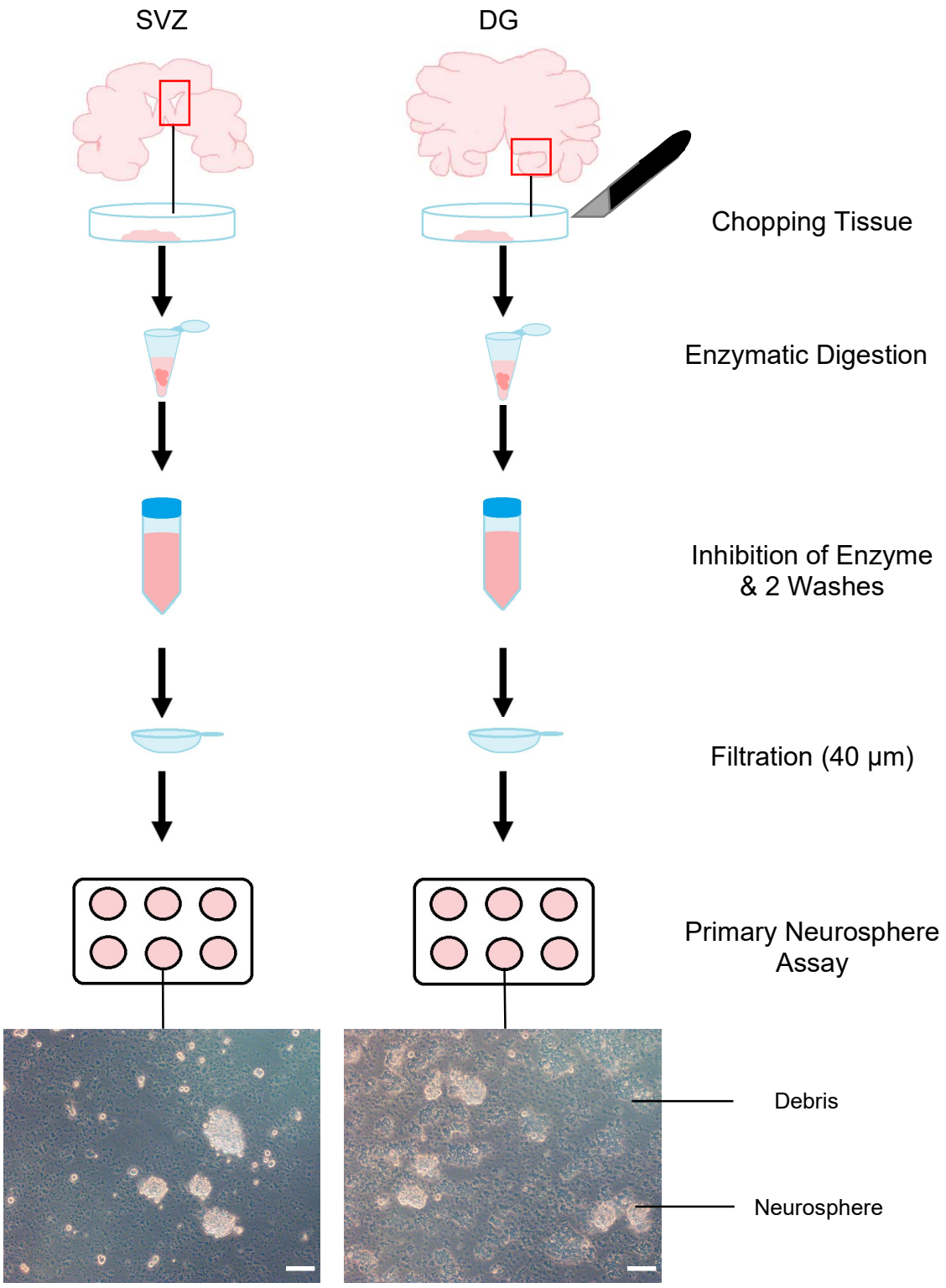

Figure 23. Illustration of the NPC isolation and culture process (Steps 6-26). The NPC niche regions are mechanically dissociated and enzymatically digested in papain. The enzymatic digestion is inhibited with FBS, followed by 2 washes in DMEM/F-12. The cells are filtered through a 40 µm mesh and plated in stem cell media at a limiting dilution. Clonal neurospheres will appear in 8-14 days as free-floating, spherical structures. Non-progenitor cells will form debris or adhere to the bottom of the wells. Scale bars, 100 µm.

TROUBLESHOOTING

Passaging – Timing: ~2-3 hours

27) Collect the neurospheres in a 15 mL Falcon tube using a 10 mL stripette.

CRITICAL STEP: Try to minimize the formation of bubbles.

28) Centrifuge the sample for 10 minutes at 750 *g* at 22°C.

29) Aspirate the supernatant and resuspend the pellet in 1 mL of TrypLE™ Express Enzyme. Pipette up and down 20 times with a P1000 pipette.

30) Incubate the sample in a 37°C water bath for 3 minutes.

CRTICIAL STEP: Do not extend the incubation period as excess exposure to TrypLE™ Express Enzyme will decrease cell viability.

31) Pipette up and down 40 times with a P1000 pipette.

32) Add 2 mL of the 10% FBS solution to neutralize the enzyme.

33) Pipette up and down 10 times with a P1000 pipette.

34) Centrifuge the sample for 5 minutes at 750 *g* at 22°C.

CRITICAL STEP: Avoid prolonged exposure in the 10% FBS solution, as FBS promotes NPC differentiation.

35) To wash the cells, aspirate the supernatant and resuspend the pellet in 2 mL of DMEM/F-12.

36) Pipette up and down 20 times with a P1000 pipette.

37) Centrifuge the sample for 5 minutes at 750 *g* at 22°C.

38) Repeat steps 35-37 one more time.

39) Resuspend the pellet in 1 mL of DMEM/F-12 and pipette up and down 40 times with a P1000 pipette. Add 9 mL of DMEM/F-12 to make a total volume of 10 mL.

40) Filter the cells through a 40 μm filter into a 50 mL Falcon tube.

41) Count the cells using an automatic cell counter (15 µL cells/ 15 µL Trypan Blue Stain, as indicated in step 23).

CRITICAL STEP: To avoid the cells sinking to the bottom of the tube, ensure the cell suspension is well mixed before removing the 15 µL sample.

TROUBLESHOOTING

42) Transfer the cells to a 15 mL Falcon tube and centrifuge the sample for 10 minutes at 750 *g* at 22°C.

43) Resuspend the pellet in 5 mL of stem cell media.

Secondary Neurosphere Assay – Timing: ~10-14 days

44) Plate the cells at density of 3,750 cells/mL in an ultra-low attachment 6-well plate. Incubate at 37°C (21% O_2, 5% CO_2, 74% N_2) for 10-14 days. It will take approximately 10-14 days for the formation of secondary neurospheres at this cell density (Figure 24c,d). The majority of neurospheres should be larger than 50 µm in diameter before further passaging the cells. After 7 days in culture, a minimum of 300 µL of fresh stem cell media should be added to the plates.

TROUBLESHOOTING

Timing

Steps 1-5, tissue isolation: ~2 hours

Steps 6-25, dissection, digestion, and purification: ~3 hours

Step 26, primary neurosphere assay: ~8-14 days

Steps 27-43, passaging: ~2-3 hours

Step 44, secondary neurosphere assay: ~10-14 days

Troubleshooting

Troubleshooting advice can be found in **Table 1**.

Table 1 | Troubleshooting table.

Step	Problem	Possible reason	Solution
23, 41	Too few viable cells	The brain tissue remained in the artificial cerebral spinal fluid for too long	Ensure that the NPC niche regions are isolated as quickly as possible
		The brain tissue was digested in papain for too long	Do not leave the tissue in papain at room temperature for longer than 10 minutes, before or after the 30-minute incubation in the water bath
		The neurospheres were dissociated in TrypLE™ Express Enzyme for too long	Do not leave the tissue in TrypLE™ at room temperature for longer than 1 minute, before or after the 3-minute incubation in the water bath
		The isolation or passaging protocol was extended beyond the recommended time	It is important to work as quickly as possible, to ensure that the NPCs can receive their growth factors in a timely manner
26, 44	A small number of neurospheres form	Moving the plates too much during the culture period	Proper neurosphere formation requires the plates to be still. Refrain from checking the cells unless necessary to quantify/ passage/ or add media
	Too many contaminating cells	Collected additional nonessential tissue during the isolation	Avoid collecting white matter or blood vessels during the isolation
	Cells are adhering to the bottom of the wells	This is normal during the first passage, as non-progenitor cells will adhere to the bottom. This is only a problem if you do not observe many cells free-floating and forming neurospheres	To avoid NPCs differentiating and adhering to the bottom, ensure that the cells are not overexposed to FBS and that the stem cell media is fresh before plating

26, 44	Cells form clumps	The cells were not properly dissociated before plating	The number of times to pipette up and down during mechanical dissociation should be used as a guide. If you see that the media is cloudy, you should continue to pipette up and down until it is clear
		The cells were not evenly distributed throughout the well during plating	Ensure that immediately after adding the cells to their respective wells, the plate is gently moved from side to side, so as to distribute the cells throughout the well

Anticipated Results

Each neonatal brain will yield a variable number of viable cells (Table 2). Several factors play a role in the number of cells that can be isolated. These include variability among baboons, the conditions of the euthanization procedure, and the tissue collection process. If the brain is collected in a short amount of time this will greatly improve the yield of viable progenitor cells. From the SVZ, we collected between 1,455,000-10,275,000 cells, depending on the sample. From the DG, we collected between 1,172,500-3,810,000 cells, depending on the sample. A large variability in cell number between samples can be attributed to different factors (Table 1).

Table 2 | Animal information.

Specimen	Baboon Species	Age (Days from the beginning of gestation)	Sex	Cell Number from SVZ	Cell Number from DG
A19	*Papio anubis*	141	Male	9,040,000	1,883,000
B19	*Papio anubis*	127	Female	5,277,500	3,810,000
C19	*Papio anubis/ Papio cynocephalus*	185	Male	3,225,000	1,172,500
D19	*Papio anubis/ Papio cynocephalus*	125	Female	1,455,000	1,467,500
E19	*Papio anubis*	190	Female	2,052,500	2,052,500
F19	*Papio anubis/ Papio cynocephalus*	194	Female	10,275,000	1,760,000

The cells will form free-floating neurospheres within 8-14 days of culture when plated in stem cell media at a density of 37,500 cells/mL. Neurospheres are spherical structures that can range in size from <50 μm to >200 μm in diameter. During the first passage, there can be over 1,000 neurospheres/ well (Figure 24a,b).

Conducting a secondary neurosphere assay will assess the self-renewal capacity of the cells. Secondary neurospheres should form within 10-14 days when plated at a density of 3,750 cells/mL. During the second passage, the amount of neurospheres per well can range from approximately 50-300 (Figure 24c,d).

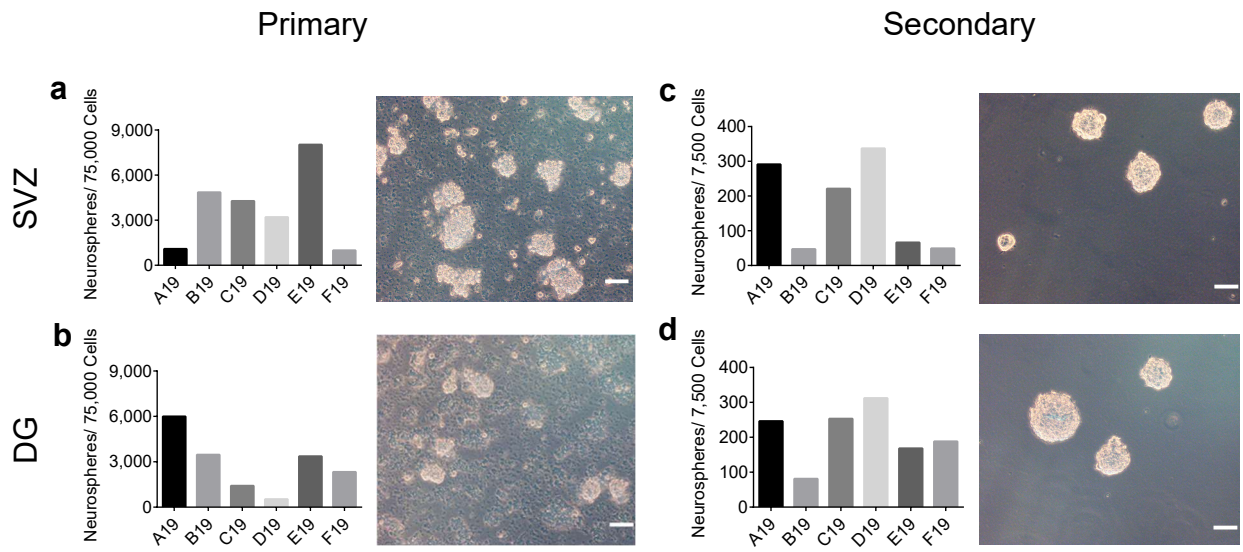

Figure 24. Approximately 1-4% of cells from the SVZ and DG of neonatal baboons will self-renew to form secondary neurospheres. (**a**) Amount of primary neurospheres formed by NPCs isolated from the SVZ. (**b**) Amount of primary neurospheres formed by NPCs isolated from the DG. (**c**) Amount of secondary neurospheres formed by NPCs isolated from the SVZ. (**d**) Amount of secondary neurospheres formed by NPCs isolated from the DG. Scale bars for representative images, 100 μm.

Recently, the ability of the neurosphere assay to accurately mimic *in vivo* conditions has been called into question[44-47]. It is critical to recognize the limitations of the assay. The NPC niche is a complex and rich environment, providing many cues that affect NPC growth and function[48,49]. The *in vitro* environment cannot fully replicate the intricate *in vivo* system. The goal of the neurosphere assays is to assess NPC function in a simplified manner, allowing one to explore mechanisms and conditions in a controlled environment. It is often best to supplement the neurosphere assay with *in vivo* data to obtain a comprehensive set of results. Moreover, conducting a tertiary neurosphere assay could further strengthen conclusions about self-renewal capability.

The isolation and culture of NPCs provides a simple, reductionist method for assessing cell function. The research of many groups, who have worked with a variety of species, has greatly enhanced our knowledge of NPCs and brain development. It is important to emphasize that this protocol is a clinically relevant tool that can be used to gain a better understanding of

neurodevelopmental disorders at unique gestational timepoints leading to potential therapies to improve the lives of patients.

Author contributions

M.A.L. designed experiments, conducted the NPC isolation and culture, acquired neurosphere images, interpreted the data, and wrote/ edited the manuscript. S.M. contributed intellectual guidance, aided with the neurosphere culture and image acquisition, and edited the manuscript. C.L.B. contributed intellectual guidance and assisted with the collection of baboon tissue. A.M. provided supplies, lab space, intellectual guidance, and edited the manuscript. S.S. contributed intellectual guidance and assisted with the collection of baboon tissue. B.T. supervised the study, contributed intellectual guidance, provided financial support, and edited the manuscript.

Acknowledgements

The authors would like to thank the University of Texas Health Science Center at San Antonio and the Texas Biomedical Research Institute for their collaboration and resources. M.A.L. was supported by a Canadian Institutes of Health Research (CIHR) Frederick Banting and Charles Best Doctoral Award and a CIHR Canada Graduate Scholarship Michael Smith Foreign Study Supplement. B.T. is supported by CIHR, The Stem Cell Network, the Ontario Institute of Regenerative Medicine, and the Children's Hospital of Eastern Ontario Foundation.

Competing interests

The authors declare no competing interests.

References

1. Zablotsky, B. *et al.* Prevalence and Trends of Developmental Disabilities among Children in the United States: 2009-2017. *Pediatrics* **144**, (2019).
2. Mullin, A. P. *et al.* Neurodevelopmental disorders: mechanisms and boundary definitions from genomes, interactomes and proteomes. *Transl Psychiatry* **3**, e329 (2013).
3. Vohr, B. R., Wright, L. L., Poole, W. K. & McDonald, S. A. Neurodevelopmental outcomes of extremely low birth weight infants <32 weeks' gestation between 1993 and 1998. *Pediatrics* **116**, 635–643 (2005).
4. Breeman, L. D., Jaekel, J., Baumann, N., Bartmann, P. & Wolke, D. Preterm Cognitive Function Into Adulthood. *Pediatrics* **136**, 415–423 (2015).
5. Volpe, J. J. Brain injury in premature infants: a complex amalgam of destructive and developmental disturbances. *Lancet Neurol.* **8**, 110–124 (2009).
6. Omizzolo, C. *et al.* Neonatal brain abnormalities and memory and learning outcomes at 7 years in children born very preterm. *Memory* **22**, 605–615 (2014).
7. Sriram, S. *et al.* Cognitive Development and Quality of Life Associated With BPD in 10-Year-Olds Born Preterm. *Pediatrics* **141**, (2018).
8. Linsell, L. *et al.* Cognitive trajectories from infancy to early adulthood following birth before 26 weeks of gestation: a prospective, population-based cohort study. *Arch. Dis. Child.* **103**, 363–370 (2018).
9. Lawn, J. E. & Kinney, M. Preterm birth: now the leading cause of child death worldwide. *Sci. Transl. Med.* **6**, 263ed21 (2014).
10. Gao, P., Sultan, K. T., Zhang, X.-J. & Shi, S.-H. Lineage-dependent circuit assembly in the neocortex. *Development* **140**, 2645–2655 (2013).

11. Kriegstein, A. & Alvarez-Buylla, A. The glial nature of embryonic and adult neural stem cells. *Annu. Rev. Neurosci.* **32**, 149–184 (2009).
12. Ming, G.-L. & Song, H. Adult neurogenesis in the mammalian brain: significant answers and significant questions. *Neuron* **70**, 687–702 (2011).
13. Reynolds, B. A. & Weiss, S. Generation of neurons and astrocytes from isolated cells of the adult mammalian central nervous system. *Science* **255**, 1707–1710 (1992).
14. Chojnacki, A. & Weiss, S. Production of neurons, astrocytes and oligodendrocytes from mammalian CNS stem cells. *Nat. Protoc.* **3**, 935–940 (2008).
15. Guo, W., Patzlaff, N. E., Jobe, E. M. & Zhao, X. Isolation of multipotent neural stem or progenitor cells from both the dentate gyrus and subventricular zone of a single adult mouse. *Nat. Protoc.* **7**, 2005–2012 (2012).
16. Fischer, J. et al. Prospective isolation of adult neural stem cells from the mouse subependymal zone. *Nat. Protoc.* **6**, 1981–1989 (2011).
17. Lim, D. A. & Alvarez-Buylla, A. The Adult Ventricular-Subventricular Zone (V-SVZ) and Olfactory Bulb (OB) Neurogenesis. *Cold Spring Harb. Perspect. Biol.* **8**, (2016).
18. Silva-Vargas, V., Maldonado-Soto, A. R., Mizrak, D., Codega, P. & Doetsch, F. Age-Dependent Niche Signals from the Choroid Plexus Regulate Adult Neural Stem Cells. *Cell Stem Cell* **19**, 643–652 (2016).
19. LaMonica, B. E., Lui, J. H., Hansen, D. V. & Kriegstein, A. R. Mitotic spindle orientation predicts outer radial glial cell generation in human neocortex. *Nat. Commun.* **4**, 1665 (2013).
20. Subramanian, L., Calcagnotto, M. E. & Paredes, M. F. Cortical Malformations: Lessons in Human Brain Development. *Front. Cell. Neurosci.* **13**, 576 (2019).

21. Bernardi, S. & Salzman, C. D. The contribution of nonhuman primate research to the understanding of emotion and cognition and its clinical relevance. *Proc. Natl. Acad. Sci.* U S A. **116**, 26305-26312 (2019).
22. Yoder, B. A. & Coalson, J. J. Animal models of bronchopulmonary dysplasia. The preterm baboon models. *Am. J. Physiol. Lung Cell Mol. Physiol.* **307**, L970-977 (2014).
23. Seidner, S. R., Jobe, A. H., Coalson, J. J. & Ikegami, M. Abnormal surfactant metabolism and function in preterm ventilated baboons. *Am. J. Respir. Crit. Care Med.* **158**, 1982–1989 (1998).
24. Verney, C. *et al.* Neuronal damage in the preterm baboon: impact of the mode of ventilatory support. *J. Neuropathol. Exp. Neurol.* **69**, 473–482 (2010).
25. Ostrem, B. E. L., Lui, J. H., Gertz, C. C. & Kriegstein, A. R. Control of outer radial glial stem cell mitosis in the human brain. *Cell Rep* **8**, 656–664 (2014).
26. Wu, M. V. *et al.* Impact of social status and antidepressant treatment on neurogenesis in the baboon hippocampus. *Neuropsychopharmacology* **39**, 1861–1871 (2014).
27. Sandstrom, R. S. *et al.* Epigenetic regulation by chromatin activation mark H3K4me3 in primate progenitor cells within adult neurogenic niche. *Sci. Rep.* **4**, 5371 (2014).
28. Geddes, J. W., Cooper, S. M., Cotman, C. W., Patel, S. & Meldrum, B. S. N-methyl-D-aspartate receptors in the cortex and hippocampus of baboon (Papio anubis and Papio papio). *Neuroscience* **32**, 39–47 (1989).
29. Fujitani, M. *et al.* TAp73 acts via the bHLH Hey2 to promote long-term maintenance of neural precursors. *Curr. Biol.* **20**, 2058–2065 (2010).
30. Lu, J., Delli-Bovi, L. C., Hecht, J., Folkerth, R. & Sheen, V. L. Generation of neural stem cells from discarded human fetal cortical tissue. *J. Vis. Exp,* e2681 (2011).

31. Wang, L. *et al.* Generation of integration-free neural progenitor cells from cells in human urine. *Nat. Methods* **10**, 84–89 (2013).
32. Marchetto, M. C. *et al.* Species-specific maturation profiles of human, chimpanzee and bonobo neural cells. *Elife* **8**, (2019).
33. Lee, H. *et al.* Human fetal brain-derived neural stem/progenitor cells grafted into the adult epileptic brain restrain seizures in rat models of temporal lobe epilepsy. *PLoS ONE* **9**, e104092 (2014).
34. McGrath, E. L. *et al.* Differential Responses of Human Fetal Brain Neural Stem Cells to Zika Virus Infection. *Stem Cell Reports* **8**, 715–727 (2017).
35. Tarasenko, Y. I., Yu, Y., Jordan, P. M., Bottenstein, J. & Wu, P. Effect of growth factors on proliferation and phenotypic differentiation of human fetal neural stem cells. *J. Neurosci. Res.* **78**, 625–636 (2004).
36. Dawes, B. E. *et al.* Human neural stem cell-derived neuron/astrocyte co-cultures respond to La Crosse virus infection with proinflammatory cytokines and chemokines. *J. Neuroinflammation* **15**, 315 (2018).
37. Di Lullo, E. & Kriegstein, A. R. The use of brain organoids to investigate neural development and disease. *Nat. Rev. Neurosci.* **18**, 573–584 (2017).
38. Lancaster, M. A. & Knoblich, J. A. Generation of cerebral organoids from human pluripotent stem cells. *Nat. Protoc.* **9**, 2329–2340 (2014).
39. Rhodes, C. T. *et al.* Cross-species Analyses Unravel the Complexity of H3K27me3 and H4K20me3 in the Context of Neural Stem Progenitor Cells. *Neuroepigenetics* **6**, 10–25 (2016).
40. Coleman, K. Caring for nonhuman primates in biomedical research facilities: scientific, moral and emotional considerations. *Am. J. Primatol.* **73**, 220–225 (2011).

41. Tardif, S. D., Coleman, K., Hobbs, T. R. & Lutz, C. IACUC review of nonhuman primate research. *ILAR J.* **54**, 234–245 (2013).
42. Chalmers, I. & Glasziou, P. Avoidable waste in the production and reporting of research evidence. *Lancet* **374**, 86–89 (2009).
43. Moher, D. *et al.* Stop this waste of people, animals and money. *Nature* **549**, 23–25 (2017).
44. Singec, I. *et al*. Defining the actual sensitivity and specificity of the neurosphere assay in stem cell biology. *Nat. Methods* **3**, 801–806 (2006).
45. Jessberger, S., Clemenson, G. D. & Gage, F. H. Spontaneous fusion and nonclonal growth of adult neural stem cells. *Stem Cells* **25**, 871–874 (2007).
46. Mori, H., Fujitani, T., Kanemura, Y., Kino-Oka, M. & Taya, M. Observational examination of aggregation and migration during early phase of neurosphere culture of mouse neural stem cells. *J. Biosci. Bioeng.* **104**, 231–234 (2007).
47. Marshall, G. P., Reynolds, B. A. & Laywell, E. D. Using the neurosphere assay to quantify neural stem cells in vivo. *Curr. Pharm. Biotechnol.* **8**, 141–145 (2007).
48. Miller, F. D. & Gauthier-Fisher, A. Home at last: neural stem cell niches defined. *Cell Stem Cell* **4**, 507–510 (2009).
49. Fuentealba, L. C., Obernier, K. & Alvarez-Buylla, A. Adult neural stem cells bridge their niche. *Cell Stem Cell* **10**, 698–708 (2012).

Manuscript 3: Pulmonary and Neurologic Therapeutic Effects of Human Mesenchymal Stromal Cell Extracellular Vesicles in a Multifactorial Lung Injury Model

Marissa A. Lithopoulos*[1, 2], Lannae Strueby*[3], Megan O'Reilly[4], Shumei Zhong[1], Marius A. Möbius[5], Farah Eaton[6], Moses Fung[4], Maria Hurskainen[7], Chanèle Cyr-Depauw[1,2], Colin Suen[1,2], Liqun Xu[1], Jennifer J.P. Collins[1,2], Arul Vadivel[1], Duncan J. Stewart[1,2], Dylan Burger[1,8], Bernard Thébaud[1,2,9]

Affiliations:

1 Regenerative Medicine Program, Ottawa Hospital Research Institute, Ottawa, ON, K1H 8L6, Canada
2 Department of Cellular and Molecular Medicine, University of Ottawa, Ottawa, ON, K1H 8M5, Canada
3 Department of Pediatrics, University of Saskatchewan, SK, S7N 0W8, Canada
4 Department of Pediatrics, University of Alberta, Edmonton, AB, T6G 2R7, Canada
5 Department of Neonatology and Pediatric Critical Care Medicine, Medical Faculty and University Hospital Carl Gustav Carus, Technische Universität Dresden, Dresden, SN, 01307, Germany
6 Faculty of Pharmacy and Pharmaceutical Sciences, University of Alberta, Edmonton, AB, T6G 2H7, Canada
7 Department of Pediatric Cardiology and Pediatric Research Center, Helsinki University Central Hospital and University of Helsinki, Helsinki, HUS, FI-00029, Finland
8 Chronic Disease Program, Ottawa Hospital Research Institute, Ottawa, ON, K1H 8L6, Canada
9 Children's Hospital of Eastern Ontario Research Institute, Ottawa, ON, K1H 8L1, Canada

*Authors contributed equally to this manuscript

Connection to Hypothesis: This manuscript provides further evidence that NPC function is impaired in a clinically relevant experimental model of BPD. Furthermore, the manuscript demonstrates that extracellular vesicles (EVs) derived from human umbilical cord-mesenchymal stromal cells (UC-MSCs) can mitigate both lung and brain injuries in experimental BPD.

Current Manuscript Status: The manuscript is under review at The American Journal of Respiratory and Critical Care Medicine.

Author Contributions: I helped with animal care/ animal model set-up. I designed the brain tissue experiments. I conducted the NPC isolation and culture experiments. I isolated and processed the brain tissue. I acquired images of the NPCs and their lineage and conducted the analyses of these images. I conducted the extracellular vesicle tracing experiments. I interpreted the data, wrote, and edited the manuscript. L.S. designed the lung tissue experiments, established the animal model, collected the lung tissue, analyzed the mean linear intercept of the lungs, analyzed the vascular density of the lungs, measured the inflammatory cytokines, and interpreted data, as well as wrote and edited the manuscript. M. O. assisted with lung tissue experiments, establishment of the animal model and collection of lung tissue. S.Z. aided with the *in vitro* NPC experiments and DiR lineage tracing experiment. M.A.M. isolated the UC-MSCs. F.E. assisted with experimental planning. M.F. quantified the vascular density of the lungs. M.H. conducted the flow cytometry analysis and measured lung tissue cytokines. C.C.D. conducted the RTq-PCR experiments and measured lung tissue cytokines. C.S. isolated and characterized extracellular vesicles from the UC-MSC conditioned media. L.X. isolated extracellular vesicles from the UC-MSC conditioned media and processed lung tissue. J.C. collected UC-MSC conditioned media. A.V. assisted with the animal model. D.J.S. provided intellectual guidance and edited the manuscript. D.B. assisted with the material/methods for isolating, labelling, and imaging extracellular vesicles, provided intellectual guidance, and edited the manuscript. B.T. provided financial support, supervised the study, provided intellectual guidance, and edited the manuscript.

Abstract

Rationale: Bronchopulmonary dysplasia, a chronic respiratory condition originating from preterm birth, is associated with abnormal neurodevelopment. Currently, there is a paucity of effective therapies for bronchopulmonary dysplasia and its associated brain injury. In preclinical trials mesenchymal stromal cell therapies demonstrate promise as a therapeutic for bronchopulmonary dysplasia. **Objectives:** To investigate whether a multifactorial neonatal mouse model of lung injury perturbs neural progenitor cell function and to assess the ability of human umbilical cord-derived mesenchymal stromal cell extracellular vesicles to mitigate pulmonary and neurologic injury. **Methods:** Mice at postnatal day 7/8 were injected intraperitoneally with lipopolysaccharide and ventilated with 40% oxygen at postnatal day 9/10 for 8 hours. Treated animals received umbilical cord mesenchymal stromal cell-derived extracellular vesicles intratracheally preceding ventilation. Lung morphology, vascularity, and inflammation were quantified. NPCs were isolated from the subventricular zone/hippocampus and assessed for self-renewal and *in vitro* differentiation ability. **Measurements and Main Results:** The multifactorial lung injury model produced alveolar and vascular rarefaction mimicking bronchopulmonary dysplasia. Neural progenitor cells from ventilation-exposed mice showed reduced neurosphere and oligodendrocyte formation. Mice treated with mesenchymal stromal cell extracellular vesicles showed significant improvement in lung architecture, vessel formation, and inflammatory modulation. Additionally, we observed significantly increased *in vitro* neurosphere formation. **Conclusions:** Our multifactorial lung injury model impairs neural progenitor cell function. Observed pulmonary and neurologic alterations are mitigated by intratracheal treatment with mesenchymal stromal cell-derived extracellular vesicles.

Key Words: Mesenchymal stromal cells; extracellular vesicles; neonatal lung disease, bronchopulmonary dysplasia; neural progenitor cell

Introduction

Extremely preterm infants (<28 weeks) are born in a vulnerable state that renders them particularly susceptible to injury from medical interventions and external stimuli (1). Bronchopulmonary dysplasia (BPD) and preterm brain injury are two of the most significant and interconnected morbidities encountered by preterm infants (2,3). BPD is the chronic lung dysfunction arising from a complex interaction of antenatal and postnatal factors imposed upon an immature lung with aberrant repair capabilities (2). BPD is not exclusively a disease of infancy. It has long lasting respiratory consequences for preterm infants. Importantly, BPD is independently associated with preterm brain injury and adverse neurodevelopmental outcomes (3). Mechanical ventilation, supplemental oxygen, and inflammation are known to be critical contributors to the development of BPD and preterm brain injury (4,5).

Multiple pathways, including hemodynamic instability secondary to invasive ventilation and systemic inflammation originating from pulmonary injury, increase the risk of white matter injury and intraventricular/periventricular brain injury in preterm infants (6,7). However, less known is the effect of these noxious stimuli on neural progenitor cells (NPCs), a brain cell population that is essential for neurodevelopment and cognitive function (8,9). NPCs primarily reside postnatally in the subventricular zone (SVZ) and the dentate gyrus (DG) of the hippocampus (10), areas potentially affected in preterm brain injury.

Currently, preterm brain injury and BPD lack effective safe therapies prompting researchers to investigate novel approaches to mitigate injury. Utilization of postnatal steroid treatment for BPD can improve pulmonary outcomes but is associated with neurodevelopmental impairments (11,12). Regenerative medicine therapies, particularly mesenchymal stromal cell (MSC) therapies, are under intense investigation as a therapeutic alternative for BPD. In preclinical

studies, MSCs have demonstrated the ability to improve lung structure, vessel density, and inflammation in experimental BPD rodent models (13). While clinical trials remain in early phases, evidence from animal models indicate that 'cell-free' cell therapies may be a viable and attractive option. In oxygen-induced BPD models, MSC conditioned media (CDM) or MSC-derived extracellular vesicles (EVs) confer therapeutic benefits on lung structure and function (14-18). Whether these therapies can improve neurological function, particularly for the NPC population, remains to be explored.

We sought to determine if cell-free MSC-derived therapies, particularly EVs, remain effective at ameliorating lung injury in a multifactorial model that more closely resembles BPD origins. This was accomplished through the incorporation of mechanical ventilation, inflammation, and supplemental oxygen close to the clinical setting. We also strove to assess the impact of this multifactorial model on NPCs, as well as investigate the effect of MSC-derived EVs on NPCs. To our knowledge, this is the first study to explore NPC function and to address the effect of MSC-derived EVs on both the lung and the brain in a multifactorial neonatal mouse model of BPD. Some of the results of these studies have been previously reported in the form of an abstract (19).

Methods

Experiments were approved by the University of Alberta Institutional Animal Care and Use Committee or the University of Ottawa Animal Care Committee. Please see the supplemental methods for further details (Appendix B).

Multifactorial Lung Injury Model and Experimental Design

Multifactorial lung injury was created by injecting neonatal mice (C57Black/6) at postnatal day (P)7/8 with intraperitoneal lipopolysaccharide (LPS; 4 μg/g) 48 hours prior to mechanical ventilation (tidal volume of 10 μL/g, 180 breaths/minute, 40% oxygen) for 8 hours. Ventilation methods were adapted from Bland et al. (20). Age-matched unventilated pups (did not receive LPS) served as controls. Animals in the lung injury group did not receive therapy while pups in treatment groups received intratracheal MSC-CDM (3 μl/g) or MSC-EVs (0.005 μg/g) immediately preceding ventilation. Vehicle placebo was administered in the same manner and volume as therapies. The vehicle placebo for CDM was α-minimum essential medium (α-MEM). The vehicle for EVs was 1X phosphate buffered saline (PBS). We also administered EV-free CDM (3 μl/g) as a further control.

Isolation of MSC CDM and EVs

Human umbilical cord (UC)-MSCs from term umbilical cords were isolated and characterized as previously described (21). Cell-free CDM was collected following a 24-hour serum-free incubation period. EVs (15-300 nm in diameter; $CD63^{+}calnexin^{-}$) were isolated using serial ultracentrifugation, modified by previously described methods (22,23).

Lung Tissue Analysis

Lungs were frozen in liquid nitrogen and stored at -80°C for cytokine assessment or fixed with zinc formalin as previously described (24) for lung morphometry and immunohistochemistry. As previously described (18,24), lung morphometry was quantified utilizing the mean linear intercept (MLI) and vascular quantification was performed by staining sections for von Willebrand Factor (vWF). All measurements were performed on coded slides to ensure assessors were blinded to the experimental groups.

NPC Isolation and Neurosphere Assays

NPCs were isolated and cultured using adapted methods from Fujitani et al. (25). Briefly, NPCs were isolated from the subependyma of the lateral ventricles and the subgranular zone of the hippocampus. The tissue was digested with papain (Worthington) and mechanically dissociated. Cells were filtered using a 40-μm cell strainer and plated at a density of 10 cells/μL. After 7-8 days primary neurospheres were counted and imaged. NPCs were then passaged and re-plated as single cells at a density of 2 cells/μL. After 7-8 days secondary neurospheres were counted and imaged.

Differentiation Assay

Following the secondary neurosphere assay, NPCs were passaged and plated as a monolayer at a minimal density of 40 cells/μL. Fetal bovine serum was added to the media to induce differentiation. Cells were fixed with 4% paraformaldehyde after 7 days of culture in differentiation medium.

Statistical Analysis

Results are expressed as the mean ± the standard error of the mean. Data was checked for normality. Comparisons between 2 experimental groups were made using a two-tailed unpaired t-test. Comparisons between >2 groups were made using a one-way ANOVA with a Tukey's post hoc test unless otherwise specified in the figure legends. A value of $P < 0.05$ was considered statistically significant. All group assignments were blinded prior to analysis.

Results

A Novel Multifactorial Neonatal Mouse Model of Lung Disease Mimics Selected Pulmonary Endpoints Observed in BPD

To recapitulate clinical conditions encountered by extremely preterm infants, neonatal wild-type C57Black/6 mice were exposed to three of the main preterm-birth associated noxious stimuli (26). First, pups were intraperitoneally injected with lipopolysaccharide (LPS, 4 μg/g) at P7/8 to simulate postnatal inflammation. Second, pups were mechanically ventilated for 8 hours at P9/10. Third, pups were administered 40% O_2 during ventilation, mimicking the oxygen and ventilation support used for infants experiencing respiratory arrest. Age-matched control animals that did not receive LPS were housed in room air for the duration of the experiment. Pups were then assessed for pulmonary and neurological outcomes (Figure 25A).

Mice from the multifactorial lung injury model showed characteristic BPD phenotypes (4). Lung morphometry quantified by the MLI score revealed lung injury animals demonstrate rarefication of the alveolar architecture compared to control animals (Figure 25B, mean ± SEM, 79.5 ± 1.5 vs. 54.3 ± 1.2, $P < 0.0001$, respectively). Similarly, vessel density in lung injury mice was significantly reduced compared to control animals (Figure 25C), as assessed via vWF staining and quantification (1.7 ± 0.1 vs. 2.6 ± 0.2, $P < 0.0001$, respectively). We also identified a remarkable increase in the expression of pro-inflammatory cytokines within the lung of ventilated mice compared to control mice, including interleukin (IL)-1β ($P < 0.05$), macrophage inflammatory protein-2 (MIP-2, $P < 0.0001$), and monocyte chemoattractant protein-1 (MCP-1, $P < 0.0001$) (Figure 25D). Lastly, flow cytometry analysis (Supplemental Figure 9) revealed that there was an influx of immune cells in the lung (Figure 25E), as measured by leukocytes ($P < 0.01$), neutrophils ($P < 0.05$), macrophages ($P < 0.01$), and monocytes ($P < 0.05$).

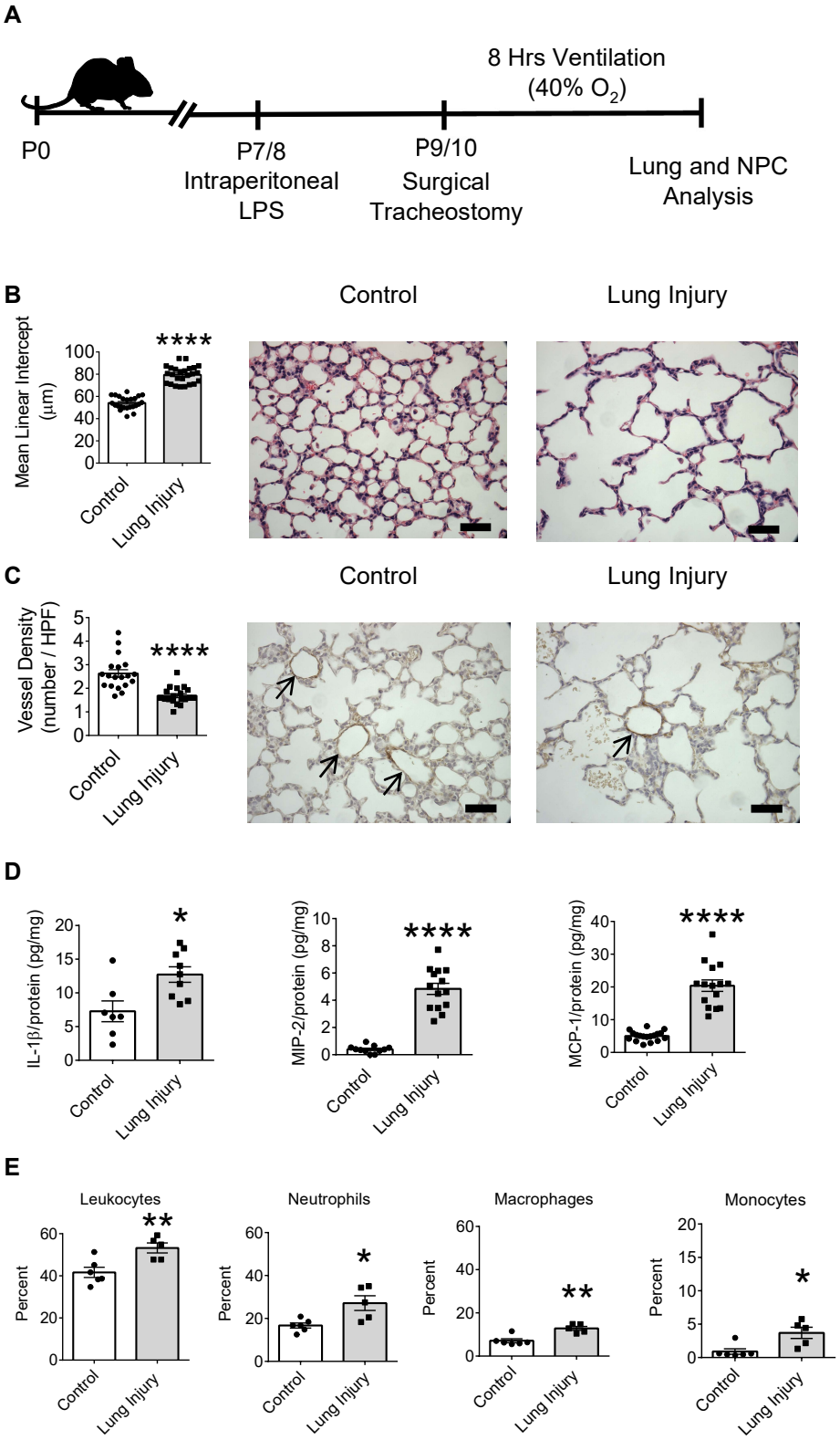

Figure 25. A multifactorial neonatal lung injury mouse model recapitulates the alveolar rarefication, reduced vessel density, and immune response of bronchopulmonary dysplasia. (*A*) Neonatal mice were intraperitoneally injected with lipopolysaccharide (LPS) at postnatal day (P)7/8. At P9/10, the pups were mechanically ventilated for 8 hours using 40% O_2 (lung injury). Age-matched animals were housed in room air for the duration of the experiment

(control). Following this period, the animals were assessed for lung injury and neural progenitor cell (NPC) functional impairments. (*B*) Ventilated mice demonstrated an increased mean linear intercept consistent with simplification of lung architecture, representative hematoxylin and eosin-stained images are shown on the right (control n=24; lung injury n=25). (*C*) Ventilated mice had a reduced vessel density (number/ high power field (HPF)) as shown by von Willebrand Factor staining (arrows indicate vessels) in the representative images on the right (control and lung injury n=19). (*D*) Increased expression of proinflammatory cytokines, interleukin-1β (IL-1β) (control n=7; lung injury n=9), macrophage inflammatory protein-2 (MIP-2) (control n=11; lung injury n=14), and monocyte chemoattractant protein-1 (MCP-1) (control n=18; lung injury n=15) in ventilated mice. (*E*) Ventilation led to an influx of immune cells, specifically quantified as leukocytes, neutrophils, macrophages, and monocytes (control n=6; lung injury n=5). Scale bar 50 μm. *$P < 0.05$, **$P < 0.01$, ****$P < 0.0001$. Unpaired Student's t-test. Data are represented as mean ± SEM.

Remote Organ Injury: NPCs Isolated from Lung Injury Mice Demonstrate Significant Deficits in Self-Renewal and Differentiation Capabilities

Mice exposed to inflammation, ventilation, and supplemental oxygen had a significantly reduced body ($P < 0.05$) and brain ($P < 0.0001$) weight compared to control mice (Supplemental Figure 10). This was the first indication that the brain may be injured in our multifactorial lung injury model. To determine whether NPC functional impairments were associated with our model, we isolated NPCs from the SVZ (Figure 26A) and hippocampus (Figure 26B) of ventilated mice. We first plated the NPCs for primary and secondary neurosphere assays to assess their self-renewal ability (27). We found no significant differences in primary neurosphere formation of NPCs from the SVZ (Figure 26C) and hippocampus (Figure 26D). Conversely, in the secondary neurosphere assay, NPCs isolated from the SVZ of lung injury mice formed significantly fewer neurospheres compared to control mice (Figure 2E), indicating a dramatic impairment in self-renewal capabilities (35.9 ± 4.7 vs. 100.5 ± 17.5, $P < 0.01$, respectively). We identified no significant differences in secondary neurosphere formation from hippocampal-derived NPCs (Figure 2F). Furthermore, we did not find any significant differences in neurosphere size (Supplemental Figure 11). This suggests that it is not the proliferation within a neurosphere that is impaired in our lung injury model, but rather the ability of NPCs to form new neurospheres (self-renewal) that is impaired.

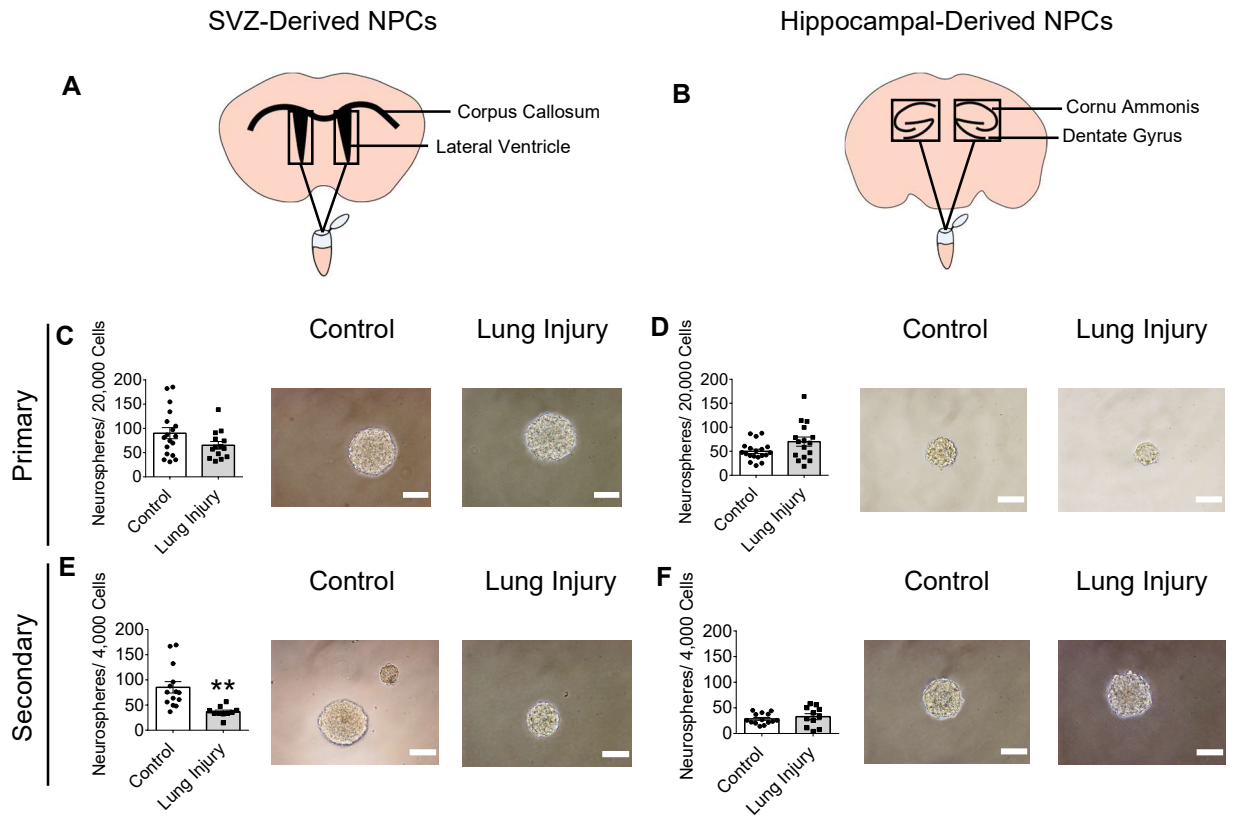

Figure 26. Neonatal lung injury leads to an impairment in neural progenitor cell (NPC) self-renewal capabilities. For the primary neurosphere assay, NPCs were plated at 20,000 cells/well in 6-well plates. For the secondary neurosphere assay, NPCs were plated at 4,000 cells/well in 6-well plates. (*A* and *B*) Schematic of the subventricular zone (SVZ) and hippocampal region dissected to isolate NPCs. (*C* and *D*) NPCs derived from the SVZ (C, control n=18; lung injury n=14) and hippocampus (D, control n=19; lung injury n=16) of control and ventilated animals form a similar number of primary neurospheres. (E) When plated for a secondary neurosphere assay, the NPCs from the SVZ of ventilated animals form significantly fewer neurospheres compared to control animals (control n=14; lung injury n=10). (F) No significant differences were identified in secondary neurosphere formation between NPCs from the hippocampus of control and lung injury mice (control n=14; lung injury n=11). Scale bar 100 μm. $^{**}P < 0.01$. Unpaired Student's t-test. Data are represented as mean ± SEM.

We next assessed the ability of NPCs to differentiate into the three main lineages of the brain—astrocytes, neurons, and oligodendrocytes (10). We did not find any significant differences between cells isolated from the SVZ of control and lung injury animals (Figure 27A). In contrast, while there were no differences in astrocyte and neuron formation, NPCs isolated from the hippocampus of lung injury mice formed significantly fewer oligodendrocytes compared to cells isolated from control animals ($P < 0.05$, Figure 27B). This finding was interesting in terms of timing and development, as NPCs in the brains of neonatal mice are actively differentiating into

oligodendrocytes (9). Furthermore, white matter injury within the brain is a common phenotype of extremely preterm infants (7).

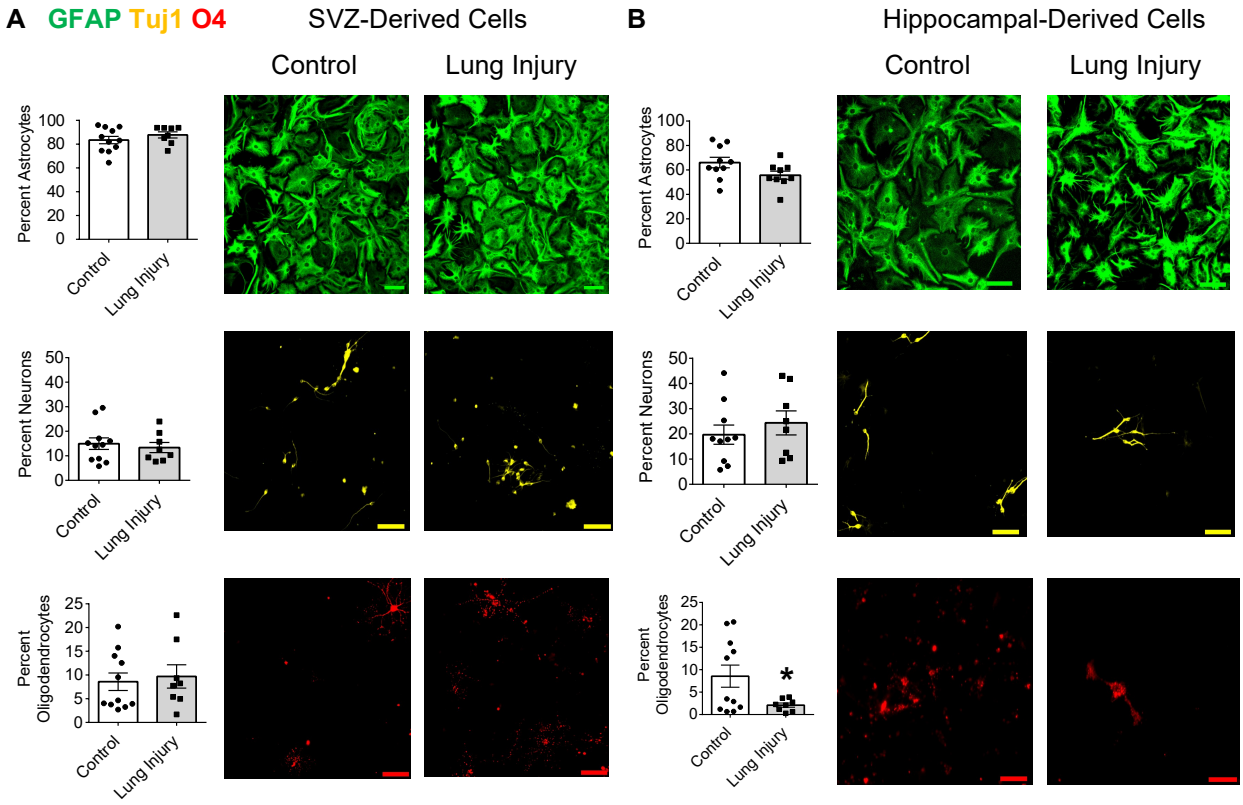

Figure 27. Neonatal lung injury significantly reduces hippocampal-derived neural progenitor cell (NPC) oligodendrocyte formation. (*A*) No significant differences were found between groups in subventricular zone (SVZ) NPC ability to form astrocytes, neurons, and oligodendrocytes (control n=11; lung injury n=8). (*B*) Hippocampal-derived NPCs from lung injury mice form similar amounts of astrocytes (control n=10; lung injury n=9) and neurons (control n=10; lung injury n=8), but significantly fewer oligodendrocytes compared to control mice (control n=11; lung injury n=8). Scale bar 50 μm. *$P < 0.05$. Unpaired Student's t-test. Data are represented as mean ± SEM. GFAP, glial fibrillary acidic protein; Tuj1, neuron-specific β3 tubulin; O4, oligodendrocyte marker O4.

UC-MSC CDM Improves Lung Structure and NPC Self-Renewal

We have previously shown that UC-MSCs and their secreted CDM improve lung morphometry and vessel density in a hyperoxia rodent model of BPD (14,28). To assess the efficacy of UC-MSC CDM to improve lung and brain outcomes in our novel multifactorial lung injury murine model, we injected CDM intratracheally (3 μL/g) prior to ventilating the mice (Figure 28A). Control animals did not receive an intratracheal injection (lung injury group) or received α-MEM (placebo group). The distribution of CDM combined with fluorescent dye (*see* Supplemental Methods)

revealed that there was a preference for right sided distribution (Figure 28B). Importantly, we found that CDM treatment greatly improved lung architecture (Figure 28C), as shown by a significant reduction in the MLI score compared to both control groups ($P < 0.0001$). Furthermore, we found that CDM administration significantly increased vessel density compared to both control groups (Figure 28D), as shown by vWF staining and quantification ($P < 0.001$). We also assessed whether *in vitro* administration of CDM could improve NPC self-renewal of NPCs isolated from lung injury mice. We added CDM at plating, allowed the NPCs to form primary neurospheres, then passaged the cells and counted the number of secondary neurospheres formed (Figure 28E). Interestingly, we found that CDM administration significantly increased secondary neurosphere formation ($P < 0.001$, Figure 28F), indicating that CDM increases NPC self-renewal capabilities.

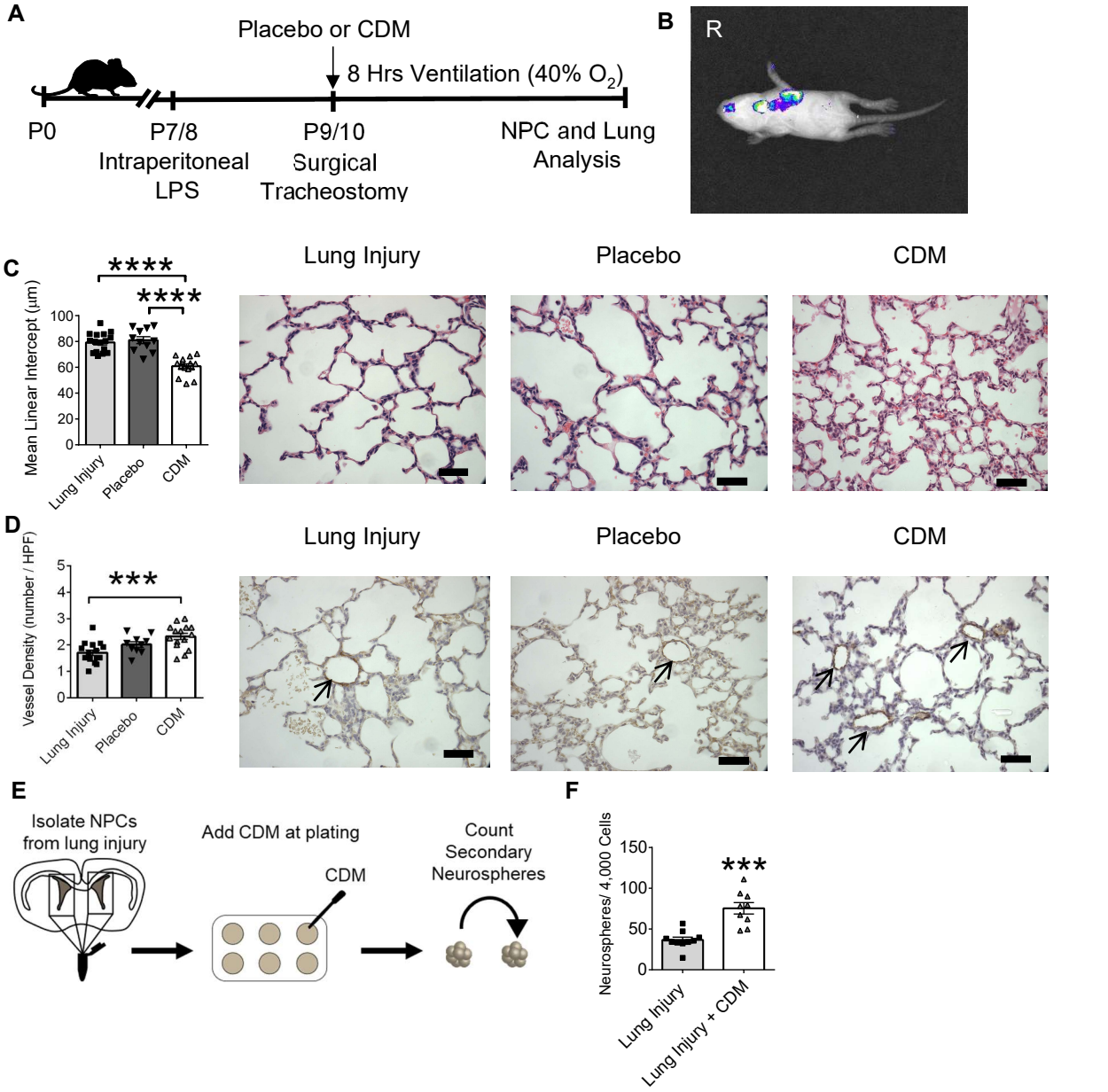

Figure 28. Umbilical cord-mesenchymal stromal cell-derived conditioned media improves lung morphology and neural progenitor cell (NPC) self-renewal in a multifactorial mouse model of neonatal lung disease. (*A*) Placebo (α-Minimum Essential Medium) or umbilical cord-mesenchymal stromal cell-derived conditioned media (UC-MSC-derived CDM) was administered intratracheally to mice who were exposed to lipopolysaccharide, ventilation, and oxygen as previously described. (*B*) Representative image of the distribution of CDM combined with fluorescent dye when intratracheally injected into mice and visualized after 30 minutes of ventilation. A preference for right sided distribution was seen in 62% of animals while bilateral distribution occurred in 25% of animals (n=8). (*C*) Mice treated with CDM had a significantly reduced mean linear intercept (lung injury n=16; placebo n=11; CDM n=15) consistent with improved lung morphology when compared to lung injury and placebo treated animals. Representative hematoxylin and eosin-stained lung sections on the right. (*D*) CDM treatment led to an increase in vessel density within the lungs of ventilated mice (lung injury n=16; placebo n=10; CDM n=15) as shown in representative von Willebrand factor-stained images (arrows indicate vessels) on right. (*E*) Methods used to test the effect of CDM on NPCs *in vitro*. NPCs were plated for the secondary neurosphere assay at 4,000 cells/well in a 6-well plate. (*F*) NPCs isolated from the SVZ of ventilated mice and treated *in vitro* with CDM formed significantly more secondary neurospheres compared to NPCs that did not received CDM (lung injury n= 10; lung injury + CDM n=9). Scale bar 50 µm. ***$P < 0.001$, ****$P < 0.0001$. Comparison between two groups was conducted via an

unpaired Student's t-test. Comparison between >2 groups was conducted via a one-way ANOVA with Tukey post hoc test. Data are represented as mean ± SEM.

UC-MSC-Derived EVs Injected Intratracheally Localize to the Lungs and the Brain

It has previously been reported that EVs constitute the therapeutic component of the MSC secretome (15,29,30). We therefore isolated EVs from UC-MSCs to assess whether EVs could act as therapeutic agents to improve neurological and pulmonary outcomes in our multifactorial mouse lung injury model. The UC-MSC EVs were isolated from MSC CDM via ultracentrifugation (*see* Supplemental Methods). The isolated EVs were on average approximately 80 nm in diameter as indicated by dynamic light scattering (Figure 29A) and nanoparticle tracking analysis (Figure 29B). Moreover, immunoblots revealed that EVs were positive for the EV marker CD63 and negative for calnexin, a negative EV marker (Figure 29C,D; Supplemental Figure 12) (31).

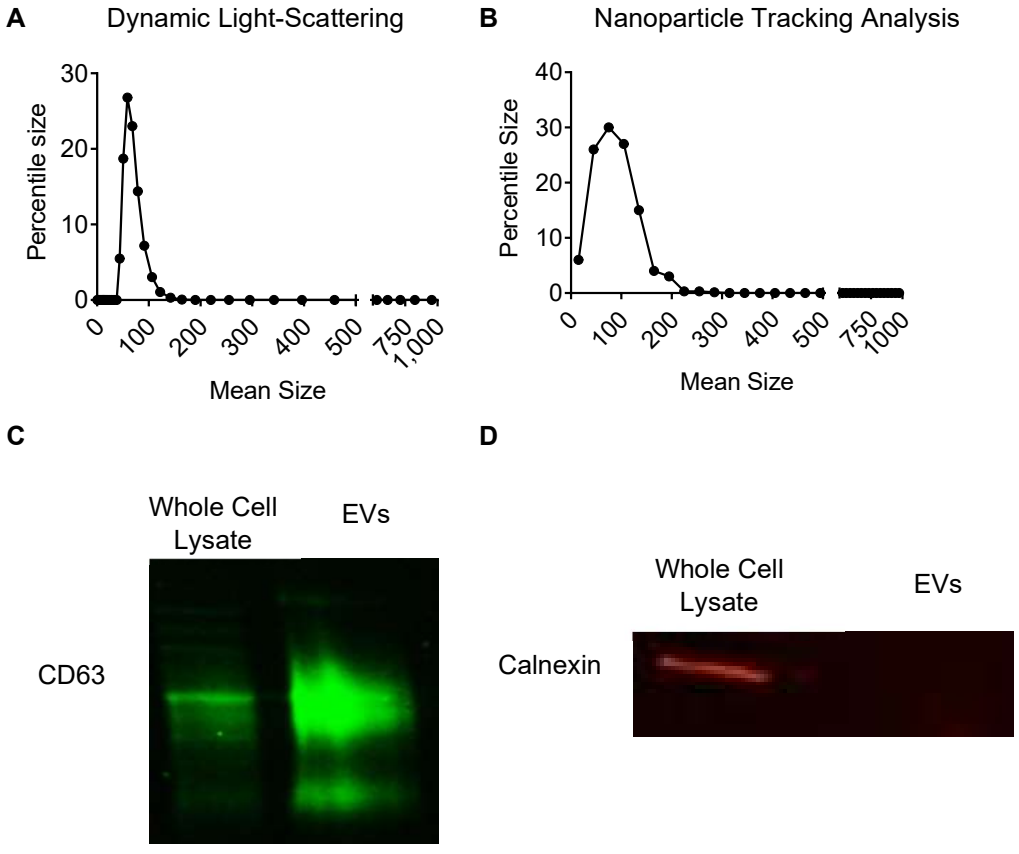

Figure 29. Characterization of the extracellular vesicles (EVs) derived from umbilical cord-mesenchymal stromal cells. (*A* and *B*) Dynamic light-scattering (A) and nanoparticle tracking analysis (B) demonstrate that the

isolated EVs are on average approximately 80 nm in diameter. (*C* and *D*) Isolated EVs are positive for EV marker CD63 (C) and show no signal for the negative EV marker calnexin (D).

Following EV characterization, we conducted EV tracing experiments to determine their localization after intratracheal injection. We first identified EVs with the lipophilic marker DiR. We injected the EVs intratracheally (0.005 μg/g) in our lung injury model described above. Brain and lung tissue were collected following 1 and 4 hours of ventilation and imaged using an IVIS Spectrum *in vivo* imaging system (PerkinElmer). We observed fluorescent signal at both the 1 and 4 hour timepoints in the brain and the lungs (Figure 30A; Supplemental Tables 2 and 3). This suggests that EVs localized to both organs over time. As expected following an intratracheal injection, the majority of DiR signal was found within the lungs. Interestingly, there was significantly more fluorescent signal within the brain over time ($P < 0.01$), indicating a possible increase in EV uptake within the brain during the ventilation period. Additionally, we also identified EVs with the lipophilic dye, PKH26. We repeated the EV injection in our lung injury model as described above. We then dissected the lung and brain tissue following 1, 4, and 8 hours of ventilation and conducted high magnification microscopy (100x). PKH26 was detected in the lungs and the brain at all time points (Figure 30B), confirming our DiR results. Moreover, PKH26 was found specifically in NPC niche regions, i.e., the SVZ and DG of the hippocampus. Although the majority of EVs seem to localize to the lungs, this finding suggests that EVs may also have direct access to the NPC population.

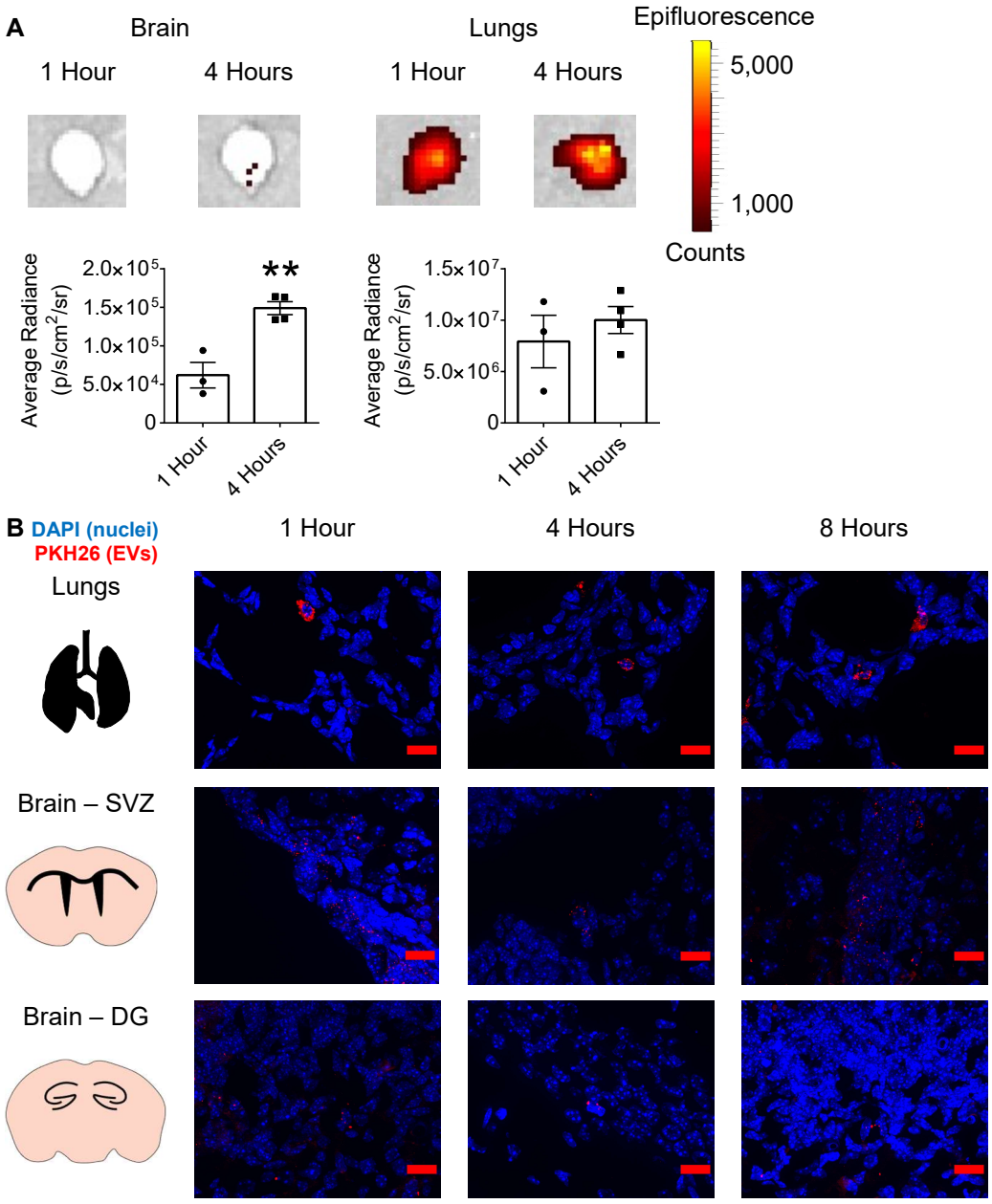

Figure 30. Umbilical cord-mesenchymal stromal cell-derived extracellular vesicles (EVs) appear to localize to both the lungs and the brain after intratracheal injection. (*A*) Mice were intratracheally injected with DiR-stained EVs; subsequently, the fluorescent signal was measured after 1 hour or 4 hours of ventilation using an IVIS Spectrum *in vivo* imaging system. There was significantly more DiR signal in the brain over time (lungs and brain, 1 hour n=3; 4 hours n=4). (*B*) Mice were intratracheally injected with PKH26-stained EVs and ventilated for 1 hour, 4 hours, or 8 hours. High magnification microscopy (100x) showed PKH26 in the lungs and in the neural progenitor cell niche regions, the subventricular zone (SVZ) and the dentate gyrus (DG) of the hippocampus. Scale bar 15 μm. $^{**}P < 0.01$. Unpaired Student's t-test. Data are represented as mean ± SEM.

UC-MSC EVs Increase Anti-Inflammatory Cytokine Expression and Ameliorate Lung Injury

To assess the effects of EVs in our multifactorial lung injury model, we compared lung injury mice to animals treated with placebo (PBS, 3 μL/g), EV-free CDM (3 μL/g), and EVs (0.005 μg/g). We found that EVs greatly improved lung morphology, with EV treated mice showing a significantly lower MLI score compared to lung injury ($P < 0.0001$), placebo ($P < 0.05$), and EV-free CDM ($P < 0.05$) treated mice (Figure 31A). Furthermore, EVs significantly improved vessel density within the lungs (Figure 31B) compared to lung injury ($P < 0.0001$), placebo ($P < 0.001$), and EV-free CDM ($P < 0.01$) treated mice, as measured by vWF staining and quantification. We did not observe significant differences in lung pro-inflammatory cytokine levels for interleukin (IL)-1β, tumour necrosis factor (TNF)-α, and IL-6 following EV treatment (Figure 31C and D). We also did not detect differences between groups in terms of immune cell quantity within the lung (Supplemental Figure 13). However, the improved lung morphology and increased vessel density following EV treatment was associated with a significant increase in anti-inflammatory cytokine expression compared to placebo treatment for IL-4 (mRNA and protein $P < 0.05$), IL-10 (mRNA $P < 0.05$), and IL-13 (mRNA and protein $P < 0.05$) (for a complete analysis of all the cytokines assessed, *see* Supplemental Figure 13).

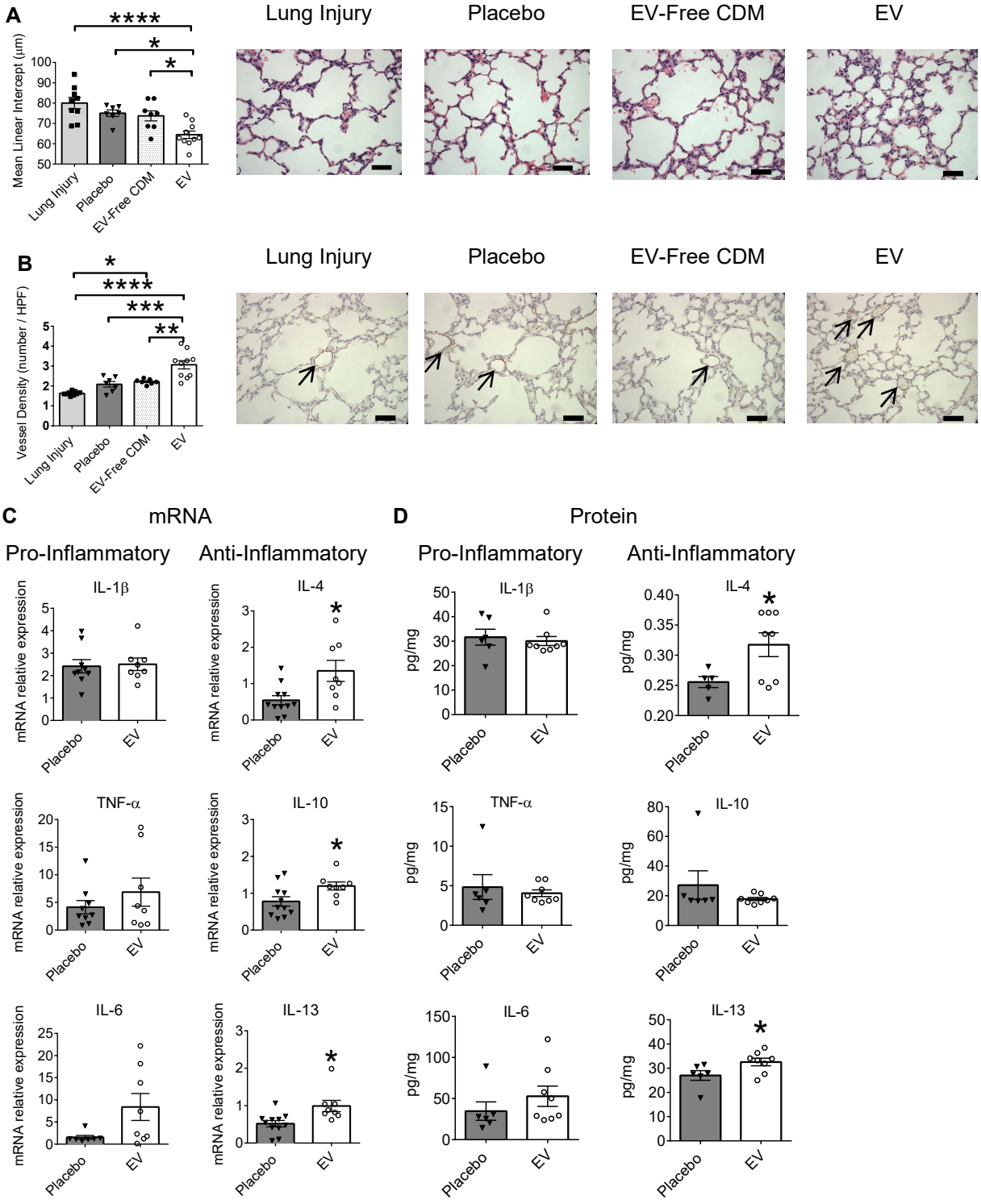

Figure 31. Umbilical cord-mesenchymal stromal cell-derived extracellular vesicles (EVs) improve lung morphology, increase vessel density, and increase anti-inflammatory cytokine expression. (*A*) Mice intratracheally injected with EVs prior to ventilation show a significantly improved lung morphology as compared to lung injury mice, or mice injected with placebo (PBS) or EV-free conditioned media (CDM), as shown via quantification by mean linear intercept (lung injury n=9; placebo n=7; EV-free CDM n=8; EV n=10). Representative

hematoxylin and eosin-stained lung sections are shown on the right. (*B*) EV treatment significantly increased vessel density within the lung compared to lung injury, placebo, or EV-free CDM treated mice, as demonstrated by quantification of the number of von Willibrand Factor-stained vessels per high power field (HPF; lung injury n=8; placebo n=7; EV-free CDM n=7; EV n=10). Representative images are displayed on the right. (*C*) EV treatment significantly increased the anti-inflammatory mRNA expression of interleukin (IL)-4, IL-10, IL-13 (placebo n=11; EV n=8). There were no differences identified between groups in pro-inflammatory cytokines IL-1β (placebo n=9; EV n=8), tumor necrosis factor alpha (TNF-α, placebo n=9; EV n=8), and IL-6 (placebo n=7; EV n=8). (*D*) EV treatment significantly increased anti-inflammatory protein expression of cytokines IL-4 (placebo n=5; EV n=8) and IL-13 (placebo, n=6; EV, n=8). There were no differences in protein levels between groups for IL-10 or pro-inflammatory cytokines IL-1β, TNF-α, and IL-6 (placebo n=6; EV n=8). Scale bar 50 μm. **P* < 0.05, ***P* < 0.01, ****P* < 0.001, *****P* < 0.0001. Comparison between two groups was conducted via an unpaired Student's t-test. Comparison between >2 groups was conducted via a one-way ANOVA with Tukey post hoc test. Data are represented as mean ± SEM.

Remote Organ Treatment: UC-MSC EVs Injected Intratracheally to Treat Neonatal Lung Injury Significantly Improve NPC Self-Renewal Capabilities

To assess whether UC-MSC EVs can specifically improve the NPC functional deficits in our multifactorial lung injury model, we treated animals from our lung injury model with placebo (PBS) or EVs (0.005 μg/g) (injected intratracheally) prior to ventilation. We then isolated NPCs from the SVZ and hippocampus and assessed 2 functional abilities, self-renewal and differentiation. Based on our previous findings (Figure 27), we closely observed oligodendrocyte formation; however, we did not find significant differences in oligodendrocyte differentiation ability following EV treatment (Supplemental Figure 14). Interestingly, there was a significant increase in neuronal differentiation of NPCs from the SVZ of EV treated mice, compared to those from placebo treated mice ($P < 0.05$, Supplemental Figure 14). We also assessed self-renewal via successive neurosphere assays. Critically, SVZ-derived NPCs from EV treated mice formed significantly more secondary neurospheres compared to NPCs from placebo treated mice ($P < 0.05$; Figure 32C). Combined with the absence of significant differences in secondary neurosphere size (Supplemental Figure 15), this suggests that UC-MSC EVs significantly increase SVZ NPC self-renewal. It should be noted that NPCs from the hippocampus of EV treated mice formed on average, smaller primary neurospheres compared to those from placebo treated mice

(Supplemental Figure 15). Furthermore, there were no significant differences in the amount of primary or secondary neurospheres formed by hippocampal-derived NPCs (Figure 32A, B, D).

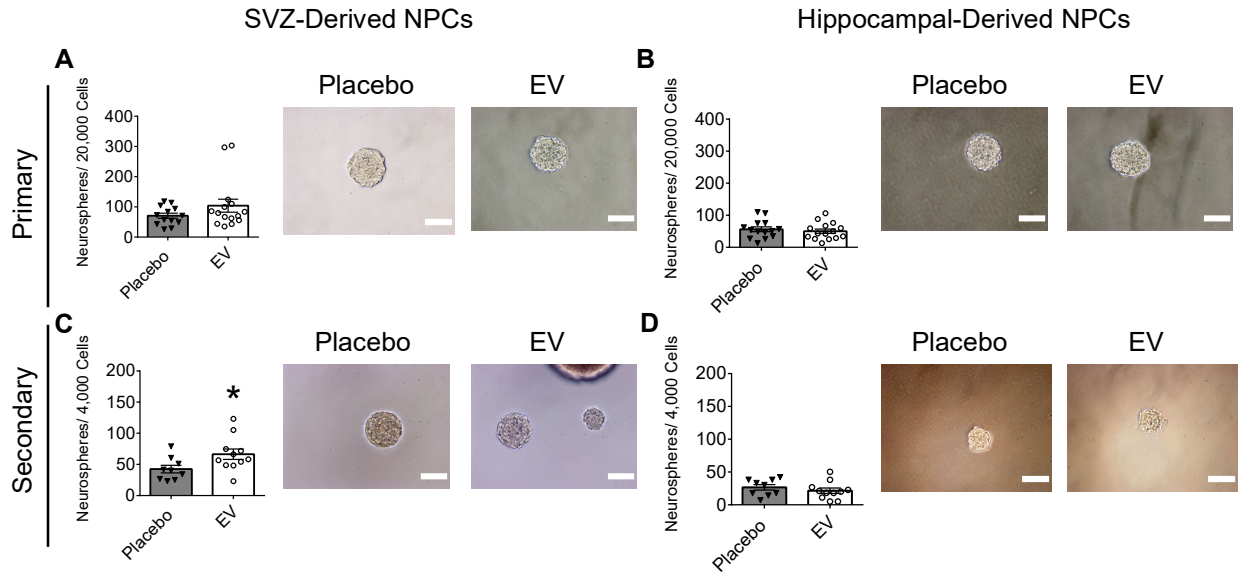

Figure 32. Neural progenitor cells derived from the subventricular zone of extracellular vesicle (EV) treated mice show a significant improvement in self-renewal capabilities compared to those from placebo treated mice. Mice were administered placebo (PBS) or EVs intratracheally prior to mechanical ventilation. Neural progenitor cells (NPCs) isolated from the subventricular zone (SVZ) and hippocampus were assessed for their ability to form neurospheres. NPCs were plated at 20,000 cells/well in 6-well plates for the primary neurosphere assay. NPCs were then plated at 4,000 cells/well in 6-well plates for the secondary neurosphere assay. (*A* and *B*) No significant differences in primary neurosphere formation of NPCs from the SVZ (placebo n=13; EV n=15) or hippocampus (placebo n=14; EV n=15. (*C*) NPCs from the SVZ of EV treated mice formed significantly more secondary neurospheres compared to placebo treated animals (placebo n=9; EV n=11). (D) No significant differences were identified in secondary neurosphere formation of NPCs from the hippocampus (placebo n=9; EV n=11). Scale 100 µm. *$P < 0.05$. Unpaired Student's t-test. Data are represented as mean ± SEM.

Discussion

This study has a number of important contributions which will aid in the development of UC-MSC-derived therapies to treat the complications of extreme prematurity. First, we developed a multifactorial mouse model of neonatal lung injury, which incorporates multiple noxious stimuli contributing to BPD and its associated abnormal neurodevelopmental outcomes. Second, we showed that our multifactorial mouse model creates a lung injury resembling BPD (reduced alveolar and vascular development) and increases inflammatory cytokines and immune cell

infiltration. Third, we found that within the context of experimental neonatal lung injury, there are also functional impairments in a critical cell population for brain development—NPCs. Fourth, we demonstrated that MSC-derived EVs, can greatly improve alveolarization and angiogenesis within the developing mouse lung. Fifth, we also demonstrated that MSC-derived EVs injected intratracheally to target the lungs can have remote tissue therapeutic effects, by improving the self-renewal abilities of NPCs.

We recognize several limitations in our study. Inherent shortcomings exist whenever a rodent model is utilized to simulate BPD (32,33). We sought to improve on the commonly utilized hyperoxia model by incorporating a multifactorial pathogenesis. The combination of intraperitoneal LPS, mechanical ventilation, and supplemental oxygen is unique to our model and had not been previously reported. However, due to the multifactorial nature it is challenging to investigate individual mechanisms contributing to injury; there is complex pathophysiology, as with the human disease (4). Our observed unequal distribution of intratracheally injected therapies is also a potential shortcoming; however, this can also occur in the clinical setting with therapies such as surfactant. Additionally, despite preferential right-sided administration, benefits in morphology and vascular density were observed in the left lung and we observed remote organ therapeutic effects minimizing the likely significance of this limitation. Additionally, we investigated only a single dose of MSC-EVs and there is the potential that alternative doses may demonstrate greater benefit. Our selected dose was extrapolated from our own effective CDM dose as well as from literature demonstrating the benefits of EVs in adult rodents (34). Ideally future research would investigate optimal weight-based dosing strategies.

A striking finding of our study was that in the context of the lung injury, there was also brain injury, as observed by NPC functional impairments. One question that arises is, are the NPCs

perturbed as a secondary effect of the lung injury or are they directly impaired by the noxious stimuli? One cannot exclude the possibility of the lung injury influencing the brain, particularly in terms of inflammation (35,36). We demonstrated a significant increase in pro-inflammatory cytokines and immune cells in the lungs. Future studies may be able to identify inflammatory cytokine upregulation in the brain and microglial activation. However, the LPS used in our model is systemically administered and therefore, may directly influence the brain. Moreover, mechanical ventilation may also play a crucial role in BPD-associated brain injury. In human preterm patients, there is a strong association between mechanical ventilation and abnormal neurodevelopmental outcomes in terms of smaller brain stem volume, impaired white matter maturation, and deficits in motor skills during childhood (5,37). Furthermore, we have previously shown in a murine model that hyperoxia alone can impair NPC function and that these impairments are associated with long-term motor and cognitive deficits (M.A.L., unpublished data). Thus, NPCs in our multifactorial lung injury model are likely affected directly by noxious stimuli and indirectly as a secondary effect of the lung injury. Moreover, based on our previous findings, the NPC impairment may have adverse effects on neurobehavioural outcomes.

A primary goal of the study was to assess the efficacy of UC-MSC-derived EVs to improve pulmonary and neurological outcomes. We focused on EVs derived from MSCs, rather than the cells themselves, for three main reasons. First, EVs have previously been shown to be the active therapeutic vector of MSCs in lung injury models (15,29,30). Second, cell-free therapies offer the benefit of having a predetermined therapeutic "dose" prior to injection. Third, EVs injected peripherally can deliver their contents to brain tissue (38). We also observed DiR and PKH26 signal in the brain, suggesting that EVs localized to the brain and may have direct access to NPC niche regions. Therefore, there exists a possibility that EVs have a direct influence on NPCs. It is

however critical to note that the majority of DiR and PKH26 signal was found within the lungs, indicating that the majority of EVs localized to the lungs and likely exerted their therapeutic effects within the lung tissue, which may have led to secondary benefits to NPCs in the brain.

Importantly, we revealed that UC-MSC EVs were able to significantly increase anti-inflammatory cytokines within the lung, as well as improve alveolar and vascular growth. Our results suggest that EVs mitigate the inflammatory environment within the lung to allow for improved lung development, although future research is required to investigate precise mechanisms. Furthermore, although we did not observe an improvement in NPC oligodendrocyte formation following EV treatment, we did find a significant improvement in self-renewal of NPCs from EV treated mice. This is a critical finding, as it suggests that EVs targeted for the lung, have the potential to improve neurological outcomes. Given that current therapeutic options for BPD, such as glucocorticoids, can impair brain development (39), utilizing UC-MSC EVs as an alternative therapy to improve lung and brain outcomes, would be of great benefit for preterm patients.

In summary, our study offers a multifactorial, clinically relevant mouse model to study experimental BPD. Furthermore, we identify MSC EVs as therapeutic agents capable of improving lung development and NPC self-renewal. Therefore, we provide a strong rationale for the translation of MSC therapy from the scientific bench toward the clinic to mitigate pulmonary and neurological complications due to preterm birth.

Acknowledgments

The authors thank Dr. Julien Yockell-Lelievre for his guidance with the ArrayScan VTI. The authors also thank Dr. Jose Viñas and Dr. Kevin Burns for their guidance with the DiR IVIS experiment. M.A.L. was supported by a Canadian Institutes of Health Research (CIHR) Frederick Banting and Charles Best Doctoral Award. L.S. was supported by the Sandra Schmirler Foundation and the Women and Children's Health Research Institute. J.J.C.P. was supported by a CIHR Postdoctoral Fellowship. B.T. is supported by a CIHR Foundation Scheme grant, The Stem Cell Network, the Ontario Institute of Regenerative Medicine, and the Children's Hospital of Eastern Ontario Foundation.

References

1. Stoll BJ, Hansen NI, Bell EF, Walsh MC, Carlo WA, Shankaran S, Laptook AR, Sánchez PJ, Van Meurs KP, Wyckoff M, Das A, Hale EC, Ball MB, Newman NS, Schibler K, Poindexter BB, Kennedy KA, Cotton M, Watterberg KL, D'Angio CT, DeMauro SB, Truog WE, Devaskar U, Higgins RD, for the Eunice Kennedy Shriver National Institute of Child Health and Human Development Neonatal Research Network. Trends in Care Practices, Morbidity, and Mortality of Extremely Preterm Neonates, 1993-2012. *JAMA* 2015;314:1039–51.
2. Jobe AH, Bancalari E. Bronchopulmonary dysplasia. *Am J Respir Crit Care Med* 2001;163:1723–9.
3. Vohr BR, Wright LL, Poole WK, McDonald SA. Neurodevelopmental outcomes of extremely low birth weight infants <32 weeks' gestation between 1993 and 1998. *Pediatrics* 2005;116:635–43.
4. Thébaud B, Goss KN, Laughon M, Whitsett JA, Abman SH, Steinhorn RH, Ashner JL, Davis PG, McGrath-Morrow SA, Soll RF, Jobe AH. Bronchopulmonary dysplasia. *Nat Rev Dis Primers* 2019;5:78.
5. Guillot M, Guo T, Ufkes S, Schneider J, Synnes A, Chau V, Grunau RE, Miller SP. Mechanical Ventilation Duration, Brainstem Development, and Neurodevelopment in Children Born Preterm: A Prospective Cohort Study. *J Pediatr* 2020;226: 87-95.e3.
6. Brouwer A, Groenendaal F, van Haastert I-L, Rademaker K, Hanlo P, de Vries L. Neurodevelopmental outcome of preterm infants with severe intraventricular hemorrhage and therapy for post-hemorrhagic ventricular dilatation. *J Pediatr* 2008;152:648–54.
7. Volpe JJ. Brain injury in premature infants: a complex amalgam of destructive and developmental disturbances. *Lancet Neurol* 2009;8:110–24.

8. Ming G, Song H. Adult neurogenesis in the mammalian central nervous system. *Annu Rev Neurosci* 2005;28:223–50.
9. Kriegstein A, Alvarez-Buylla A. The glial nature of embryonic and adult neural stem cells. *Annu Rev Neurosci* 2009;32:149–84.
10. Ming G-L, Song H. Adult neurogenesis in the mammalian brain: significant answers and significant questions. *Neuron* 2011;70:687–702.
11. Yeh TF, Lin YJ, Lin HC, Huang CC, Hsieh WS, Lin CH, Tsai CH. Outcomes at school age after postnatal dexamethasone therapy for lung disease of prematurity. *N Engl J Med* 2004;350:1304–13.
12. Needelman H, Evans M, Roberts H, Sweney M, Bodensteiner JB. Effects of postnatal dexamethasone exposure on the developmental outcome of premature infants. *J Child Neurol* 2008;23:421–4.
13. Augustine S, Avey MT, Harrison B, Locke T, Ghannad M, Moher D, Thébaud B. Mesenchymal Stromal Cell Therapy in Bronchopulmonary Dysplasia: Systematic Review and Meta-Analysis of Preclinical Studies. *Stem Cells Transl Med* 2017;6:2079–93.
14. Pierro M, Ionescu L, Montemurro T, Vadivel A, Weissmann G, Oudit G, Emery D, Bodiga S, Eaton F, Péault B, Mosca F, Lazzari L, Thébaud B. Short-term, long-term and paracrine effect of human umbilical cord-derived stem cells in lung injury prevention and repair in experimental bronchopulmonary dysplasia. *Thorax* 2013;68:475–484.
15. Willis GR, Fernandez-Gonzalez A, Anastas J, Vitali SH, Liu X, Ericsson M, Kwong A, Mitsialis AS, Kourembanas S. Mesenchymal Stromal Cell Exosomes Ameliorate Experimental Bronchopulmonary Dysplasia and Restore Lung Function through Macrophage Immunomodulation. *Am J Respir Crit Care Med* 2018;197:104–16.

16. Chaubey S, Thueson S, Ponnalagu D, Alam MA, Gheorghe CP, Aghai Z, Singh H, Bhandari V. Early gestational mesenchymal stem cell secretome attenuates experimental bronchopulmonary dysplasia in part via exosome-associated factor TSG-6. *Stem Cell Res Ther* 2018;9:173.
17. Porzionato A, Zaramella P, Dedja A, Guidolin D, Van Wemmel K, Macchi V, Jurga M, Perilongo G, De Carlo R, Baraldi E, Muraca M. Intratracheal administration of clinical-grade mesenchymal stem cell-derived extracellular vesicles reduces lung injury in a rat model of bronchopulmonary dysplasia. *Am J Physiol Lung Cell Mol Physiol* 2019;316:L6–19.
18. van Haaften T, Byrne R, Bonnet S, Rochefort GY, Akabutu J, Bouchentouf M, Rey-Parra GJ, Galipeau J, Haromy A, Eaton F, Chen M, Hasimoto K, Abley D, Korbutt G, Archer SL, Thébaud B. Airway delivery of mesenchymal stem cells prevents arrested alveolar growth in neonatal lung injury in rats. *Am J Respir Crit Care Med* 2009;180:1131–42.
19. Strueby L, O'Reilly M, Möbius M.A., Eaton F, Fung M, Suen C, Collins JJP, Thébaud B. Protective Effect of Human Umbilical Cord Mesenchymal Stromal Cell-Derived Exosomes on Multifactorial Lung Injury in Neonatal Mice [abstract]. *Am J Respir Crit Care Med* 2016; 193:A3840.
20. Bland RD, Mokres LM, Ertsey R, Jacobson BE, Jiang S, Rabinovitch M, Xu L, Shinwell ES, Zhang F, Beasley MA. Mechanical ventilation with 40% oxygen reduces pulmonary expression of genes that regulate lung development and impairs alveolar septation in newborn mice. *Am J Physiol Lung Cell Mol Physiol* 2007;293:L1099-1110.
21. Zhu Y, Xu L, Collins JJP, Vadivel A, Cyr-Depauw C, Zhong S, Mense L, Möbius M.A, Thébaud B. Human Umbilical Cord Mesenchymal Stromal Cells Improve Survival and Bacterial Clearance in Neonatal Sepsis in Rats. *Stem Cells Dev* 2017;26:1054–64.

22. Ferrer E, Dunmore BJ, Hassan D, Ormiston ML, Moore S, Deighton J, Long L, Yang XD, Stewart DJ, Morrell NW. A Potential Role for Exosomal Translationally Controlled Tumor Protein Export in Vascular Remodeling in Pulmonary Arterial Hypertension. *Am J Respir Cell Mol Biol* 2018;59:467–78.
23. Lytvyn Y, Xiao F, Kennedy CRJ, Perkins BA, Reich HN, Scholey JW, Cherney DZ, Burger D. Assessment of urinary microparticles in normotensive patients with type 1 diabetes. *Diabetologia* 2017;60:581–4.
24. Vadivel A, van Haaften T, Alphonse RS, Rey-Parra G-J, Ionescu L, Haromy A, Eaton F, Michelakis E, Thébaud B. Critical role of the axonal guidance cue EphrinB2 in lung growth, angiogenesis, and repair. *Am J Respir Crit Care Med* 2012;185:564–74.
25. Fujitani M, Cancino GI, Dugani CB, Weaver ICG, Gauthier-Fisher A, Paquin A, Mak TW, Wojtowicz MJ, Miller FD, Kaplan DR. TAp73 acts via the bHLH Hey2 to promote long-term maintenance of neural precursors. *Curr Biol* 2010;20:2058–65.
26. Jobe AH. The new bronchopulmonary dysplasia. Curr Opin Pediatr 2011;23:167–72.
27. Reynolds BA, Weiss S. Generation of neurons and astrocytes from isolated cells of the adult mammalian central nervous system. *Science* 1992;255:1707–10.
28. O'Reilly M, Möbius MA, Vadivel A, Ionescu L, Fung M, Eaton F, Greer JJ, Thébaud B. Late Rescue Therapy with Cord-Derived Mesenchymal Stromal Cells for Established Lung Injury in Experimental Bronchopulmonary Dysplasia. *Stem Cells Dev* 2020;29:364–71.
29. Morrison TJ, Jackson MV, Cunningham EK, Kissenpfennig A, McAuley DF, O'Kane CM, Krasnodembskaya AD. Mesenchymal Stromal Cells Modulate Macrophages in Clinically Relevant Lung Injury Models by Extracellular Vesicle Mitochondrial Transfer. *Am J Respir Crit Care Med* 2017;196:1275–86.

30. Monsel A, Zhu Y, Gennai S, Hao Q, Hu S, Rouby J-J, Rosenzwajg M, Matthay MA, Lee JW. Therapeutic Effects of Human Mesenchymal Stem Cell-derived Microvesicles in Severe Pneumonia in Mice. *Am J Respir Crit Care Med* 2015;192:324–36.
31. Willms E, Johansson HJ, Mäger I, Lee Y, Blomberg KEM, Sadik M, Alaarg A, Smith ECI, Lehtiö J, El Andaloussi S, Wood MJA, Vader Pieter. Cells release subpopulations of exosomes with distinct molecular and biological properties. *Sci Rep* 2016;6:22519.
32. Berger J, Bhandari V. Animal models of bronchopulmonary dysplasia. The term mouse models. *Am J Physiol Lung Cell Mol Physiol* 2014;307:L936-947.
33. O'Reilly M, Thébaud B. Animal models of bronchopulmonary dysplasia. The term rat models. *Am J Physiol Lung Cell Mol Physiol* 2014;307:L948-958.
34. Lee C, Mitsialis SA, Aslam M, Vitali SH, Vergadi E, Konstantinou G, Sdrimas K, Fernandez-Gonzalez A, Kourembanas S. Exosomes mediate the cytoprotective action of mesenchymal stromal cells on hypoxia-induced pulmonary hypertension. *Circulation* 2012;126:2601–11.
35. Jafri A, Belkadi A, Zaidi SIA, Getsy P, Wilson CG, Martin RJ. Lung inflammation induces IL-1β expression in hypoglossal neurons in rat brainstem. *Respir Physiol Neurobiol* 2013;188:21–8.
36. Balan KV, Kc P, Mayer CA, Wilson CG, Belkadi A, Martin RJ. Intrapulmonary lipopolysaccharide exposure upregulates cytokine expression in the neonatal brainstem. *Acta Paediatr* 2012;101:466–71.
37. Raffay TM, Martin RJ. Preemie Brains Don't Like Mechanical Ventilation! *J Pediatr* 2020; 226:12-14.
38. Alvarez-Erviti L, Seow Y, Yin H, Betts C, Lakhal S, Wood MJA. Delivery of siRNA to the mouse brain by systemic injection of targeted exosomes. *Nat Biotechnol* 2011;29:341–5.

39. Tam EWY, Chau V, Ferriero DM, Barkovich AJ, Poskitt KJ, Studholme C, Fok EDY, Grunau RE, Glidden DV, Miller SP. Preterm cerebellar growth impairment after postnatal exposure to glucocorticoids. *Sci Transl Med.* 2011;3:105ra105.

Discussion

This dissertation provides strong evidence in support of our two-fold hypothesis. First, we predicted that NPC function is impaired in experimental BPD and that this impairment is associated with abnormal neurodevelopment. Second, we predicted that UC-MSC therapy could improve NPC functional outcomes. Manuscript 1 established that NPCs are functionally impaired *in vivo* and *in vitro* in a murine model of experimental BPD. Neurosphere assays with baboon-derived NPCs further confirmed this finding. This impairment was shown to be associated with motor and cognitive deficits in late adulthood. Manuscript 2 outlined the methods used for the novel neonatal baboon NPC isolation. Manuscript 3 demonstrated that UC-MSC therapy, specifically UC-MSC EVs administered intratracheally, can mitigate NPC functional impairments. Taken together, these results show that NPCs are functionally impaired in experimental BPD, that this impairment is associated with abnormal neurodevelopment, and that UC-MSC therapy can mitigate NPC functional deficits. Importantly, these manuscripts are the first to establish an association between experimental BPD and NPCs, furthering our understanding of BPD-associated abnormal neurodevelopment. Furthermore, Manuscript 3 is the first of its kind to present UC-MSC EVs as an effective therapeutic to mitigate pulmonary and neurologic adverse outcomes in a multifactorial experimental BPD model.

Preterm Infants are Born During a Vulnerable Period of Development

Unlike a term infant who is biologically equipped to continue development outside the uterus, a preterm infant does not possess the biological mechanisms usually in place to enable them to thrive in an external environment. Thus, preterm infants are born during a period of selective vulnerability (Figure 33). The biological mechanisms that preterm infants lack include antioxidant defenses[31], vascular autoregulation[32–35], and the normal developmental cues of organ systems. This

dissertation focuses on 2 organ systems—the lungs and the brain—as these are the most susceptible to preterm birth-associated morbidities due to their ongoing development during late gestational stages[72]. However, it is important to note that there are a wide variety of preterm birth-associated complications that arise in different organ systems such as, patent ductus arteriosus (a fetal vascular shunt between the lung and the heart that fails to close), necrotising enterocolitis (inflammation of the gut), and chronic kidney disease[162–164]. Although studying these complications is beyond the scope of this dissertation, future research is required to determine if and how these further complications affect one another. This dissertation demonstrates the interconnected nature of different organ systems and emphasizes the importance of considering the body as a whole system.

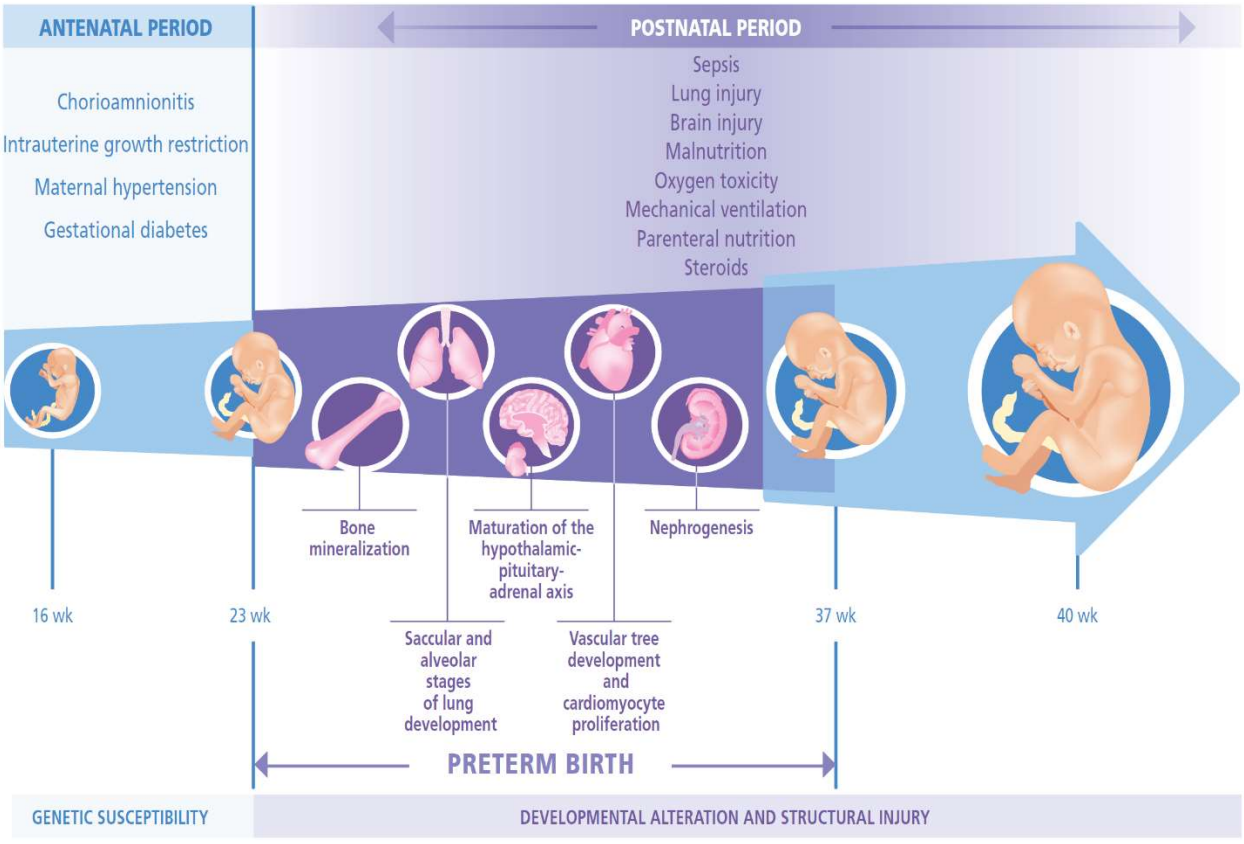

Figure 33. Preterm infants are born during a period of developmental vulnerability. Adapted from Luu et al.[165], with permission (*see* authorizations).

Sex-Related Differences of Preterm Birth Complications

Sex-related differences are an important area of investigation in research[166,167]. Many complications of preterm birth are more severe for males than for females. Male infants born prematurely have higher mortality rates compared to females[168,169]. Male sex is also an independent risk factor for BPD[168,170–172] and lung function is worse in male preterm infants[173,174]. Furthermore, preterm born males have a higher incidence of moderate-severe cerebral palsy and a greater percentage of males score <70 on the Bayley Mental Development Index and Psychomotor Development Index[175], suggesting that males have worse neurodevelopmental outcomes. Lingappan et al.[176], have also observed that male C57Black/6 mice have a more severe lung injury phenotype following 5 days of 95% oxygen exposure from P1-P5. Given these findings, we tested both male and female animals in our studies. We do not present the data as a direct comparison between the sexes, but where appropriate we displayed each data point to allow for transparency in the distribution of samples. Our data does not show distinct differences between the sexes. Moreover, we found significant differences between our control animals and experimental BPD animals with both sexes present. An interesting future research endeavour would be to increase the sample size for certain endpoints in our studies to statistically determine if males have worse outcomes in our BPD models.

Key Contributors to Alveolar Rarefication in BPD

It is not surprising that BPD, a chronic lung disease, is the most common complication of extreme prematurity[36], as the respiratory system is the first to receive the noxious stimuli of supplemental oxygen and mechanical ventilation administered to preterm patients for respiratory arrest[17,29,30]. Ante-/post-natal inflammation also play a role in the pathology of the disease[13,14]. Together, these noxious stimuli create a multifactorial lung injury. Our data demonstrates that neonatal

supplemental oxygen, mechanical ventilation, and inflammation, lead to the characteristic BPD-like phenotype of an arrest in lung development in mice. In experimental BPD, the alveoli appear much larger and fewer, even 14 months post exposure, indicating a chronic, life-long phenotype. The factors leading to an impairment in alveolarization reported in this dissertation include: i) a reduction in vessel density; ii) an increase in pro-inflammatory cytokines; iii) and an influx of immune cells (Figure 34).

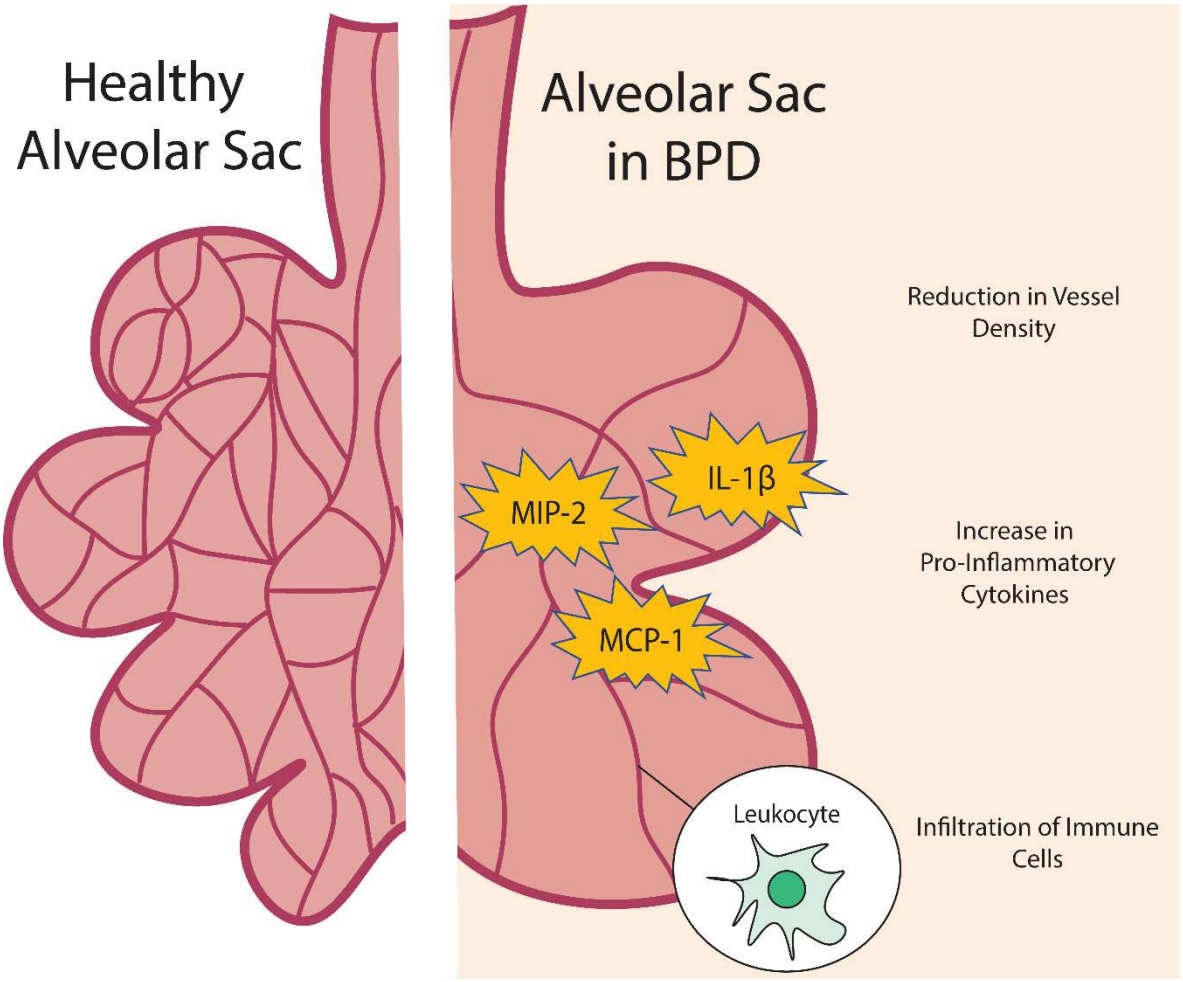

Figure 34. Multiple factors lead to the rarefication of alveoli in BPD. IL-1β, interleukin1β; MIP-2, macrophage inflammatory protein-2; MCP-1, monocyte chemoattractant protein-1.

First, vessel formation within the lung has previously been shown to be crucial for alveolar development[27]. VEGF-driven angiogenesis is disrupted in experimental BPD and this is associated with impaired alveolarization[37]. This is likely due to hyperoxia inhibiting HIF-1α activity within

the lung, leading to reduced expression of VEGF, vascular remodelling, and ultimately an arrest in alveolarization[27,177]. Second, in response to the noxious stimuli of extreme prematurity, endothelial, mesenchymal, and epithelial cells of the lung secrete pro-inflammatory cytokines[178]. These cytokines are thought to directly impact important developmental signalling pathways for alveolar formation. Sucre et al.[179], have shown in experimental BPD that IL-1β (a cytokine which we observed to be significantly increased in our BPD model), increases the expression of Wnt5 from mesenchymal cells within the lung, which in turn increases Wnt signalling in alveolar type II cells, and ultimately leads to reduced alveolar formation. Pro-inflammatory cytokines also act as mediators for immune responses and are further secreted by the third factor, immune cells[180]. Immune cells play an important role in the alveolar simplification of experimental BPD. In our ventilation-induced BPD model, we report an influx of various leukocytes, including neutrophils, monocytes, and macrophages. Kalymbetova et al.[181], demonstrated that alveolar macrophages become activated following hyperoxia exposure and directly disrupt alveolar formation. Therefore, it is clear that all three factors contribute to the arrest in lung growth in experimental BPD.

The Brain Vasculature and NPCs—Crucial Players in BPD-Associated Brain Injury

BPD is also an independent risk factor for abnormal neurodevelopment[44]. The link between this chronic lung disease and its associated abnormal neurodevelopmental outcomes was previously unclear. This dissertation demonstrates that two crucial players involved in brain development, i.e., the brain vasculature and NPCs, are functionally perturbed following neonatal hyperoxia exposure in an experimental model of BPD. In the traditional hyperoxia model of BPD, we expose mouse pups to 85% O_2 starting at P0, as this corresponds to human lung and brain development in extremely preterm infants[116,117]. Thus, our hyperoxia murine model, allows for normal development *in utero*. During murine brain development *in utero*, blood vessels grow in tandem

with neural structures[182]. The central nervous system (CNS) begins to develop as the neural plate folds to form the neural tube at E7.5[182]. The CNS starts to become vascularized between E8.5-E10 by the perineural vascular plexus (PNVP)[183]. The PNVP will cover the entire CNS without spatial or temporal cues[184]. At E11.5, an independent periventricular vascular plexus (PVP) will extend vessel growth to the cortex and the SVZ, guided by specific ventral/dorsal transcription factors expressed in vascular ECs[184]. The PNVP and PVP will continue to branch and eventually fuse, forming the cortical vascular network[184] (Figure 35). When we begin to administer hyperoxia at P0, the blood vessels of the brain continue to develop. Extensive sprouting occurs in the first postnatal month, followed by pruning[185]. We demonstrate that neonatal hyperoxia exposure disrupts this vascular growth and remodelling process. This leads to significantly reduced vessel density and branching at P14 in the cortex, which continues throughout the lifespan.

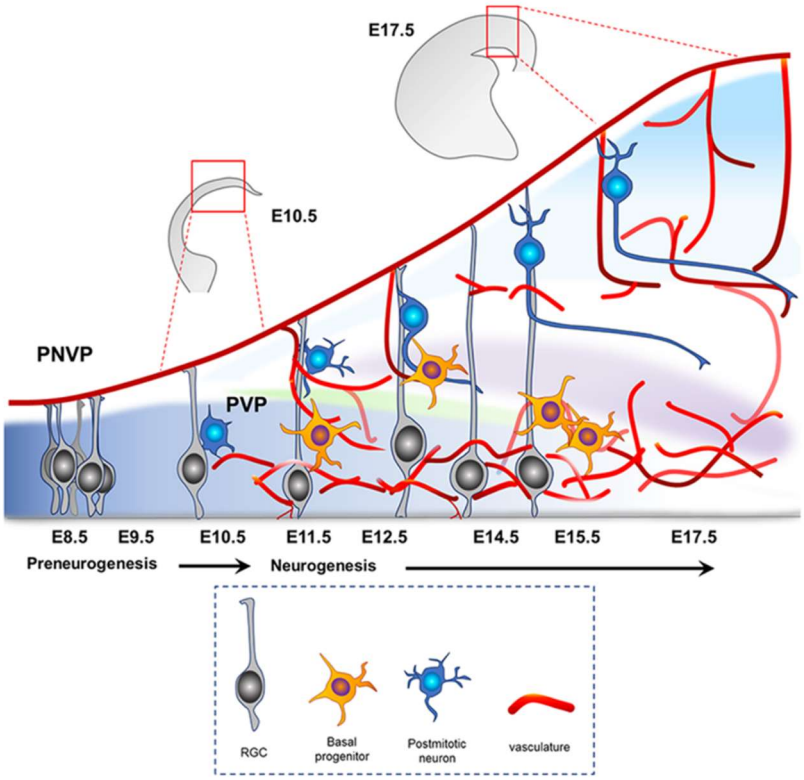

Figure 35. Vascular and neural structures develop in tandem in the embryonic brain. PNVP, perineural vascular plexus; PVP, periventricular vascular plexus; E, embryonic day; RGC, radial glial cell. Adopted from Karakatsani[186], with permission (*see* authorizations).

Importantly, as mentioned in the introduction, Licht et al.[115], have shown that vessel immaturity plays a critical role in the vulnerability of certain brain regions to injury. Specifically, the periventricular region of the brain, i.e., the SVZ, is the last to develop its vasculature and therefore, the vessels in this neurogenic niche region may be the most susceptible to noxious stimuli[115]. Furthermore, in addition to the above structural impairments, we also demonstrate hyperoxia-induced functional vascular impairments. We show that hyperoxia exposure during early development leads to neurovascular uncoupling that continues into adulthood. Damage to the structural integrity of the neurovascular unit may contribute to this impairment in neurovascular coupling in experimental BPD. Under normal physiological processes, in response to a metabolic demand for more nutrients, neurons will signal to smooth muscle cells to relax, thereby causing vasodilation of the vessels, which leads to an increase in blood flow and an increase in the availability of nutrients[187]. Chow et al.[188], have shown that arteriolar ECs act as mediators between neurons and smooth muscle cells and that an impairment in arteriolar ECs leads to neurovascular uncoupling. We show that vascular ECs ($CD31^+$) are impaired in experimental BPD, suggesting that the neurovascular unit is impaired which may contribute to deficits in neurovascular function.

There is an unequivocal relationship between blood vessels in neurogenic niche regions and NPCs[108]. Secreted factors as well as physical anchorage points between the two cell types provide important cues for NPCs to maintain their population[103–114]. We show that neonatal hyperoxia exposure greatly reduces the number of NPC anchorage points to blood vessels in the neurogenic niche. Moreover, we demonstrate that the NPC population is significantly reduced in experimental BPD, and that this striking phenotype becomes more pronounced with age. It is possible that the reduction in available anchorage points between NPC endfeet and ECs contributes

to the decline in the NPC population, although further work is required to elucidate an exact mechanism. Laminin, ephrinB2, and Jagged1 have been identified as important ligands in anchoring NPCs to ECs[103,109] and thus, future investigation could determine whether loss of these ligands plays an important role in experimental BPD. In Manuscript 1, we assessed the anchorage points between NPCs and ECs within the DG of the hippocampus. Future studies will need to characterize this neurovascular interaction within the SVZ. Zhu et al.[114], have provided important insight into this neurovascular niche. They reported that capillaries within the SVZ region expressed stromal cell-derived factor 1 (SDF1), but other vessels such as arterioles and venules did not. Proliferating NPCs were observed in closer proximity to $SDF1^{+}$ vessels, while quiescent NPCs were found closer to $SDF1^{-}$ vessels. The heterogeneity in vessels and how this affects NPC function in experimental BPD would be interesting to explore. Especially, since capillaries are more permeable than other vessels[114], and therefore, noxious stimuli, such as pro-inflammatory cytokines, may have greater access to proliferating NPCs rather than quiescent NPCs. Furthermore, Zhu et al.[114] found a reduction in the NPC population with age and interestingly, observed that older mice had an increased expression of SDF1, but decreased levels of its receptor CXCR4. This was associated with reduced NPC proliferation, as well as an increased distance between NPCs and vessels. Since we observed reduced NPCs and vessels in aging-hyperoxia-exposed animals, this would be an interesting mechanism to explore within the context of experimental BPD.

Another important finding presented in this dissertation is that isolated NPCs from hyperoxia-exposed mice show significant impairments in self-renewal capabilities 2 weeks following their removal from the neurovascular niche. This finding suggests that the self-renewal deficits are intrinsic to the NPCs themselves, rather than solely reliant on impairments in the

vascular niche. One possible explanation is that the NPCs are also functionally impaired due to an increase in intracellular ROS. Hyperoxia exposure during the neonatal period has been shown to increase ROS production in other brain cell populations[189,190]. Furthermore, ROS play an important role in the regulation of NPC fate. Increased ROS signalling activates NPC self-renewal inhibitory genes and differentiation genes[191]. Therefore, it will be important in future experiments to measure NPC ROS levels following neonatal hyperoxia exposure. This can be accomplished using ROS fluorogenic indicators, such as MitoSOX, to quantify superoxide levels[191].

Although we demonstrate a hyperoxia-induced reduction in the NPC population, future investigation will need to determine the fate of the "lost" NPCs. We show that there was a decline in newborn neuron formation in NPC niche regions in experimental BPD, thus NPCs are not differentiating along the neuronal lineage. Other fate possibilities include apoptosis, senescence, or differentiation into non-neuronal lineages of the brain. Terminal deoxynucleotidyl transferase dUTP nick end labeling (TUNEL) and β-galactosidase staining, can be used to assess apoptosis and senescence, respectively. Lineage tracing experiments using a nestin-CreERT2/R26R-yellow fluorescent protein (YFP) mouse would allow for NPCs and their progeny to be labelled throughout development and into adulthood[192]. Additionally, using single-cell RNA-sequencing to analyze cells from NPC niche regions[193] would provide a detailed characterization of NPC fate following early developmental hyperoxia exposure.

Developmental Origins of Adult Diseases

The brain takes decades to fully develop and is not considered "mature" until the mid-20s[74,75]. This means that any significant exposure to harmful factors in early life can disrupt normal patterns of brain development for decades to come. One crucial aspect of Manuscript 1 is the long-term follow-up of experimental BPD and its associated neurodevelopmental outcomes. We followed

hyperoxia-exposed mice to 12+ months of age. The data clearly demonstrates that mice did not recover from early life hyperoxia exposure simply by housing them in room air. Rather, this early life injury had pulmonary and neurological repercussions that seemed to last the lifespan of the animal. This finding strongly supports the "Barker hypothesis". This hypothesis was proposed in the 90s by Barker et al.[194] and suggests that adult diseases can be linked to poor fetal health. Originally, the work focused on fetal nutritional deficits influencing adult coronary heart disease, but the hypothesis has since been expanded to incorporate many developmental deficits influencing a number of chronic diseases including BPD and neurological pathologies such as Alzheimer's Disease[195]. Currently, there is strong evidence that pulmonary and neurological preterm birth-associated complications continue into early adulthood[68,196]. However, due to a lack of long-term follow-up of preterm-born patients into late adulthood, we do not yet have a clear understanding of outcomes throughout the lifespan.

Since it is well characterized that pulmonary and neurological function decline through the normal aging process, it is hypothesized that this decline may be accelerated in preterm-born patients. Baraldi et al.[197], have proposed a theoretical model of lung function of BPD patients in late adulthood (Figure 36), as measured by forced expiratory volume in 1 second (FEV_1). In the model, there is a wide range of FEV_1 values for BPD survivors, representing the variability in severity of the disease. However, all the FEV_1 values for BPD survivors are lower than healthy subjects at the equivalent age. Long-term follow-up studies are urgently required to determine whether this model is accurate, and if so, whether more appropriate care may need to be administered to these patients throughout life.

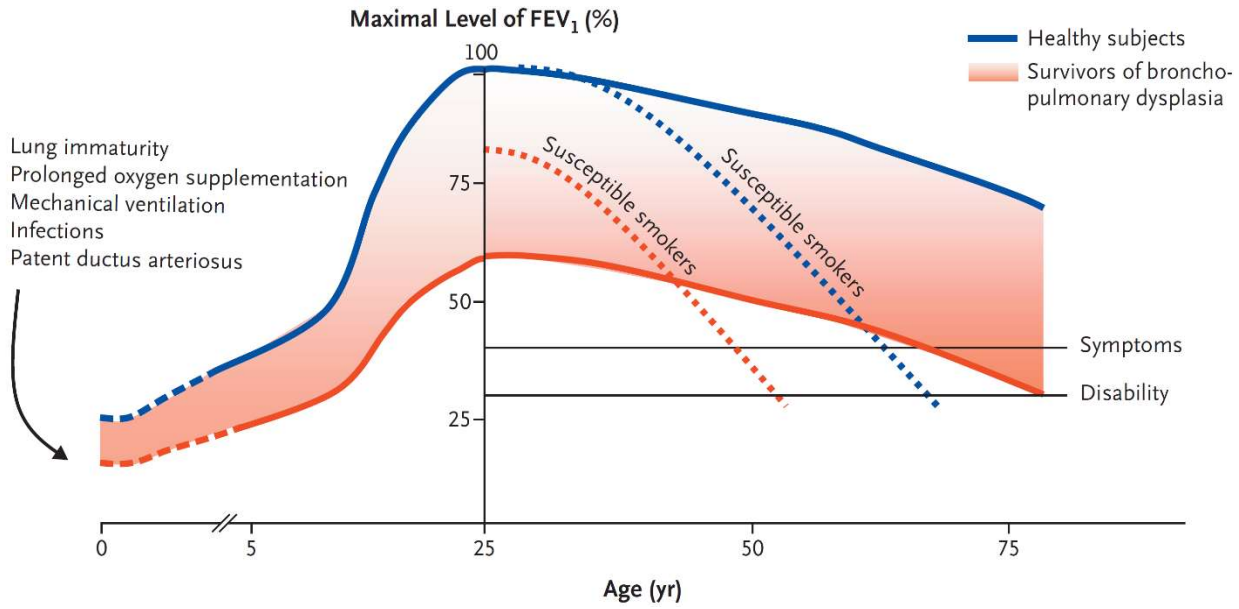

Figure 36. Theoretical model of long-term lung function of BPD survivors. FEV_1, forced expiratory volume in 1 second. Adopted from Baraldi et al.[197], with permission (*see* authorizations).

Further work is also required to determine the long-term neurological outcomes associated with preterm birth complications. In Manuscript 1, we demonstrate that with age, hyperoxia-exposed mice have a more severe decline in the NPC population, NPC anchorage points to blood vessels, neurogenesis, motor learning, and motor coordination compared to control mice. These findings suggest that with age, there may be an accelerated decline in brain function in survivors of BPD. Long-term follow-up of these patients may help detect early onset dementia or other cognitive disorders. This would allow for early intervention therapies which could greatly improve the well-being of BPD-survivors.

Curbing Developmental Origins of Adult Diseases: Strengthening the Rationale for MSC Therapy in the Clinic (With a Word of Caution)

This dissertation also presents a UC-MSC-derived therapy as a potential treatment for both pulmonary and neurological outcomes in experimental BPD. We use umbilical cord-derived MSCs, rather than other sources such as bone marrow, due to: i) ease of access (with consent) and

ii) the "young" age of the progenitor cells. To the latter point, there is evidence emerging that MSCs from younger donors demonstrate greater progenitor-like abilities, such as greater potential to differentiate into desired lineages[198] and a greater ability to regenerate damaged tissue[199].

Our lab and others, have previously demonstrated that MSCs aid in lung regeneration in experimental BPD via a paracrine effect[125,142,200]. Further work in the MSC field by Bruno et al.[201], and Lai et al.[202], determined that the primary therapeutic component of the MSC secretome are EVs. In Manuscript 3, we demonstrated that EVs derived from UC-MSCs can improve lung architecture and vessel density in a multifactorial BPD model. These improvements were associated with an increase in anti-inflammatory cytokine expression within the lung. Willis et al.[159] have also demonstrated that UC-MSC-derived EVs can reduce pro-inflammatory cytokine expression in a hyperoxia-induced murine model of BPD. This data supports further studies[157,158] which demonstrate that MSC-derived EVs exert therapeutic effects by modulating inflammation. As with cell therapy[147], the presence of EVs may stimulate an innate immune response. This can create a microenvironment that is more accommodating for resident progenitor cells to repair injured tissue.

Manuscript 3 touched upon why it was preferable to use MSC-derived EVs rather than MSCs. One reason was that EVs provided a more standardized "dose" that can be administered to patients. However, this could be a disadvantage. Using MSCs, rather than a pre-set "dose" would allow for the cells to sense their microenvironment and modulate their secretome to meet the requirements of the tissue. This could be particularly important in a multifactorial disease such as BPD. The severity and the duration of supplemental oxygen, mechanical ventilation, and ante-/post-natal infections will vary from infant to infant. Thus, having a biological therapeutic that can adapt to its environment could prove to be the most effective way to mitigate BPD-related

complications among a heterogeneous patient population. Currently, this is speculative, and further research is required to determine which MSC therapy is more effective at mitigating the complications of preterm birth.

It is also important to address the controversy surrounding the use of MSCs. The term "MSC" was first introduced by Dr. Arnold Caplan in the 1990s[203] as an abbreviation for "mesenchymal stem cell". MSCs were considered stem cells because they could be expanded and differentiate into multiple lineages *in vitro*. However, due to their limited differentiation abilities *in vivo*[204], it is now apparent that this is no longer an appropriate term for these cells. The International Society for Cellular Therapy (ISCT) has since issued a statement, declaring that the standard terminology for these cells should be "mesenchymal stromal cell"[148], which is used in this dissertation. The ISCT also described basic criteria for a cell to be defined as an MSC, as mentioned in the introduction of this dissertation. Unfortunately, the term "mesenchymal stem cell" continues to be abundantly used in the field, leading many people to believe that these cells will differentiate into any tissue they are delivered to, which is simply not the case[205]. Furthermore, the basic criteria used to characterize MSCs is not useful to the therapeutic applications these cells are used for. For example, one set of criteria is that MSCs must be able to differentiate along the adipogenic, chondrogenic, and osteogenic lineages[148]. Whether or not MSCs can differentiate into fat, cartilage, or bone has no relevance on their ability to repair the arrest in alveolar and vascular development within the lung in BPD. Due to the vague definition, "MSC" is used as an all-encompassing term for cells with progenitor-like abilities from mesenchymal tissue[206]. This has led to a misrepresentation of the capabilities of these cells and has created considerably more "hype" than "hope"[205]. Furthermore, systematic reviews of MSC treatment for lung injuries have revealed that there has been poor reporting of methodologies used in studies, in terms of MSC

characterization, method of randomization, and blinding[152,207]. It is therefore the responsibility of all researchers working with "MSCs" to properly characterize the cells, to not overstate their reparative abilities, and to be transparent when reporting data.

Scientific Rigour

It is important to note the steps taken to uphold scientific rigour in the studies described in this dissertation. First, there were quality control measures taken. Some examples include ensuring that time-sensitive reagents were used within their expiration date, using fresh media when conducting cell culture experiments, and calibrating equipment before use. Second, there was validation of key resources. Rather than using cell lines, primary cells were used in our studies. We therefore carefully controlled the cell environment and validated each cell type using recognized international standards in respective fields. Third, when appropriate, investigators were blinded to experimental groups to remove bias and this is explicitly stated in the studies. Fourth, all statistical analyses were described, and non-significant results were reported alongside significant results to allow for transparency of data.

Limitations and Future Directions—Understanding Mechanisms of Action of BPD-Associated Brain Injury and MSC Therapeutic Effects

There are several limitations with the studies described in this dissertation. First, mouse models were used to mimic BPD. Although several considerations were made to replicate the clinical conditions associated with preterm birth, murine models cannot fully replicate human diseases. Given this limitation, a non-human primate model of prematurity was incorporated in Manuscripts 1 and 2. To further strengthen the findings in the dissertation, future work could utilize the baboon model of BPD[133] to assess the *in vivo* NPC population following treatment with UC-MSCs or UC-MSC-derived EVs. Second, the dose of UC-MSC EVs for murine BPD treatment studies is likely

not appropriate for humans. Again, utilization of the baboon model of BPD to investigate dose responses could be an important future step. Third, future work will need to determine precise molecular mechanisms of BPD-associated NPC functional impairment. The work in this dissertation provides an important first step in describing the NPC functional impairments in experimental BPD and makes a crucial association to abnormal neurobehavior. There was variability in outcomes between NPCs from the SVZ and NPCs from the DG. Further work can investigate how and why the NPC populations are affected differently in experimental BPD. Moreover, an outstanding question that arises from this dissertation is, are the neurological impairments in experimental BPD caused by a direct effect from the noxious stimuli or are they a secondary effect due to the lung injury? It is likely that both factors play a part in abnormal neurodevelopment in experimental BPD and this could be explored in future research. Fourth and lastly, this dissertation does not provide a molecular mechanism to explain the beneficial effects of UC-MSC therapy on the lungs and the brain. Future studies will need to identify which factors within UC-MSC EVs exert the therapeutic benefit. A main goal of this dissertation was to determine whether UC-MSC therapy could provide benefits to both organs, and if so, to describe these benefits. This dissertation was successful in meeting this goal and therefore, provides a strong rationale for the translation of UC-MSC therapy to the clinic.

Conclusion

This dissertation seeks to address critical gaps in our knowledge surrounding BPD-related injury and recovery. Previously, it was unclear whether oxygen therapy administered to extremely preterm infants perturbs the NPC population, thus contributing to abnormal neurodevelopment. We are the first to demonstrate that neonatal mice exposed to hyperoxia have impairments in NPC self-renewal, neurogenesis, and vascular remodelling. Furthermore, we show that NPC functional impairment is associated with abnormal learning and memory in aging mice. Additionally, no safe treatment exists which can prevent abnormal neurodevelopmental outcomes in this vulnerable neonatal patient population. The protective/reparative capabilities of UC-MSCs as a therapy for neonatal lung injury was previously demonstrated in rodent models. We have now shown that UC-MSC therapy improves lung structural and vascular impairments, increases anti-inflammatory cytokine expression in the lungs, and promotes NPC self-renewal. Taken together, our data identifies a novel mechanism of neonatal brain injury, with far-reaching effects into adulthood and highlights a potential therapy, as well as new targets for treatment.

References

1. Lawn, J. E. & Kinney, M. Preterm birth: now the leading cause of child death worldwide. *Sci Transl Med* **6**, 263ed21 (2014).
2. Peacock, J. L., Bland, J. M. & Anderson, H. R. Preterm delivery: effects of socioeconomic factors, psychological stress, smoking, alcohol, and caffeine. *BMJ* **311**, 531–535 (1995).
3. Kyrklund-Blomberg, N. B. & Cnattingius, S. Preterm birth and maternal smoking: risks related to gestational age and onset of delivery. *Am. J. Obstet. Gynecol.* **179**, 1051–1055 (1998).
4. Windham, G. C., Hopkins, B., Fenster, L. & Swan, S. H. Prenatal active or passive tobacco smoke exposure and the risk of preterm delivery or low birth weight. *Epidemiology* **11**, 427–433 (2000).
5. O'Leary, C. M., Nassar, N., Kurinczuk, J. J. & Bower, C. The effect of maternal alcohol consumption on fetal growth and preterm birth. *BJOG* **116**, 390–400 (2009).
6. Patra, J. *et al.* Dose-response relationship between alcohol consumption before and during pregnancy and the risks of low birthweight, preterm birth and small for gestational age (SGA)-a systematic review and meta-analyses. *BJOG* **118**, 1411–1421 (2011).
7. Hayatbakhsh, M. R. *et al.* Birth outcomes associated with cannabis use before and during pregnancy. *Pediatr. Res.* **71**, 215–219 (2012).
8. Gouin, K., Murphy, K., Shah, P. S., & Knowledge Synthesis group on Determinants of Low Birth Weight and Preterm Births. Effects of cocaine use during pregnancy on low birthweight and preterm birth: systematic review and metaanalyses. *Am. J. Obstet. Gynecol.* **204**, 340.e1–12 (2011).

9. Galinsky, R., Polglase, G. R., Hooper, S. B., Black, M. J. & Moss, T. J. M. The consequences of chorioamnionitis: preterm birth and effects on development. *J Pregnancy* **2013**, 412831 (2013).

10. Powers, W. F. & Kiely, J. L. The risks confronting twins: a national perspective. *Am. J. Obstet. Gynecol.* **170**, 456–461 (1994).

11. Martin, J. A. & Park, M. M. Trends in twin and triplet births: 1980-97. *Natl Vital Stat Rep* **47**, 1–16 (1999).

12. Public Health Agency of Canada. Perinatal Health Indicator for Canada 2017. (2017).

13. Stoll, B. J. *et al.* Trends in Care Practices, Morbidity, and Mortality of Extremely Preterm Neonates, 1993-2012. *JAMA* **314**, 1039–1051 (2015).

14. Goldenberg, R. L., Culhane, J. F., Iams, J. D. & Romero, R. Epidemiology and causes of preterm birth. *Lancet* **371**, 75–84 (2008).

15. Goldenberg, R. L., Hauth, J. C. & Andrews, W. W. Intrauterine infection and preterm delivery. *N. Engl. J. Med.* **342**, 1500–1507 (2000).

16. Lamont, R. F. & Sawant, S. R. Infection in the prediction and antibiotics in the prevention of spontaneous preterm labour and preterm birth. *Minerva Ginecol* **57**, 423–433 (2005).

17. Laughon, M. *et al.* Patterns of respiratory disease during the first 2 postnatal weeks in extremely premature infants. *Pediatrics* **123**, 1124–1131 (2009).

18. Whitsett, J. A., Wert, S. E. & Trapnell, B. C. Genetic disorders influencing lung formation and function at birth. *Hum. Mol. Genet.* **13 Spec No 2**, R207-215 (2004).

19. Burri, P. H. Structural aspects of postnatal lung development - alveolar formation and growth. *Biol. Neonate* **89**, 313–322 (2006).

20. Warburton, D. *et al.* Lung organogenesis. *Curr. Top. Dev. Biol.* **90**, 73–158 (2010).

21. Schittny, J. C. Development of the lung. *Cell Tissue Res.* **367**, 427–444 (2017).

22. Thébaud, B. *et al.* Bronchopulmonary dysplasia. *Nat Rev Dis Primers* **5**, 78 (2019).

23. Ward, H. E. & Nicholas, T. E. Alveolar type I and type II cells. *Aust N Z J Med* **14**, 731–734 (1984).

24. Fehrenbach, H. Alveolar epithelial type II cell: defender of the alveolus revisited. *Respir. Res.* **2**, 33–46 (2001).

25. Whitsett, J. A. & Alenghat, T. Respiratory epithelial cells orchestrate pulmonary innate immunity. *Nat. Immunol.* **16**, 27–35 (2015).

26. Hall, S. M., Hislop, A. A., Pierce, C. M. & Haworth, S. G. Prenatal origins of human intrapulmonary arteries: formation and smooth muscle maturation. *Am. J. Respir. Cell Mol. Biol.* **23**, 194–203 (2000).

27. Thébaud, B. *et al.* Vascular endothelial growth factor gene therapy increases survival, promotes lung angiogenesis, and prevents alveolar damage in hyperoxia-induced lung injury: evidence that angiogenesis participates in alveolarization. *Circulation* **112**, 2477–2486 (2005).

28. Iliodromiti, Z. *et al.* Acute lung injury in preterm fetuses and neonates: mechanisms and molecular pathways. *J. Matern. Fetal. Neonatal. Med.* **26**, 1696–1704 (2013).

29. Donn, S. M. & Sinha, S. K. Minimising ventilator induced lung injury in preterm infants. *Arch. Dis. Child. Fetal Neonatal Ed.* **91**, F226-230 (2006).

30. Martherus, T. *et al.* Comparison of Two Respiratory Support Strategies for Stabilization of Very Preterm Infants at Birth: A Matched-Pairs Analysis. *Front Pediatr* **7**, 3 (2019).

31. Gitto, E., Pellegrino, S., D'Arrigo, S., Barberi, I. & Reiter, R. J. Oxidative stress in resuscitation and in ventilation of newborns. *Eur. Respir. J.* **34**, 1461–1469 (2009).

32. Milligan, D. W. Failure of autoregulation and intraventricular haemorrhage in preterm infants. *Lancet* **1**, 896–898 (1980).

33. Pryds, O., Greisen, G., Lou, H. & Friis-Hansen, B. Heterogeneity of cerebral vasoreactivity in preterm infants supported by mechanical ventilation. *J. Pediatr.* **115**, 638–645 (1989).

34. Perlman, J. M., Goodman, S., Kreusser, K. L. & Volpe, J. J. Reduction in intraventricular hemorrhage by elimination of fluctuating cerebral blood-flow velocity in preterm infants with respiratory distress syndrome. *N. Engl. J. Med.* **312**, 1353–1357 (1985).

35. Hoffman, S. B., Cheng, Y.-J., Magder, L. S., Shet, N. & Viscardi, R. M. Cerebral autoregulation in premature infants during the first 96 hours of life and relationship to adverse outcomes. *Arch. Dis. Child. Fetal Neonatal Ed.* **104**, F473–F479 (2019).

36. Jobe, A. H. & Bancalari, E. Bronchopulmonary dysplasia. *Am. J. Respir. Crit. Care Med.* **163**, 1723–1729 (2001).

37. Thébaud, B. & Abman, S. H. Bronchopulmonary dysplasia: where have all the vessels gone? Roles of angiogenic growth factors in chronic lung disease. *Am. J. Respir. Crit. Care Med.* **175**, 978–985 (2007).

38. Northway, W. H., Rosan, R. C. & Porter, D. Y. Pulmonary disease following respirator therapy of hyaline-membrane disease. Bronchopulmonary dysplasia. *N. Engl. J. Med.* **276**, 357–368 (1967).

39. Husain, A. N., Siddiqui, N. H. & Stocker, J. T. Pathology of arrested acinar development in postsurfactant bronchopulmonary dysplasia. *Hum. Pathol.* **29**, 710–717 (1998).

40. Jobe, A. H. The new bronchopulmonary dysplasia. *Curr. Opin. Pediatr.* **23**, 167–172 (2011).

41. Bhatt, A. J. *et al.* Disrupted pulmonary vasculature and decreased vascular endothelial growth factor, Flt-1, and TIE-2 in human infants dying with bronchopulmonary dysplasia. *Am. J. Respir. Crit. Care Med.* **164**, 1971–1980 (2001).

42. Lassus, P., Ristimäki, A., Ylikorkala, O., Viinikka, L. & Andersson, S. Vascular endothelial growth factor in human preterm lung. *Am. J. Respir. Crit. Care Med.* **159**, 1429–1433 (1999).

43. Lassus, P. *et al.* Pulmonary vascular endothelial growth factor and Flt-1 in fetuses, in acute and chronic lung disease, and in persistent pulmonary hypertension of the newborn. *Am. J. Respir. Crit. Care Med.* **164**, 1981–1987 (2001).

44. Vohr, B. R., Wright, L. L., Poole, W. K. & McDonald, S. A. Neurodevelopmental outcomes of extremely low birth weight infants <32 weeks' gestation between 1993 and 1998. *Pediatrics* **116**, 635–643 (2005).

45. Marret, S. *et al.* Brain injury in very preterm children and neurosensory and cognitive disabilities during childhood: the EPIPAGE cohort study. *PLoS ONE* **8**, e62683 (2013).

46. Roberts, G., Anderson, P. J., De Luca, C., Doyle, L. W., & Victorian Infant Collaborative Study Group. Changes in neurodevelopmental outcome at age eight in geographic cohorts of children born at 22-27 weeks' gestational age during the 1990s. *Arch. Dis. Child. Fetal Neonatal Ed.* **95**, F90-94 (2010).

47. Moore, T. *et al.* Neurological and Developmental Outcome in Extremely Preterm Children Born in England in 1995 and 2006: The EPICure Studies. *Obstetrical & Gynecological Survey* **68**, 274–275 (2013).

48. Serenius, F. *et al.* Neurodevelopmental outcome in extremely preterm infants at 2.5 years after active perinatal care in Sweden. *JAMA* **309**, 1810–1820 (2013).

49. Wood, N. S., Marlow, N., Costeloe, K., Gibson, A. T. & Wilkinson, A. R. Neurologic and developmental disability after extremely preterm birth. EPICure Study Group. *N. Engl. J. Med.* **343**, 378–384 (2000).

50. Ishii, N. *et al.* Outcomes of infants born at 22 and 23 weeks' gestation. *Pediatrics* **132**, 62–71 (2013).

51. Hagmann-von Arx, P. *et al.* Gait in Very Preterm School-Aged Children in Dual-Task Paradigms. *PLoS ONE* **10**, e0144363 (2015).

52. Church, C. *et al.* Longitudinal change in foot posture in children with cerebral palsy. *J Child Orthop* **11**, 229–236 (2017).

53. Hirvonen, M. *et al.* Visual and Hearing Impairments After Preterm Birth. *Pediatrics* **142**, (2018).

54. Volpe, J. J. Brain injury in premature infants: a complex amalgam of destructive and developmental disturbances. *Lancet Neurol* **8**, 110–124 (2009).

55. Omizzolo, C. *et al.* Neonatal brain abnormalities and memory and learning outcomes at 7 years in children born very preterm. *Memory* **22**, 605–615 (2014).

56. Sriram, S. *et al.* Cognitive Development and Quality of Life Associated With BPD in 10-Year-Olds Born Preterm. *Pediatrics* **141**, (2018).

57. Gough, A. *et al.* Executive functioning deficits in young adult survivors of bronchopulmonary dysplasia. *Disabil Rehabil* **37**, 1940–1945 (2015).

58. Short, E. J. *et al.* Cognitive and academic consequences of bronchopulmonary dysplasia and very low birth weight: 8-year-old outcomes. *Pediatrics* **112**, e359 (2003).

59. Robertson, C. M., Etches, P. C., Goldson, E. & Kyle, J. M. Eight-year school performance, neurodevelopmental, and growth outcome of neonates with bronchopulmonary dysplasia: a comparative study. *Pediatrics* **89**, 365–372 (1992).

60. Singer, L., Yamashita, T., Lilien, L., Collin, M. & Baley, J. A longitudinal study of developmental outcome of infants with bronchopulmonary dysplasia and very low birth weight. *Pediatrics* **100**, 987–993 (1997).

61. Filippone, M., Sartor, M., Zacchello, F. & Baraldi, E. Flow limitation in infants with bronchopulmonary dysplasia and respiratory function at school age. *Lancet* **361**, 753–754 (2003).

62. Fawke, J. *et al.* Lung function and respiratory symptoms at 11 years in children born extremely preterm: the EPICure study. *Am. J. Respir. Crit. Care Med.* **182**, 237–245 (2010).

63. Vollsæter, M., Røksund, O. D., Eide, G. E., Markestad, T. & Halvorsen, T. Lung function after preterm birth: development from mid-childhood to adulthood. *Thorax* **68**, 767–776 (2013).

64. Landry, J. S., Chan, T., Lands, L. & Menzies, D. Long-term impact of bronchopulmonary dysplasia on pulmonary function. *Can. Respir. J.* **18**, 265–270 (2011).

65. Doyle, L. W. *et al.* Bronchopulmonary dysplasia in very low birth weight subjects and lung function in late adolescence. *Pediatrics* **118**, 108–113 (2006).

66. Northway, W. H. *et al.* Late pulmonary sequelae of bronchopulmonary dysplasia. *N. Engl. J. Med.* **323**, 1793–1799 (1990).

67. Gough, A. *et al.* Impaired lung function and health status in adult survivors of bronchopulmonary dysplasia. *Eur. Respir. J.* **43**, 808–816 (2014).

68. Vrijlandt, E. J. L. E., Gerritsen, J., Boezen, H. M., Grevink, R. G. & Duiverman, E. J. Lung function and exercise capacity in young adults born prematurely. *Am. J. Respir. Crit. Care Med.* **173**, 890–896 (2006).

69. Lovering, A. T. *et al.* Ventilatory and sensory responses in adult survivors of preterm birth and bronchopulmonary dysplasia with reduced exercise capacity. *Ann Am Thorac Soc* **11**, 1528–1537 (2014).

70. Hack, M. Adult outcomes of preterm children. *J Dev Behav Pediatr* **30**, 460–470 (2009).

71. Doyle, L. W. & Anderson, P. J. Adult outcome of extremely preterm infants. *Pediatrics* **126**, 342–351 (2010).

72. Saigal, S. & Doyle, L. W. An overview of mortality and sequelae of preterm birth from infancy to adulthood. *Lancet* **371**, 261–269 (2008).

73. Linsell, L. *et al.* Cognitive trajectories from infancy to early adulthood following birth before 26 weeks of gestation: a prospective, population-based cohort study. *Arch. Dis. Child.* **103**, 363–370 (2018).

74. Johnson, S. B., Blum, R. W. & Giedd, J. N. Adolescent maturity and the brain: the promise and pitfalls of neuroscience research in adolescent health policy. *J Adolesc Health* **45**, 216–221 (2009).

75. Pujol, J., Vendrell, P., Junqué, C., Martí-Vilalta, J. L. & Capdevila, A. When does human brain development end? Evidence of corpus callosum growth up to adulthood. *Ann. Neurol.* **34**, 71–75 (1993).

76. Harada, C. N., Natelson Love, M. C. & Triebel, K. L. Normal cognitive aging. *Clin. Geriatr. Med.* **29**, 737–752 (2013).

77. Park, D. C. & Reuter-Lorenz, P. The adaptive brain: aging and neurocognitive scaffolding. *Annu Rev Psychol* **60**, 173–196 (2009).

78. Brouwer, A. *et al.* Neurodevelopmental outcome of preterm infants with severe intraventricular hemorrhage and therapy for post-hemorrhagic ventricular dilatation. *J. Pediatr.* **152**, 648–654 (2008).

79. Cheong, J. L. Y. *et al.* Abnormal white matter signal on MR imaging is related to abnormal tissue microstructure. *AJNR Am J Neuroradiol* **30**, 623–628 (2009).

80. Volpe, J. J. The encephalopathy of prematurity--brain injury and impaired brain development inextricably intertwined. *Semin Pediatr Neurol* **16**, 167–178 (2009).

81. Reich, B., Hoeber, D., Bendix, I. & Felderhoff-Mueser, U. Hyperoxia and the Immature Brain. *Dev. Neurosci.* **38**, 311–330 (2016).

82. Ming, G. & Song, H. Adult neurogenesis in the mammalian central nervous system. *Annu. Rev. Neurosci.* **28**, 223–250 (2005).

83. Kriegstein, A. & Alvarez-Buylla, A. The glial nature of embryonic and adult neural stem cells. *Annu. Rev. Neurosci.* **32**, 149–184 (2009).

84. Moreno-Jiménez, E. P. *et al.* Adult hippocampal neurogenesis is abundant in neurologically healthy subjects and drops sharply in patients with Alzheimer's disease. *Nat. Med.* **25**, 554–560 (2019).

85. Bond, A. M., Ming, G.-L. & Song, H. Adult Mammalian Neural Stem Cells and Neurogenesis: Five Decades Later. *Cell Stem Cell* **17**, 385–395 (2015).

86. Martínez-Cerdeño, V. & Noctor, S. C. Neural Progenitor Cell Terminology. *Front Neuroanat* **12**, 104 (2018).

87. Vescovi, A. L., Galli, R. & Reynolds, B. A. Brain tumour stem cells. *Nat. Rev. Cancer* **6**, 425–436 (2006).

88. Kempermann, G. & Gage, F. H. New nerve cells for the adult brain. *Sci. Am.* **280**, 48–53 (1999).

89. Gage, F. H. Mammalian neural stem cells. *Science* **287**, 1433–1438 (2000).

90. Ming, G.-L. & Song, H. Adult neurogenesis in the mammalian brain: significant answers and significant questions. *Neuron* **70**, 687–702 (2011).

91. Lazarini, F. & Lledo, P.-M. Is adult neurogenesis essential for olfaction? *Trends Neurosci.* **34**, 20–30 (2011).

92. Lledo, P.-M., Alonso, M. & Grubb, M. S. Adult neurogenesis and functional plasticity in neuronal circuits. *Nat. Rev. Neurosci.* **7**, 179–193 (2006).

93. Lois, C. & Alvarez-Buylla, A. Long-distance neuronal migration in the adult mammalian brain. *Science* **264**, 1145–1148 (1994).

94. Jankovski, A. & Sotelo, C. Subventricular zone-olfactory bulb migratory pathway in the adult mouse: cellular composition and specificity as determined by heterochronic and heterotopic transplantation. *J. Comp. Neurol.* **371**, 376–396 (1996).

95. Zhao, C., Teng, E. M., Summers, R. G., Ming, G.-L. & Gage, F. H. Distinct morphological stages of dentate granule neuron maturation in the adult mouse hippocampus. *J. Neurosci.* **26**, 3–11 (2006).

96. Toni, N. *et al.* Neurons born in the adult dentate gyrus form functional synapses with target cells. *Nat. Neurosci.* **11**, 901–907 (2008).

97. Faulkner, R. L. *et al.* Development of hippocampal mossy fiber synaptic outputs by new neurons in the adult brain. *Proc. Natl. Acad. Sci. U.S.A.* **105**, 14157–14162 (2008).

98. Deng, W., Aimone, J. B. & Gage, F. H. New neurons and new memories: how does adult hippocampal neurogenesis affect learning and memory? *Nat. Rev. Neurosci.* **11**, 339–350 (2010).

99. Kee, N., Teixeira, C. M., Wang, A. H. & Frankland, P. W. Preferential incorporation of adult-generated granule cells into spatial memory networks in the dentate gyrus. *Nat. Neurosci.* **10**, 355–362 (2007).

100. Garthe, A., Behr, J. & Kempermann, G. Adult-generated hippocampal neurons allow the flexible use of spatially precise learning strategies. *PLoS ONE* **4**, e5464 (2009).

101. Saxe, M. D. *et al.* Ablation of hippocampal neurogenesis impairs contextual fear conditioning and synaptic plasticity in the dentate gyrus. *Proc. Natl. Acad. Sci. U.S.A.* **103**, 17501–17506 (2006).

102. Rafii, S., Butler, J. M. & Ding, B.-S. Angiocrine functions of organ-specific endothelial cells. *Nature* **529**, 316–325 (2016).

103. Shen, Q. *et al.* Adult SVZ stem cells lie in a vascular niche: a quantitative analysis of niche cell-cell interactions. *Cell Stem Cell* **3**, 289–300 (2008).

104. Tavazoie, M. *et al.* A specialized vascular niche for adult neural stem cells. *Cell Stem Cell* **3**, 279–288 (2008).

105. Culver, J. C., Vadakkan, T. J. & Dickinson, M. E. A specialized microvascular domain in the mouse neural stem cell niche. *PLoS ONE* **8**, e53546 (2013).

106. Sun, G. J. *et al.* Tangential migration of neuronal precursors of glutamatergic neurons in the adult mammalian brain. *Proc. Natl. Acad. Sci. U.S.A.* **112**, 9484–9489 (2015).

107. Palmer, T. D., Willhoite, A. R. & Gage, F. H. Vascular niche for adult hippocampal neurogenesis. *J. Comp. Neurol.* **425**, 479–494 (2000).

108. Goldman, S. A. & Chen, Z. Perivascular instruction of cell genesis and fate in the adult brain. *Nat. Neurosci.* **14**, 1382–1389 (2011).

109. Ottone, C. *et al.* Direct cell-cell contact with the vascular niche maintains quiescent neural stem cells. *Nat. Cell Biol.* **16**, 1045–1056 (2014).

110. Shen, Q. *et al.* Endothelial cells stimulate self-renewal and expand neurogenesis of neural stem cells. *Science* **304**, 1338–1340 (2004).

111. Ramírez-Castillejo, C. *et al.* Pigment epithelium-derived factor is a niche signal for neural stem cell renewal. *Nat Neurosci* **9**, 331–339 (2006).

112. Andreu-Agulló, C., Morante-Redolat, J. M., Delgado, A. C. & Fariñas, I. Vascular niche factor PEDF modulates Notch-dependent stemness in the adult subependymal zone. *Nat Neurosci* **12**, 1514–1523 (2009).

113. Crouch, E. E., Liu, C., Silva-Vargas, V. & Doetsch, F. Regional and stage-specific effects of prospectively purified vascular cells on the adult V-SVZ neural stem cell lineage. *J Neurosci* **35**, 4528–4539 (2015).

114. Zhu, C., Mahesula, S., Temple, S. & Kokovay, E. Heterogeneous Expression of SDF1 Retains Actively Proliferating Neural Progenitors in the Capillary Compartment of the Niche. *Stem Cell Reports* **12**, 6–13 (2019).

115. Licht, T., Dor-Wollman, T., Ben-Zvi, A., Rothe, G. & Keshet, E. Vessel maturation schedule determines vulnerability to neuronal injuries of prematurity. *J. Clin. Invest.* **125**, 1319–1328 (2015).

116. Berger, J. & Bhandari, V. Animal models of bronchopulmonary dysplasia. The term mouse models. *Am. J. Physiol. Lung Cell Mol. Physiol.* **307**, L936-947 (2014).

117. Semple, B. D., Blomgren, K., Gimlin, K., Ferriero, D. M. & Noble-Haeusslein, L. J. Brain development in rodents and humans: Identifying benchmarks of maturation and vulnerability to injury across species. *Prog. Neurobiol.* **106–107**, 1–16 (2013).

118. Bonikos, D. S., Bensch, K. G., Ludwin, S. K. & Northway, W. H. Oxygen toxicity in the newborn. The effect of prolonged 100 per cent O2 exposure on the lungs of newborn mice. *Lab. Invest.* **32**, 619–635 (1975).

119. Bonikos, D. S., Bensch, K. G. & Northway, W. H. Oxygen toxicity in the newborn. The effect of chronic continuous 100 percent oxygen exposure on the lungs of newborn mice. *Am. J. Pathol.* **85**, 623–650 (1976).

120. Warner, B. B., Stuart, L. A., Papes, R. A. & Wispé, J. R. Functional and pathological effects of prolonged hyperoxia in neonatal mice. *Am. J. Physiol.* **275**, L110-117 (1998).

121. Yee, M. *et al.* Neonatal oxygen adversely affects lung function in adult mice without altering surfactant composition or activity. *Am. J. Physiol. Lung Cell Mol. Physiol.* **297**, L641-649 (2009).

122. Rogers, L. K., Tipple, T. E., Nelin, L. D. & Welty, S. E. Differential responses in the lungs of newborn mouse pups exposed to 85% or >95% oxygen. *Pediatr. Res.* **65**, 33–38 (2009).

123. Park, M. S. *et al.* Altered expressions of fibroblast growth factor receptors and alveolarization in neonatal mice exposed to 85% oxygen. *Pediatr. Res.* **62**, 652–657 (2007).

124. Yee, M. *et al.* Neonatal hyperoxia causes pulmonary vascular disease and shortens life span in aging mice. *Am. J. Pathol.* **178**, 2601–2610 (2011).

125. Aslam, M. *et al.* Bone marrow stromal cells attenuate lung injury in a murine model of neonatal chronic lung disease. *Am. J. Respir. Crit. Care Med.* **180**, 1122–1130 (2009).

126. Schmitz, T. *et al.* Cellular changes underlying hyperoxia-induced delay of white matter development. *J. Neurosci.* **31**, 4327–4344 (2011).

127. Hilgendorff, A., Reiss, I., Ehrhardt, H., Eickelberg, O. & Alvira, C. M. Chronic lung disease in the preterm infant. Lessons learned from animal models. *Am. J. Respir. Cell Mol. Biol.* **50**, 233–245 (2014).

128. Bland, R. D. *et al.* Mechanical ventilation with 40% oxygen reduces pulmonary expression of genes that regulate lung development and impairs alveolar septation in newborn mice. *Am. J. Physiol. Lung Cell Mol. Physiol.* **293**, L1099-1110 (2007).

129. Velten, M., Heyob, K. M., Rogers, L. K. & Welty, S. E. Deficits in lung alveolarization and function after systemic maternal inflammation and neonatal hyperoxia exposure. *J. Appl. Physiol.* **108**, 1347–1356 (2010).

130. Letsiou, E. *et al.* Differential and opposing effects of imatinib on LPS- and ventilator-induced lung injury. *Am. J. Physiol. Lung Cell Mol. Physiol.* **308**, L259-269 (2015).

131. Jobe, A. H. Animal Models, Learning Lessons to Prevent and Treat Neonatal Chronic Lung Disease. *Front Med (Lausanne)* **2**, 49 (2015).

132. Yoder, B. A. & Coalson, J. J. Animal models of bronchopulmonary dysplasia. The preterm baboon models. *Am. J. Physiol. Lung Cell Mol. Physiol.* **307**, L970-977 (2014).

133. Seidner, S. R., Jobe, A. H., Coalson, J. J. & Ikegami, M. Abnormal surfactant metabolism and function in preterm ventilated baboons. *Am. J. Respir. Crit. Care Med.* **158**, 1982–1989 (1998).

134. Coalson, J. J., Winter, V. T., Siler-Khodr, T. & Yoder, B. A. Neonatal chronic lung disease in extremely immature baboons. *Am. J. Respir. Crit. Care Med.* **160**, 1333–1346 (1999).

135. Inder, T., Neil, J., Yoder, B. & Rees, S. Non-human primate models of neonatal brain injury. *Semin. Perinatol.* **28**, 396–404 (2004).

136. Chi, J. G., Dooling, E. C. & Gilles, F. H. Gyral development of the human brain. *Ann. Neurol.* **1**, 86–93 (1977).

137. Marin-Padilla, M. Prenatal and early postnatal ontogenesis of the human motor cortex: a golgi study. I. The sequential development of the cortical layers. *Brain Res.* **23**, 167–183 (1970).

138. Rees, S. M. *et al.* Cerebellar development in a baboon model of preterm delivery: impact of specific ventilatory regimes. *J Neuropathol Exp Neurol* **68**, 605–615 (2009).

139. Inder, T., Neil, J., Yoder, B. & Rees, S. Patterns of cerebral injury in a primate model of preterm birth and neonatal intensive care. *J. Child Neurol.* **20**, 965–967 (2005).

140. Cox, L. A. *et al.* Baboons as a model to study genetics and epigenetics of human disease. *ILAR J* **54**, 106–121 (2013).

141. Oh, J. Y. *et al.* Intravenous mesenchymal stem cells prevented rejection of allogeneic corneal transplants by aborting the early inflammatory response. *Mol. Ther.* **20**, 2143–2152 (2012).

142. Pierro, M. *et al.* Short-term, long-term and paracrine effect of human umbilical cord-derived stem cells in lung injury prevention and repair in experimental bronchopulmonary dysplasia. *Thorax* **68**, 475–484 (2013).

143. Prockop, D. J. & Oh, J. Y. Mesenchymal stem/stromal cells (MSCs): role as guardians of inflammation. *Mol. Ther.* **20**, 14–20 (2012).

144. Valle-Prieto, A. & Conget, P. A. Human mesenchymal stem cells efficiently manage oxidative stress. *Stem Cells Dev.* **19**, 1885–1893 (2010).

145. Meirelles, L. da S., Fontes, A. M., Covas, D. T. & Caplan, A. I. Mechanisms involved in the therapeutic properties of mesenchymal stem cells. *Cytokine Growth Factor Rev.* **20**, 419–427 (2009).

146. Koh, S.-H. *et al.* Implantation of human umbilical cord-derived mesenchymal stem cells as a neuroprotective therapy for ischemic stroke in rats. *Brain Res.* **1229**, 233–248 (2008).

147. Vagnozzi, R. J. *et al.* An acute immune response underlies the benefit of cardiac stem cell therapy. *Nature* **577**, 405–409 (2020).

148. Dominici, M. *et al.* Minimal criteria for defining multipotent mesenchymal stromal cells. The International Society for Cellular Therapy position statement. *Cytotherapy* **8**, 315–317 (2006).

149. Sacchetti, B. *et al.* No Identical 'Mesenchymal Stem Cells' at Different Times and Sites: Human Committed Progenitors of Distinct Origin and Differentiation Potential Are Incorporated as Adventitial Cells in Microvessels. *Stem Cell Reports* **6**, 897–913 (2016).

150. Galipeau, J. & Sensébé, L. Mesenchymal Stromal Cells: Clinical Challenges and Therapeutic Opportunities. *Cell Stem Cell* **22**, 824–833 (2018).

151. O'Reilly, M. *et al.* Late Rescue Therapy with Cord-Derived Mesenchymal Stromal Cells for Established Lung Injury in Experimental Bronchopulmonary Dysplasia. *Stem Cells Dev* **29**, 364–371 (2020).

152. Augustine, S. *et al.* Mesenchymal Stromal Cell Therapy in Bronchopulmonary Dysplasia: Systematic Review and Meta-Analysis of Preclinical Studies. *Stem Cells Transl Med* **6**, 2079–2093 (2017).

153. Matei, A. C., Antounians, L. & Zani, A. Extracellular Vesicles as a Potential Therapy for Neonatal Conditions: State of the Art and Challenges in Clinical Translation. *Pharmaceutics* **11**, (2019).

154. van Niel, G., D'Angelo, G. & Raposo, G. Shedding light on the cell biology of extracellular vesicles. *Nat. Rev. Mol. Cell Biol.* **19**, 213–228 (2018).

155. Raposo, G. & Stoorvogel, W. Extracellular vesicles: exosomes, microvesicles, and friends. *J. Cell Biol.* **200**, 373–383 (2013).

156. Cruz, F. F. *et al.* Systemic Administration of Human Bone Marrow-Derived Mesenchymal Stromal Cell Extracellular Vesicles Ameliorates Aspergillus Hyphal Extract-Induced Allergic Airway Inflammation in Immunocompetent Mice. *Stem Cells Transl Med* **4**, 1302–1316 (2015).

157. Monsel, A. *et al.* Therapeutic Effects of Human Mesenchymal Stem Cell-derived Microvesicles in Severe Pneumonia in Mice. *Am. J. Respir. Crit. Care Med.* **192**, 324–336 (2015).

158. Morrison, T. J. *et al.* Mesenchymal Stromal Cells Modulate Macrophages in Clinically Relevant Lung Injury Models by Extracellular Vesicle Mitochondrial Transfer. *Am. J. Respir. Crit. Care Med.* **196**, 1275–1286 (2017).

159. Willis, G. R. *et al.* Mesenchymal Stromal Cell Exosomes Ameliorate Experimental Bronchopulmonary Dysplasia and Restore Lung Function through Macrophage Immunomodulation. *Am. J. Respir. Crit. Care Med.* **197**, 104–116 (2018).

160. Alvarez-Erviti, L. *et al.* Delivery of siRNA to the mouse brain by systemic injection of targeted exosomes. *Nat. Biotechnol.* **29**, 341–345 (2011).

161. Kaminski, N. *et al.* Mesenchymal Stromal Cell-Derived Extracellular Vesicles Reduce Neuroinflammation, Promote Neural Cell Proliferation and Improve Oligodendrocyte Maturation in Neonatal Hypoxic-Ischemic Brain Injury. *Frontiers in Cellular Neuroscience* **14**, (2020).

162. Crump, C., Sundquist, J., Winkleby, M. A. & Sundquist, K. Preterm birth and risk of chronic kidney disease from childhood into mid-adulthood: national cohort study. *BMJ* **365**, l1346 (2019).

163. Ward, R. M. & Beachy, J. C. Neonatal complications following preterm birth. *BJOG* **110 Suppl 20**, 8–16 (2003).

164. Hamrick, S. E. G. & Hansmann, G. Patent ductus arteriosus of the preterm infant. *Pediatrics* **125**, 1020–1030 (2010).

165. Luu, T. M., Katz, S. L., Leeson, P., Thébaud, B. & Nuyt, A.-M. Preterm birth: risk factor for early-onset chronic diseases. *CMAJ* **188**, 736–746 (2016).

166. Granger, M. W. *et al.* A TgCRND8 Mouse Model of Alzheimer's Disease Exhibits Sexual Dimorphisms in Behavioral Indices of Cognitive Reserve. *J Alzheimers Dis* **51**, 757–773 (2016).

167. Shansky, R. M. & Woolley, C. S. Considering Sex as a Biological Variable Will Be Valuable for Neuroscience Research. *J Neurosci* **36**, 11817–11822 (2016).

168. Costeloe, K., Hennessy, E., Gibson, A. T., Marlow, N. & Wilkinson, A. R. The EPICure study: outcomes to discharge from hospital for infants born at the threshold of viability. *Pediatrics* **106**, 659–671 (2000).

169. Stevenson, D. K. *et al.* Sex differences in outcomes of very low birthweight infants: the newborn male disadvantage. *Arch Dis Child Fetal Neonatal Ed* **83**, F182-185 (2000).

170. Trembath, A. & Laughon, M. M. Predictors of bronchopulmonary dysplasia. *Clin Perinatol* **39**, 585–601 (2012).

171. Zysman-Colman, Z., Tremblay, G. M., Bandeali, S. & Landry, J. S. Bronchopulmonary dysplasia - trends over three decades. *Paediatr Child Health* **18**, 86–90 (2013).

172. Binet, M.-E. *et al.* Role of gender in morbidity and mortality of extremely premature neonates. *Am J Perinatol* **29**, 159–166 (2012).

173. Thomas, M. R. *et al.* Respiratory function of very prematurely born infants at follow up: influence of sex. *Arch Dis Child Fetal Neonatal Ed* **91**, F197-201 (2006).

174. Stocks, J., Henschen, M., Hoo, A. F., Costeloe, K. & Dezateux, C. Influence of ethnicity and gender on airway function in preterm infants. *Am J Respir Crit Care Med* **156**, 1855–1862 (1997).

175. Hintz, S. R. *et al.* Gender differences in neurodevelopmental outcomes among extremely preterm, extremely-low-birthweight infants. *Acta Paediatr* **95**, 1239–1248 (2006).

176. Lingappan, K., Jiang, W., Wang, L. & Moorthy, B. Sex-specific differences in neonatal hyperoxic lung injury. *Am J Physiol Lung Cell Mol Physiol* **311**, L481-493 (2016).

177. Vadivel, A. *et al.* Hypoxia-inducible factors promote alveolar development and regeneration. *Am J Respir Cell Mol Biol* **50**, 96–105 (2014).

178. Speer, C. P. Pulmonary inflammation and bronchopulmonary dysplasia. *J Perinatol* **26 Suppl 1**, S57-62; discussion S63-64 (2006).

179. Sucre, J. M. S. *et al.* Hyperoxia Injury in the Developing Lung Is Mediated by Mesenchymal Expression of Wnt5A. *Am J Respir Crit Care Med* **201**, 1249–1262 (2020).

180. Thompson, A. & Bhandari, V. Pulmonary Biomarkers of Bronchopulmonary Dysplasia. *Biomark Insights* **3**, 361–373 (2008).

181. Kalymbetova, T. V. *et al.* Resident alveolar macrophages are master regulators of arrested alveolarization in experimental bronchopulmonary dysplasia. *J Pathol* **245**, 153–159 (2018).

182. Paredes, I., Himmels, P. & Ruiz de Almodóvar, C. Neurovascular Communication during CNS Development. *Dev Cell* **45**, 10–32 (2018).

183. Hogan, K. A., Ambler, C. A., Chapman, D. L. & Bautch, V. L. The neural tube patterns vessels developmentally using the VEGF signaling pathway. *Development* **131**, 1503–1513 (2004).

184. Vasudevan, A., Long, J. E., Crandall, J. E., Rubenstein, J. L. R. & Bhide, P. G. Compartment-specific transcription factors orchestrate angiogenesis gradients in the embryonic brain. *Nat Neurosci* **11**, 429–439 (2008).

185. Harb, R., Whiteus, C., Freitas, C. & Grutzendler, J. In vivo imaging of cerebral microvascular plasticity from birth to death. *J Cereb Blood Flow Metab* **33**, 146–156 (2013).

186. Karakatsani, A., Shah, B. & Ruiz de Almodovar, C. Blood Vessels as Regulators of Neural Stem Cell Properties. *Front Mol Neurosci* **12**, 85 (2019).

187. Iadecola, C. The Neurovascular Unit Coming of Age: A Journey through Neurovascular Coupling in Health and Disease. *Neuron* **96**, 17–42 (2017).

188. Chow, B. W. *et al.* Caveolae in CNS arterioles mediate neurovascular coupling. *Nature* (2020) doi:10.1038/s41586-020-2026-1.

189. Gerstner, B. *et al.* Hyperoxia causes maturation-dependent cell death in the developing white matter. *J. Neurosci.* **28**, 1236–1245 (2008).

190. Kwak, D. J., Kwak, S. D. & Gauda, E. B. The effect of hyperoxia on reactive oxygen species (ROS) in rat petrosal ganglion neurons during development using organotypic slices. *Pediatr Res* **60**, 371–376 (2006).

191. Khacho, M. *et al.* Mitochondrial Dynamics Impacts Stem Cell Identity and Fate Decisions by Regulating a Nuclear Transcriptional Program. *Cell Stem Cell* **19**, 232–247 (2016).

192. Lagace, D. C. *et al.* Dynamic contribution of nestin-expressing stem cells to adult neurogenesis. *J Neurosci* **27**, 12623–12629 (2007).

193. Shin, J. *et al.* Single-Cell RNA-Seq with Waterfall Reveals Molecular Cascades underlying Adult Neurogenesis. *Cell Stem Cell* **17**, 360–372 (2015).

194. Barker, D. J. & Martyn, C. N. The maternal and fetal origins of cardiovascular disease. *J Epidemiol Community Health* **46**, 8–11 (1992).

195. Calkins, K. & Devaskar, S. U. Fetal origins of adult disease. *Curr Probl Pediatr Adolesc Health Care* **41**, 158–176 (2011).

196. O'Reilly, H., Johnson, S., Ni, Y., Wolke, D. & Marlow, N. Neuropsychological Outcomes at 19 Years of Age Following Extremely Preterm Birth. *Pediatrics* **145**, (2020).

197. Baraldi, E. & Filippone, M. Chronic lung disease after premature birth. *N. Engl. J. Med.* **357**, 1946–1955 (2007).

198. Ramkisoensing, A. A. *et al.* Human embryonic and fetal mesenchymal stem cells differentiate toward three different cardiac lineages in contrast to their adult counterparts. *PLoS One* **6**, e24164 (2011).

199. Khong, S. M. L. *et al.* Single-Cell Transcriptomics of Human Mesenchymal Stem Cells Reveal Age-Related Cellular Subpopulation Depletion and Impaired Regenerative Function. *Stem Cells* **37**, 240–246 (2019).

200. van Haaften, T. *et al.* Airway delivery of mesenchymal stem cells prevents arrested alveolar growth in neonatal lung injury in rats. *Am. J. Respir. Crit. Care Med.* **180**, 1131–1142 (2009).

201. Bruno, S. *et al.* Mesenchymal stem cell-derived microvesicles protect against acute tubular injury. *J Am Soc Nephrol* **20**, 1053–1067 (2009).

202. Lai, R. C. *et al.* Exosome secreted by MSC reduces myocardial ischemia/reperfusion injury. *Stem Cell Res* **4**, 214–222 (2010).

203. Caplan, A. I. Mesenchymal stem cells. *J Orthop Res* **9**, 641–650 (1991).

204. Keating, A. Mesenchymal stromal cells. *Curr Opin Hematol* **13**, 419–425 (2006).

205. Sipp, D., Robey, P. G. & Turner, L. Clear up this stem-cell mess. *Nature* **561**, 455–457 (2018).

206. Caplan, A. I. Mesenchymal Stem Cells: Time to Change the Name! *Stem Cells Transl Med* **6**, 1445–1451 (2017).

207. McIntyre, L. A. *et al.* Efficacy of Mesenchymal Stromal Cell Therapy for Acute Lung Injury in Preclinical Animal Models: A Systematic Review. *PLoS One* **11**, e0147170 (2016).

Appendices

Appendix A – Supplemental Information for Manuscript 1

Neonatal hyperoxia in mice impairs cerebrovascular function, neurogenesis, and behaviour into adulthood

Marissa A. Lithopoulos, Xavier Toussay, Shumei Zhong, Liqun Xu, Shamimunisa B. Mustafa, Cesar H. Comin, Hayam A. Bassam, Adam N. Baker, Alvaro Moreira, Cynthia Blanco, Arul Vadivel, Catherine Tsilfidis, Steven Seidner, Ruth Slack, Diane Lagace, Jing Wang, Baptiste Lacoste, Bernard Thébaud

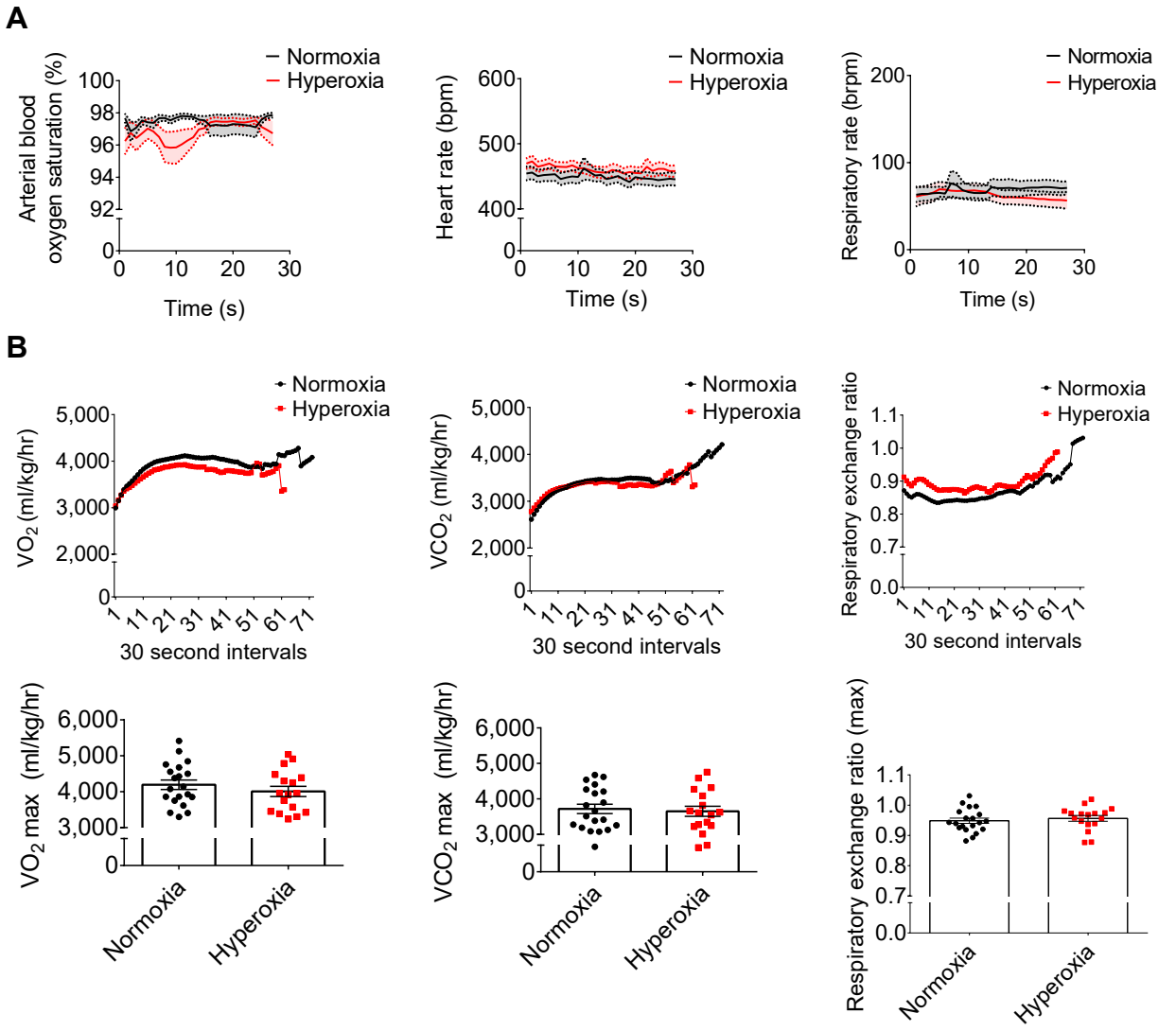

Supplemental Figure 1. Early life hyperoxia does not influence arterial oxygen saturation, oxygen consumption, or carbon dioxide production in adulthood. (**A**) Three outcome measures were assessed for 12-14-month-old mice at rest. From left to right: blood oxygen saturation of the femoral artery; heart rate (beats per minute, bpm); and respiratory rate (breaths per minute, brpm) (normoxia, n=20; hyperoxia, n=17; two-way ANOVA with Sidak post hoc test for group comparisons). (**B**) Volume of oxygen consumption, volume of carbon dioxide release, and the respiratory exchange ratio (VCO_2 / VO_2) for the total duration of metabolic treadmill testing (top) and at maximum capacity (bottom) (normoxia, n=20; hyperoxia, n=17; two-way ANOVA with Sidak post hoc test for multiple comparisons and unpaired Student's t test, respectively). Mice were tested at 12-14 months of age. Data are expressed as mean ± SEM.

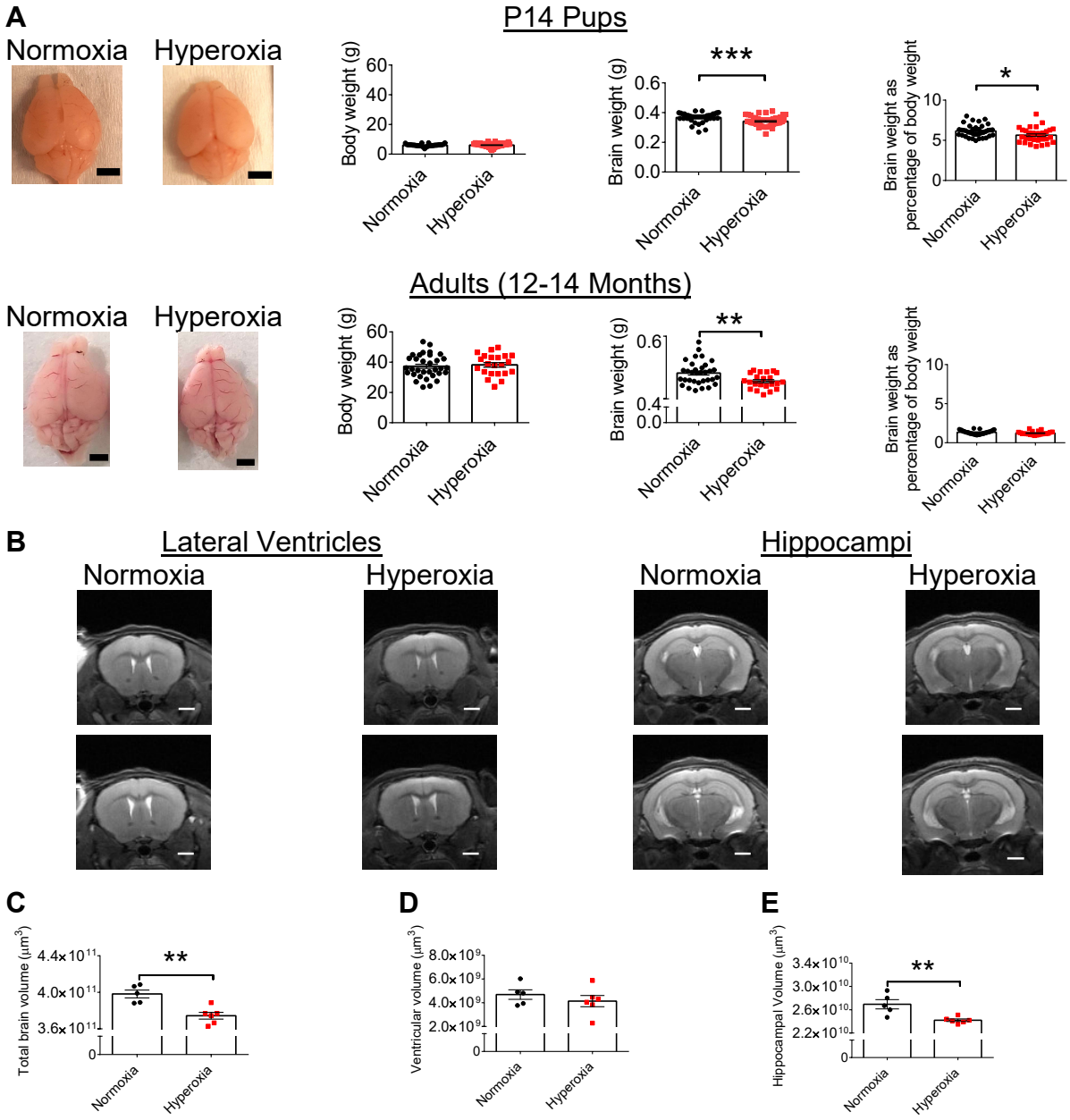

Supplemental Figure 2. Delayed brain growth after early developmental hyperoxia exposure. (**A**) Representative images (left) of brains from normoxia and hyperoxia-exposed mice at P14 and 12 months, scale bar, 3mm. Body weight (g), brain weight (g), and brain weight as a percentage of body weight (right) for P14 (top, normoxia, n= 38, hyperoxia, n=48) and adult mice (bottom, normoxia, n=33, hyperoxia, n=22); *$P < 0.05$, **$P < 0.01$, ***$P < 0.001$; unpaired Student's t test. (**B**) Representative MRI images of the ventricular (left) and hippocampal (right) regions of a normoxia and hyperoxia-exposed mouse. Scale bar, 1500 µm. (**C**) Quantification of the total brain volume (normoxia, n=5; hyperoxia, n=6; **$P < 0.01$; unpaired Student's t test). (**D**) Quantification of the volume of the lateral ventricles (normoxia, n=5; hyperoxia, n=6; unpaired Student's t test). (**E**) Quantification of the volume of the hippocampal regions (normoxia, n=5; hyperoxia, n=6; **$P < 0.01$; unpaired Student's t test). Data are expressed as mean ± SEM.

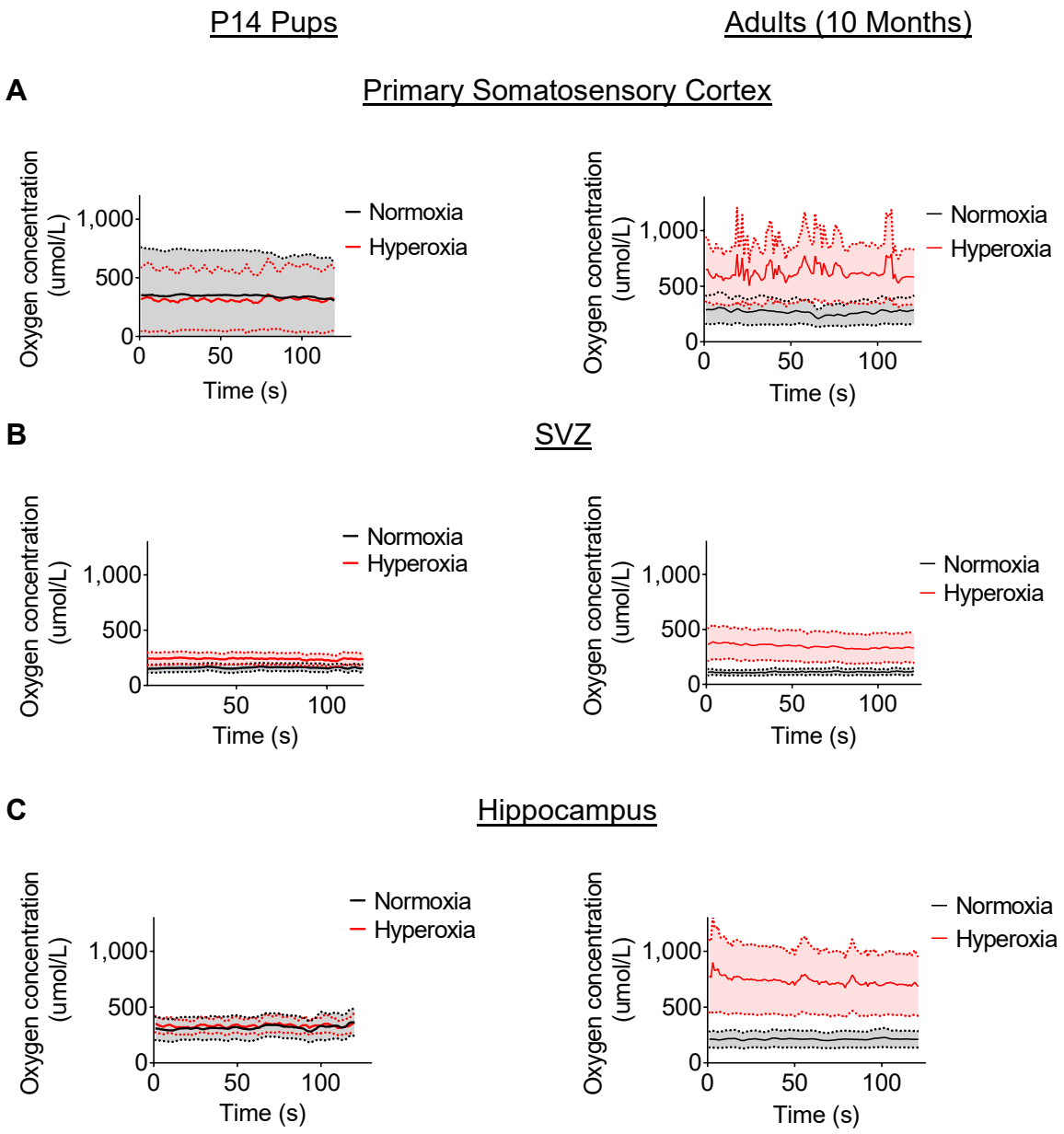

Supplemental Figure 3. Brain regions of hyperoxia-exposed mice show trend of becoming progressively hyperoxic during aging. (**A**) Oxygen concentration (µmol/L) of the primary somatosensory cortex in live P14 (left) and 10-month-old (right) mice (P14, normoxia, n=8; hyperoxia, n=9; 10-month-old, normoxia, n=12; hyperoxia, n=11). Two-way ANOVA with Sidak post hoc test for multiple comparisons. (**B**) Oxygen concentration (µmol/L) of the subventricular zone (SVZ) region in live P14 (left) and 10-month-old (right) mice (P14, normoxia, n=6; hyperoxia, n=9; 10-month-old, normoxia, n=10; hyperoxia, n=11). Two-way ANOVA with Sidak post hoc test for multiple comparisons. (**C**) Oxygen concentration (µmol/L) of the hippocampal region in live P14 (left) and 10-month-old (right) mice (P14, normoxia, n=9; hyperoxia, n=8; 10-month-old, normoxia, n=11; hyperoxia, n=10). Two-way ANOVA with Sidak post hoc test for multiple comparisons. Data are expressed as mean ± SEM.

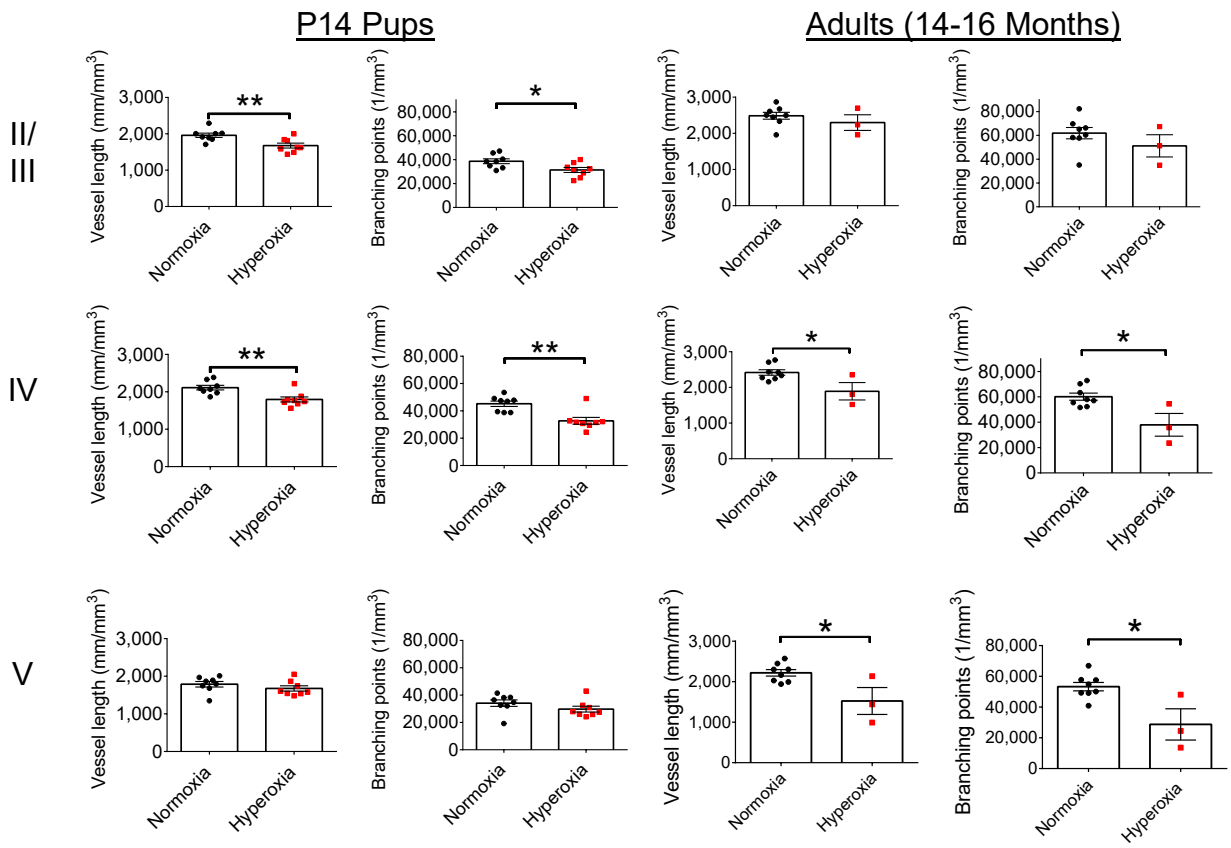

Supplemental Figure 4. Vascular remodelling in multiple neocortical layers after early life hyperoxia exposure. Vessel length and number of branching points in neocortical layers II/III, IV, and V for P14 and 14-16-month-old mice (P14 mice, normoxia, n=8, hyperoxia, n=8; adult mice, normoxia, n=8, hyperoxia, n=3; $*P < 0.05$, $**P < 0.01$; unpaired Student's t test). Data are expressed as mean ± SEM.

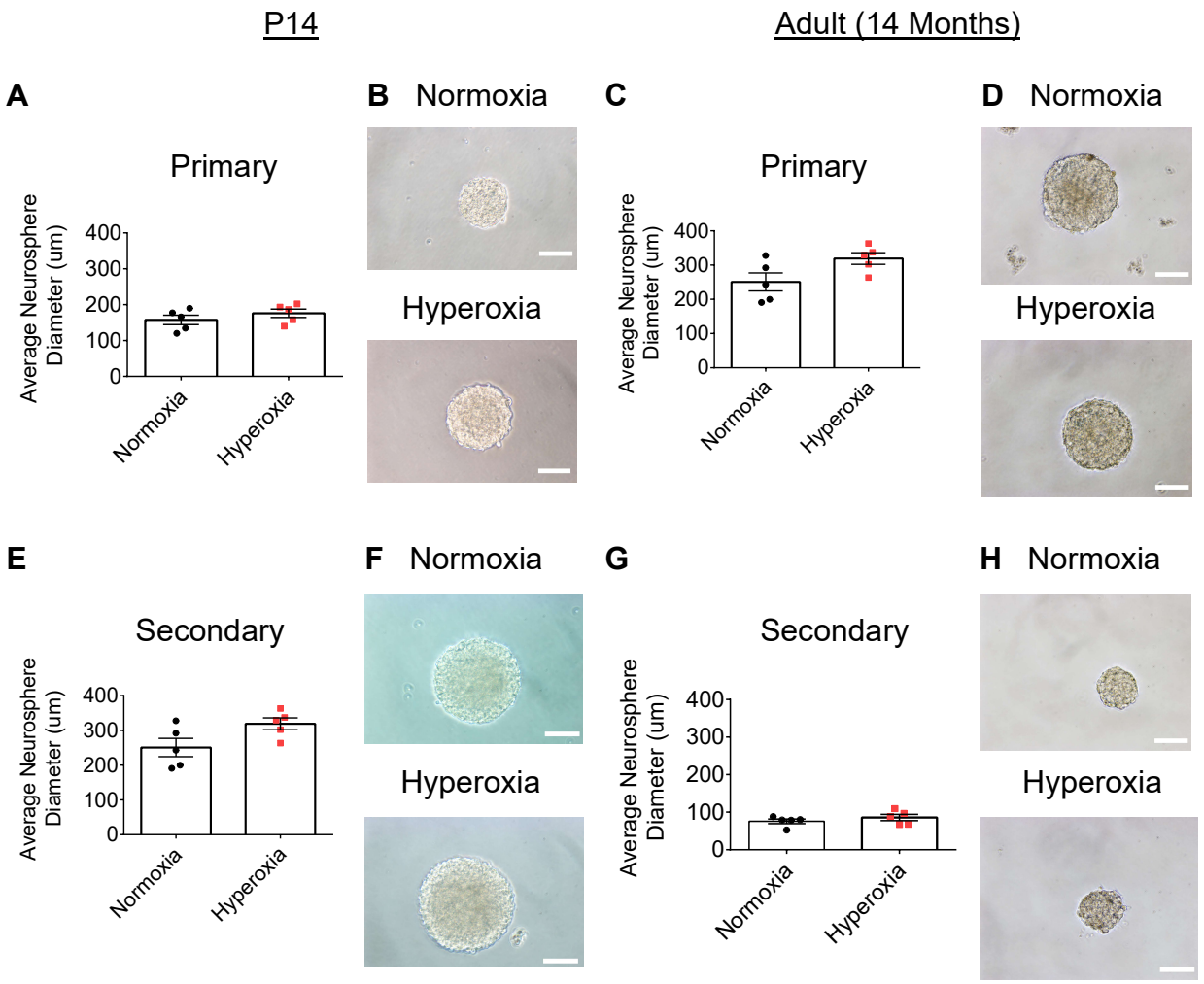

Supplemental Figure 5. NPCs from mice exposed to hyperoxia form neurospheres of similar size compared to those from normoxia mice. (**A** and **B**) Quantification (A) and representative images (B) of the average primary neurosphere diameter formed by NPCs from P14 mice. (**C** and **D**) Quantification (C) and representative images (D) of the average primary neurosphere diameter formed by NPCs from 14-month-old mice. (**E** and **F**) Quantification (E) and representative images (F) of the average secondary neurosphere diameter formed by NPCs from P14 mice. (**G** and **H**) Quantification (G) and representative images (H) of the average secondary neurosphere diameter formed by NPCs from 14-month-old mice. Normoxia, n=5; hyperoxia, n=5; unpaired Student's t test. Data are expressed as mean ± SEM. Scale bar, 100 µm.

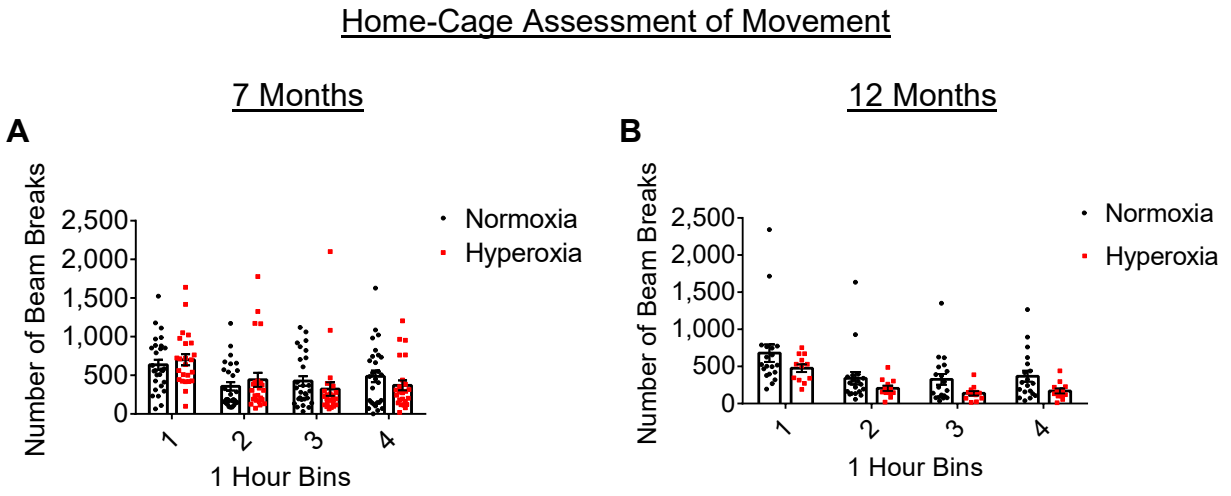

Supplemental Figure 6. Hyperoxia-exposed mice show a trend of less movement at 12 months of age compared to normoxia exposed mice. (**A** and **B**) Distance travelled (cm) during the home-cage assessment of movement for 7-month-old mice (A, normoxia, n=28; hyperoxia, n=24) and 12-month-old mice (B, normoxia, n=19; hyperoxia, n=12). Two-way ANOVA with Sidak post hoc test for group comparisons. Data are expressed as mean ± SEM.

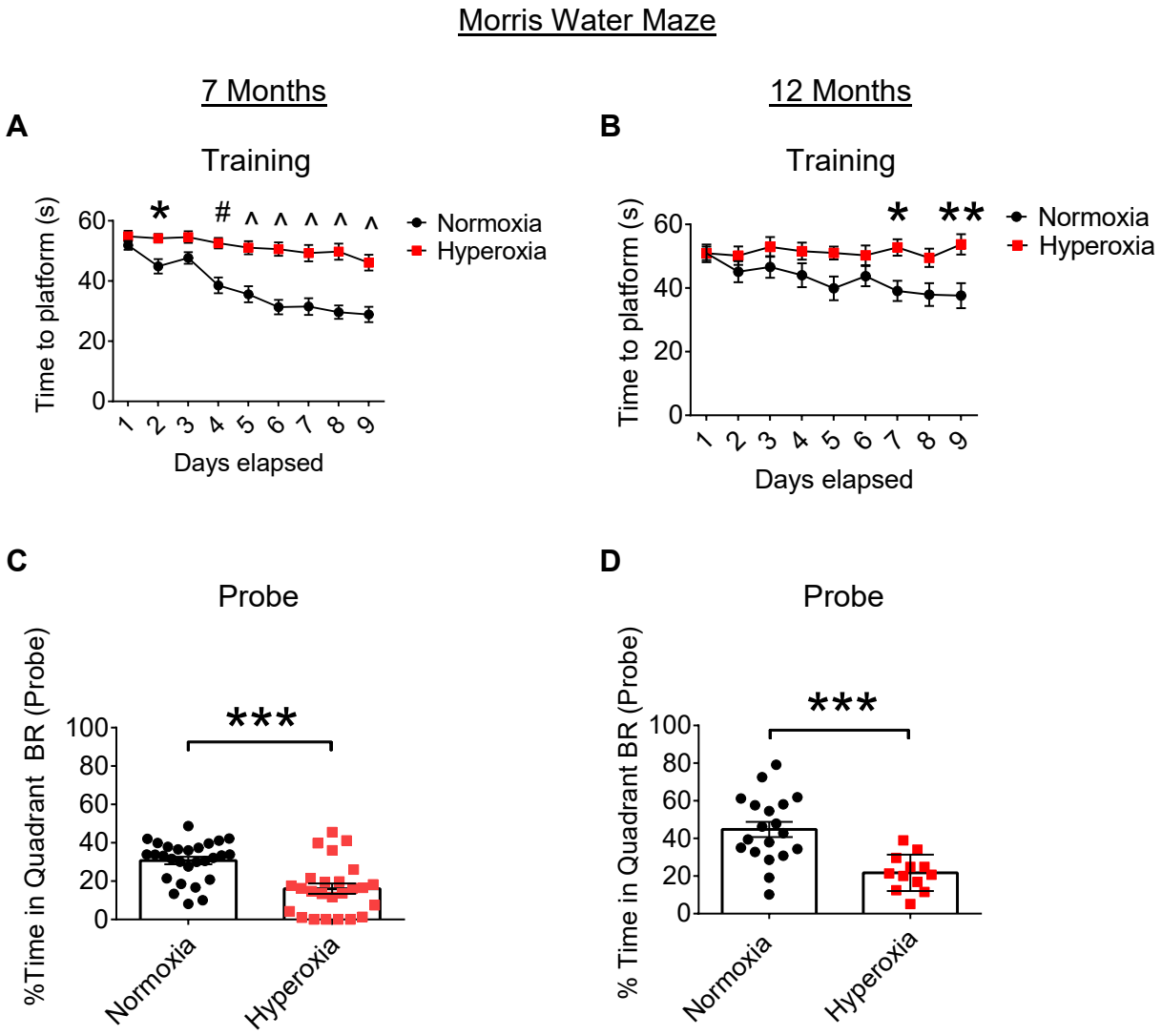

Supplemental Figure 7. Hyperoxia-exposed mice perform poorly on the Morris Water Maze (MWM) learning and memory assessment. (**A** and **B**) Amount of time for mice to reach the platform (s) during MWM training at 7 months (A, normoxia, n=28; hyperoxia, n=25) and 12 months (B, normoxia, n=19; hyperoxia, n=12). Two-way ANOVA with Sidak post hoc test for multiple comparisons. (**C** and **D**) Percent time that mice spent in the correct quadrant on the MWM test (probe) day at 7 months (C, normoxia, n=28; hyperoxia, n=25) and 12 months (D, normoxia, n=19; hyperoxia, n=12). *$P < 0.05$; ** $P < 0.01$; ***$P < 0.001$; #$P < 0.001$; ^$P < 0.0001$. Data are expressed as mean ± SEM.

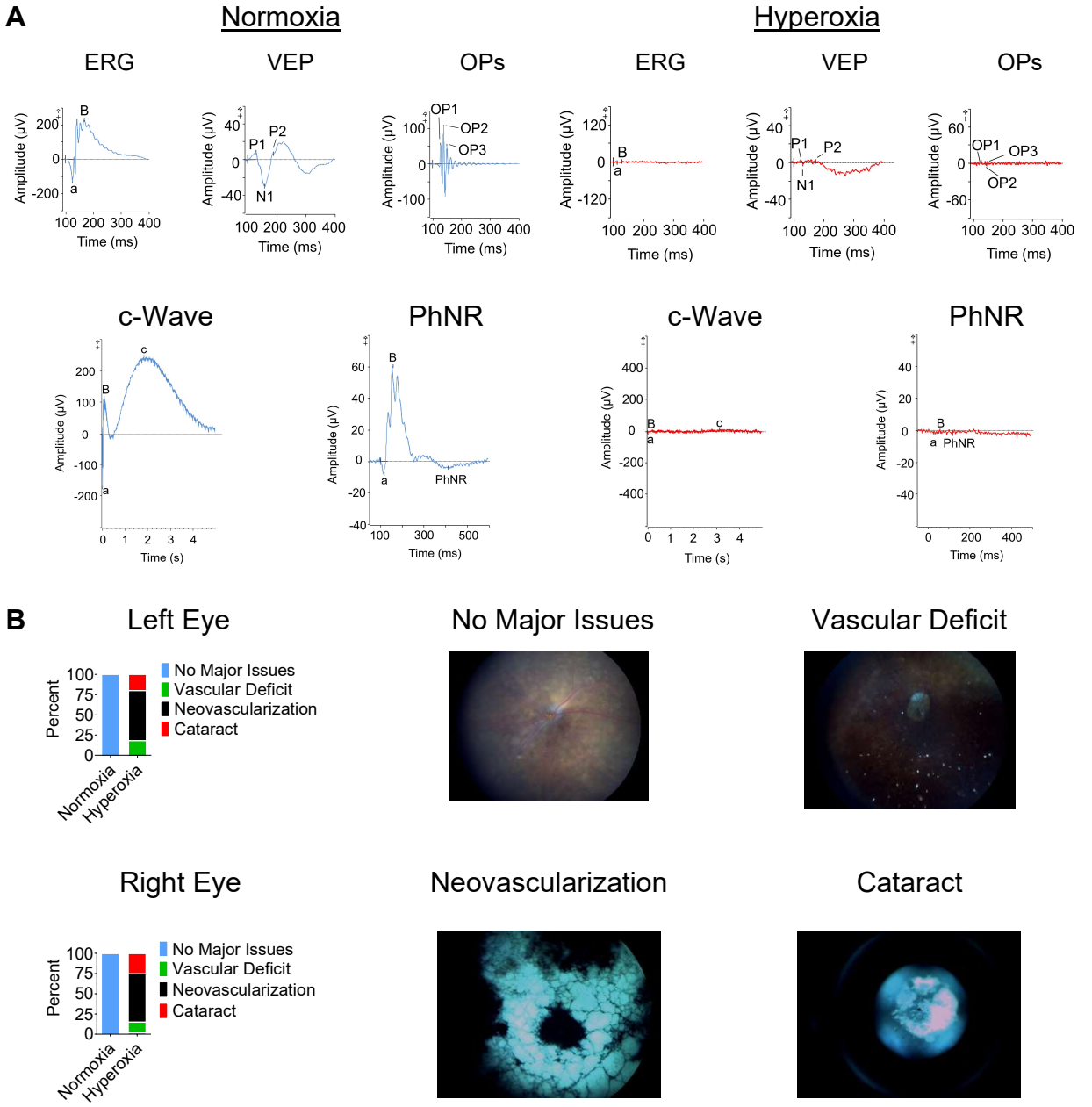

Supplemental Figure 8. Hyperoxia exposure causes major ocular damage to the retinal vasculature, leading to blindness. (**A**) Representative electrophysiological traces of retinas from normoxia (left) vs. hyperoxia (right)-exposed mice. ERG, electroretinography; VEP, visually evoked potentials; OPs, oscillatory potentials; PhNR, photopic negative response; P, positive; N, negative. Each wave represents the excitation of specific retinal cells: a-wave, cones and rods; b-wave, muller glia, bipolar cells; c-wave, retinal pigmented epithelium; VEPs, visually evoked signal in the visual cortex; OPs, amacrine cells; PhNR, retinal ganglion cells. (**B**) Quantification (%) of the number of mice with no major ocular issues, vascular deficits, neovascularization, and cataracts (left) of mice at 6, 9, and 15-17 months of age (normoxia, n=40; hyperoxia, n=45). Representative fundus images of retinas (right).

Supplemental Table 1. Antibody Information.

Antibody	Vendor	Catalogue Number	Dilution
Rat anti-CD31	BD Pharmingen	553370	1:200
Goat anti-Nestin	R&D Systems	AF2736	1:500
Rabbit anti-Sox2	Abcam	ab97959	1:500
Goat anti-Doublecortin	Santa Cruz	sc-8066	1:500
Donkey α-Rat IgG (H+L) Highly Cross-Adsorbed Secondary Antibody, Alexa Fluor 488	Invitrogen	A-21208	1:300
Donkey anti-Rabbit IgG (H+L) Highly Cross-Adsorbed Secondary Antibody, Alexa Fluor Plus 555	Invitrogen	A-32794	1:1000
Donkey anti-Goat IgG (H+L) Highly Cross-Adsorbed Secondary Antibody, Alexa Fluor Plus 647	Invitrogen	A-32849	1:1000

Appendix B – Supplemental Information for Manuscript 3

Pulmonary and Neurologic Effects of Mesenchymal Stromal Cell Extracellular Vesicles in a Multifactorial Lung Injury Model

Marissa A. Lithopoulos*, Lannae Strueby*, Megan O'Reilly, Shumei Zhong, Marius A. Möbius, Farah Eaton, Moses Fung, Maria Hurskainen, Chanèle Cyr-Depauw, Colin Suen, Liqun Xu, Jennifer J. P. Collins, Arul Vadivel, Duncan J. Stewart, Dylan Burger, Bernard Thébaud

*Authors contributed equally to this manuscript

Supplemental Methods

Multifactorial Lung Injury Model

Prior to surgical tracheostomy, neonatal mice received ketamine (60 µg/g, Bimeda-MTC Animal Health Inc.) combined with xylazine (12 µg/g, Bayer Animal Health). Response to painful stimulus was assessed prior to surgery and additional anesthesia was provided as required. Under a dissecting microscope a surgical tracheostomy was created and a custom tracheal tube, prepared using 24-gauge IV catheters (BD Insyte-W), was inserted and secured with sutures. Anesthetized pups received mechanical ventilation for 8 hours with 40% oxygen at a rate of 180 breaths/minute and a tidal volume of 10 µL/g using a small animal ventilator (MicroVent Model 848; Hugo Sachs Elektronik - Harvard Apparatus). Pups were continuously monitored throughout the 8 hours of ventilation with response to tactile stimulation assessed every 30 minutes to indicate depth of anesthesia. Additional doses of ketamine (20 µg/g)/xylazine (4 µg/g) solution were administered as required. Temperature was monitored using a mercury thermometer placed adjacent to pups during ventilation and thermal mattresses were adjusted to maintain a temperature between 30-35°C. The lung injury group displayed in Figure 25, contains all the experimental lung injury subjects over the course of the study (n=25). The lung injury group in subsequent figures contains only the lung injury subjects used for each specific experiment (Figure 28 n=16; Figure 31 n=9).

Human Umbilical Cord-Mesenchymal Stromal Cell Isolation and Culture

Human umbilical cord-mesenchymal stromal cells (UC-MSCs) were isolated and characterized as previously described (E1) in accordance with the minimal criteria for MSCs, as defined by The International Society for Cellular Therapy (E2). With consent of the parents, UC-MSCs were isolated from the umbilical cord after a term birth with no adverse complications. The umbilical cord was removed from the placenta, milked (to remove intravascular blood), and stored in a

solution of 30% citrate phosphate dextrose adenine anticoagulant in 1X phosphate buffered saline (PBS). The umbilical cord was disinfected with povidone-iodine (Purdue Pharma). To digest the cord, multiple incisions were made into the epithelium. Sterile cord tape (Ethicon) was utilized for vessel ligation, and the cord was incubated in a digestion solution, containing 750 U/mL collagenase and 500 U/mL hyaluronidase (both from Worthington) in Dulbecco's PBS with Ca2+, Mg2+, glucose, and pyruvate (Thermo Fisher Scientific), for 4 hours at 38°C. The cord was then incubated for an additional 30 minutes once 2,000 BAEE-U/mL trypsin and 3 mM ethylenediaminetetraacetic acid (EDTA) (both from MilliporeSigma) were added to the digestion solution. To stop the digestion, the solution was placed on ice and 10% fetal bovine serum (FBS, MilliporeSigma) was added. The solution was then filtered through a 40 μm strainer (BD Biosciences). The cells were washed in 1X PBS and plated in α-Minimum Essential Medium (MilliporeSigma) containing 20% FBS and antibiotics (Thermo Fisher Scientific) in plastic flasks treated for tissue culture purposes (Grenier Bio-One). The cells were cultured at 5% O_2 and 37°C. Cell media was changed every 3rd day and the cells were passaged using recombinant trypsin (Thermo Fisher Scientific) once they reached 80-90% confluency.

Conditioned Media Collection

Once the cells reached passage 4, they were washed with 1X PBS, and incubated in serum-free media for 24 hours. To remove cell debris, the medium was collected and centrifuged for 5 minutes at 300 *g* at 4°C. The supernatant was then transferred to an Amicon Ultra Centrifugal Filter Unit (MilliporeSigma) and centrifuged at 4,000 *g* at 4°C for 45 minutes. The concentrated conditioned media (CDM) was stored at -80°C until the EV isolation.

EV isolation and Characterization

All centrifugations were performed at 4°C. CDM was thawed on ice and centrifuged at 2,000 *g* for 10 minutes to remove debris. The supernatant was collected, transferred to a Centricon® Plus-70 Centrifugal Filter Unit (MilliporeSigma), and centrifuged at 3,500 *g* for 30 minutes. The filtrate was then discarded, and the sample was reconstituted with 1X PBS and centrifuged at 3,500 *g* for another 30 minutes. The filtrate was again discarded, the device was inverted, and the sample was centrifuged at 1,000 *g* for 2 minutes. The concentrate cup was then removed, and the supernatant was transferred to ultracentrifuge tubes. To further remove debris and larger vesicles, the supernatant was centrifuged at 10,000 *g* for 30 minutes and filtered through a 0.22 μm vacuum filter. The supernatant was then stored at -80°C. The following day, the microparticle solution was transferred to a polyallomer tube and centrifuged at 100,000 *g* for 70 minutes. The supernatant was removed, and the pellet was reconstituted in 1X PBS. The solution was then centrifuged at 100,000 *g* for 60 minutes. The supernatant was again removed, and the EV pellet was reconstituted in 1X PBS and stored at -80°C.

Dynamic Light-Scattering

Dynamic Light Scattering (DLS) measurements were performed with a ZetaSizer NanoS (Malvern Instruments, UK). EV isolates were diluted in 1X PBS to the required count rate of 50–300 kilocounts per second and equilibrated at 21°C. 2 × 10 measurement runs were performed, with standard settings (Refractive Index = 1.331, viscosity = 0.89, temperature = 21°C). Data are presented as the distribution of the mean hydrodynamic size of the particles.

Nanoparticle Tracking Analysis

Nanoparticle tracking analysis (NTA) was carried out using the ZetaView PMX110 Multiple Parameter Particle Tracking Analyzer (Particle Metrix, Meerbusch, Germany) using ZetaView software (version 8.02.28). EV isolates were diluted in 1X PBS to the working range of the system

and vesicle profiles were recorded and analyzed at 11 camera positions with a 2 second video length, a camera frame rate of 30 frames per second and a temperature of 21˚C.

CD63 Immunoblotting

EVs were incubated in Laemmlli buffer and heated to 97 °C for 5 minutes. They were then loaded onto 4-12% NuPage gels with a Novex pre-stained ladder and separated at 150 V for 70 minutes. The cell lysates were transferred onto a nitrocellulose membrane using the iBlot 1 system for 7 minutes at 25 V (Thermo Fisher Scientific) and then blocked for 1 hour in 5% milk with Tris Buffered Saline with Tween 20 (TBS-T). The membranes were incubated overnight at 4°C with an anti-CD63 antibody (1:200; Abcam) in 5% bovine serum albumin (BSA) in TBS-T. The following day the membranes were washed 3X with TBS-T and incubated with IRDye® 800CW goat anti-mouse IgG secondary antibody (1:10,000, LI-COR) for 1 hour. The membranes were washed 3X with TBS-T and imaged using the Odyssey Imaging System (LI-COR). An uncropped version of the blot can be found in Supplemental Figure 12.

Calnexin Immunoblotting

EVs were resuspended in radioimmunoprecipitation assay (RIPA) buffer and Laemmli sample buffer. Samples were sonicated in a water bath at 60 kHz for 10 seconds and gently vortexed for 10 seconds 3X. EVs were then boiled at 70° C for 10 minutes. The sample was loaded on a 4–20% Mini-PROTEAN® TGX™ Precast Protein Gel (Bio-Rad). The protein was run at 200 V for approximately 30 minutes. The gel was transferred to a polyvinylidene difluoride (PVDF) membrane (Thermo Fisher Scientific) using the iBlot System as described above. The membrane was then blocked in a 5% solution of skim milk in TBS-T buffer for 1 hour, while gently rocked on an orbital shaker at room temperature. The membrane was washed with TBS-T 3X (10 minutes each) on a slow-moving orbital rocker. The membrane was incubated overnight at 4°C on a slow-

moving orbital rocker, with an anti-calnexin antibody (1:1000; Cell Signaling Technology) diluted in 5% milk TBS-T solution. The following morning, the membrane was washed 3X with TBS-T as before. The membrane was then incubated with IRDye® 680LT donkey anti-rabbit IgG secondary antibody (1:15,000; LI-COR) diluted in 0.5% milk in TBS-T solution. The membrane was washed 3X with TBS-T as before, then imaged using the Odyssey Imaging System. An uncropped version of the blot can be found in Supplemental Figure 12.

Lung Morphometry and Immunohistochemistry

Lungs were fixed *in situ* via the trachea with a zinc formalin solution at a pressure of 20 cm H_2O. The trachea was ligated and the lungs were placed in zinc formalin overnight. Excess tissue was removed and the lungs were transferred to a 70% ethanol solution. Subsequently, the lungs were paraffin embedded, sectioned (5 μm thick) and stained with hematoxylin and eosin. Alveolar injury was quantified in the left lung in a blinded manner using the mean linear intercept (MLI) as an estimate of alveolar diameter. MLI was determined using a motorized microscope stage (Leica Microsystems) and OpenLab software. Briefly, in a minimum of 240 fields of view per lung, at 400x magnification, a 155.34 μm line was superimposed on each field of view and the number of alveolar septae crossing this line were counted. Multiplying the length of the line by the number of fields of view and dividing this product by the total number of intersections calculated the MLI for each animal.

Vascular quantification was performed by staining paraffin embedded left lung sections for von Willebrand Factor (vWF) (1:200, Dako). Sections were deparaffinized in an ethanol series and antigen retrieval was performed by incubating slides in heated sodium citrate buffer (10 mM pH 6.0) for 20 minutes, followed by blocking of endogenous peroxidase activity in 3% H_2O_2/1X PBS for 20 minutes. Non-specific binding was blocked by incubating in Tris-HCl/NaCl/BSA

buffer overnight at 4°C. Sections were incubated with vWF antibody (primary antibody) diluted in antibody diluent (Dako) for 45 minutes at room temperature followed by rinsing with 1X PBS. Sections were incubated with biotinylated goat anti-rabbit IgG secondary antibody (1:1000, Invitrogen) diluted in Dako antibody diluent for 1 hour at room temperature. Amplification of antibody signal was achieved by incubation with streptavidin-horseradish peroxidase (HRP) complex (1:1000 in Dako diluent; Invitrogen) for 30 minutes at room temperature and visualized with 3,3′-Diaminobenzidine (DAB) staining. Sections were then counterstained in Mayer's hematoxylin and dehydrated in an ethanol series.

Lung sections were analyzed using photographs taken at 400x magnification on a Leica microscope. The number of vWF-positive vessels were quantified by a blinded observer in fifteen representative high-power fields (HPF) per animal, using OpenLab software. The average number of vessels per HPF was calculated for each animal.

ELISAs

Lung tissue was snap frozen in liquid nitrogen and stored at -80°C for quantification of inflammatory cytokines. Frozen lung samples were homogenized in 0.5% Tween-20/1X PBS + protease inhibitor cocktail and centrifuged. Interleukin 1 beta (IL-1beta, R&D Systems) Macrophage Inflammatory Protein – 2 (MIP-2, R&D Systems) and Monocyte Chemoattractant Protein – 1 (MCP-1, R&D Systems) were quantified using an enzyme-linked immunosorbent assay (ELISA). Assay procedures were conducted according to manufacturer instructions.

***In Vitro* Flow Cytometry Analysis**

Lungs were harvested immediately after ventilation. Prior to harvesting, lungs were perfused through the pulmonary artery with cold 1X PBS for blood removal. The lobes were separated and the tissue was processed with the GentleMACS OCtoHeater (Miltenyi Biotec, programme LDK1)

in digestion buffer containing 30 U neutral protease (Worthington Biochemical Corporation), 2,500 U collagenase type 1 (Worthington Biochemical Corporation), and 500 U DNAseI (MilliporeSigma) in 10 ml of Dulbecco's PBS (DPBS) with Calcium and Magnesium (Thermo Fisher Scientific). The sample was filtered through a 70 μm filter (Thermo Fisher Scientific) and washed twice in cold fluorescence-activated cell sorting (FACS) buffer (5% FBS, MilliporeSigma) in 1X PBS with 0.5 mM EDTA. Fc blocking step was performed using CD16/32 antibody (BD Biosciences). After tissue dissociation, lung cells were stained with CD11b-APCCy7 (BD Biosciences), CD45-FITC (eBioscience), CD64-PE (BioLegend), Ly6C-eFluor450 (eBioscience), Ly6G-AF700 (BD Biosciences), SigleCF-AF647 (BD Biosciences), MHCII-PerCPCy5.5 (BD Biosciences) and Fixable Viability Stain 510 (BD Biosciences) antibodies. After staining, samples were fixed with 4% paraformaldehyde (PFA). Fluorescence minus one, single, and no stain controls were used as necessary. Flow cytometry was performed by the Ottawa Hospital Research Institute core facility using BD LSRFortessa (Beckton Dickinson Biosciences). Sample compensation was performed with BD FACSDIVA software and data was analyzed using FlowJo v10 (FlowJo LLC).

NPC Isolation and Culture

Isolation: Brains were collected and weighed. NPCs were isolated and cultured using adapted methods from Fujitani et al (E3). Briefly, the subependymal region of the lateral ventricles and the hippocampi were dissected from the brain tissue, mechanically separated, and enzymatically digested with papain (Worthington). The digestion was stopped with 10% FBS in Dulbecco's Modified Eagle Medium/Nutrient Mixture F-12 (DMEM/F-12) media (Thermo Fisher Scientific) and the cells were purified using a 40 μm filter unit (Corning). The cells were plated in DMEM/F-12 containing 2% B-27 (Life Technologies), 20 ng/mL fibroblast growth factor-2

(MilliporeSigma), 20 ng/mL epidermal growth factor (MilliporeSigma), 2 µg/mL heparin (MilliporeSigma), and 1% antibiotic-antimycotic (Thermo Fisher Scientific) in ultra-low attachment plates (Corning). The cells were cultured at 37°C and 21% O_2.

Neurosphere Assays: NPCs were plated for a primary neurosphere assay at a limiting dilution of 10 cells/µL. After 7-8 days, neurospheres were counted and imaged. The neurospheres were then separated into single cells using TrypLE™ Express Enzyme (Thermo Fisher Scientific). The reaction was stopped using 10% FBS in DMEM/F-12. The cells were then washed in DMEM/F-12 and plated for a secondary neurosphere assay in the media described above at a limiting dilution of 2 cells/µL. The neurospheres were counted and imaged after 7-8 days in culture. The images were acquired at 20x magnification on a Nikon Eclipse TE2000-E microscope.

Differentiation Assay: The neurospheres were again separated into single cells and washed as described above. The single cells were then plated as a monolayer on laminin (Thermo Fisher Scientific) coated plates at a minimal density of 40 cells/µL in media containing DMEM/F-12 with 1% FBS, 1% N-2 (Thermo Fisher Scientific), 2 µg/mL heparin, and 1% antibiotic-antimycotic. Removal of critical NPC growth factors (epidermal growth factor and fibroblast growth factor-2) and the addition of FBS induces spontaneous differentiation. After 7 days of culture, the cells were fixed with 4% PFA. The cells were then incubated in blocking solution (3% BSA in 1X PBS) for 1 hour at room temperature. The cells were incubated overnight at 4°C with an antibody for O4 (1:500; R & D systems) in blocking solution. The following day, the plates were washed 3X with 1X PBS and the cells were permeabilized with 0.1% Triton X-100 in 1X PBS for 10 minutes at room temperature. The cells were then washed twice for 5 minutes with 1X PBS. The cells were incubated overnight at 4°C with antibodies for glial fibrillary acidic protein (1:500; Dako) and Tuj1 (1:500; R & D Systems) in blocking solution. The following day, the cells were washed 3X

with 1X PBS and incubated for 1 hour at room temperature with DAPI (1:200, Invitrogen) and the following secondary antibodies (1:1000): Cy3 conjugated affiniPure F(ab')2 Fragment Donkey Anti-mouse IgM, u chain Specific (Jackson ImmunoResearch), Alexa Fluor 488 donkey anti-rabbit IgG (Thermo Fisher Scientific), and Alexa Fluor 647 donkey anti mouse IgG (Thermo Fisher Scientific) (used to identify cell nuclei, oligodendrocytes, astrocytes, and neurons, respectively). The cells were then washed 3X with 1X PBS and stored in 1X PBS in the dark at 4°C. High throughput, full scans of the wells (10x magnification) were acquired and analysed using the ArrayScan VTI (Thermo Fisher Scientific). Data was quantified as the percent of cells that differentiated into astrocytes (identified with glial fibrillary acidic protein, GFAP), neurons (identified with neuron specific β3 tubulin, Tuj1), and oligodendrocytes (identified with oligodendrocyte marker 4, O4).

CDM In Vitro Assay: UC-MSC CDM was collected as described above. CDM (3.4 μL/well of 9.5 cm^2) was added at plating to the freshly isolated NPCs from ventilated mice. The amount of CDM was calculated to correspond to the amount produced/ cm^2 by the UC-MSCs in culture. The primary and secondary neurosphere assays were then conducted as described above. Secondary neurosphere counts were compared to NPCs from ventilated animals that did not receive *in vitro* CDM (as shown in Figure 28).

Conditioned Media *In Vivo* Distribution

The lung distribution of intratracheally administered MSC CDM was assessed utilizing MSC CDM in a 1:1 ratio with fluorescent dye (CellBrite Cytoplasmic Membrane Dye, Biotium Inc.) at a total volume of 3 μL/g. Following injection, the surgical tracheostomy was created and pups were mechanically ventilated for 30 minutes with 40% oxygen at a rate of 180 breaths/minute

and tidal volume of 10 μL/g. Distribution of MSC CDM/fluorescent dye was visualized using In-vivo Imaging System FX PRO (Bruker Molecular Imaging).

IVIS® Spectrum DiR EV Tracing Experiment

EVs were isolated as described above. EVs were incubated with DiR (Thermo Fisher Scientific) for 15 minutes at room temperature in the dark. EVs were then ultracentrifuged at 100,000 *g* for 90 minutes. The supernatant was removed and the EVs were resuspended in 1X PBS to produce a final concentration of 0.0017 μg/μL. The EVs or 1X PBS (placebo) were injected in ventilated experimental animals as described above. Mice were ventilated for 1 or 4 hours. Following euthanasia, the lungs and the brain of animals were imaged using the IVIS Spectrum in vivo imaging system (PerkinElmer) at 745 nm of excitation and 800 nm of emission. Image display and quantification were adapted from methods described by Kang et al. (E4). The images were displayed as the count measurements (uncalibrated values of photons in a pixel), to normalize between images acquired at varying time points. The fluorescent signal of a region of interest (ROI) was measured using the Living Image Software (version 3.2, Caliper Lifesciences) as the average radiance (number of photons per second per centimeter square per steradian; $p/s/cm^2/sr$), which is a calibrated value of photon emission. Background fluorescence was measured from mice injected with 1X PBS and subtracted from the values of EV injected mice (Supplemental Table 2 and 3).

PKH26 EV Tracing Experiment

EVs were isolated as described above. EVs were incubated with PKH26 (MilliporeSigma) for 10 minutes at room temperature in the dark. EVs were then ultracentrifuged, processed, and injected as described in the DiR labelling methods above. Following ventilation, lungs were perfused with 1X PBS and optimal cutting temperature compound (OCT, 1:1), embedded in OCT and frozen at

-80°C. The lung tissue was cut using a cryostat into 8 µm thick sections and mounted onto slides using Fluoroshield with DAPI (MilliporeSigma). The brains were fixed overnight at 4°C in 4% PFA. The brains were then transferred to a 20% sucrose solution in 1X PBS until they sank to the bottom of the Falcon tube. The brains were embedded in OCT and frozen at -80°C. Brain tissue was cut coronally into 20 µm free-floating sections in 1X PBS. The sections were then mounted onto slides using Fluoroshield with DAPI (Sigma). Lung and brain tissue were imaged at 100x magnification using a Zeiss Axio Imager M2 microscope with an ApoTome.2 system. Three-dimensional 8 µm z-stack images were acquired and displayed as maximum intensity Z-projections. Due to the stronger intensity of the fluorescent signal in the lung tissue, the lung images are shown at a different intensity than the brain images to display an accurate signal.

Total RNA extraction and quantitative RT-qPCR

Lungs were harvested and snap frozen. For RNA isolation, tissue was lysed as previously described (E5), and total RNA was extracted using RNeasy Plus Mini Kit (Qiagen) according to the manufacturer's protocol. RNA concentration and quality were assessed by NanoDrop spectrophotometer (ThermoFisher Scientific) and subjected to reverse transcription-quantitative PCR (RT-qPCR) as previously described (E6). Briefly, cDNA was synthesized using iScript™ Reverse Transcription Supermix (Bio-Rad). RT-qPCR analysis was performed using CFX96 or CFX384 Touch Real Time PCR (Bio-Rad), and iQ™ SYBR Green Supermix (Bio-Rad). The primer sequences used were as follow: *Il4* forward*, 5'*-GGTCTCAACCCCCAGCTAGT-3'; *Il4* reverse, 5'-GCCGATGATCTCTCTCAAGTGAT-3'; *Il10* forward, 5'-GCTTCATCCCTGAAAACTGT-3'; *Il10* reverse, 5'-GGCAGACAAACAATACACCA-3'; *Il13* forward, 5'-GATTCCCTGACCAACATCTC-3'; *Il13* reverse, 5'-AGTGGGCTACTTCGATTTTG-3'; *Il33* forward, 5'- CCCTGGTCCCGCCTTGCAAAA-3';

Il33 reverse, 5'- AGTTCTCTTCATGCTTGGTACCCGA-3'; *Il6* forward, 5'-CTCTGGGAAATCGTGGAAATG-3'; *Il6* reverse, 5'- CAAGTGCATCATCGTTGTTCATAC-3'; *Il1b* forward, 5'- ATGGAATCCGTGTCTTCCTA-3'; Il1b reverse, 5'-CTAAGGAGTCCCCTGGAGAT-3'; *Tnfa* forward, 5'-TCTACTGAACTTCGGGGTGA-3'; *Tnfa* reverse, 5'-CTCCTCCACTTGGTGGTTTG-3'; *Cxcl1* forward, 5'-GACCATGGCTGGGATTCACC-3'; *Cxcl1* reverse, 5'-TCAGAAGCCAGCGTTCACCA-3'; *Tgfb1* forward*, 5'*-AGCCCGAAGCGGACTACTAT-3'; *Tgfb1* reverse, 5'-CCCGAATGTCTGACGTATTG-3'. The normalized expression level of the target genes for each condition was calculated using the average threshold cycle value from triplicate measurements by the Pfaffl method (6). *Hprt* was identified as a stable housekeeping gene using geNorm and BestKeeper.

Multiplex Assay

Lung tissue homogenates were diluted to equal amount of protein (3,130 µg/mL). Cytokines/chemokines were quantified simultaneously by Eve Technologies Corp, Calgary, AB, Canada using a Discovery Assay (Mouse Cytokine Array / Chemokine Array 31-Plex). The minimum detectable concentration starts at 0.3 pg/mL. Values were normalized to the total amount of protein/ sample.

Supplemental Table 2. Average radiance measurements of brain tissue. Average radiance of the PBS control was subtracted from the average radiance of the brain of each EV injected pup.

Animal	Average Radiance ($p/s/cm^2/sr$)	Average Radiance of PBS Control ($p/s/cm^2/sr$)	Final Average Radiance Value ($p/s/cm^2/sr$)
1 (1 Hour)	2,485,000	2,431,000	54,000
2 (1 Hour)	2,469,000	2,431,000	38,000
3 (1 Hour)	2,525,000	2,431,000	94,000
4 (4 Hours)	2,589,000	2,426,000	163,000
5 (4 Hours)	2,560,000	2,426,000	134,000
6 (4 Hours)	2,561,000	2,426,000	135,000
7 (4 Hours)	2,590,000	2,426,000	164,000

Supplemental Table 3. Average radiance measurements of lung tissue. Average radiance of the PBS control was subtracted from the average radiance of the lung of each EV injected pup.

Animal	Average Radiance ($p/s/cm^2/sr$)	Average Radiance of PBS Control ($p/s/cm^2/sr$)	Final Average Radiance Value ($p/s/cm^2/sr$)
1 (1 Hour)	5,502,000	2,408,000	3,094,000
2 (1 Hour)	11,300,000	2,408,000	8,892,000
3 (1 Hour)	14,250,000	2,408,000	11,842,000
4 (4 Hours)	15,340,000	2,443,000	12,897,000
5 (4 Hours)	9,105,000	2,443,000	6,662,000
6 (4 Hours)	13,370,000	2,443,000	10,927,000
7 (4 Hours)	12,040,000	2,443,000	9,597,000

References (Supplemental Methods)

E1. Zhu Y, Xu L, Collins JJP, Vadivel A, Cyr-Depauw C, Zhong S, Mense L, Möbius MA, Thébaud B. Human Umbilical Cord Mesenchymal Stromal Cells Improve Survival and Bacterial Clearance in Neonatal Sepsis in Rats. *Stem Cells Dev* 2017;26:1054–64.

E2. Dominici M, Le Blanc K, Mueller I, Slaper-Cortenbach I, Marini F, Krause D, Deans RJ, Keating A, Prockop DJ, Horwitz EM. Minimal criteria for defining multipotent mesenchymal stromal cells. The International Society for Cellular Therapy position statement. *Cytotherapy* 2006;8:315–7.

E3. Fujitani M, Cancino GI, Dugani CB, Weaver ICG, Gauthier-Fisher A, Paquin A, Mak TW, Wojtowicz MJ, Miller FD, Kaplan DR. TAp73 acts via the bHLH Hey2 to promote long-term maintenance of neural precursors. *Curr Biol* 2010;20:2058–65.

E4. Kang MH, van Lieshout LP, Xu L, Domm JM, Vadivel A, Renesme L, Mühlfeld C, Hurskainen M, Mižíková I, Pei Y, van Vloten JP, Thomas SP, Milazzo C, Cyr-Depauw C, Whitsett JA, Nogee LM, Wootton S, Thébaud B. A lung tropic AAV vector improves survival in a mouse model of surfactant B deficiency. *Nat Commun* 2020;11:3929.

E5. Cyr-Depauw C, Hurskainen M, Vadivel A, Mižíková I, Lesage F, Thébaud B. Characterization of the innate immune response in a novel murine model mimicking bronchopulmonary dysplasia. *Pediatr Res* 2021;89:803-813.

E6. Pfaffl MW. A new mathematical model for relative quantification in real-time RT-PCR. Nucleic Acids Res 2001;29:e45.

Supplemental Data

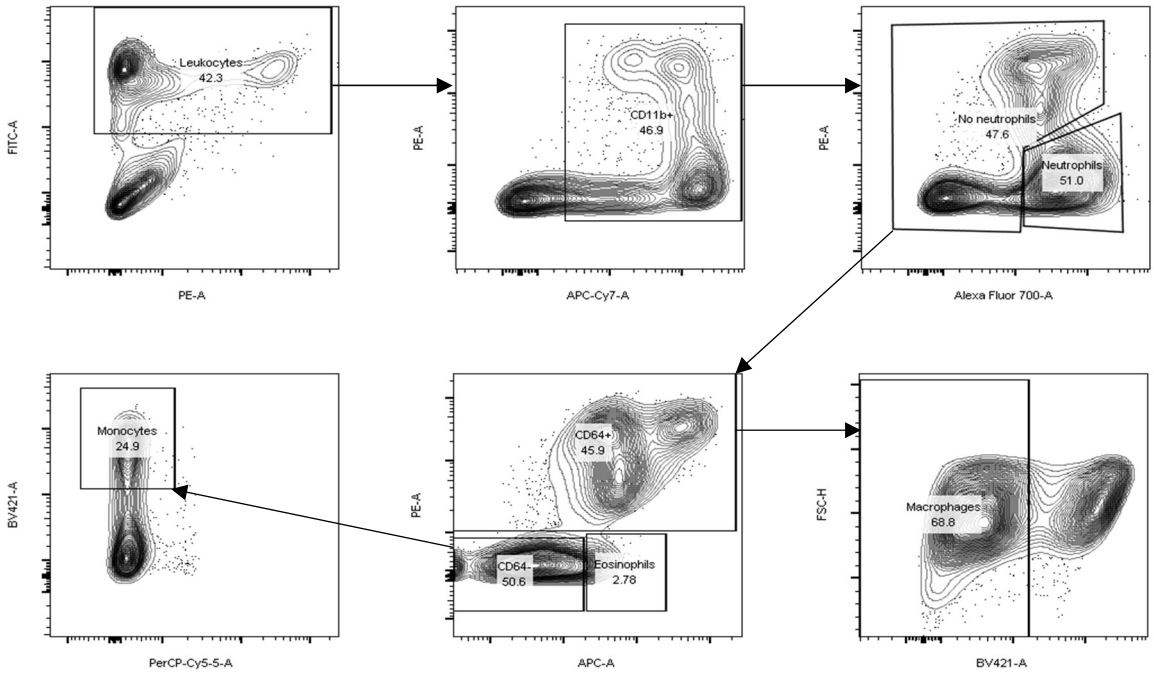

Supplemental Figure 9. Representative flow cytometry gating strategy used to identify immune cells. Mouse lung tissue was dissociated and live immune cells were identified as CD45-FITC^{+} (leukocytes) and CD11b-APC-Cy7^{+}. The specific immune cell populations were further defined as follows: neutrophils (Ly6G-AF700^{+}), monocytes (CD64-PE^{-}, SiglecF-AF647^{-}, Ly6G-AF700^{-}, MHCII-PerCPCy5.5^{-}, Ly6C-eFluor450^{+}), macrophages, (CD64-PE^{+}, Ly6C-eFluor450^{-}) and eosinophils (SiglecF-AF647^{+}, CD64-PE^{-}). FSC-H, forward scatter height.

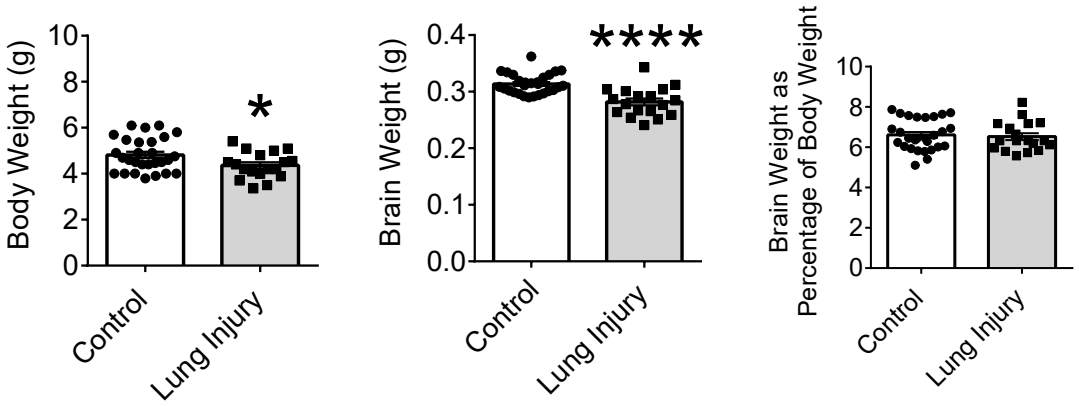

Supplemental Figure 10. A multifactorial lung injury model incorporating mechanical ventilation, supplemental oxygen, and inflammation leads to reduced body and brain weight in neonatal mice. Mice were exposed to intraperitoneal lipopolysaccharide (4 μg/g) at postnatal day (P)7/8 and 8 hours of mechanical ventilation (40% O_2) at P9/10. Following mechanical ventilation mice were assessed for body and brain weight (control n=29; lung injury n=19). *$P < 0.05$, ****$P < 0.0001$. Unpaired Student's t-test. Data are represented as mean ± SEM.

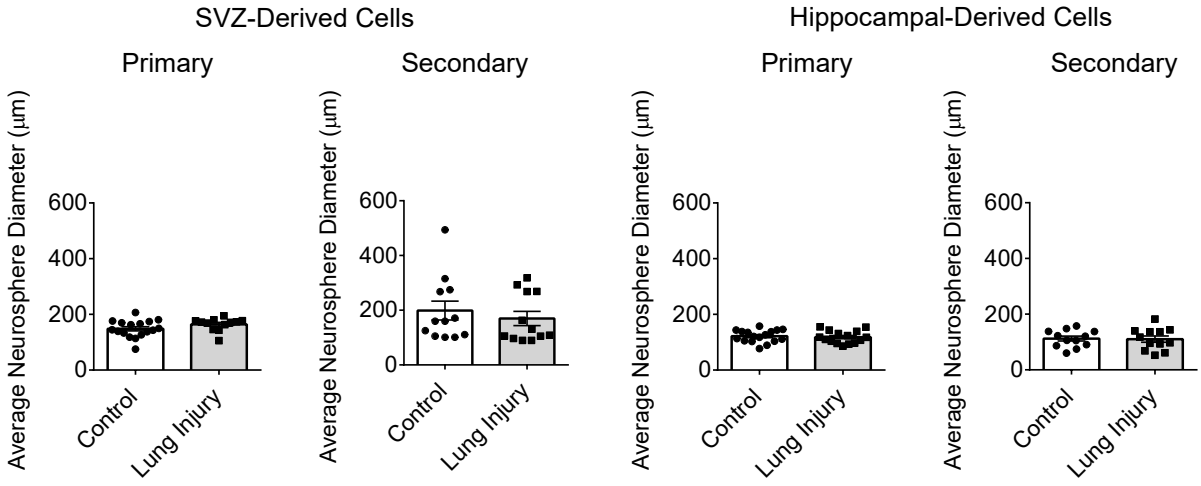

Supplemental Figure 11. No significant differences were found between the control and lung injury groups in terms of average neurosphere diameter (μm). Mice were housed in room air (control) or exposed to noxious stimuli as described above (lung injury). Neural progenitor cells were isolated from the subventricular zone (SVZ) and hippocampus and plated for sequential neurosphere assays. Neurosphere diameter (μm) was measured from approximately 30 fields of view per sample and averaged. Primary SVZ-derived neurospheres (control n=17; lung injury n=12); secondary SVZ-derived neurospheres (control n=12; lung injury n=12); primary hippocampal-derived neurospheres (control n=17; lung injury n=15); secondary hippocampal-derived neurospheres (control n=12; lung injury n=12). Unpaired Student's t-test. Data are represented as mean ± SEM.

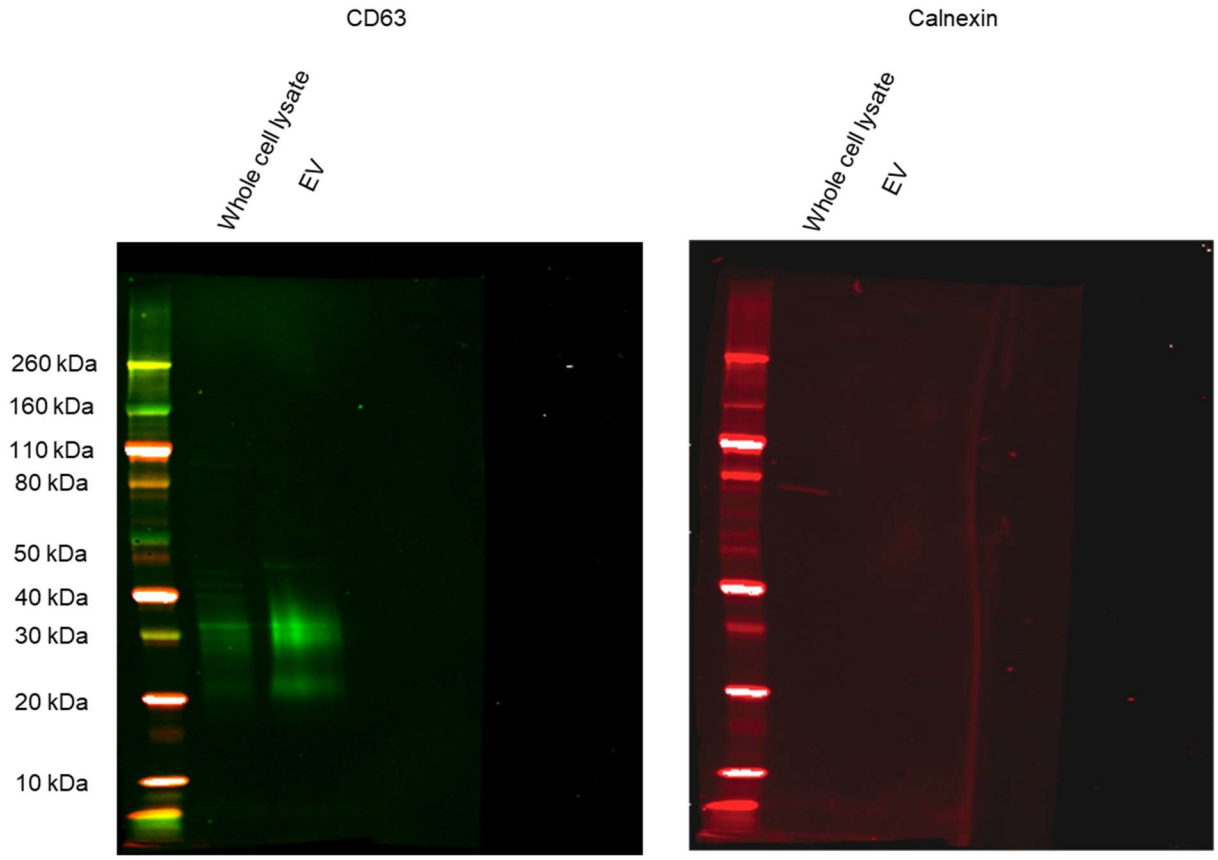

Supplemental Figure 12. Western blots of positive extracellular vesicle (EV) marker CD63 and negative EV marker calnexin. Western blots of UC-MSC whole cell lysate and EVs probed with an anti-CD63 antibody (left) and an anti-calnexin antibody (right).

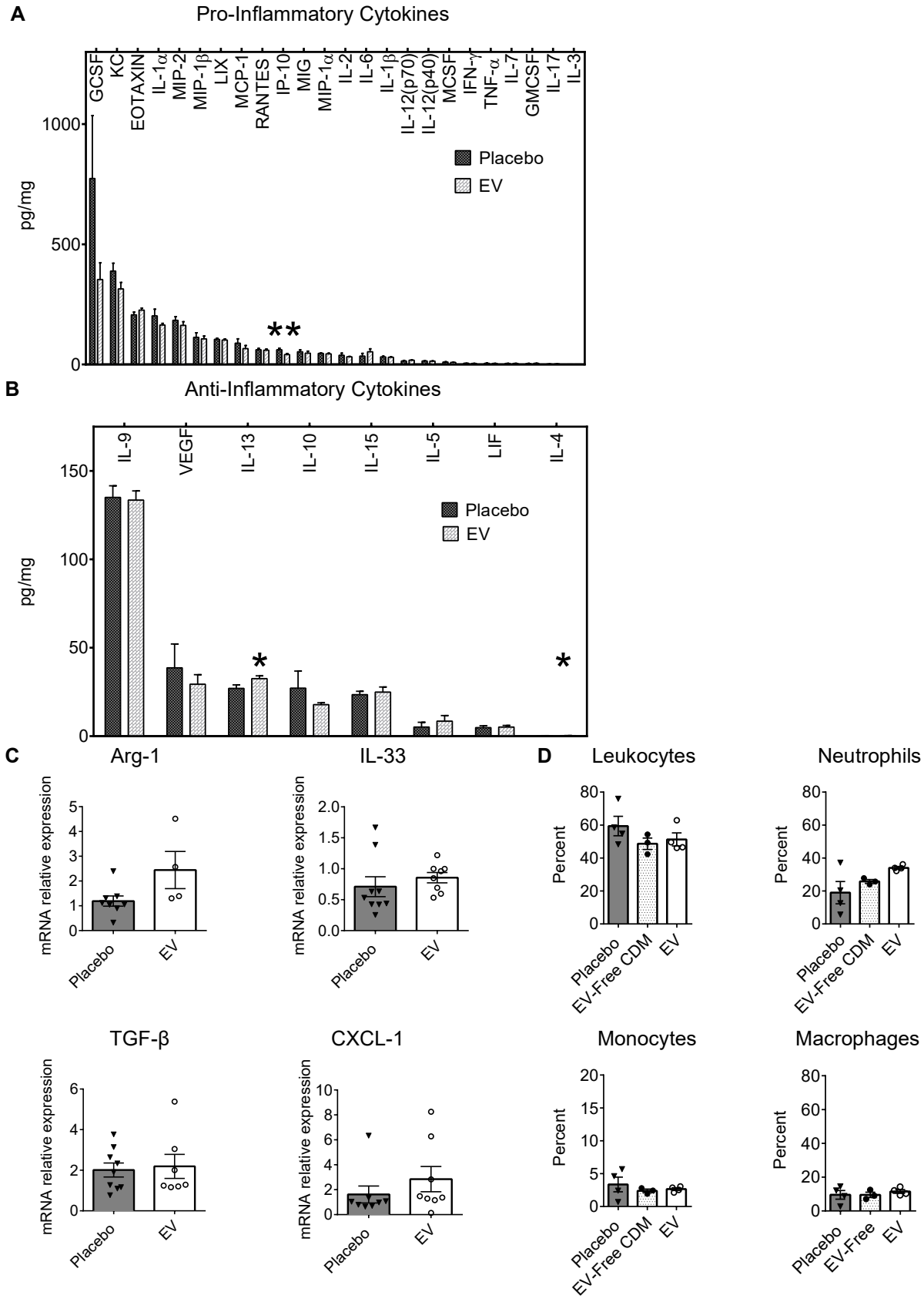
A
Pro-Inflammatory Cytokines
GCSF
KC
EOTAXIN
IL-1α
MIP-2
MIP-1β
LIX
MCP-1
RANTES
IP-10
MIG
MIP-1α
IL-2
IL-6
IL-1β
IL-12(p70)
IL-12(p40)
MCSF
IFN-γ
TNF-α
IL-7
GMCSF
IL-17
IL-3
pg/mg
1000
500
0
Placebo
EV
**
B
Anti-Inflammatory Cytokines
IL-9
VEGF
IL-13
IL-10
IL-15
IL-5
LIF
IL-4
pg/mg
150
100
50
0
Placebo
EV
*
*
C
Arg-1
IL-33
TGF-β
CXCL-1
mRNA relative expression
Placebo
EV
D
Leukocytes
Neutrophils
Monocytes
Macrophages
Percent
Placebo
EV-Free CDM
EV
EV-Free

Supplemental Figure 13. Extracellular vesicle (EV) treated mice have an increased expression of anti-inflammatory cytokines interleukin (IL)-13 and IL-4 and a decreased expression of pro-inflammatory cytokine interferon gamma-induced protein (IP)-10 compared to placebo (PBS) treated mice. Mice were exposed to intraperitoneal lipopolysaccharide at postnatal day (P)7/8. At P9/10, mice were treated with either umbilical cord-mesenchymal stromal cell-derived EVs or placebo (PBS) and mechanically ventilated (40% O_2) for 8 hours. Lung tissue was dissociated and assessed for cytokine levels and immune cells. (*A*) There was a significant decrease in IP-10 protein expression in the lungs of EV treated mice compared to placebo treated mice (placebo n=6; EV n=8). (*B*) There was a significant decrease in IL-13 and IL-4 protein expression in the lungs of EV treated mice compared to placebo treated mice (placebo n=6; EV n=8). (*C*) There were no significant differences found in mRNA expression between groups for arginase-1 (Arg-1, placebo n=8; EV n=4), IL-33 (placebo n=9; EV n=8), transforming growth factor (TGF)-β (placebo n=9; EV n=7), and C-X-C motif ligand-1 (CXCL-1, placebo n=8; EV n=8). (*D*) There were no significant differences found between groups in terms of immune cell quantity (placebo n=4; EV-free CDM n=3; EV n=4). **P* < 0.05, ***P* < 0.01. For data represented as >3 groups, a multiple t-test was conducted with a Holm-Sidak post hoc test. For data represented as >2 groups, a one-way ANOVA was conducted with a Tukey post hoc test. For data represented as 2 groups, an unpaired Student's t-test was conducted. Data are represented as mean ± SEM. GCSF, granulocyte colony stimulating factor; KC, keratinocyte chemoattractant; MIP, macrophage inflammatory protein; LIX, C-X-C motif ligand-5; MCP-1, monocyte chemoattractant protein-1; RANTES, regulated on activation, normal T cell expressed and secreted; MIG, monocyte induced by gamma interferon; p70, 70 kDa; p40, 40kDa; MCSF, macrophage colony-stimulating factor; IFN-γ, interferon-γ; TNF-α, tumour necrosis factor-α; GMCSF, granulocyte-macrophage colony-stimulating factor; VEGF, vascular endothelial growth factor; LIF, leukemia inhibitory factor.

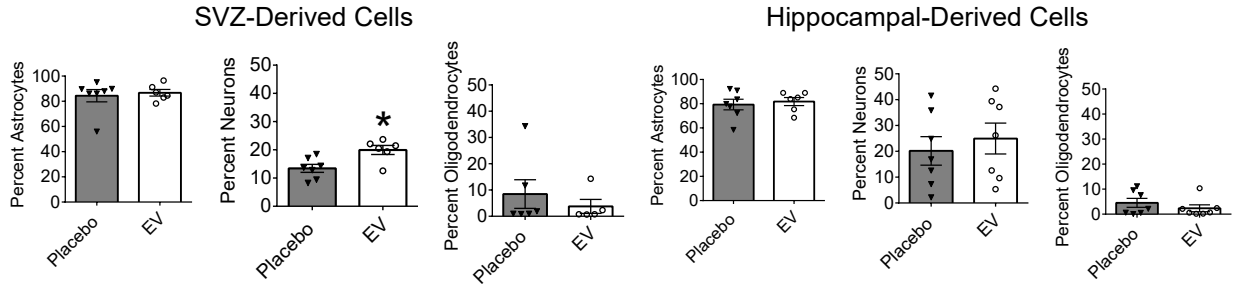

Supplemental Figure 14. Increased neuronal differentiation from SVZ NPCs isolated from ventilated mice treated with extracellular vesicles (EVs). Neonatal mice were injected intraperitoneally with LPS at P7/8. At P9/10 mice were treated intratracheally with placebo (PBS) or EVs and mechanically ventilated for 8 hours. NPCs were isolated from the subventricular zone (SVZ) and hippocampus and allowed to spontaneously differentiate into the three brain lineages (astrocytes, neurons, oligodendrocytes). SVZ-derived cells (percent astrocytes: placebo n=7, EV n=6; percent neurons: placebo n=7, EV n=6; percent oligodendrocytes: placebo n=6, EV n=5). Hippocampal-derived cells (percent astrocytes: placebo n=7, EV n=6; percent neurons: placebo n=7, EV n=7; percent oligodendrocytes: placebo n=7, EV n=7). **P* < 0.05. Unpaired Student's t-test. Data are represented as mean ± SEM.

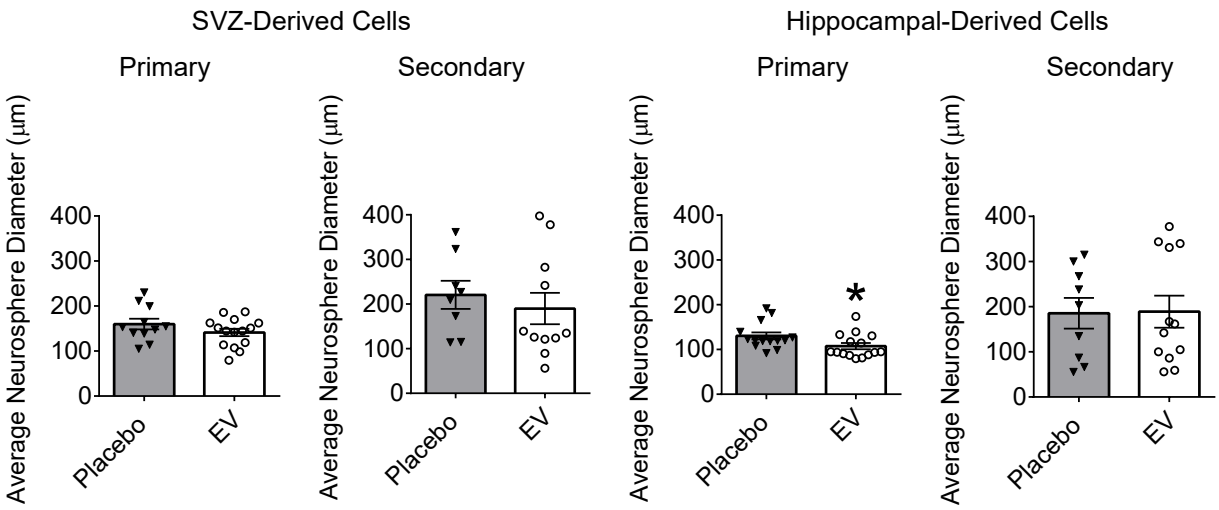

Supplemental Figure 15. Hippocampal NPCs from EV treated mice formed on average, smaller primary neurospheres compared to those from placebo treated animals. Neonatal mice were exposed to inflammation, mechanical ventilation, and supplemental oxygen and treated with either placebo (PBS) or extracellular vesicles (EVs) as described above. Neural progenitor cells (NPCs) were isolated from the subventricular zone (SVZ) and hippocampus of mice. NPCs were plated for primary and secondary neurosphere assays. Neurosphere diameter (μm) was measured from approximately 30 fields of view per sample and averaged. Primary SVZ-derived neurospheres (placebo n=11; EV n=15); secondary SVZ-derived neurospheres (placebo n=8; EV n=11); primary hippocampal-derived neurospheres (placebo n=14; EV n=15); secondary hippocampal-derived neurospheres (placebo n=9; EV n=12). **P* < 0.05. Unpaired Student's t-test. Data are represented as mean ± SEM.